

Comprehensive Study of Secondary Organic Aerosol Particles from the Amazon Rainforest by High-Resolution Mass Spectrometry

Dissertation
zur Erlangung des Grades
„Doktor der Naturwissenschaften“
im Promotionsfach Chemie

am Fachbereich Chemie, Pharmazie, Geographie und
Geowissenschaften
der Johannes Gutenberg-Universität in Mainz

vorgelegt von
Denis Leppla
Geboren in Speyer

Mainz, Februar 2021

Dekan:

1. Gutachter:

2. Gutachter:

Tag der mündlichen Prüfung: 23.04.2021

D77 Dissertation der Johannes Gutenberg-Universität Mainz

I hereby declare that I wrote the dissertation submitted without any unauthorized external assistance and used only sources acknowledged in the work. All textual passages which are appropriated verbatim or paraphrased from published and unpublished texts as well as all information obtained from oral sources are duly indicated and listed in accordance with bibliographical rules. In carrying out this research, I complied with the rules of standard scientific practice as formulated in the statutes of Johannes Gutenberg University Mainz to insure standard scientific practice.

Mainz, February 25, 2021

“You just said a bunch of stuff I don’t know.”

Joey Tribbiani

Zusammenfassung

Die meisten chemischen Prozesse in der Atmosphäre werden durch anorganische und organische Spurenverbindungen wie Stickstoffdioxid, Ozon, Kohlenwasserstoffe, Aromaten oder Terpenoide gesteuert. Im Allgemeinen befinden sich diese Substanzen in der Gasphase. Durch atmosphärische Reaktionen und Umwandlungen können jedoch Moleküle mit ausreichend geringer Flüchtigkeit gebildet werden, um sich in der Partikelphase anzureichern. Die daraus entstehenden Aerosole haben je nach ihren physikalisch-chemischen Eigenschaften erhebliche Auswirkungen auf das Klima der Erde. So wird durch Aerosole der globale Energiehaushalt beeinflusst, da die Partikel Sonnenstrahlung absorbieren und streuen können. Außerdem sind sie an den Prozessen zur Wolkenbildung beteiligt und steuern dabei die Anzahl und Lebensdauer. Vor allem in städtischen Regionen sind Aerosole für verminderte Sichtverhältnisse und menschliche Atemwegs- und Herz-Kreislauf-Erkrankungen verantwortlich. Folglich hat die Erforschung atmosphärischer Aerosole und deren Auswirkungen auf die Umwelt in den letzten Jahrzehnten an Aufmerksamkeit dazu gewonnen.

Insbesondere organische Aerosole (OA) machen einen bedeutenden Anteil des luftgetragenen Feinstaubes (*particulate matter*, PM) aus und bestehen in der Regel aus unzähligen verschiedenen Verbindungen. Die chemische Zusammensetzung von Aerosolen ist hochdynamisch und verändert sich kontinuierlich noch lange nach der Entstehung durch atmosphärische Prozesse. Um die OA-Bildung sowie die chemische Umwandlung nachzuvollziehen, müssen spezifische Markerspezies zuverlässig identifiziert und quantifiziert werden. Die zeitliche und räumliche Variabilität der OA-Zusammensetzung stellt jedoch erhebliche Anforderungen an derzeitige Analysetechniken. Massenspektrometrie (MS) hat sich als geeignetes Werkzeug für die Analyse von Aerosolen etabliert. Die Entwicklung von Geräten mit hohem Auflösungsvermögen und Massengenauigkeit ermöglichte die Untersuchung von Aerosolpartikeln auf molekularer Ebene. Trotz des großen Potenzials der ultrahochauflösenden Massenspektrometrie (UHRMS) für die Aerosolforschung haben sich komplementäre Techniken wie die Gaschromatographie (GC) und die Flüssigchromatographie (LC) als vielseitige Ergänzungen erwiesen. Durch die vorherige Trennung organischer Aerosolbestandteile können Interferenzen erheblich reduziert werden.

Ziel dieser Studie war es, die chemische Zusammensetzung von organischen Aerosolpartikeln aus dem Amazonas-Regenwald zu untersuchen. Dieses nahezu unberührte Ökosystem spielt eine Schlüsselrolle für das globale Klima, den Wasser- und Kohlenstoffkreislauf sowie die Artenvielfalt. Aus diesem Grund wurde das Amazon Tall Tower Observatory (ATTO) gegründet, um Langzeitmessungen der Atmosphäre zu ermöglichen. Zu unterschiedlichen Jahreszeiten und auf verschiedenen Höhen an ATTO wurden PM_{2.5} und größen aufgelöste Aerosolpartikel beprobt. Zur chemischen Charakterisierung des OA wurde Hochleistungsflüssigchromatographie (HPLC) mit Elektrospray-Ionisation (ESI) UHRMS gekoppelt. Ein softwarebasierter, non-targeted Ansatz wurde in dieser Studie entwickelt und erfolgreich etabliert. In Kombination mit geeigneten Visualisierungstechniken (Van Krevelen, Kendrick-Massendefekt, Kohlenstoff-Oxidationszustand etc.) war es möglich, tausende organische Verbindungen auf molekularer Ebene zu identifizieren. Diesen konnten Summenformeln mit der elementaren Zusammensetzung CHO sowie möglichen Stickstoff- und/oder Schwefelfunktionalitäten zugeordnet werden. Die Verbindungen wurden hauptsächlich Oxidationsprodukten von Isopren und Monoterpenen (α -, β -Pinen, Limonen) zugeordnet, was die Relevanz biogener Emissionen im Amazonas Regenwald hervorhebt. Der Vergleich zwischen den Jahreszeiten hat große Unterschiede in der OA-Zusammensetzung ergeben. Die trockeneren Perioden zeichneten sich dabei durch stark oxidierte und gealterte organische Spezies aus. Zusätzlich

wurde eine große Anzahl von aromatischen Verbindungen nachgewiesen, die meist mit der Verbrennung von Biomasse in Verbindung gebracht wurden. Im Gegensatz dazu waren die Regenzeiten durch weniger gealtertes OA und niedrige Partikelkonzentrationen gekennzeichnet. Während der zweiten Regenperiode wurden jedoch ebenfalls Aromaten nachgewiesen, die durch Verbrennungsprozesse entstehen, was auf einen zunehmenden Einfluss anthropogener Aktivitäten hindeutet. Darüber hinaus wurden höhenaufgelöste Quantifizierungen spezifischer Markerspezies durchgeführt, um lokale und regionale Einflüsse aufzulösen. Hierbei bestätigte sich das Blätterdach als Hauptquelle für biogene Emissionen.

Zusätzlich wurde die chirale Trennung beider Pinsäure-Enantiomere während der Studie erzielt. Die Analyse der Filterproben zeigte, dass das chirale Verhältnis mit zunehmender Höhe variiert. Ein ähnlicher Trend wurde für das Vorläufermolekül α -Pinen in der Gasphase beobachtet. Die Ergebnisse deuten darauf hin, dass die chirale Information auf die Partikelphase übertragen wird, da die atmosphärische Oxidation von α -Pinen ohne Stereopräferenz erfolgt. Somit kann das chirale Verhältnis der langlebigen Pinsäure in der Partikelphase für eine großräumige Einschätzung der Vorläuferemissionen herangezogen werden.

Abstract

Most chemical processes in the atmosphere are controlled by inorganic and organic trace species such as nitrogen dioxide, ozone, hydrocarbons, aromatics, or terpenoids, *etc.* Generally, these compounds can be found in the gas-phase. However, atmospheric reactions and transformations can generate molecules with sufficiently low volatilities to accumulate in the particle-phase. The resulting aerosols pose major impacts on Earth's climate depending on their physicochemical properties. They affect the global energy budget by scattering and absorbing solar radiation. Moreover, aerosols are involved in cloud formation processes and control their abundance and lifetime. Especially in urban regions, they are responsible for reduced visibility and human respiratory and cardiovascular diseases. Consequently, research on atmospheric aerosols and their impact on the environment has received increased attention over the last decades.

In particular, organic aerosols (OA) comprise a large fraction of airborne particulate matter (PM) and usually consist of innumerable different molecules. The aerosol chemical composition is highly dynamic and continuously transforms long after its formation by atmospheric processes. To comprehend OA formation and chemical alteration, specific marker species must be reliably identified and quantified. However, the temporal and spatial fluctuation of OA composition places considerable demands on current analytical techniques. Mass spectrometry (MS) has been established as a suitable tool for the analysis of atmospheric aerosols. The development of instruments with high resolving power and mass accuracy enabled the investigation of particulate matter on a molecular level. Despite the great potential of ultrahigh-resolution mass spectrometry (UHRMS) for organic aerosol research, complementary techniques such as gas chromatography (GC) and liquid chromatography (LC) have proven to be versatile additions. The pre-separation of OA constituents reduces interferences significantly.

The goal of this study was to investigate the chemical composition of organic aerosol particles from the Amazon rainforest. This pristine ecosystem plays a key role in the global climate, the water and carbon cycle, and biodiversity. For this reason, the Amazon Tall Tower Observatory (ATTO) was established to provide atmospheric long-term measurements. PM_{2.5} and size-resolved aerosol particles were collected on filters at different altitudes at ATTO during various seasons. To characterize the OA chemical composition, high-performance liquid chromatography (HPLC) was coupled to electrospray ionization (ESI) UHRMS. A software-based non-targeted approach was developed and successfully established in the present study. In combination with appropriate visualization techniques (Van Krevelen, Kendrick mass defect, carbon oxidation state, *etc.*) it was possible to identify thousands of different organic compounds on a molecular level. Subsequently, molecular formulae with the elemental composition CHO and potential nitrogen and/or sulfur functionalities could be assigned. They were mainly attributed to isoprene and monoterpene (i.e., α -, β -pinene, limonene) oxidation products, emphasizing the relevance of biogenic emissions in the Amazon rainforest. The comparison between the seasons has revealed major differences in the OA composition with highly oxidized and processed organic species during drier periods. Additionally, a large number of aromatic compounds were detected, which were mostly associated with the combustion of biomass. In contrast, the wet seasons were characterized by less aged OA and low particle number concentrations. However, the second wet period revealed several biomass burning related aromatics, suggesting an increasing impact of anthropogenic activities. Height-resolved quantification of specific marker species was performed to resolve local and regional influences supporting the forest canopy as the main source for biogenic emissions.

Furthermore, the chiral separation of pinic acid enantiomers was achieved. The analysis of filter samples from ATTO has shown that the chiral ratio varies with increasing altitude above the canopy. A similar trend was reported for the gas-phase precursor α -pinene. The results indicate that chiral information is transferred to the particle phase since the atmospheric oxidation of α -pinene occurs without stereo preference. Thus, the chiral ratio of the long-lived pinic acid in the particle phase can be used for large-scale estimations of precursor emissions.

Table of Contents

Zusammenfassung	I
Abstract	III
1 Introduction	1
1.1 Atmospheric Aerosols	3
1.2 Secondary Organic Aerosol	6
1.2.1 Formation of SOA	6
1.2.2 Gas-to-particle Conversion	9
1.2.3 Chemistry in the Condensed Phase	10
1.2.4 SOA Formation from Isoprene	11
1.2.5 SOA Formation from α -Pinene	13
1.3 Cloud Condensation Nuclei	15
1.4 Aerosol Particle Collection	16
1.4.1 Filter Sampling	17
1.4.2 Sampling Location: The Amazon Rainforest	19
1.5 Sample Analysis by Chromatography	21
1.6 Mass Spectrometry as a Versatile Candidate for Aerosol Analysis	22
1.6.1 Online Mass Spectrometry	23
1.6.2 Offline Mass Spectrometry	25
1.6.3 Orbitrap Mass Spectrometry	27
1.7 Motivation and Thesis Objectives	28
2 Molecular Characterization of SOA Particles	31
2.1 Introduction	32
2.2 Experimental Section	34
2.2.1 Aerosol Sample Collection	34
2.2.2 Aerosol Sample Analysis	35
2.2.3 Non-Targeted Data Evaluation	36
2.3 Results and Discussion	38
2.3.1 Background SOA Characteristics	41
2.3.2 Detailed Non-Targeted Data Evaluation	51
2.3.3 Targeted Analysis for Selected Marker Species	59
2.4 Conclusion	63
2.5 Additional Information	66
2.5.1 Method Evaluation	66

2.5.2	Data Processing by MZmine 2.30	69
2.5.3	Hierarchical Cluster Analysis.....	71
3	Chirally Specified Analysis of Pinic Acid.....	75
3.1	Introduction	76
3.2	Experimental Section	78
3.2.1	Measurement Campaigns and Filter Sampling.....	78
3.2.2	Chamber Experiments	79
3.2.3	Sample Preparation and LC-MS Analysis.....	79
3.3	Results and Discussion.....	80
3.3.1	Vertical Concentration Gradients of Pinic Acid on PM2.5 Filter Samples.....	81
3.3.2	Daily Variations of Pinic Acid Concentrations	85
3.3.3	Particle Size Resolved Measurements at the Triangular Mast	86
3.4	Conclusion.....	89
4	Conclusions and Outlook.....	91
5	References	95
6	Appendix	117
6.1	Supporting Information to Chapter 2	117
6.2	Supporting Information to Chapter 3	128
6.3	UHRMS Data	130
6.4	List of Related Publications and Presentations	155

Abbreviations

AMS	aerosol mass spectrometer
APCI	atmospheric pressure chemical ionization
ATTO	Amazon tall tower observatory
BC	black carbon
CCN	cloud condensation nuclei
CRM	charged residue model
DBE	double bond equivalents
ELVOC	extremely low-volatility organic compound
ESI	electrospray ionization
FTICR	Fourier transform ion cyclotron resonance
GC	gas chromatography
HCA	hierarchical cluster analysis
HOM	highly oxidized multifunctional organic compound
IEM	ion evaporation model
IEPOX	isoprene epoxydiol
ISOPOOH	isoprene hydroxyhydroperoxide
ITCZ	intertropical convergence zone
KMD	Kendrick mass defect
LC	liquid chromatography
LVOC	low-volatile organic compound
MBTCA	3-methyl-1,2,3-butanetricarboxylic acid
MOUDI	micro-orifice uniform deposit impactor
MS	mass spectrometry
NOS	nitrooxy organosulfates
OS _c	carbon oxidation state
PBA	primary biogenic aerosol
PBL	planetary boundary layer
PM	particulate matter
SOA	secondary organic aerosol
SVOC	semi-volatile organic compound
ToF	time of flight

UHRMS	ultrahigh-resolution mass spectrometry
VK	Van Krevelen diagram
VOC	volatile organic compound
Xc	aromaticity equivalent

1 Introduction

Atmospheric chemistry has considerably gained increased attention over the last decades. In times of rising temperatures, shrinking ice shelves, disappearing glaciers, and increasing sea levels the dramatic events of climate change have driven not only atmospheric scientists to act. In this context, researchers mainly focus on three fundamental questions (IPCC, 2014; NASA, 2020):

- What are the causes of climate change?
- What are the impacts of climate change?
- What are the solutions to climate change?

With these questions in mind, it is necessary to consider all processes which affect the climate either by warming or cooling the atmosphere. One important measure to express Earth's energy budget represents the radiative forcing. It describes the capability of an emitted compound to change the global energy balance (Forster et al., 2007). Positive values will lead to an overall increase in the energy budget and will consequently warm the surface. Accordingly, negative values will result in cooler temperatures. Both natural and anthropogenic drivers can modify the Earth's energy budget and therefore influence the current climate (IPCC, 2013; Kirk-Davidoff, 2018). Estimates of radiative forcing for significant drivers in the year 2011 relative to 1750 are shown in Figure 1.1. The burning of fossil fuels and the associated release of the greenhouse gas carbon dioxide (CO_2) has the most significant impact on warming Earth's climate and is mostly related to human activities. Also, other greenhouse gases like methane (CH_4) and nitrous oxide (N_2O) have considerably increased because of human activities like agriculture and landfills (Forster et al., 2007) and subsequently contribute to surface warming. In addition to greenhouse gases, aerosol particles occupy an important role in Earth's climate due to various particle size distributions and complex chemical compositions. The particles can both, directly and indirectly, alter the energy budget through the interaction with solar radiation and the variation of cloud properties (Haywood, 2016). The total contribution to radiative forcing by aerosol particles is negative and hence leading to surface cooling. However, as can be seen in Figure 1.1 aerosols also have a positive contribution to radiative forcing, mainly attributed to the absorption of solar radiation by black carbon (soot), which results in surface warming through circulation and mixing of air masses. Despite the obvious impacts of human emissions since 1750, also natural processes influence Earth's climate. Besides naturally emitted greenhouse gases and aerosol particles, also changes in solar radiation cause

a positive radiative forcing. But their contribution to the total estimated forcing is small compared to the effects of human activities (Forster et al., 2007; Haywood, 2016; IPCC, 2014).

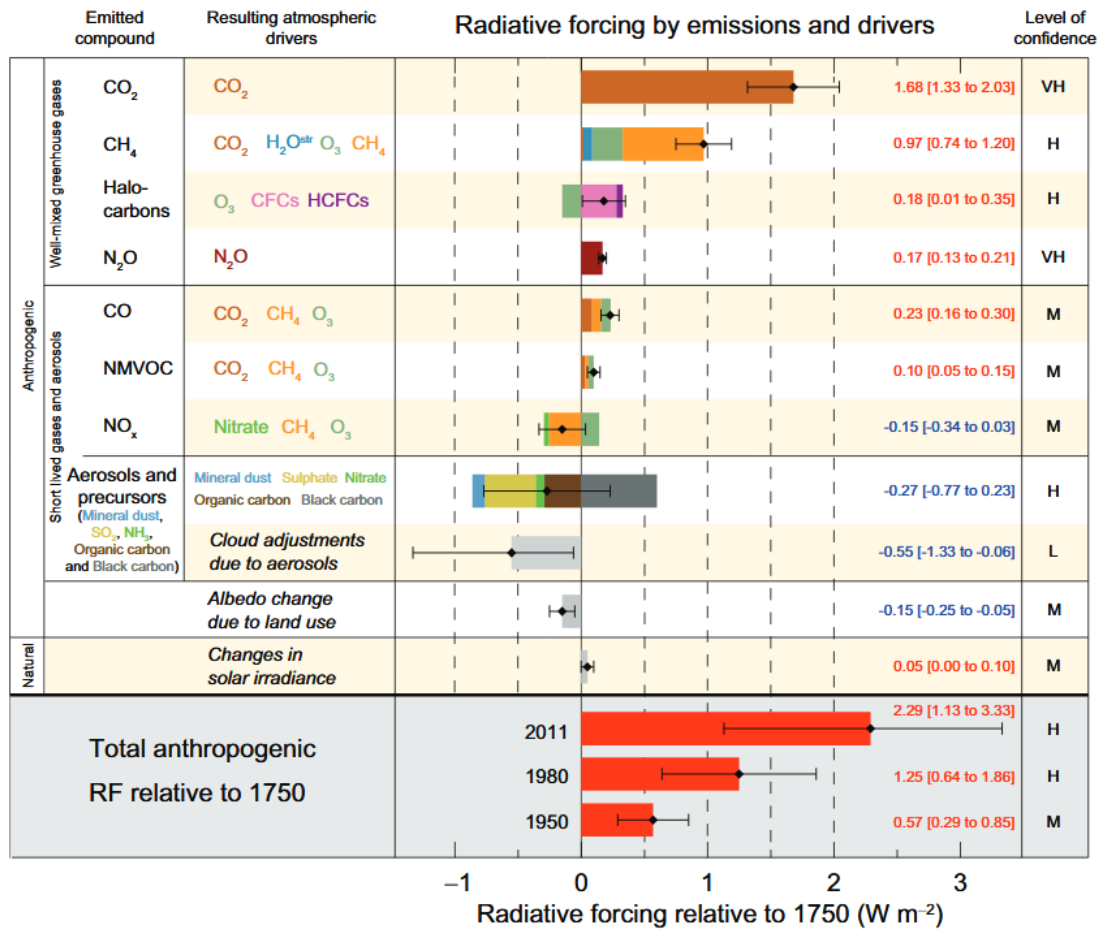


Figure 1.1: Estimates of radiative forcing for specific anthropogenic and natural climate drivers in the year 2011 relative to 1750. The best estimates are represented as black diamonds together with the corresponding uncertainty interval. The confidence level of respective contributions to the net forcing is provided on the right side of the figure with the following abbreviations: VH – very high, H – high, M – medium, L – low (IPCC, 2013).

Long-term measurements and observations of surface warming are in good agreement with current model calculations, attributing a high level of confidence to the estimates of direct effects from greenhouse gases and aerosol particles (IPCC, 2013; National Research Council, 2005). However, the contribution of aerosol-cloud interaction to the net radiative forcing still remains unclear. In contrast to long-lived greenhouse gases, the average aerosol lifetime is short and the spatial distribution in the atmosphere highly inconsistent (Pöschl, 2005; Williams et al., 2002). Because of the complex chemical composition of aerosol particles and their constant transformation in atmospheric heterogeneous and multiphase reactions, radiative forcing estimates cannot accurately be obtained (Ravishankara, 1997). Therefore, it is essential to reliably characterize aerosol particles in terms of their chemical composition and number to precisely assess their importance for future climate predictions.

In the following sections of this chapter, the fundamental processes regarding the formation of atmospheric aerosols and their relevance for this study will be discussed. This includes specific biogenic hydrocarbons as well as their respective oxidation products. Additionally, important analytical techniques applied in this study will be illustrated shortly.

1.1 Atmospheric Aerosols

Earth's climate is a complex phenomenon that is both, globally and locally, characterized by the interaction of solar radiation, clouds, ocean currents, and the circulation and composition of air masses (Seinfeld and Pandis, 2016; Kirk-Davidoff, 2018). This synergy leads to temperature and pressure variations in the atmosphere with increasing altitude forming distinct layers. The troposphere is the lowest layer and ranges from the surface to up to 10 – 15 km altitude. The temperature is declining almost constantly with height due to increasing distance to the heated surface of the Earth. This region can be divided into the planetary boundary layer (PBL) (~ 1 km altitude) and the free troposphere. The PBL height shifts according to diurnal temperature variations. During the night it is located at lower altitudes, as radiative cooling leads to a stable state of the surface layer. In contrast, surface heating induces convective turbulence resulting in the rapid mixing of air masses and consequently the rise of the PBL (Liu and Liang, 2010). The adjacent stratosphere expands up to 45 km and has a reversed temperature profile as a result of the absorption of ultraviolet radiation by ozone (Seinfeld and Pandis, 2016; Warneck, 2000). Both regions are heavily exposed to anthropogenic and natural emissions and therefore crucial for Earth's climate. The superjacent layers mesosphere, thermosphere, and exosphere extend up to 500 km and are far less influenced by human and natural activities (Graedel and Crutzen, 1994). This study focuses on the PBL unless otherwise stated.

The main constituents of Earth's atmosphere are N₂ (78%), O₂ (21%), Ar (~1%), and trace gases (< 1%) such as CO₂, Ne, He, and CH₄ (Allen, 1991). Although the trace gases just amount to less than 1% of the atmosphere, they play a central role in the chemical and physical processes of Earth's climate. Moreover, atmospheric aerosols also have crucial impacts on the climate. They are defined as liquid or solid particles suspended in air and originate both from biogenic and anthropogenic sources (Seinfeld and Pandis, 2016). A simplified scheme of involved atmospheric species and processes for aerosol formation is illustrated in Figure 1.2. Depending on their formation, aerosols are divided into two classes. Primary biogenic aerosol (PBA) particles are directly emitted into the atmosphere by natural sources like volcanic eruptions, pollen, or fungal spores. Additionally, anthropogenic sources such as biomass burning or fossil fuel combustion also account for the emission of primary particles. However, secondary particles are formed in the atmosphere by gas-to-particle conversion, e.g. heterogeneous and

multiphase oxidation reactions of volatile organic compounds (VOC). The subsequent nucleation and condensation processes are leading to secondary particles (Hallquist et al., 2009; Kroll and Seinfeld, 2008).

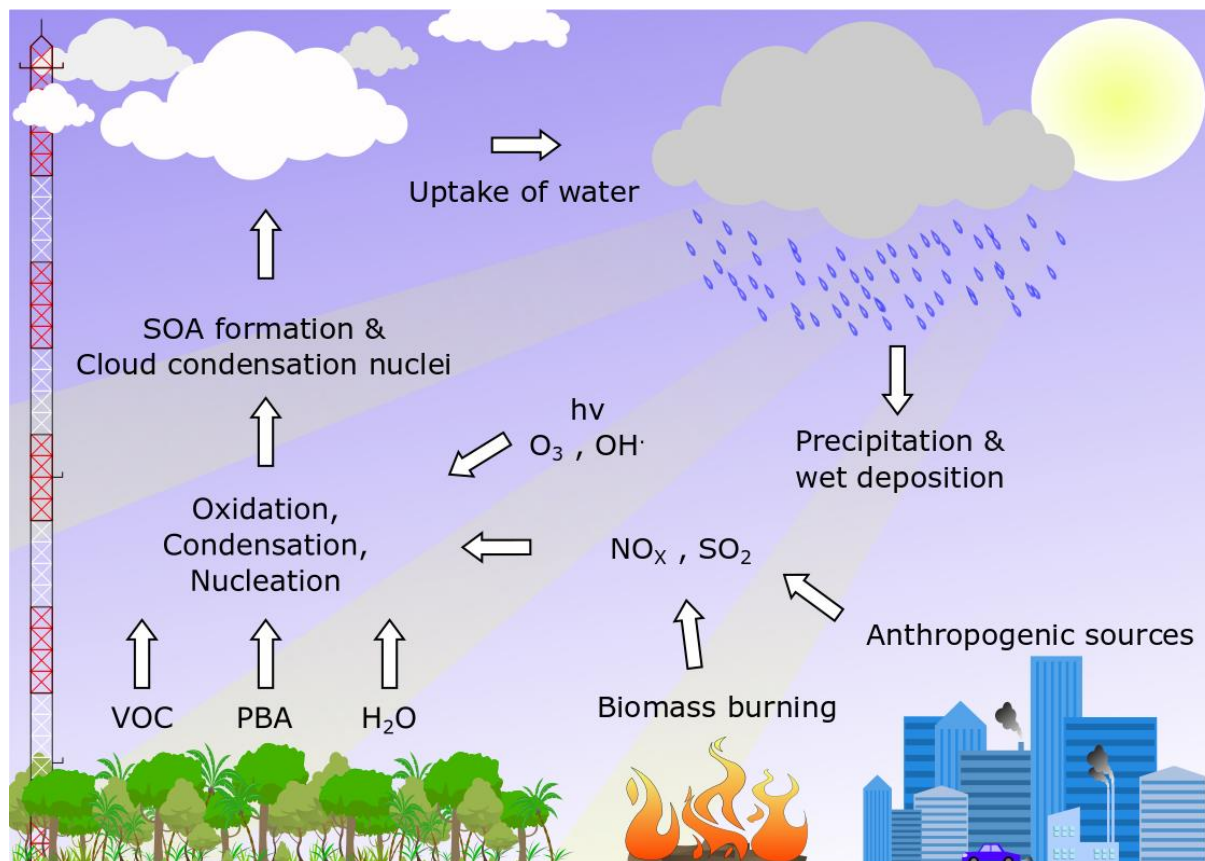


Figure 1.2: Simplified principles of atmospheric particle formation (VOC = volatile organic compound, PBA = primary biogenic aerosol, SOA = secondary organic aerosol).

The formation mechanism mainly defines the particle size range. Particles larger than $2.5\ \mu\text{m}$ diameter (*coarse* particles) are primarily formed by mechanical processes and largely contribute to the total aerosol mass (Seinfeld and Pandis, 2016). In contrast, particles smaller than $2.5\ \mu\text{m}$ diameter (*fine* particles) largely contribute to the total aerosol particle number and surface area. Moreover, these particles can be categorized into three modes. The *nucleation* mode consists of particles with diameters less than $10\ \text{nm}$ formed by nucleation and condensation processes of atmospheric compounds onto stable clusters (Kulmala et al., 2013). Subsequent coagulation with other particles and condensation of vapors lead to rapid growth. The size range between 10 to $100\ \text{nm}$ diameters is referred to as the *Aitken* mode, followed by the *accumulation* mode up to $2.5\ \mu\text{m}$ diameter. *Coarse* Particles are effectively removed from the atmosphere by rapid gravitational settling. Furthermore, particles in the *Nucleation* and *Aitken* mode have short atmospheric residence times caused by the fast coagulation with other

particles (Seinfeld and Pandis, 2016). However, these removal mechanisms are ineffective for particles in the accumulation mode, which are mainly removed by wet deposition. Thus, they remain considerably longer in the atmosphere and can be transported over wider distances (Seinfeld and Pandis, 2016; Whitby, 1978). Figure 1.3 provides an overview of the aerosol particle size range classifications and involved transformation processes.

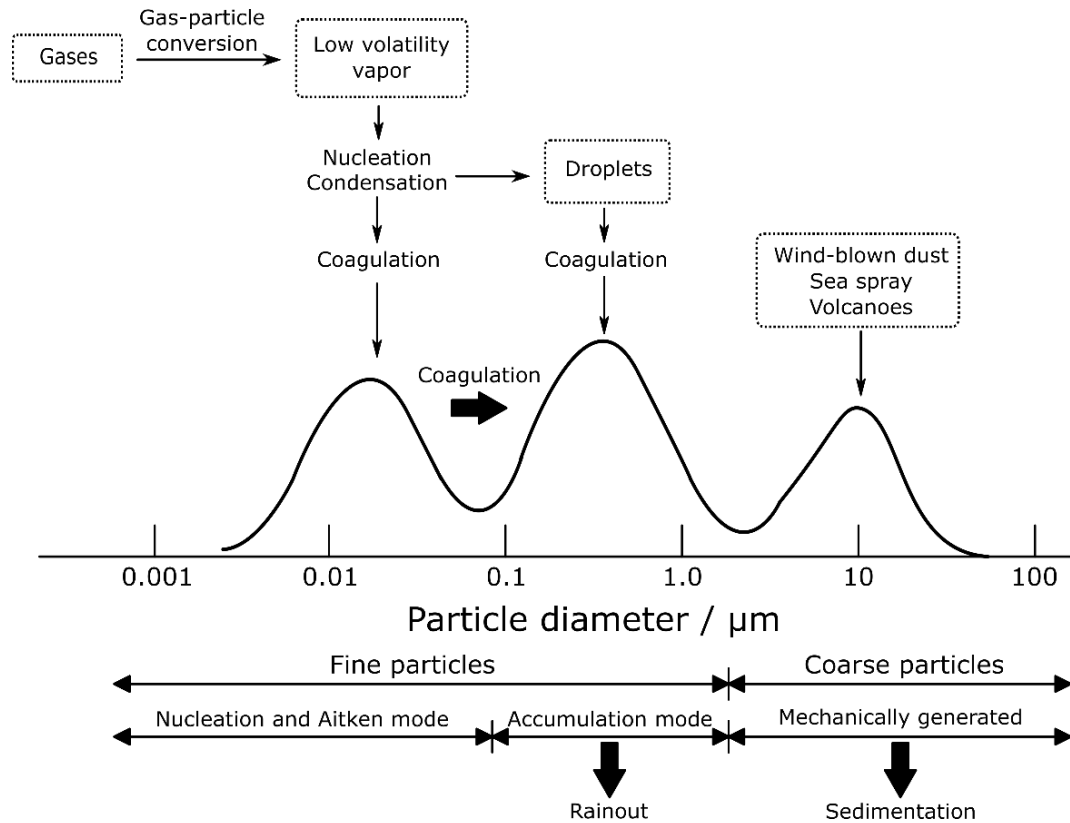


Figure 1.3: Schematic overview of aerosol size distribution with the respective size range classifications, sources and sinks, and the involved transformation processes. The figure is adapted by Whitby, 1978.

In reference to Figure 1.1, the chemical composition of aerosol particles has a huge impact on the radiative forcing. The corresponding constituents can be divided into organics, inorganics, and black carbon. The most frequent inorganic ions include sulfate (SO_4^{2-}), nitrate (NO_3^-), chloride (Cl^-), and ammonia (NH_4^+), which can be quantified directly by an aerosol mass spectrometer (AMS) (Jimenez et al., 2009). In contrast, the organic fraction is significantly less characterized caused by the vast amount of possible oxidation products of organic compounds in the atmosphere. Depending on the geographic region the contribution of organic aerosol to the overall particulate mass can strongly vary between 20% – 50% in urban areas and even up to 90% in forested areas such as the Amazon rainforest (Saxena and Hildemann, 1996; Kanakidou et al., 2004; Andreae and Crutzen, 1997).

The effects of aerosol particles on the climate can be distinguished between direct and indirect processes. Particulate matter can directly affect Earth's radiative balance as a result of scattering or absorbing solar radiation (Satheesh and Moorthy, 2005). Indirect impacts of aerosol particles, on the other hand, result from their capability to act as cloud condensation nuclei (CCN) or ice nuclei (IN). Additionally, aerosol particles can be classified according to their net radiative forcing (see Figure 1.1). According to IPCC, 2013, black carbon (BC) has, after carbon dioxide, the second strongest contribution to global warming caused by the efficient absorption of solar radiation. Sulfate particles, in contrast, effectively scatter solar radiation and hence leading to a net cooling of the atmosphere (Schwartz, 1996). They also cause brighter clouds than BC because of a larger number of smaller droplets. As a result, they are less likely to precipitate and thus having prolonged lifetimes. This leads to a net cooling outcome and is described as cloud albedo effect (Boucher and Lohmann, 1995). It highlights the importance of particulate matter for the climate as it is not only influencing the Earth's radiative balance but also the hydrological cycle (Ramanathan et al., 2001).

Furthermore, several epidemiological studies have been carried out on fine particulate matter affecting human health. Especially the cardiovascular and respiratory systems are getting impaired by particles with a diameter smaller than 2.5 μm (PM_{2.5}, particulate matter) which can be responsible for premature mortality (Lelieveld et al., 2015; Pope, 2000).

1.2 Secondary Organic Aerosol

It is generally accepted that secondary organic aerosol (SOA) contributes a large fraction of the total organic aerosol (Heald et al., 2005; Zhang et al., 2007; Jimenez et al., 2009). However, recent studies and models based on laboratory results have shown that the calculated SOA mass is still underestimated (Volkamer et al., 2006; Goldstein and Galbally, 2007), which reveals major knowledge gaps for sources, sinks, and atmospheric processing of SOA. To reduce uncertainties in global climate predictions it is necessary to better understand the chemical formation and transformation of SOA. The most important atmospheric processes will be described in the following sections in more detail.

1.2.1 Formation of SOA

In 1960, F.W. Went first described the phenomenon of blue haze above forested countryside with small populations during summer (Went, 1960). He suggested that submicroscopic particles in the atmosphere are responsible for the wavelength-dependent scattering of sunlight, resulting in this visible

bluish haze formation. He concluded that these particles are formed by photooxidation of volatile organic compounds (VOCs) with ozone.

Both anthropogenic and biogenic sources emit a large number of VOCs including saturated, unsaturated, and oxygenated compounds. Moreover, the emissions comprise a wide variety of chemical functionalities such as alkanes, alkenes, carbonyls, alcohols, esters, and acids. Biogenic emissions exceed anthropogenic emissions by a factor of 10 on a global scale. Forested regions such as the Amazon rainforest are responsible for the emission of huge amounts of VOCs and thus contribute to a substantial part of the SOA (Kesselmeier and Staudt, 1999). In urban regions, however, anthropogenic emissions predominate (Atkinson and Arey, 2003b). Biogenic VOCs are primarily secondary metabolites consisting of isoprene (C_5H_8 , 2-methyl-1,3-butadiene) and monoterpenes as the most dominant compounds for SOA formation (Kesselmeier and Staudt, 1999; Seinfeld and Pandis, 2016). These biochemical products are build up by repeating C_5 units and can be subdivided into hemiterpenes (C_5 , e.g. isoprene), monoterpenes (C_{10} , e.g. α -pinene), sesquiterpenes (C_{15} , e.g. β -caryophyllene), diterpenes (C_{20} , e.g. retinol), etc. (McGarvey and Croteau, 1995; Davis and Croteau, 2000) and are responsible for typical scents in forested areas. After the emission, the subsequent gas-phase oxidation reaction occurs in the atmosphere with the most prominent oxidant species such as the hydroxyl radical (OH), ozone (O_3), and the nitrate radical (NO_3) (Finlayson-Pitts and Pitts, 2000). A simplified oxidation mechanism is illustrated in Figure 1.4.

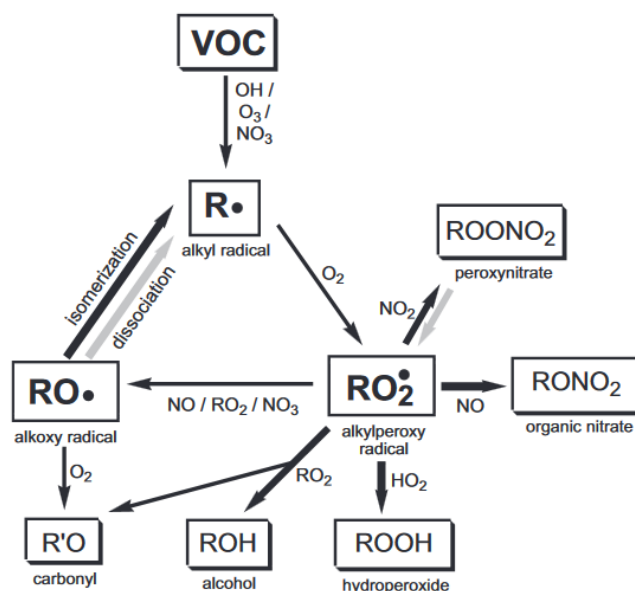


Figure 1.4: Simplified scheme for the gas-phase oxidation of VOCs by atmospheric oxidants. Bold black arrows indicate reactions that can lead to a significant decrease in vapor pressure. In contrast, grey arrows indicate reactions that can lead to an increase in vapor pressure (Kroll and Seinfeld, 2008).

The resulting alkyl (R) radicals can further react with oxygen to generate alkylperoxy radicals (RO₂) (Atkinson and Arey, 2003b; Kroll and Seinfeld, 2008). The RO₂ radicals are responsible for a wide range of products with lower vapor pressures such as peroxy nitrates, organic nitrates, alcohols, hydroperoxides, and carbonyls. The preferred reaction pathway depends on the ambient concentrations of RO₂, NO_x, and HO₂ radicals. Additionally, alkoxy (RO) radicals can be formed which can subsequently be isomerized or dissociated resulting again in alkyl radicals. This oxidation cycle continues to finally produce H₂O and CO₂ or until the compounds are withdrawn by wet or dry deposition. The capability to form SOA is largely depending on the volatility of resulting oxidation products (Kroll and Seinfeld, 2008; Pankow et al., 2001). Reaction pathways which include the addition of polar functional groups or extending the carbon chain length of the initial VOC will significantly decrease the vapor pressure. Thus, the gas-to-particle conversion of VOCs to SOA is enhanced. However, in case the reaction pathway includes the fragmentation of the carbon chain the vapor pressure will be increased. Hence, the oxidation product remains in the gas-phase (Pankow et al., 2001; Kroll et al., 2011). Remarkably, numerous biogenic VOCs are present in cyclic molecular structures with a C-C double bond integrated. Thus, the attack of RO₂ or ozone does not lead to the fragmentation of the molecule. Instead, a ring-opening reaction takes place and two functional groups can be added, resulting in a significant decrease in the vapor pressure (Kroll and Seinfeld, 2008; Hallquist et al., 2009).

Ehn et al. suggested another reaction pathway to generate highly oxidized multifunctional organic molecules (HOMs) with extremely low vapor pressure, therefore, referred to as extremely low-volatility organic compounds (ELVOCs) (Ehn et al., 2012; Ehn et al., 2014; Mentel et al., 2015). The corresponding formation mechanism is illustrated in Figure 1.5. These compounds are suggested to play a substantial role in SOA formation (Bianchi et al., 2016; Kirkby et al., 2016). The initially formed RO₂ radical can undergo an internal hydrogen abstraction (*H-shift*). The freshly formed alkyl radical can further react with oxygen in an autooxidation reaction to finally form ELVOCs. Continuing H-shifts and oxygen additions can generate highly oxidized monomers, dimers, or organic nitrates depending on the concentrations of available reaction partners such as RO₂, HO₂, and NO (Ehn et al., 2014).

Although the understanding of SOA formation has largely advanced during the last decades, there are still discrepancies between model calculations and measurements of SOA mass (Heald et al., 2005; de Gouw, 2005; Volkamer et al., 2006). Remarkably, Volkamer and co-workers (2009) observed SOA formation from acetylene (C₂H₂) on ammonium sulfate ((NH₄)₂SO₄) seed particles after OH radical oxidation. This finding highlights that the volatility of oxidation products does not exclusively determine their ability to generate SOA.

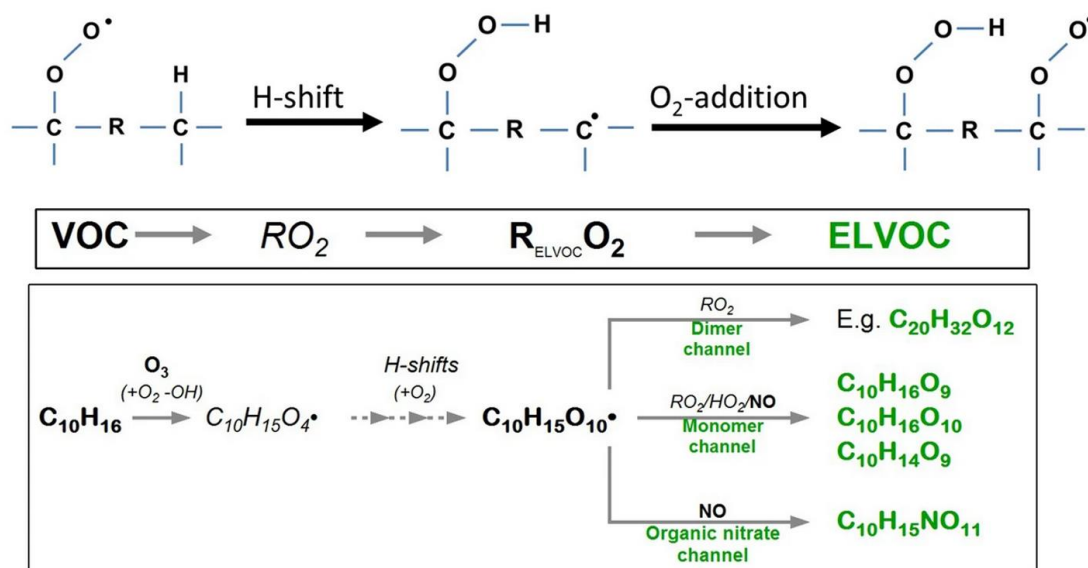


Figure 1.5: Simplified overview of ELVOC formation. The upper part describes the formation mechanism including internal hydrogen abstraction by an RO_2 and the subsequent oxygen addition at the newly formed alkyl radical to finally generate highly oxidized peroxy radicals. The lower part illustrates the ozonolysis reaction of (α)-pinene ($\text{C}_{10}\text{H}_{16}$) leading to highly oxidized monomers, dimers, or organic nitrates depending on the oxidant concentrations (Ehn et al., 2014).

1.2.2 Gas-to-particle Conversion

In addition to the nucleation of new aerosol particles, an important aspect of SOA formation is the condensation of lower volatility compounds onto preexisting particles. However, not all oxidized compounds with sufficiently low vapor pressures will necessarily condensate and remain in the particle-phase (Pankow et al., 2001; Hallquist et al., 2009). In fact, they are referred to as semi-volatile organic compounds (SVOCs) which partition between the gas- and particle-phase. This process depends on the partition equilibrium and was first described by Pankow (Pankow, 1994a, 1994b) and later extended to SOA considerations by Odum et al. (Odum et al., 1996). Each compound is characterized by an equilibrium partitioning coefficient $K_{p,i}$ [$\text{m}^3 \mu\text{g}^{-1}$] or the inverse saturation vapor concentration C_i^* [$\mu\text{g m}^{-3}$] (Hallquist et al., 2009; Donahue et al., 2006). The correlation is shown in Equation (1.1).

$$\frac{C_i^p}{C_i^g} = K_{p,i} C_{OA} = \frac{C_{OA}}{C_i^*} \quad (1.1)$$

The mass concentrations of a compound i per unit volume of air [$\mu\text{g m}^{-3}$] in the gas-phase and the particle-phase is described by C_i^g and C_i^p , respectively. Accordingly, C_{OA} is the mass concentration of the total absorbing particle-phase. This implies that, with increasing amounts of available particulate

mass, a fraction of a specific semi-volatile compound will increasingly partition into the particle-phase even if the saturation concentration, C_i^* , is not reached (Pankow, 1994b). Equation (1.2) can be used to calculate the fraction F_i of a semi-volatile compound in the particle-phase (Hallquist et al., 2009).

$$F_i = \frac{C_i^p}{C_i^p + C_i^g} = \frac{K_{p,i}C_{OA}}{1 + K_{p,i}C_{OA}} = \frac{1}{1 + C_i^*/C_{OA}} \quad (1.2)$$

It can be concluded that if $C_{OA} \gg C_i^*$, the major amount of the semi-volatile compound i can be found in the particle-phase. Moreover, as soon as this total amount of particulate mass with a high fraction of SVOCs will be diluted (e.g., from vehicle exhaust into the atmosphere), certain SVOCs will partition back into the gas-phase to some extent where further oxidation reactions take place. The resulting less volatile products condense into the particle-phase once more leading to an increased total particle mass (Robinson et al., 2007; Shrivastava et al., 2006). Including the above-mentioned considerations into an air quality model study, Robinson et al. (2007) were able to improve predictions of ambient aerosol concentrations. However, there are still various aspects that complicate the evaluation of partitioning processes (Hallquist et al., 2009). The calculations and principles are applied to highly complex and dynamic systems where the chemical composition changes almost constantly by oxidation with available radicals or photolysis with UV light (Kroll et al., 2005; Presto et al., 2005a, 2005b). Additionally, these systems are largely depending on temperature, since the saturation vapor concentration C^* varies with temperature according to the Clausius-Clapeyron equation (Chung, 2002). Finally, the interpretation of C_{OA} has not yet been precisely defined. Thus, it is uncertain whether to include primary aerosol mass, the relevance of water-uptake, and inorganic compounds into the calculations (Song et al., 2007; Hallquist et al., 2009).

1.2.3 Chemistry in the Condensed Phase

Besides gas-phase reactions where low-volatility compounds are formed through the oxidation of VOCs, chemical reactions in the condensed phase are also relevant for an increase of SOA mass. It is distinguished between heterogeneous reactions on the surface of an already existing particle and multiphase reactions within the liquid condensed medium (Ravishankara, 1997). Moreover, Kroll and Seinfeld (2008) extended the character of these reactions to be either non-oxidative (the average oxidation state of carbon remains unchanged) or oxidative (the average carbon oxidation state increases). Non-oxidative or accretion reactions play a crucial role in SOA formation since the resulting oligomeric and high molecular weight species (HMWs) have considerably lower vapor pressures than the parent

organic compounds (Barsanti and Pankow, 2006; Kroll and Seinfeld, 2008). These reactions include the formation of peroxyhemiacetals, acetal, ester and acid anhydrides, and sulfate esters. Moreover, even highly volatile and reactive VOCs, such as isoprene and glyoxal, can contribute to SOA formation via oligomerization reactions (Claeys et al., 2004b; Carlton et al., 2009).

Similar to gas-phase reactions, organic compounds in the particle-phase are also undergoing oxidative reactions with atmospheric oxidants such as OH radicals, NO₃ radicals, and ozone. This chemical transformation of aerosols is often referred to as *aerosol aging* and is reviewed by Rudich et al. (2007). The involved chemical mechanisms are equivalent to the reactions within the gas-phase. However, the branching ratios may largely vary which has a substantial impact on the products' volatility (Kroll and Seinfeld, 2008).

1.2.4 SOA Formation from Isoprene

Terrestrial vegetation is responsible for the emission of a huge variety of biogenic VOCs. Isoprene is the most dominant species accounting for approximately 50% of the total global non-methane biogenic VOC emissions (Guenther et al., 2012). Initially, it was supposed that isoprene does not contribute to the formation of SOA (Pandis et al., 1991; Pandis et al., 1992). However, Claeys et al. (2004b) reported significant concentrations of diastereomeric 2-methyltetrols in aerosol samples from the Amazon, which are produced by photooxidation of isoprene. Various field and laboratory experiments were following to prove the SOA formation by isoprene oxidation (Edney et al., 2005; Kroll et al., 2006; Kleindienst et al., 2009). Moreover, model studies estimated the isoprene emissions at more than 500 Tg y⁻¹ (Wang and Shallcross, 2000; Guenther et al., 2006), so that even minor aerosol yields might lead to considerable concentrations of particulate matter (Carlton et al., 2009).

Isoprene is mainly emitted through the stomata of plants, which is why a diel concentration pattern can be observed with increased levels during daytime (Monson and Fall, 1989; Fall and Monson, 1992). Due to its conjugated double bonds isoprene is highly reactive towards atmospheric oxidants (Carlton et al., 2009; Wennberg et al., 2018). Especially, the reaction with OH radicals is the predominant oxidation mechanism with typical lifetimes of 1 h – 2 h, followed by the reaction with O₃ and NO₃ radicals (Atkinson and Arey, 2003a; Atkinson et al., 2006). Subsequent atmospheric reactions produce a multitude of later-generation oxidation products of isoprene, which are relevant for SOA formation. In their detailed review, Wennberg et al. (2018) give comprehensive insights into atmospheric oxidation mechanisms and the impact on SOA formation. Furthermore, Surratt et al. (2010) investigated isoprene-derived SOA under low- and high-NO_x conditions. Both limitations are controlled by separate reaction pathways resulting in different aerosol yields and different isoprene oxidation products (Kleindienst et

al., 2009; Paulot et al., 2009a; Lin et al., 2013; Schwantes et al., 2019). At low- NO_x levels, the primary reaction mechanism for isoprene SOA formation is illustrated in Figure 1.6.

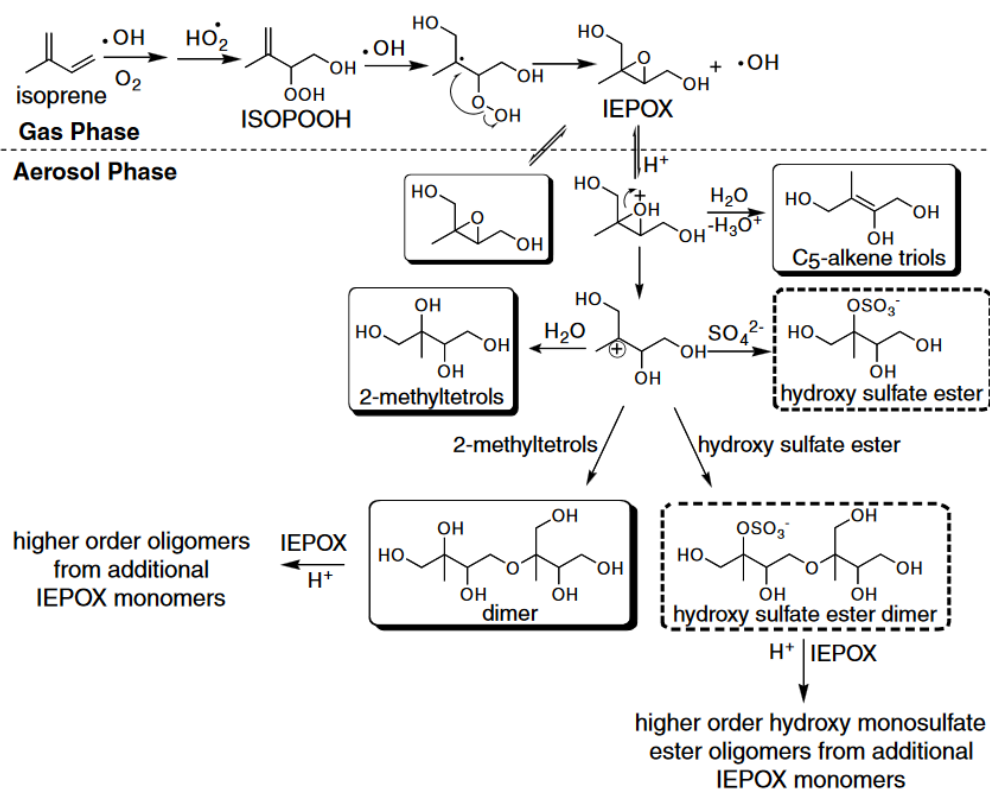


Figure 1.6: Reaction pathway for the isoprene SOA formation under low- NO_x conditions according to Surratt et al. (2010). Isomeric structures are omitted for clarity reasons. In absence of NO_x , reactions with HO_2 radicals are preferred leading to the formation of isoprene-derived hydroxyhydroperoxides (ISOPOOH) and subsequently to epoxydiols (IEPOX).

Paulot et al. (2009b) have shown that the OH-radical initiated oxidation of isoprene is primarily followed by the reaction with HO_2 radicals to produce hydroxyhydroperoxides (ISOPOOH). Subsequent addition of OH yields epoxydiols (IEPOX) by intramolecular ring-closure and loss of OH. The acid-catalyzed reactive uptake of IEPOX on preexisting particles leads to the formation of later-generation oxidation products of isoprene, such as 2-methyltetrols, C₅-alkene triols, and organosulfates (Surratt et al., 2006; Kleindienst et al., 2009; Surratt et al., 2010). Furthermore, oligomeric structures can be formed by acid-catalyzed polymerization of IEPOX. Consequently, isoprene-derived SOA yields are significantly enhanced by acidic sulfate aerosol particles as reported in the literature (Edney et al., 2005; Surratt et al., 2006; Kleindienst et al., 2009). It should be noted that all involved oxidation products are present in various structural isomers leading to a highly complex mixture of isoprene SOA constituents.

In contrast, under high-NO_x conditions isoprene primarily reacts with NO instead of HO₂ radicals to form methacrolein (MACR) (Kroll et al., 2006; Surratt et al., 2006; Schwantes et al., 2019). The proposed reaction mechanism is shown in Figure 1.7.

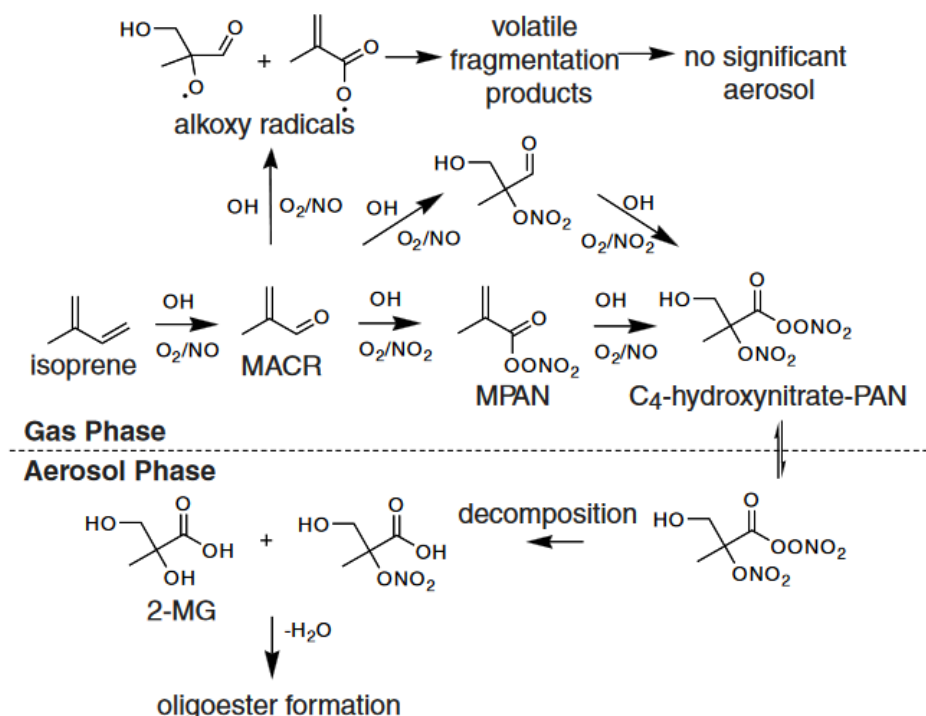


Figure 1.7: Proposed mechanism for the isoprene SOA formation under high-NO_x conditions according to Surratt et al. (2010). These conditions facilitate the production of methacrolein (MACR) and methylacryloyl peroxyxynitrate (MPAN). Further oxidation yields 2-methylglyceric acid (2-MG).

Further oxidation produces methylacryloyl peroxyxynitrate (MPAN) and various hydroxynitrates as key products for the SOA formation (Paulot et al., 2009a; Wennberg et al., 2018). Surratt et al. (2010) suggested subsequent decomposition into 2-methylglyceric acid (2-MG) and corresponding oligomers in the condensed phase, which have already been detected in a field study (Hallquist et al., 2009). It should be emphasized that the isoprene SOA formation for both low- and high-NO_x reaction pathways cannot be strictly separated under ambient atmospheric conditions. It is therefore certain that anthropogenic emissions (i.e., NO₂ and SO₂) have a substantial impact on the SOA formation from isoprene (Surratt et al., 2010).

1.2.5 SOA Formation from α -Pinene

Besides isoprene, monoterpenes are the most emitted VOCs by terrestrial vegetation (Kesselmeier and Staudt, 1999; Kuhn, 2002). This compound class is well known to play an important role in plant

signaling and communication under stress effects, such as parasites or injuries (Gershenson and Dudareva, 2007; Vickers et al., 2009; Mori, 2014). Their major contribution to the SOA formation is due to the generation of low-volatile oxidation products by the reaction with atmospheric oxidants (Zhao et al., 2015; Yáñez-Serrano et al., 2018). However, a large number of isomeric monoterpenes with the molecular formula $C_{10}H_{16}$ exist, all of them leading to varying aerosol yields and different SOA compositions (Hallquist et al., 2009). Among these structures, α -pinene is the most abundant monoterpene in boreal and tropical forests (Praplan et al., 2015; Yáñez-Serrano et al., 2018) and was already studied in laboratory and field experiments (e.g., Tolocka et al., 2004; Eddingsaas et al., 2012; Aljawhary et al., 2016; Beck and Hoffmann, 2016). A simplified scheme for different α -pinene oxidation pathways is shown in Figure 1.8.

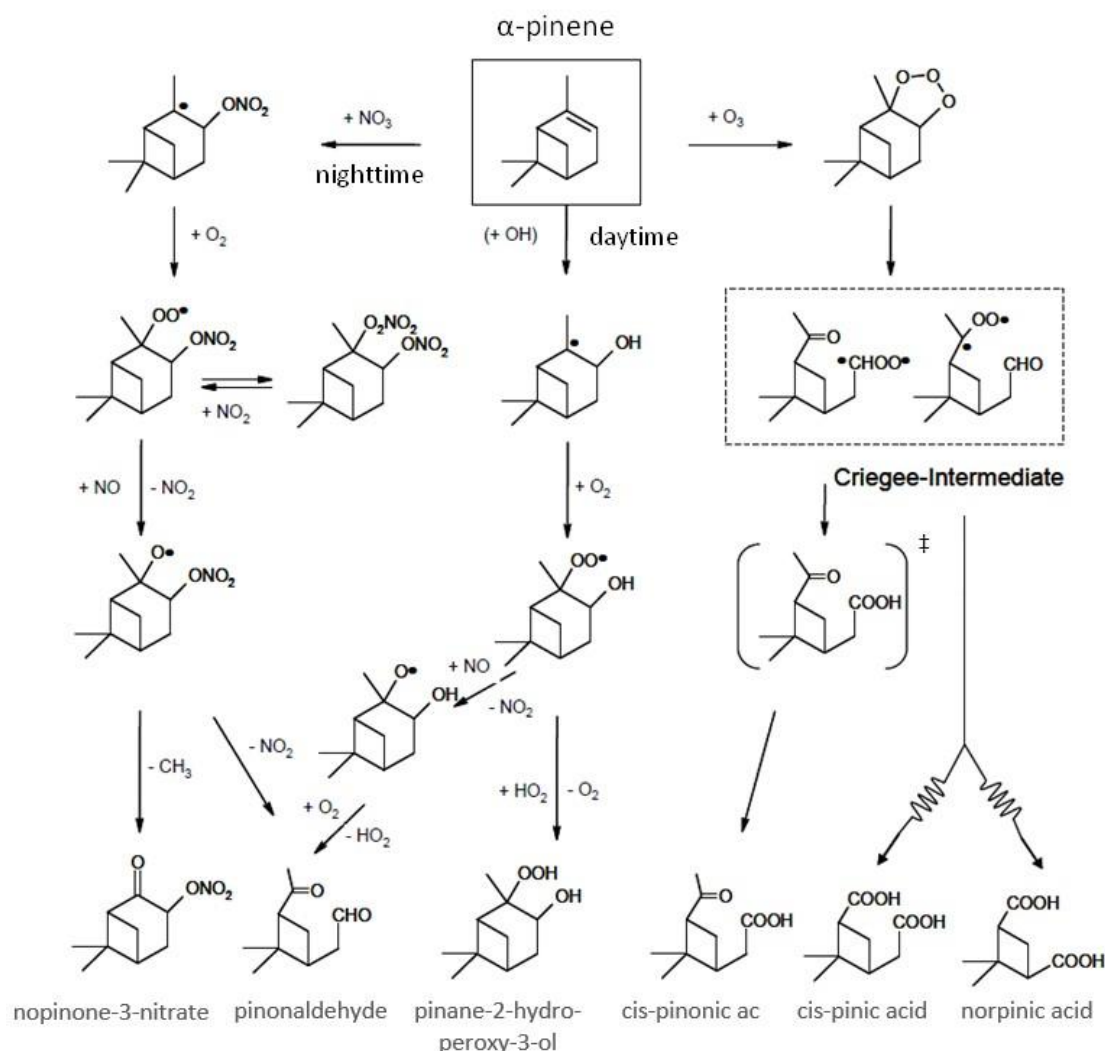


Figure 1.8: Simplified mechanism of the α -pinene oxidation by NO_3 radicals, OH radicals, and O_3 . Reaction scheme adapted from Hoffmann and Klockow (1998).

The oxidation by NO_3 and OH radicals are dominant during nighttime and daytime, respectively. They follow the reactions discussed in section 1.2.1. The addition of O_3 to the double bond leads to the formation of a primary ozonide readily decomposing into Criegee intermediates (Ma et al., 2008; Kroll and Seinfeld, 2008). Further processing results in low-volatile carboxylic acids and carbonyls, such as pinic acid, pinonic acid, and 3-methyl-1,2,3-butane tricarboxylic acid (MBTCA) (Christoffersen et al., 1998; Jenkin et al., 2000; Szmigielski et al., 2007). Additionally, α -pinene exists in two enantiomeric structures. Upon atmospheric oxidation, the chiral information should be retained for oxidation products with intact four-membered carbon rings. Recently, Zannoni et al. (2020) found varying enantiomeric ratios of α -pinene above the Amazon rainforest. Thus, chirally specified measurements of oxidation products in the particle-phase could be useful to directly link biogenic VOC emissions and aerosol concentrations.

1.3 Cloud Condensation Nuclei

Earth's climate is affected by direct processes (interaction between aerosol particles and solar radiation) but also by indirect processes since aerosol particles can be activated to form cloud condensation nuclei. Because the formation of cloud droplets by condensation of water molecules would require supersaturations of several hundred percent, a condensation nucleus is essential under reasonable atmospheric conditions (Seinfeld and Pandis, 2016). Both the diameter and the chemical composition of such a particle influence the ability to act as CCN (Dusek et al., 2006; Hudson, 2007; Andreae and Rosenfeld, 2008). Whether the particle is able to form CCN is largely depending on two opposing fundamental effects, the Kelvin effect and the Raoult effect, described in the Köhler theory (Köhler, 1936; Hinds, 1999; Wex et al., 2008). It is stated that the water vapor saturation over the droplet surface S_d is linked with the droplet diameter d_d . The connection is illustrated in Figure 1.9. The Kelvin effect highlights the increase in S_d caused by the strong curvature of the droplet in comparison to a flat surface. Conversely, the Raoult effect tends to decrease S_d since the equilibrium water vapor pressure above a diluted solution is lower than over pure water. It should be noted, that both effects increase for smaller droplet diameters but the Raoult effect increases much faster (Seinfeld and Pandis, 2016; Andreae and Rosenfeld, 2008). In Figure 1.9 can be seen that a specific critical supersaturation S_c can be defined for each particle size of dry and soluble ammonium sulfate. At this point, the differences between the Kelvin and Raoult effects reach a maximum and any increase in droplet size will consequently result in spontaneous growth. In contrast, smaller droplets will remain inactivated and finally shrink caused by water evaporation (Andreae and Rosenfeld, 2008). Köhler theory concludes that increasing the particle size of a soluble compound concurrently reduces S_c . However, insoluble compounds can also affect

cloud droplet formation since they contribute to the droplet volume and replacing water equivalents for a given droplet diameter. Thus, the solution concentration will be higher which facilitates droplet growth caused by the Raoult effect (Seinfeld and Pandis, 2016; Hinds, 1999). Especially hydrophilic substances can enhance the process by increasing the curvature radius of a droplet and hence counteracting the Kelvin effect (Petters and Kreidenweis, 2007; Andreae and Rosenfeld, 2008). Similarly, certain organic substances may oppose the Kelvin effect caused by the reduction of surface tension (Facchini et al., 1999; Hitznerberger, 2002). All principles and mechanisms mentioned earlier demonstrate that the gas-phase and particle-phase cannot be considered separately in order to understand CCN activity.

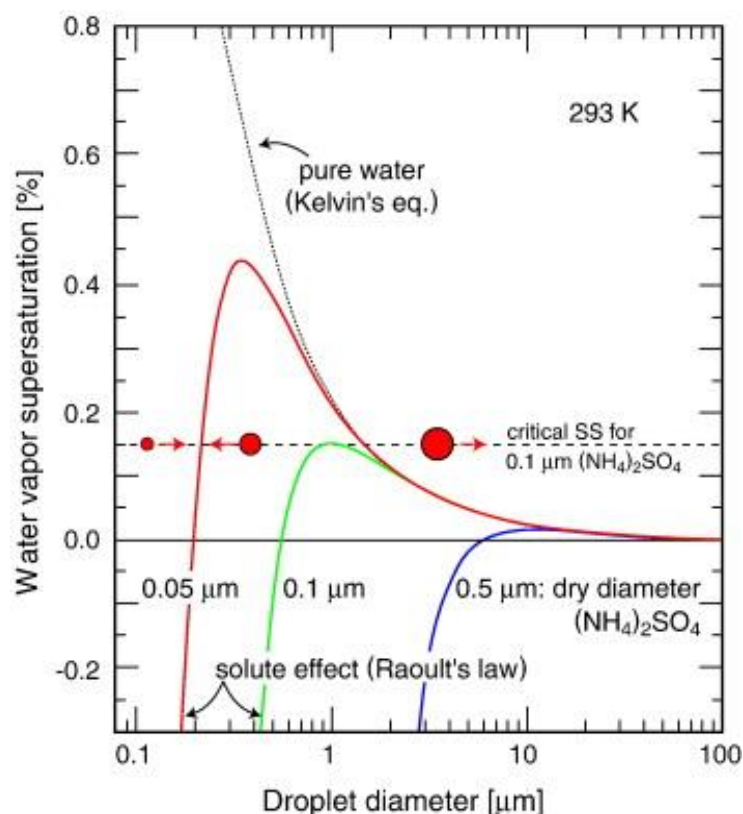


Figure 1.9: Köhler curves illustrating the equilibrium water vapor supersaturation at 293 K for certain masses of dissolved ammonium sulfate (colored solid lines) depending on the droplet diameter. Additionally, the Köhler curve for pure water is shown (dotted line) to highlight the impact of the Kelvin effect. The activation of particles into cloud droplets takes place at diameters above the critical supersaturation S_c (maximum of the Köhler curve) (Andreae and Rosenfeld, 2008).

1.4 Aerosol Particle Collection

One crucial aspect of aerosol research is the reliable collection of representative samples from the atmosphere. These samples need to precisely display the aerosol particle concentration, size distribution, and chemical composition. Since the latter is highly dependent on the sampling location and the

surrounding ecosystem, the samples may not only contain particles from close proximity but also aged air masses from both biogenic and anthropogenic sources (Alfarra et al., 2004; Putaud et al., 2004). Therefore, special requirements are placed on the sample collection. In the following sections, sampling techniques relevant to this study will be introduced shortly. Additionally, the unique sampling location in the Amazon rainforest as one of the most remote regions on Earth will be highlighted.

1.4.1 Filter Sampling

Aerosol filter sampling is the most common technique to transfer aerosol particles from the air on a filter material to store and transport them. It is an approved method in regards to its ease, flexibility, and low cost (Kulkarni et al., 2011). However, filter samples require manual processing. Considering intensive field campaigns, the number of collected filters can be extraordinarily large resulting in demanding analysis efforts. The sample collection is usually achieved by sucking air through a certain filter material. The instrumental requirements are rather simple consisting of a pump with flow regulation, a flow controller, a filter holder, and a potential particle pre-separator. Depending on the application an appropriate filter medium should be chosen. The schematic setup is illustrated in Figure 1.10.

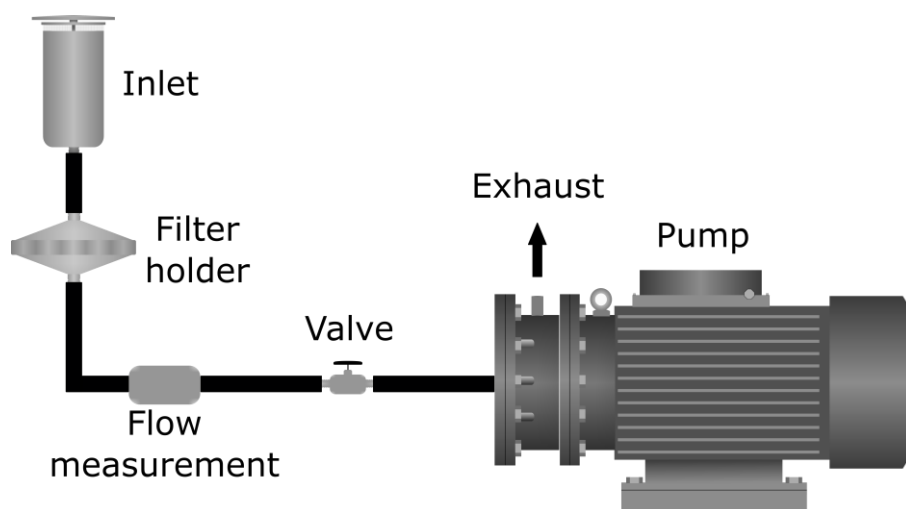


Figure 1.10: Instrumental setup of an aerosol filter collection system. In this study, a PM_{2.5} pre-separator was used as an inlet.

Aerosol sampling, however, still remains a bottleneck in aerosol research (Parshintsev et al., 2017; Raynor et al., 2011). The filter analysis requires a sufficient aerosol mass which is associated with prolonged sampling durations. Usually, several hours of sampling are adequate for urban areas but pristine areas often need up to 24 hours due to lower ambient particle number concentrations. This may

alter the chemical composition of collected particles caused by reactive aerosol species which potentially induce the oxidation of already sampled compounds. Additionally, SVOCs can evaporate from or condensate onto the sample inducing negative or positive artifacts (Parshintsev et al., 2017; McMurry, 2000). In order to correct for errors during the aerosol collection, blank samples should be analyzed, which are handled in the same sampling procedure.

Generally, the aerosol particle collection can be performed with various kinds of sampling inlets such as impactors or cyclones to exclude specific particle diameters. Depending on the impactor PM10, PM2.5, and PM1 particle size separation can be achieved (PM – particulate matter). This particle size-exclusion may become necessary to prevent contamination of PM2.5 samples with pollen or fungal spores. The working principle of impactors is based on the impaction of particles in an airstream on a plate within their flight path if their inertia is sufficiently large. Smaller particles with less inertia, however, can follow the streamlines and will not collide with the impaction plate (Mitchell and Pilcher, 1959; Marple and Olson, 2011). In the case of measurements where particle size distributions are desired, a series of impaction stages can be aligned as a cascade. This cascade impactor allows the separation of discrete particle size ranges. A specialized setup developed by Marple et al. (1991) is the microorifice uniform deposit impactor (MOUDI). It features the uniform particle collection on interchangeable impaction slides for adjustable field campaigns. Similar to the aerosol inlet, the applied filter material needs to match the requirements of aerosol sampling and subsequent analysis. Important factors including high collection efficiency, a low pressure drop, mechanical firmness, and cost may influence the optimal choice (Raynor et al., 2011; McMurry, 2000). A broad variety of different filter materials is commercially available. Only fibrous filters, which are relevant for this study, will be shortly described in the following. These filters consist of fine fibers arranged perpendicular to the airflow with porosities up to 99% (Hinds, 1999). Quartz filters are advantageous for their low amounts of contamination and chemical inertness. Glass fiber filters typically provide high collection efficiencies of more than 99% for all particles and are resilient against moisture (Raynor et al., 2011). The collection efficiency of a filter describes the capability to remove particles from a passing airstream and basically depends on various deposition mechanisms (Hinds, 1999):

- *Interception* occurs if a particle follows the airstream around the fiber but finally collides with it because the fiber happens to lie within the particle radius.
- *Impaction* occurs for particles with sufficient momentum to escape the streamlines to consequently collide with the fiber.
- *Diffusion* occurs for small particles that are moving randomly caused by Brownian motion and eventually diffuse on the fiber.

- *Settling* occurs for large particles that are affected by gravity and finally impact with the fibers

The total aerosol collection efficiency can be simplified calculated by the sum of all individual efficiencies for the above-mentioned mechanisms. Figure 1.11 illustrates the total collection efficiency along with the single deposition mechanisms depending on the particle diameter. It can be seen, that particles larger than $0.5\ \mu\text{m}$ are collected by mechanisms depending on the aerodynamic diameter, while particles smaller than $0.5\ \mu\text{m}$ are collected by mechanisms relying on the physical diameter (Hinds, 1999).

Finally, appropriate processing of the collected aerosol particles is required regarding the subsequent analysis. Filter samples are rarely suited for direct analysis such as microscopic techniques. Usually, the particles need to be separated from the filter material. The most common technique represents liquid extraction with suitable solvents combined with temperature or ultrasonic treatment (Schmeling and Klockow, 1997; Barrado et al., 2012).

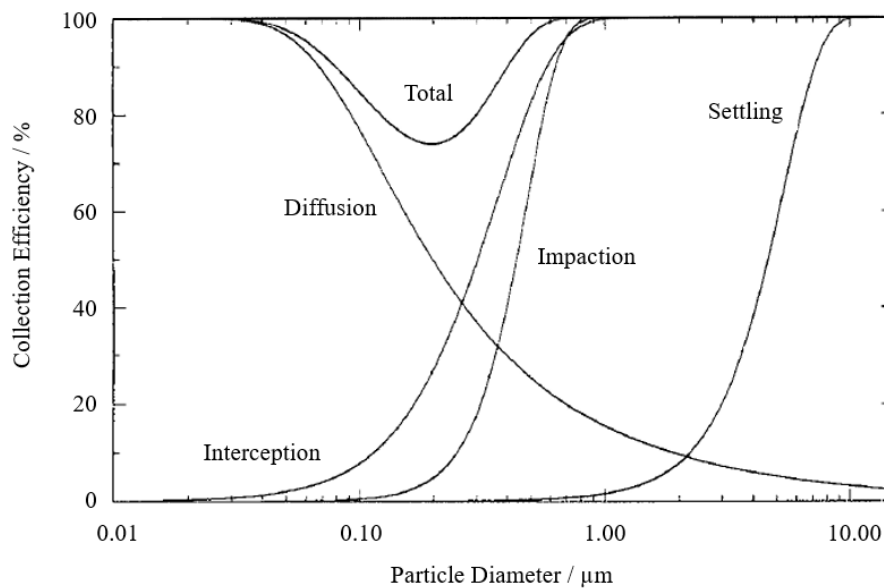


Figure 1.11: Aerosol particle collection efficiency for individual deposition mechanisms and the resulting total efficiency. Figure adapted by Hinds (1999).

1.4.2 Sampling Location: The Amazon Rainforest

The Amazon Basin is one of the most pristine environments on Earth and covers a region of about $6.9 \cdot 10^6\ \text{km}^2$ of South America. Approximately 80% of this region is covered with rain forests which accounts for circa 40% of all tropical forests on the globe (Goulding and Barthem, 2003; Andreae et al.,

2015). Various studies estimated the total carbon content of the Amazon forest at about 80 Pg C (Houghton et al., 2001; Saatchi et al., 2007), which demonstrates its crucial role in climate change and life on Earth in general. Wang and coworkers (2014) indicated a strong correlation between tropical temperature variations and the increase of CO₂ in the atmosphere. Similar to the carbon cycle, the hydrological cycle provided by the Amazon river is responsible for the most species-rich ecosystem on the planet (Hoorn et al., 2010; Wittmann et al., 2013). The immense biodiversity, however, is constantly threatened by deforestation and land-use change (Vieira et al., 2008). Especially biomass burning events during the hotter dry season (August – November) are a huge danger to numerous habitats and cause aerosol particle concentrations comparable to heavily polluted urban areas (Artaxo, 2002; Andreae et al., 2004). In contrast, the Amazon rain forest exhibits the lowest aerosol concentrations during the cooler rainy season (February – May) without anthropogenic pollution from distant sources and mainly consisting of biogenic emissions (Pöschl et al., 2010; Martin et al., 2010; Artaxo et al., 2013; Andreae et al., 2015). This huge variety of aerosol concentrations and aerosol sources is heavily affecting the radiation budget, precipitation, and cloud physics and is a result of massive seasonal shifts of the Intertropical Convergence Zone (ITCZ) (Schafer, 2002; Andreae et al., 2004; Lin et al., 2006; Oliveira et al., 2007). Periodically, Saharan dust, African biomass smoke, and marine aerosols are transported into the Amazon Basin to further contribute to the tremendous complexity of aerosols in the tropical rain forest.

It is obvious that this versatile ecosystem is under constant development and long-term measurements are required to understand the coherence between the atmosphere and biosphere (Zeri et al., 2014; Andreae et al., 2015). For this reason, the 325 m tall Amazon Tall Tower Observatory (ATTO) was established within the Amazon rainforest in 2014 as a Brazilian-German partnership (Andreae et al., 2015). In addition to two smaller 80 m tall towers, ATTO allows measurements throughout the planetary boundary layer. Thus, aerosol samples close to the canopy display local processes while aerosol samples at elevated altitudes can reveal regional and transregional impacts with a continental footprint area of about $1.5 \cdot 10^6 \text{ km}^2$ (Bakwin et al., 1998; Pöhlker et al., 2019). The research site is located about 150 km northeast of Manaus in Brazil and roughly 12 km northeast of the Uatumã river within the Uatumã Sustainable Development Reserve (USDR). Figure 1.12 illustrates the location as well as the connection from Manaus.

The tall tower is positioned on a plateau at ~ 120 m above sea level and surrounded by dense, non-flooded upland forests (terra firme) while floodplain forests, campinas (savanna on white-sand soils) and campinaranas (white-sand forest) dominate between the river and the plateau (Andreae et al., 2015). Andreae and coworkers (2015) give detailed insights into ecological, gas-phase, and particle-phase measurements covered by the ATTO project.

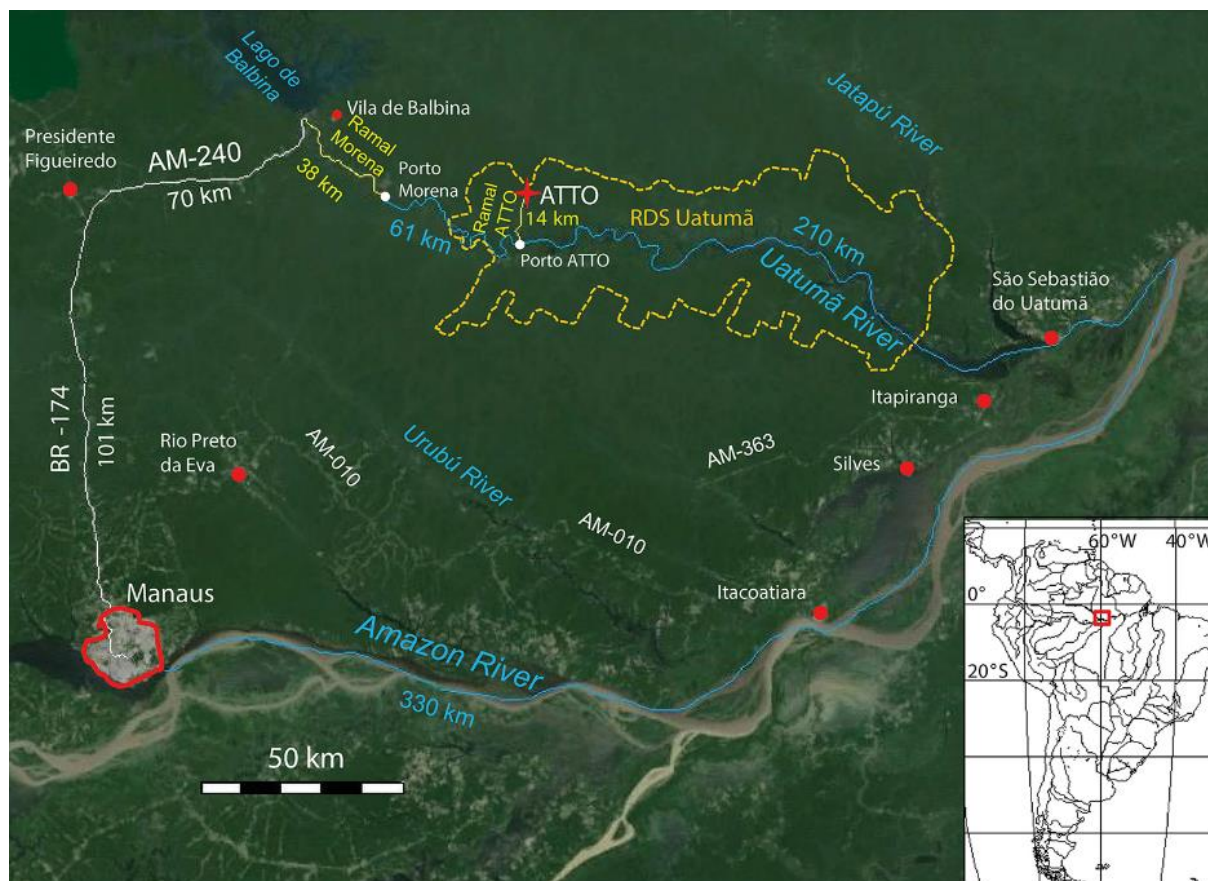


Figure 1.12: Location of the ATTO research site and the connection from Manaus by car and riverboat (Andreae et al., 2015).

1.5 Sample Analysis by Chromatography

Chromatography is a separation technique based on physicochemical processes. Varying partition equilibria of analyte species between a stationary phase and a mobile phase induce their separation (Skoog and Leary, 1996). In the last decades, high-performance liquid chromatography (HPLC) has been established as an important technique in analytical chemistry. The fundamental setup is shown in Figure 1.13. The system consists of reservoirs for different eluent solutions, a pump for high pressures, a sample injection system, the separation column, and a detector, e.g., UV/Vis detector, fluorescence detector, or a mass spectrometer (MS). A degasser removes dissolved gases, such as nitrogen and oxygen, to prevent flow fluctuations of the mobile phase. Finally, the eluent solutions are mixed in the mixing chamber, which enables gradient separation as well as isocratic separation (Meyer, 2009). For analysis, a small sample volume is injected into the eluent flow and carried through the separation column. Different interaction efficiencies of the analytes with the sorbent material cause a separation of

all sample compounds into fractions. Consequently, the resulting chromatograms contain qualitative information (retention time) and quantitative information (signal area or height).

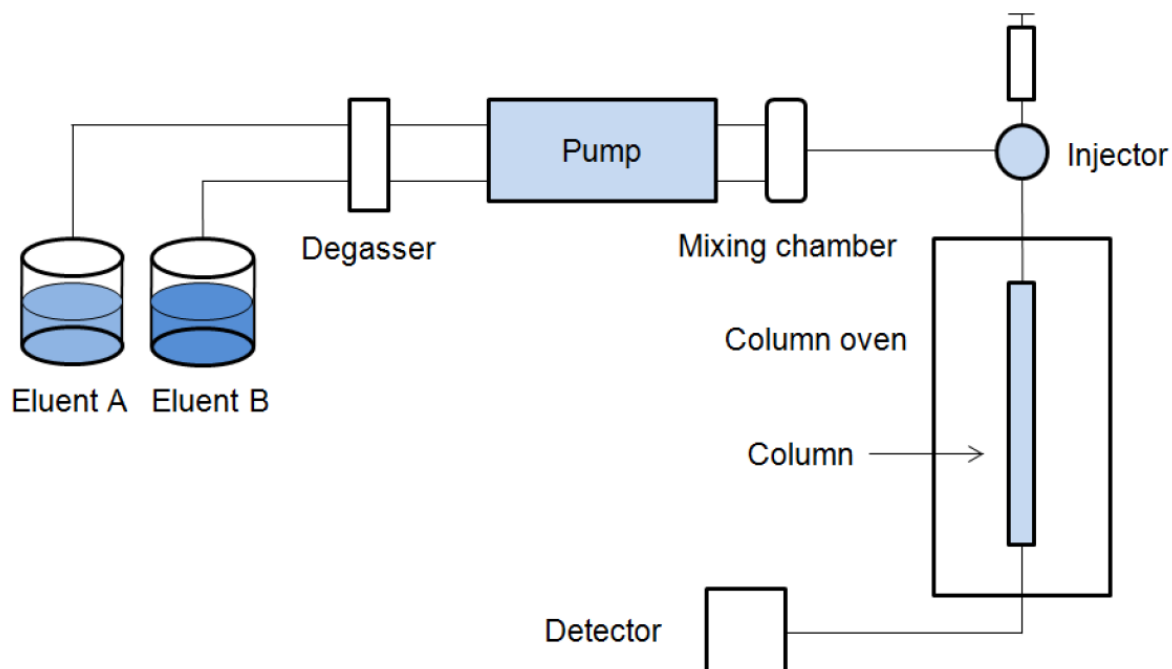


Figure 1.13: Simplified setup of an HPLC system.

Generally, chemically modified silica gel is used as packing materials for columns. The particle size of the porous material varies commonly between 1.5 μm and 10 μm . Efficient analyte separation is achieved by small particle sizes. However, higher system pressures are the consequence, resulting in the need for ultra high-pressure liquid chromatography (UPLC) instruments (Jorgenson, 2010; Harris, 2014). The separation efficiency can be controlled by modifying the hydroxyl groups on the silica surface. For reversed phase (RP) HPLC, alkyl chains can be added, e.g., n-butyl (C4), n-octyl (C8), n-octadecyl (C18), or phenyl-alkyl. In combination with polar solvents, analytes with the highest polarity elute first. In general, acetonitrile and methanol are used with various percentages of water. In contrast, normal phase (NP) HPLC uses non-polar solvents and polar column materials, resulting in stronger retention of polar analytes.

1.6 Mass Spectrometry as a Versatile Candidate for Aerosol Analysis

The understanding of atmospheric processes of particulate matter, such as formation and transformation processes, largely relies on the complete characterization of the entire aerosol. This task

requires analytical techniques to resolve the molecular level (Johnston and Kerecman, 2019). The molecular analysis enables the identification of individual marker compounds that can be attributed to certain sources or formation processes. Thus, primary and secondary particles can be distinguished as fresh and aged particles. Additionally, aerosol transformation mechanisms can be resolved by identifying and quantifying specific products of atmospheric reactions. Mass spectrometry (MS) meets the requirements for molecular analysis through the connection of high sensitivity and molecular specificity and is consequently the most common technique applied in aerosol research (Pratt and Prather, 2012a; Farmer and Jimenez, 2010). The basic principle of MS is the formation of ionized molecules from inorganic and organic compounds which can subsequently be separated and detected depending on their mass-to-charge ratio (m/z) (Gross, 2011). Moreover, the application of ultrahigh-resolution mass spectrometry (UHRMS), such as Fourier transform ion cyclotron (FTICR)-MS or Orbitrap MS, allows the determination of the exact molecular mass of a compound which can be assigned to an unambiguous sum formula. Additionally, structural information of the molecules can be obtained by MS/MS experiments utilizing quadrupole time-of-flight (QToF)-MS, triple quadrupole MS or ion traps. Mass spectrometry comprises several methods, each suitable for a specific task. Thus, an appropriate choice is crucial for reliable results. It can be distinguished between offline and online techniques. Generally, offline mass spectrometry provides more detailed molecular and structural information at the expense of time resolution since the aerosol particles are collected (e.g., on filters or sorbents) before the analysis. Consequently, individual compounds with low concentrations can be detected (Pratt and Prather, 2012a). Particularly the combination of MS with pre-separation techniques such as high-performance liquid chromatography (HPLC) and gas chromatography (GC) can largely increase the selectivity for aerosol components. In contrast, online techniques enable high time resolution which allows observing the chemical composition as well as transformation processes in real-time. As a result, diurnal patterns of aerosol concentrations and transient events can be revealed (Zhang et al., 2015) which are not resolved by offline MS. Simultaneously, possible sampling artifacts can be eliminated (Pratt and Prather, 2012b). In the following sections, a short overview of applied and relevant MS techniques will be provided. For further details, it is referred to recently published literature (Pratt and Prather, 2012a, 2012b; Nozière et al., 2015; Johnston and Kerecman, 2019).

1.6.1 Online Mass Spectrometry

Online MS instruments can be further divided into two subclasses. Firstly, instruments for bulk aerosol measurements where thousands of particles are ionized collectively after they were thermally vaporized. This allows the analysis of the average chemical composition of the bulk aerosol. Secondly,

instruments for single particle measurements where individual particles are analyzed successively. Using a pulsed laser, it is possible to desorb and ionize single particles (Pratt and Prather, 2012b). One of the most common instruments for the chemical characterization of submicron aerosol particles is the Aerodyne aerosol mass spectrometer (AMS) (Canagaratna et al., 2007). The schematic setup is illustrated in Figure 1.14. The aerosol particles are drawn through an aerodynamic lens which generates a precise particle beam. In the following vacuum chamber, non-refractory components are thermally vaporized on a heated tungsten surface at roughly 600 °C and subsequently ionized by electron impact (EI). Thus, refractory components that cannot be vaporized at 600 °C under a high vacuum are not accessible by AMS (DeCarlo et al., 2006). Finally, the ions are detected by time-of-flight (ToF)-MS or quadrupole (Q)-MS. An alternative operation mode allows the application of a rotating chopper which divides the incoming particle beam into small packages in order to obtain chemically resolved particle size distributions (Canagaratna et al., 2007).

Electron impact is referred to as a hard ionization technique that induces a high degree of fragmentation. Although this prevents detailed molecular and structural speciation, the characteristic fragments can be utilized to reliably quantify compound classes such as nitrates, sulfates, ammonium, chloride, and organics since they typically do not interfere with other chemical species (DeCarlo et al., 2006; Canagaratna et al., 2007).

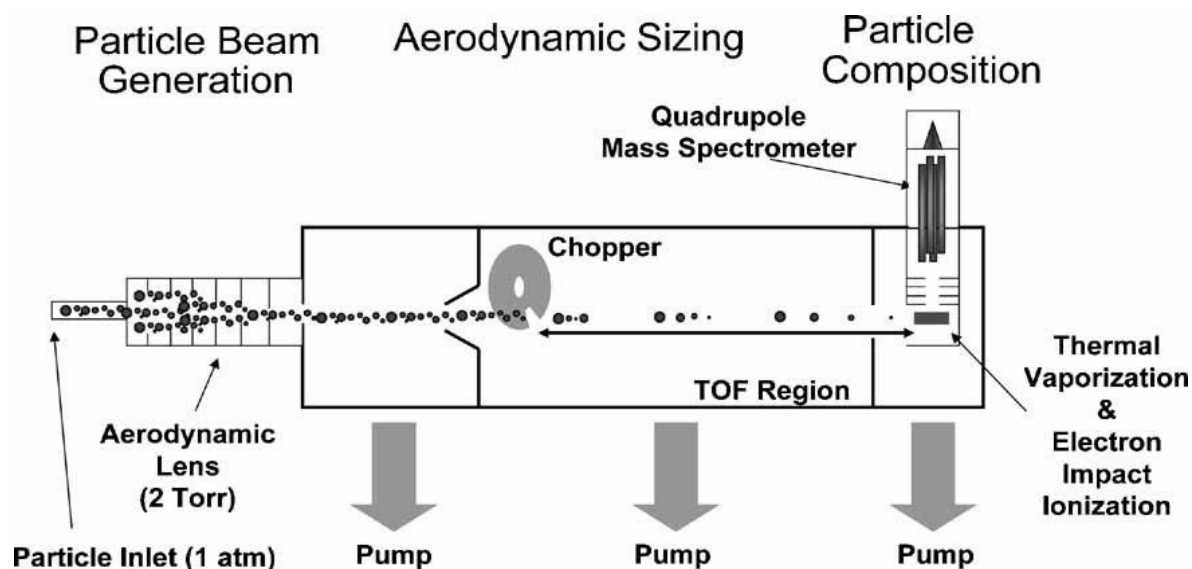
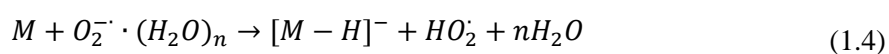
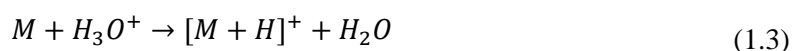


Figure 1.14: Simplified setup of an AMS including chopper measurements. The following mass analyzer was omitted due to clarity reasons (Canagaratna et al., 2007).

To tackle the disadvantage of limited molecular information, the MS can be coupled with soft ionization techniques. In various studies, atmospheric pressure chemical ionization (APCI) has already been used for online measurements (Kückelmann et al., 2000; Hoffmann et al., 2002; Vogel et al., 2013).

This ionization method mostly retains the molecular structure of organic compounds and was first reported by Horning et al. (1973). The aerosol particle stream is heated within a ceramic tube to transfer the analytes into the gas-phase. Upon a corona discharge between a needle and the MS transfer capillary, the buffer gas (usually N₂) is ionized which subsequently leads to the formation of analyte ions. Depending on the applied potential difference, positive or negative ions can be generated after the reaction of the analyte M with H₃O⁺ ions and O₂⁻ radicals (Gross, 2011). The principle reactions for both ionization modes resulting in analyte ions are shown in Equation (1.3) and (1.4).



In the positive mode, a sequence of initial reactions in the corona discharge region leading to the formation of N₄⁺ radicals. In the presence of water vapor, following ion-molecule reactions will finally generate H₃O⁺ reagent ions which can ionize analyte components via proton transfer. Only analytes with higher gas-phase basicity than H₃O⁺ are accessible by this operation mode. In the negative mode, in contrast, the O₂⁻ radicals are directly formed by the corona discharge and act as reagent ions. Via proton abstraction, the analyte molecules are ionized forming deprotonated [M-H]⁻ ions. Thus, only analytes with higher gas-phase acidity are accessible by this operation mode (Horning et al., 1973; Dzidic et al., 1976; Andrade et al., 2008).

1.6.2 Offline Mass Spectrometry

The applications of offline mass spectrometry have considerably increased over the last decades. Particularly, the proceedings in molecular identification of organic analytes are highly beneficial for aerosol research. Offline MS techniques largely contributed to the understanding of heterogeneous reactions as well as oligomerization reactions (Hallquist et al., 2009). Offline MS provides high selectivity and molecular speciation of SOA compounds, especially in combination with pre-separation techniques such as HPLC and GC which compensates for the requirement of previous aerosol collection (Sullivan and Prather, 2005; Pratt and Prather, 2012a). Nowadays, LC-MS is a common technique for the identification and quantification of polar, nonvolatile, and thermally labile organic compounds in SOA samples even without prior derivatization (Hallquist et al., 2009; Johnston and Kerecman, 2019). Through a broad variety of different columns with specific functionalities, LC is highly adaptable. There is a considerable amount of studies regarding the application of offline MS in the field of aerosol

research (e.g., Surratt et al., 2007b, Lukács et al., 2009). It has been shown that organosulfates are relevant contributors to atmospheric SOA and can directly be formed in the particle-phase. These findings highlight the potential of high-resolution MS in combination with pre-separation techniques.

Similar to online MS, APCI is suitable for offline MS. However, electrospray ionization (ESI) is favored for the operation of LC-MS systems (Ardrey, 2003). ESI also ionizes analytes with no or little fragmentation and thus preserves the intact molecular structure which allows the analysis of sensitive and fragile compounds. Through the formation of multiply charged species, ESI enables the determination of large compounds on MS instruments with limited m/z ranges (Konermann et al., 2013). The ionization mechanism is schematically illustrated in Figure 1.15. Through the ESI capillary the LC sample solution can be introduced into a strong electrical field (typically 2 – 6 kV). The generation of ions can be separated into three main steps: i) the initial formation of charged droplets, ii) droplet size reduction by the evaporation of the solvent, iii) formation of gaseous ions (Konermann et al., 2013; Gross, 2011). Through the applied electric field at the needle tip, charged molecules are separated in the solution. Finally, a distorted *Taylor cone* is formed at the liquid surface caused by the balance between surface tension and the repulsion of equally charged molecules (*Coulombic repulsion*). With increasing distance to the capillary, the *Taylor cone* gets unstable and emits a fine jet of droplets. These droplets undergo rapid solvent evaporation causing a growing charge density on the droplet surface. Upon reaching the *Rayleigh limit*, the *Coulombic repulsion* exceeds the surface tension resulting in the emission of nanodroplets (Cech and Enke, 2001; van Berkel and Kertesz, 2007; Kebarle and Verkerk, 2009).

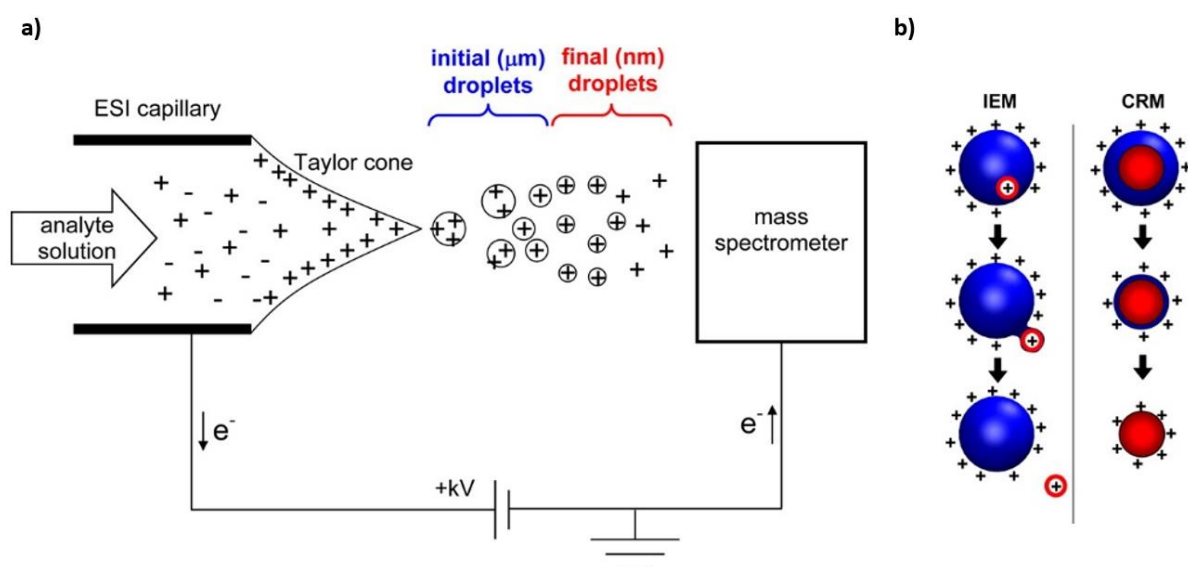


Figure 1.15: a) Schematic drawing of an ESI source operating in positive ion mode. Gas-phase ions are generated from analytes in solution. b) Processes of different ionization mechanisms. IEM: ion evaporation model, small ions are ejected from charged nanodroplets. CRM: charged residue model, single analyte ions are released after the evaporation of the solvent (adapted by Konermann et al. (2013)).

The ion formation out of nanodroplets is commonly described by two different models. The *ion evaporation model* (IEM) suggests that desolvated analyte ions are directly emitted from the surface of highly charged nanodroplets. In contrast, the *charged residue model* (CRM) suggests ion formation from Rayleigh-charged nanodroplets which contain only a single analyte molecule by complete solvent evaporation. It is widely accepted that the IEM applies to low molecular weight analytes, while the CRM applies to large molecular species (Koner mann et al., 2013).

1.6.3 Orbitrap Mass Spectrometry

The field of mass spectrometry is characterized by an incredible variety of different ionization techniques, mass analyzers, and detection methods. While the kind of ionization determines the accessible analyte classes, the synergy of mass analyzer and detector is responsible for the quality of the analysis (Zubarev and Makarov, 2013). For this reason, FTICR-MS and Orbitrap MS have gained increased attention in the field of aerosol research over the past decade. The Orbitrap mass analyzer offers high resolution (e.g., $R = 140\,000$ at m/z 200) in combination with high mass accuracy (<2 ppm) and is therefore referred to as ultrahigh-resolution mass spectrometry (UHRMS) (Makarov, 2000; Nizkorodov et al., 2011). Although FTICR-MS offers similar characteristics, the Orbitrap requires no magnetic field which lowers cost and needed space.

The Orbitrap technique relies on the ion trapping within an electrostatic field. First, the ions are focused by collisional cooling in a curved C – trap. Afterward, the ions can be either injected into the Orbitrap for direct analysis or into the higher-energy collisional cell (HCD) for fragmentation and MS/MS experiments. A schematic drawing of the Q-Exactive Orbitrap MS is shown in Figure 1.16. The Orbitrap consists of an inner electrode encased by a barrel-shaped outer electrode, which is separated into two parts by an insulating ceramic ring. The cross-section illustrates the ion movement along the z-axis. In this process, the electrostatic attraction of the ions towards the inner electrode is compensated by a centrifugal force caused by the tangential velocity resulting in a complex axial harmonic oscillation ω (Scigelova and Makarov, 2006; Perry et al., 2008). The corresponding frequency is proportional to the square root of the reciprocal m/z ratio and can be described by Equation (1.5). It is shown that the ions oscillate with different frequencies depending on their m/z ratio. Solely the oscillation in the z-direction is relevant for the measurement.

$$\omega = \sqrt{\left(\frac{z}{m}\right) \cdot k} \quad (1.5)$$

The parameter k describes the force constant of the electric field and is referred to as the axial restoring force. The frequency is independent of the initial kinetic energy of the ions and can be measured as an image current on the outer electrodes. A subsequent Fourier transformation deconvolutes the respective image currents into high-resolution mass spectra (Scigelova and Makarov, 2006; Perry et al., 2008).

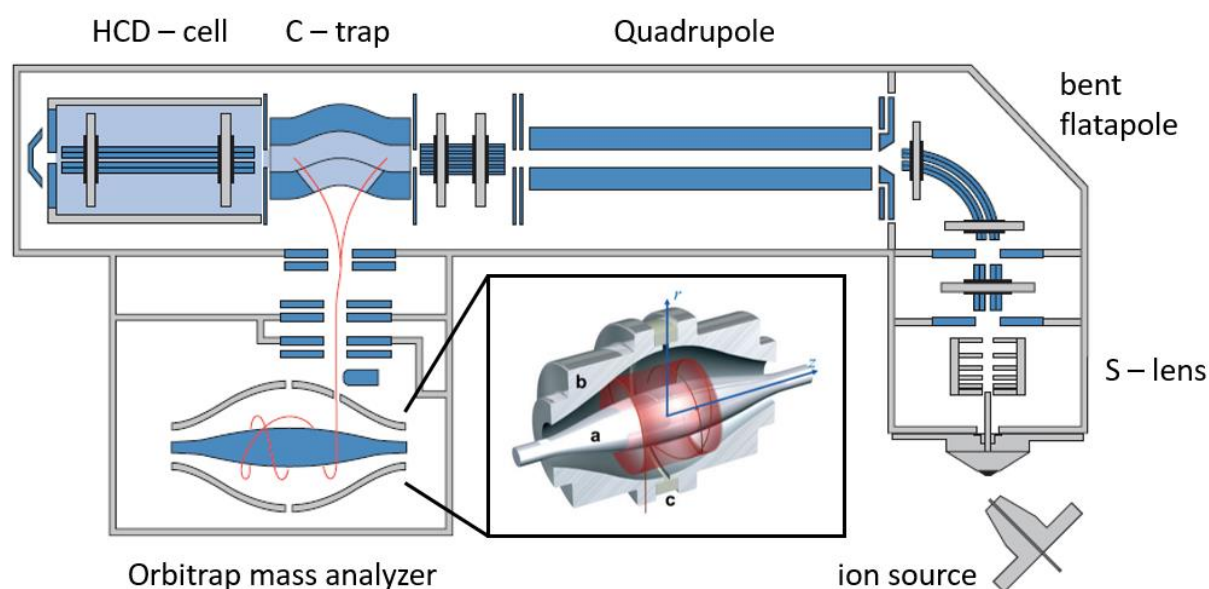


Figure 1.16: Schematic setup of the Q-Exactive Orbitrap MS used in this study (adapted by (Thermo Fisher Scientific, 2011)). The insert illustrates the cross-section of the Orbitrap mass analyzer with a) the inner electrode, b) the barrel-shaped outer electrode, and c) an insulating ceramic ring that separates the two parts of the outer electrode. The ion movement along the z-axis is indicated by red-colored orbits (Scigelova and Makarov, 2006).

1.7 Motivation and Thesis Objectives

The contribution of secondary organic aerosols to the total estimated radiative forcing is still uncertain. In order to better understand the formation, as well as the fate and impact of SOA particles, the chemical composition needs to be unraveled completely and accurately. However, the analysis of complex and dynamic ambient aerosol samples repeatedly challenges atmospheric research. Thousands of different organic species are involved in transformation and aging processes covering a huge variety of functionalities, polarities, and volatilities. Consequently, the instrumental requirements cannot be accomplished by a single analytical method. This issue highlights the need to adapt existing techniques and to improve the subsequent data evaluation. Mass spectrometry has proven a promising tool for aerosol research, as it combines high selectivity and molecular specificity. In particular, high-resolution mass spectrometry offers the ability to identify unambiguous molecular formulas of organic SOA

compounds. Although detailed information is obtained by this technique, multiple data processing steps are necessary to reliably interpret the results. Furthermore, mass spectrometry is relying on complementary analytical approaches. The introduction of complex organic mixtures into the MS system might cause ion suppression and adduct formation resulting in erroneous results. Prior separation of organic analytes by liquid chromatography could help to overcome this issue while also distinguishing isomeric compounds.

The main aspect of this work was to develop a suitable LC-ESI-MS method for the trace analysis of organic aerosol filter samples from the Amazon rainforest. The Amazon basin plays a superior role in the global climate and allows the investigation of atmospheric processes under almost pristine conditions. Besides the identification and quantification of certain organic marker compounds, a comprehensive characterization of the organic fraction should be achieved. For this purpose, regional representative aerosol samples (PM_{2.5} and MOUDI samples) were collected at the ATTO research site in the Amazon rainforest during the following field campaigns:

- Wet seasons: April 2018, March 2019
- Dry seasons: October 2018, September 2019

In this study, differences in the aerosol composition were investigated between the respective seasons and years. Additionally, vertical concentration profiles of specific aerosol marker compounds were evaluated. Height-resolved measurements throughout the boundary layer may help to assess the SOA contribution of both local emission sources and long-range transportations. The unique sampling location should help to clarify the anthropogenic impact of the combustion of biomass during the dry periods. In contrast, clean periods can reveal pristine aerosol compositions mainly characterized by biogenic emissions. To characterize the organic aerosol fraction, a non-targeted approach was applied with the assistance of software-based data treatment.

This thesis investigates important aspects of method development and mass spectral data processing. Various standard solutions with relevant marker compounds were prepared to determine the instrumental detection limits. Additionally, the recovery rate for filter extractions was calculated by spiking blank filters with a known concentration of a standard solution. An optimized parametrization for subsequent non-targeted data evaluation is presented.

Furthermore, this study focuses on the chemical characterization of filter samples from ATTO. Seasonal differences in the chemical composition of aerosol particles were investigated using comprehensive non-targeted visualization methods, such as Van-Krevelen diagrams, Kendrick mass defect, and average carbon oxidation states. For a detailed overview, all signals were classified as either

background compounds or non-background compounds. While background compounds characterize the local SOA chemical composition, non-background compounds present individual plume events (e.g., anthropogenic emissions, biomass combustion, long-range transportation). Furthermore, a targeted analysis was applied for certain marker species representing important SOA precursor molecules. This approach should help to evaluate their contribution to aerosol formation and to identify potential emission sources. In particular, the enantiomeric ratio of pinic acid was calculated. The results directly link chiral measurements of α -pinene in the gas-phase to the oxidation product in the particle-phase.

2 Molecular Characterization of SOA Particles

This chapter is a reprint of the manuscript:

Denis Leppla, Nora Zannoni, Leslie Kremper, Maria Praß, Bruna Hollanda, Jonathan Williams, Florian Ditas, Christopher Pöhlker, Stefan Wolff, Marta Sá, Maria Christina Solci, Thorsten Hoffmann

Comprehensive Non-Targeted Molecular Characterization of Secondary Organic Aerosols from the Amazon Rainforest by High-Resolution Mass Spectrometry

In preparation for *Atmospheric Chemistry and Physics*



Abstract

The Amazon rainforest plays a crucial role in the global climate and allows the investigation of organic aerosol constituents under almost pristine conditions. However, human activities affect this ecosystem substantially. Here, ambient aerosol samples were characterized by high-resolution mass spectrometry (HR-MS) collected at the Amazon Tall Tower Observatory (ATTO) at two dry and wet seasons, respectively. Comprehensive non-targeted data evaluation was applied to identify thousands of molecular formulae. They were mainly associated with isoprene and monoterpene (i.e., α -, β -pinene, limonene) oxidation products, highlighting the predominance of biogenic emissions at ATTO. The chemical composition revealed distinct seasonal patterns with more processed organic compounds during drier seasons including highly oxidized and oligomeric species. Long-range transportation and less removal by wet deposition might favor increased abundances of later-generation oxidation products. Additionally, higher numbers of mono- and polycyclic heteroaromatic components were attributed to enhanced biomass burning (BB) activities during the dry seasons. The wet seasons were generally characterized by less oxidized compounds, associated with freshly formed aerosol particles. However, the second wet season revealed a high abundance of BB related aromatics, indicating a growing influence of anthropogenic activities. Height-resolved measurements supported the forest canopy as the main source for biogenic emissions with higher concentrations of certain marker species. Although, prominent differences in the chemical composition could not be observed. The present study demonstrates the growing impact of deforestation on this unique environment, while also presenting a detailed overview of aerosol molecular characteristics and emissions source apportionment at ATTO.

2.1 Introduction

Organic particulate matter (PM) significantly contributes (up to 90%) to the total atmospheric aerosol mass (Kanakidou et al., 2005; Kroll and Seinfeld, 2008; Jimenez et al., 2009). While primary organic aerosols (POA) are emitted directly into the atmosphere (e.g., combustion of biomass), secondary organic aerosols (SOA) are produced by oxidative processes and transformations of volatile organic compounds (VOC) in the atmosphere (Seinfeld and Pankow, 2003). Numerous studies have already illustrated the complex chemical composition of organic aerosols covering various compound classes and thousands of different organic species (Tolocka et al., 2004; Zhang et al., 2007; Goldstein and Galbally, 2007; Wozniak et al., 2008; Nizkorodov et al., 2011). Their physicochemical characteristics have a substantial impact on the climate and human health (Pöschl, 2005; Hallquist et al.,

2009). Consequently, clarifying the chemical composition of organic aerosols is an essential task of atmospheric related studies.

Compounds in OA feature a huge variety of functionalities, polarities, and volatilities at various concentration regimes (Goldstein and Galbally, 2007). This poses major challenges for analytical techniques (Nozière et al., 2015). Traditional gas chromatography and liquid chromatography systems coupled to mass spectrometry (GC/MS, LC/MS) have proven useful to identify certain OA species (Hoffmann et al., 2011). However, these methods are limited to compounds with specific physicochemical properties and, thus, not adequate to resolve complex organic mixtures. In contrast, the Aerodyne aerosol mass spectrometer (AMS) is capable of elucidating the elemental composition of OA samples to clarify atmospheric processes (Canagaratna et al., 2007; Dall'Osto et al., 2012) at the expense of information on the molecular level. Hence, high-resolution mass spectrometry (HR-MS) with enhanced resolving power ($\geq 100\ 000$) and high mass accuracy (≤ 5 ppm) has received more and more attention in aerosol research. The combination with soft ionization methods, such as electrospray ionization (ESI), allows a detailed characterization of complex OA samples (Nizkorodov et al., 2011). Several studies have already proven the potential of HR-MS in smog chamber experiments. Hundreds of different organic species have been detected in SOA samples generated by isoprene and monoterpene oxidation (Tolocka et al., 2004; Bateman et al., 2008; Nguyen et al., 2010). Additionally, OA samples from urban and pristine environments have been analyzed by HR-MS to identify transformation processes as well as potential sources of aerosol constituents. Wang et al. (2017) investigated the chemical composition of OA from Shanghai by Orbitrap MS. The authors observed distinct seasonal variations with a strong contribution of biomass burning related compounds in the winter months. Furthermore, Tong et al. (2016) detected several mono- and polycyclic aromatic species at a road tunnel in Birmingham, UK. Their results suggested vehicle exhaust as the primary emission source. In contrast, Kourtchev et al. (2013) showed that the remote boreal forest from Hyytiälä, Finland, is mainly characterized by aliphatic species. However, they observed an increased number of aromatic compounds during periods influenced by continental air masses.

The Amazon basin is one of the most pristine ecosystems accounting for approximately 40% of all tropical forests on Earth (Goulding and Barthem, 2003; Baccini et al., 2012). The immense biodiversity of this environment highlights its crucial role in the global climate and atmospheric chemistry. However, the Amazon region is dramatically affected by anthropogenic activities such as deforestation and urbanization (Andreae et al., 2015). As a result, large seasonal differences in OA concentrations can be observed influencing the radiative balance and cloud processing (Pöschl et al., 2010; Artaxo et al., 2013). In this study, LC-HR-MS was used to analyze aerosol filter samples from the Amazon rainforest covering several seasons from 2018 and 2019. Sophisticated non-targeted analytical techniques were

applied to link the OA molecular composition with meteorological conditions, potential emission sources, and (trans)formation processes.

2.2 Experimental Section

2.2.1 Aerosol Sample Collection

Ambient PM_{2.5} aerosol samples were collected in the Amazon rainforest at the ATTO research station (Amazon Tall Tower Observatory). In total, four measurement campaigns were performed to investigate seasonal variations on the SOA chemical composition. The sampling time covered the wet season 2018 (04/14/2018 – 04/19/2018), the dry season 2018 (10/22/2018 – 10/31/2018), the wet season 2019 (03/04/2019 – 03/14/2019), and the dry season 2019 (09/20/2019 – 09/26/2019). The research site allows height-resolved measurements on a 325 m tall tower in the central Amazon basin (coordinates: S 02°08.752' W 59°00.335') and is described in detail by Andreae et al. (2015). Shortly, the nearest urban region is Manaus which is located approximately 150 km southwest of ATTO. The station is part of the Uatumã Sustainable Development Reserve (UDSR) and is reached via the roughly 12 km distant Uatumã river. The location is shown in Figure 2.1. The tower is located at about 120 m above sea level on a plateau that is embedded in a dense, non-flooded forest (terra firme) with adjacent floodplain forests and white-sand soil savannas (campinas) and forests (campinaranas). The area at ATTO is characterized by a canopy height of about 40 m. The meteorological conditions at ATTO are depending on the location of the Intertropical Convergence Zone (ITCZ) providing clean and rainy circumstances from February until May and polluted and drier conditions from August to November with strong contributions from anthropogenic deforestation and land-use change (Pöhlker et al., 2019). Relevant meteorological parameters were constantly measured and are shown in the supporting information (Figure S1, Figure S2). The corresponding wind profiles and backward trajectories were generated by the HYSPLIT Trajectory Model (Stein et al., 2015; Rolph et al., 2017).

Ambient PM_{2.5} filter samples were collected at three different heights at ATTO (wet season 2018: 42 m, 150 m, 320 m; dry season 2018 and wet season 2019: 80 m, 150 m, 320 m; dry season 2019: 0 m, 80 m, 320 m) using borosilicate glass microfiber filter bonded with PTFE (Pallflex® Emfab, 70 mm diameter). A pre-separator (Digitel, DPM2.3) was set up in front of the filter to only collect the size fraction with aerodynamic particle diameters below 2.5 µm at constant flow rates of 38 L min⁻¹. The sampling duration was set to 10 h – 14 h to allow daytime and nighttime related sample collection while ensuring sufficient particle mass on the filter material. Additionally, a micro-orifice uniform deposit impactor (MOUDI) was installed at the neighboring 80 m triangular mast (coordinates: S 02°08.602' W

59°00.033') to collect aerosol particles according to their aerodynamic diameter. Thirteen stages enabled sampling of particles covering diameters between 10 nm to 10 μm at a constant flow of 10 L min^{-1} . The aerosol inlet was located at 60 m height. Blank filters were collected according to the mentioned procedures but with disabled pumps. In total, 246 filter samples were collected and stored in the freezer before their analysis.



Figure 2.1: Excerpt of a map showing the location of the measurement site ATTO. The tower is located approximately 150 km northeast of Manaus. The map was drawn and provided by Iris Moebius, Max Planck Institute for Biogeochemistry, Jena, Germany.

2.2.2 Aerosol Sample Analysis

A part of each filter sample (1/2) was extracted three times by adding 1.5 mL of a 9:1 mixture of methanol and water (Fisher Scientific, Optima™ grade). The samples were subsequently agitated for 30 min on a laboratory shaker. The combined liquid phases were filtered afterward through a 0.2 μm PTFE syringe filter (Carl Roth, Rotilabo® KC 94.1) and evaporated completely by a gentle stream of N_2 . The residue was then reconstituted in 700 μL of a 9:1 mixture of water and acetonitrile (Fisher Scientific, Optima™ grade).

Ten microliters of each sample were analyzed three times by ultra high-performance liquid chromatography (UHPLC) (ThermoFisher Scientific, UltiMate 3000) coupled to a high-resolution Orbitrap mass spectrometer (MS) (ThermoFisher Scientific, Q Exactive™). A heated ESI source was installed and operated in the negative ionization mode. The instrument was externally calibrated with a

calibration solution (Fisher Scientific, Pierce™) and a 2 mM sodium acetate aqueous solution providing mass accuracies below 1 ppm. The sample analysis was performed in the range of m/z 50 – 750 at a mass resolving power of 140 000 at m/z 200. The following ESI-MS parameters were used for the measurements: ESI capillary temperature 300 °C; spray voltage –3.2 kV; sheath gas flow 30; auxiliary gas flow 10, S-lens RF level 50%. The UHPLC system was operated with an HSS T3 column (100 × 2.1 mm ID, 1.8 μm, Waters, ACQUITY UPLC®) and the mobile phase A (water with 2% acetonitrile and 0.04% formic acid) and mobile phase B (acetonitrile with 2% water). The conditions for gradient elution were as follows: 0 – 2 min 0% B, 2 – 9 min linear increase to 30% B, 9 – 15 min linear increase to 95% B, 15 – 17.5 min 95% B, 17.5 – 19 min linear decrease to 0% B, 19 – 21 min 0% B at a constant flow rate of 350 μL min⁻¹.

2.2.3 Non-Targeted Data Evaluation

The LC/MS data were processed by MzMine 2.30 to obtain molecular formulae C_cH_hO_oN_nS_s with the following limitations: $2 \leq C \leq 40$, $2 \leq H \leq 100$, $0 \leq O \leq 40$, $0 \leq N \leq 4$, $0 \leq S \leq 2$. The mass tolerance for the formula assignment was set to ± 2 ppm considering isotope patterns. Adducts were removed and only ions present in all three repeated measurements were retained. The signal intensities per sample were averaged afterward. Blank samples were processed accordingly and subtracted. Only compounds with signal-to-background ratios ≥ 3 were kept for further evaluations.

The number of rings and double bonds can be described by the double bond equivalent (DBE) for each assigned formula. It provides information on the degree of unsaturation. However, heteroatoms with different varying valence values (e.g., oxygen, nitrogen, and sulfur) may lead to uncertainties (Badertscher et al., 2001). The following Equation (2.1) can be used to calculate the DBE:

$$DBE = n_C - \frac{n_H}{2} + \frac{n_N}{2} + \frac{n_S}{2} + 1 \quad (2.1)$$

where n describes the number of the respective element. Based on the DBE values the aromaticity equivalent (X_c) can be calculated to identify mono- and polycyclic aromatic compounds. This metric has been suggested by Yassine et al. (2014) and can be determined following Equation (2.2):

$$X_c = \frac{3(DBE - (p \cdot n_O + q \cdot n_S)) - 2}{DBE - (p \cdot n_O + q \cdot n_S)} \quad (2.2)$$

where p and q represent the fraction of oxygen and sulfur atoms that are involved in the π -bond structure of the molecule. Consequently, these values can vary according to different compound classes. While $p = q = 0.5$ is suggested for carboxylic acids, esters, and nitro functional groups, p and q are set to either 0 or 1 for aldehydes, ketones, alcohols, ethers, and nitroso classes. In the present study, $p = q = 0.5$ was used to calculate X_c considering that negative ESI analysis is highly sensitive to carboxylic acids (Kourtchev et al., 2016; Wang et al., 2017). According to Yassine et al. (2014), $X_c \geq 2.50$ and $X_c \geq 2.71$ are indicating monocyclic and polycyclic aromatic compounds, respectively.

The carbon oxidation state (OS_C) was suggested by Kroll et al. (2011). The authors introduced this value to provide information on oxidative processes in the atmosphere from complex organic samples. Since nitrogen and sulfur can have multiple oxidation states, the OS_C values were calculated for CHO compounds only following the simplified Equation (2.3):

$$OS_C \approx 2 \cdot \frac{n_O}{n_C} - \frac{n_H}{n_C} \quad (2.3)$$

with the elemental ratios O/C and H/C , respectively (Kroll et al., 2011).

Furthermore, the saturation vapor pressure (C_0) has been used in SOA related studies to investigate gas-to-particle partitioning properties of organic compounds (Shiraiwa et al., 2014; Li et al., 2016). The elemental composition and the molecular structure define C_0 , which allows an estimation of the volatility of organic species (Pankow, 1994b; Odum et al., 1996; Murphy et al., 2014). Equation (2.4) can be used to predict the volatility of OA compounds according to Donahue et al. (2011) and Li et al. (2016):

$$\log_{10}C_0 = (n_C^0 - n_C) \cdot b_c - n_O b_O - 2 \cdot \frac{n_C n_O}{n_C + n_O} \cdot b_{CO} - n_N b_N - n_S b_S \quad (2.4)$$

where n_C^0 describes the reference carbon number, b represents the contribution of each element to $\log_{10}C_0$, and b_{CO} denotes the carbon-oxygen nonideality (Donahue et al., 2011). The C_0 values have been calculated for compound classes containing C, H, O, N, and S atoms. The parameters for the calculation based on Li et al. (2016) are listed in the supporting information (Table S1).

Kendrick mass (KM) analysis has been proven to be an effective tool for the interpretation of complex organic mixtures. It allows the assignment of homologous series of the detected compounds, which vary only in the number of a defined base unit (Kendrick, 1963; Hughey et al., 2001). In the present study, CH_2 was chosen as the base unit by rescaling the exact mass of 14.01565 to 14.00000. Following Equation (2.5) the KM_{CH_2} can be calculated for each compound with its exact mass:

$$KM_{CH_2} = exact\ mass \cdot \left(\frac{14.00000}{14.01565} \right) \quad (2.5)$$

which renormalizes the exact mass scale (Hughey et al., 2001). Subsequently, the Kendrick mass defect (KMD) can be calculated by following Equation (2.6):

$$KMD_{CH_2} = nominal\ KM - KM_{CH_2} \quad (2.6)$$

where *nominal KM* describes the KM rounded to the next integer. Consequently, compounds differing only in their number of CH₂ units have the same KMD values. These homologous series can be identified as horizontal lines in KMD plots.

2.3 Results and Discussion

The main focus of this study was to evaluate the complex chemical composition of secondary organic aerosols regarding highly oxidized organic compounds. The atmospheric oxidation of isoprene and monoterpenes are of special interest since they produce highly functionalized molecules with an increased proportion of oxygen atoms (Peeters et al., 2001; Bates and Jacob, 2019). It is assumed that most of these compounds contain carboxyl and hydroxyl groups. Consequently, they can produce deprotonated ions which is why negative ESI mode was applied for the sample analysis (Cech and Enke, 2001). Figure 2.2 illustrates typical high-resolution mass spectra in the negative ESI mode from filter samples of the dry season 2018 and the wet season 2019. The y-axis is enlarged to show 50% of the relative signal intensity as maximum to also visualize low-intensity ions. All detected compounds were separated by reversed-phase HPLC before the MS analysis, reducing ion suppression in the ESI source. The most intense ion signal of all samples was attributed to the deprotonated formic acid dimer with the molecular formula C₂H₃O₄ at *m/z* 91.0036. Formic acid was added to the aqueous LC solvent and was consequently omitted in the mass spectra due to clarity reasons. The chemical composition of the SOA samples was mainly characterized by seasonal influences throughout the measurement campaigns. The majority of compounds were attributed to molecular weights (MW) below 250 Da for both seasons, while the mass spectra from the dry season additionally displayed signals in the oligomeric region between 300 Da – 450 Da with lower intensities. In contrast, several studies have demonstrated that the ozonolysis of biogenic VOCs (i.e. α-pinene, β-pinene, isoprene) in smog chamber experiments generates high molecular weight compounds with increased signal intensities in the oligomeric region (Kourtchev

et al., 2014a; Reinhardt et al., 2007). Although ions above 450 Da were detected in all samples, they solely contributed insignificantly to the total number of compounds.

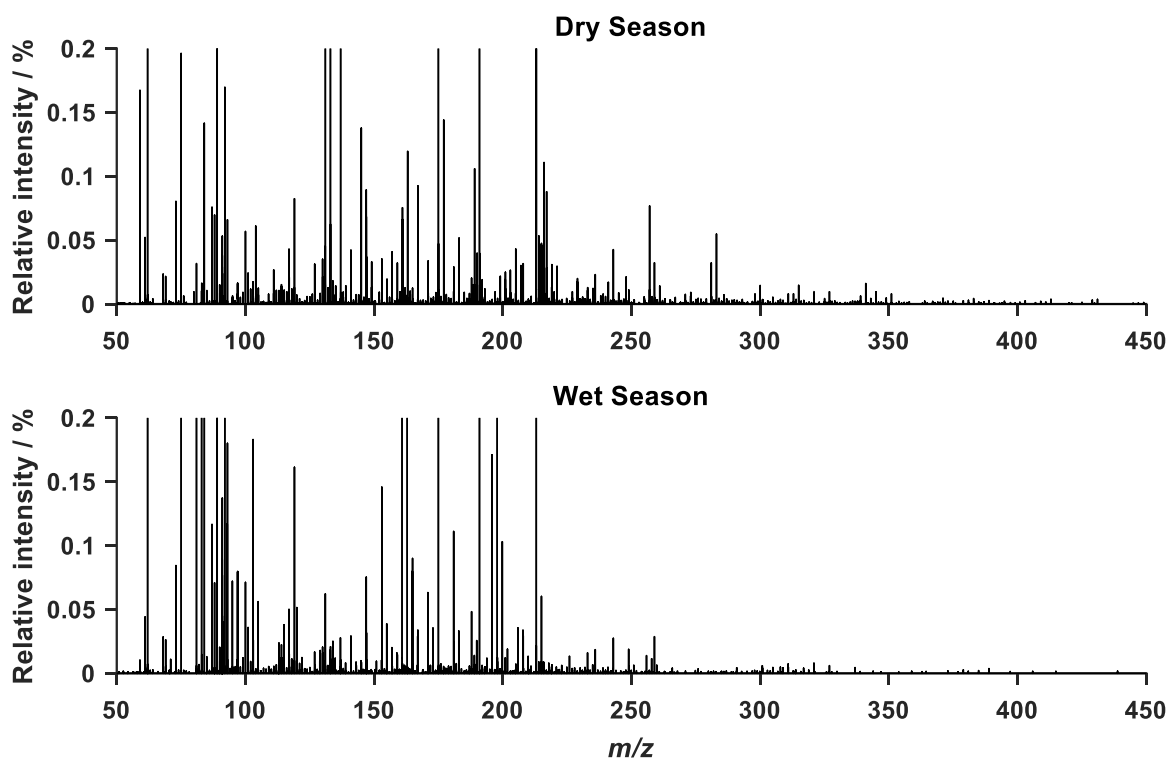


Figure 2.2: Typical high-resolution mass spectra obtained in the negative ESI mode from filter samples of the dry season 2018 and wet season 2019, respectively. A UHPLC system separated the compounds before the injection into the mass spectrometer. The most intense ion signal at m/z 91.0036 was omitted for clarity reasons. It was attributed to the deprotonated formic acid dimer ($C_2H_3O_4$), which was added to the aqueous LC solvent.

Depending on the season, all filter samples revealed a high chemical diversity with 875 – 1940 unambiguously assigned molecular formulae after the non-targeted data processing, as can be seen in Table 2.1. It should be emphasized that signal detection is dependent on the minimal intensity threshold and the signal-to-noise threshold applied in data processing. Relatively high values were chosen for both parameters to exclude species with low intensities for the evaluation. A large fraction of isomeric compounds, 69% – 85%, was detected in all samples, highlighting the importance of pre-separating the samples by HPLC. The identified molecular formulae were divided into four subgroups according to their elemental composition: CHO (i.e., compounds containing exclusively carbon, hydrogen, and oxygen atoms), CHON, CHONS, and CHOS (additionally containing nitrogen and/or sulfur atoms). In all samples the CHO subgroup was predominant with $(56 \pm 6)\%$, followed by CHON with $(20 \pm 7)\%$, CHOS $(17 \pm 5)\%$, and CHONS $(7 \pm 1)\%$, although the contribution of sulfur- and/or nitrogen-containing compounds increases at higher MWs. This trend is in good agreement with similar studies from remote environments (e.g. Amazonia, Brazil, Kourtchev et al., 2016; Hyytiälä, Finland, Kourtchev et al., 2013),

while studies from a suburban and urban environment revealed enhanced contributions of CHON and CHONS compounds (Pearl River Delta region, China, Lin et al., 2012; Cambridge, UK, Rincón et al., 2012; Shanghai, China, Wang et al., 2017), indicating an increased relevance of nitrogen and sulfur chemistry in more polluted areas. The calculated elemental ratios were highly variable throughout the seasonal measurement campaigns with 0.60 ± 0.37 (mean value \pm standard deviation of the data set) and 1.47 ± 0.49 for O/C and H/C during the dry season and 0.49 ± 0.32 and 1.56 ± 0.45 during the wet season, respectively. The wide variability indicates a high chemical complexity within the data set. Kourtchev et al. (2013) reported comparable values from the boreal forest in Hyytiälä, Finland (0.58 and 1.54 for O/C and H/C, respectively). Additionally, the elemental ratios obtained in this study are consistent with smog chamber experiments using certain BVOCs for SOA generation, e.g. α -pinene (0.42 – 0.55 for O/C and 1.5 for H/C, Putman et al., 2012) and limonene (0.5 – 0.6 for O/C and 1.5 – 1.6 for H/C, Kundu et al., 2012). However, it should be noted that all detected subgroups have different signal responses and detection sensitivities which might lead to uncertainties.

Table 2.1: Summary of all observed MS signals with unambiguous molecular formula assignment for the four measurement campaigns in 2018 and 2019 (wet season = WS, dry season = DS). The signals are divided into four subgroups regarding their elemental composition. Additionally, the average values¹ of molecular weight (MW), carbon oxidation state (OS_C), aromaticity index (X_c), and isomeric fraction are listed.

Season	Height m	Signals	CHO %	CHON %	CHONS %	CHOS %	MW Da	OS _C ²	X _c	Isomers %
WS18	42	1095	54	30	6	10	271	-0.647	0.872	77
	150	875	67	15	7	11	261	-0.606	0.977	80
	320	1293	43	41	7	9	293	-0.681	0.822	70
DS18	80	1856	51	19	7	23	245	-0.324	1.050	83
	150	1940	51	18	8	23	240	-0.353	1.051	85
	320	1720	52	18	8	22	245	-0.330	1.070	84
WS19	80	1555	55	19	5	21	250	-0.535	0.907	81
	150	1081	57	18	7	18	252	-0.486	0.922	81
	320	1287	62	17	6	15	255	-0.558	1.017	82
DS19	0	1328	60	17	5	18	237	-0.425	0.831	69
	80	1225	61	14	6	19	233	-0.439	0.906	84
	320	1050	62	15	6	17	246	-0.525	0.975	77

¹ Average values are calculated based on the molecular composition of each compound.

² Only CHO compounds are considered in the calculation of OS_C.

2.3.1 Background SOA Characteristics

The chemical complexity of the SOA samples is highly influenced by irregular regional events and meteorological conditions between the sampling days. To only consider characteristic species in the evaluation, all molecules were excluded, which were exclusively detected on individual samples. Therefore, only compounds observed in more than 75% of all samples were included in the discussion of this section and are referred to hereafter as background ions. They presumably describe the local SOA characteristics since they are not considered to be dependent on unique emission events. The tentatively identified background ions are listed in Table 2.2. In total, 72 – 215 organic compounds were detected during the dry seasons while fewer compounds were observed during the wet seasons with 28 – 60 different molecular formulae. This is in agreement with another study in central Amazonia by Kourtchev et al. (2016), who observed a more complex chemical composition during the drier period 2014. The discrepancy between the seasons might be explained by comparing the wind profiles for the different seasons. For further details, it is referred to the supporting information.

Table 2.2: Average values¹ of the detected background ions for the wet and dry seasons in 2018 and 2019. The listed molecules were detected in at least 75% of all corresponding samples.

Season	Height m	Signals	CHO %	CHON %	CHONS %	CHOS %	MW Da	OS _c ²	X _c
WS18	42	36	89	0	0	11	170	0.031	0.060
	150	45	82	5	2	11	177	-0.039	0.180
	320	28	82	0	0	18	174	0.040	0.024
DS18	80	211	90	4	1	5	191	-0.404	0.724
	150	215	90	4	1	4	188	-0.418	0.738
	320	209	89	4	1	5	188	-0.407	0.755
WS19	80	51	94	0	2	4	197	-0.497	0.696
	150	52	98	0	2	0	195	-0.464	0.577
	320	60	97	0	2	2	196	-0.499	0.606
DS19	0	72	94	4	1	0	196	-0.367	0.424
	80	108	95	4	0	1	182	-0.424	0.480
	320	75	97	3	0	0	191	-0.398	0.279

¹ Average values are calculated based on the molecular composition of each compound.

² Only CHO compounds are considered in the calculation of OS_c.

The highest number of compounds were detected during the dry season in 2018, whereas significantly lower numbers were observed during the wet season in 2018. The corresponding wind roses (Figure S3) illustrate that incoming air masses at ATTO have passed a larger surrounding area in the wet seasons. Consequently, more possible emission sources must be taken into account, which leads to increased chemical variability but simultaneously fewer background ions. Similar considerations can be made for the comparison between the dry periods. The air masses during the dry season 2019 covered a wider area at ATTO resulting in lower numbers of background ions compared to the dry season 2018. Other parameters that influence the background SOA are the wind speed and air mass origins. The wet seasons are characterized by long-range trade wind pathways from the northeast of ATTO, predefined by the seasonal shift of the ITCZ (Pöhlker et al., 2019). The seven-day HYSPLIT backward trajectories (Stein et al., 2015) show that the air masses need approximately 6 – 7 days from the west coast of Africa to pass the Atlantic Ocean towards ATTO (Figure S4, Figure S5). As a consequence, higher wind speeds of up to 15 – 20 m s⁻¹ were observed during the wet seasons, leading to a dilution of the particle phase at ATTO as already suggested by Kourtchev et al. (2014b). In combination with cleaner marine air masses from the ocean lower background signals are detected during the wet seasons. In contrast, the dry seasons are considerably influenced by biomass burning and other anthropogenic emissions from the eastern regions in Brazil (Artaxo, 2002; Andreae et al., 2015), resulting in higher concentrations of particulate matter (PM) as can be seen in the SMPS data in Figure S6 and Figure S7. Concentrations up to 15 µg m⁻³ have been observed during the dry periods while approximately ten times lower concentrations were detected during the wet season.

To further evaluate the particle phase on a molecular level, van Krevelen (VK) diagrams have been used to visualize varieties between the seasons and sampling heights. This technique is a useful tool to classify organic compounds in complex mixtures with certain chemical properties (Nizkorodov et al., 2011; Nozière et al., 2015). In a VK diagram, the H/C ratio is illustrated as a function of the O/C ratio for each molecular formula detected in a sample. This helps to visualize the degree of oxidation of the particle phase as the most oxidized molecules are located at the lower right corner. Consequently, the most saturated and reduced species are found in the upper left region. Figure 2.3 and Figure 2.4 represent VK diagrams for all four measurement campaigns and sampling heights, respectively. The signal intensity is proportional to the size of the symbols. However, the signal intensities between various compounds should be compared with caution because of their different detection sensitivities. The most intense ion signals for all campaigns are summarized in Table 2.3 with their molecular formula, their possible identity, and precursor species. These compounds are all non-aromatics with a high degree of oxygenation (O/C ≥ 0.5) and either C4-5 or C7-8 backbones, potentially resulting from isoprene and monoterpene (mainly α-pinene, β-pinene, and limonene) oxidation (Kleindienst et al., 2007; Nguyen et

al., 2010; Worton et al., 2013; Hammes et al., 2019). These precursor compounds are the most prevalent biogenic VOCs in the Amazon rainforest, released by a large diversity of terrestrial vegetation (Guenther et al., 1995; Greenberg et al., 2004). As expected, the high signal intensities of the detected background compounds suggest that biogenic sources are the main contributor to the SOA loading at ATTO. Interestingly, the ion at m/z 149.0455 ($C_5H_{10}O_5$) was observed in all analyzed filter samples with high intensities. This component has previously been detected in isoprene oxidation chamber experiments as well as field studies using SOA filter sampling (Krechmer et al., 2015; Chen et al., 2020). Krechmer et al. (2015) identified $C_5H_{10}O_5$ as the most dominant species produced during the photooxidation of isoprene hydroxy hydroperoxides (ISOPOOH), which are important products of the isoprene oxidation under low-NO conditions (Paulot et al., 2009b; Nagori et al., 2019). The authors indicated that the OH-initiated oxidation of ISOPOOH leading to only 2.5% to organic aerosols including $C_5H_{10}O_5$, while approximately 90% resulting in the formation of isoprene epoxydiol (IEPOX) and other gas-phase products. However, Jaoui et al. (2019) also observed $C_5H_{10}O_5$ during isoprene ozonolysis as well as during isoprene photooxidation under high-NO conditions. Consequently, the latter pathways appear to be the dominant reactions during the dry seasons with increased NO concentrations (Figure S8), while the ISOPOOH-SOA pathway under low-NO conditions is presumed during the wet seasons.

The wet season 2018 samples revealed the ion at m/z 215.0231 ($C_5H_{12}O_7S$) as the most intense signal, related to IEPOX-derived organosulfates (OS) (Surratt et al., 2007b; Surratt et al., 2008). It is established that these OSs are formed from the reactive uptake of IEPOX on acidic sulfate particles under low-NO conditions, which is in agreement with our findings. Kourtchev et al. (2016) also identified IEPOX-OS on filter samples from the Amazon rainforest. The authors observed the highest intensities on filters highly affected by surrounding forest fires. Interestingly, the lowest number of active fires was recorded during the wet season 2018 campaign (Table S2) (INPE - Instituto Nacional de Pesquisas Espaciais, 2020). This suggests IEPOX-OS as a relevant SOA constituent independent of the current season and agrees with the idea of mixed anthropogenic-biogenic sources. As indicated by Andreae et al. (2015), the sulfate concentrations during the wet seasons are mainly attributed to biogenic and marine sources, while increased levels during drier seasons are related to combustion activities. The wet season 2019 campaign was mainly characterized by intense ion signals at m/z 157.0506 ($C_7H_{10}O_4$) and m/z 171.0662 ($C_8H_{12}O_4$), presumably attributed to limonene and α -pinene oxidation products (Hammes et al., 2019; Eddingsaas et al., 2012).

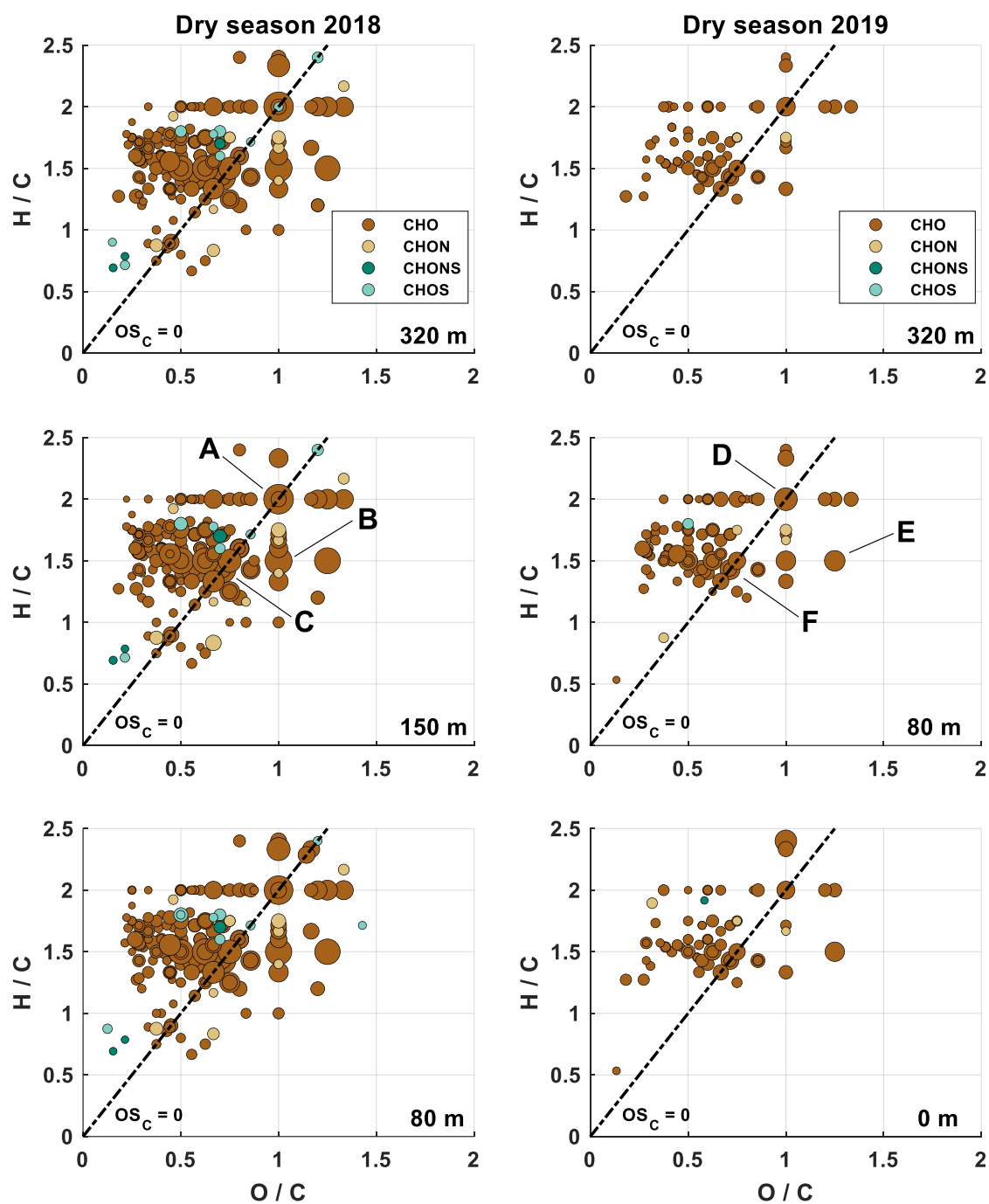


Figure 2.3: Van Krevelen plots from the dry season 2018 (left panel; sampling heights: 320 m, 150 m, 80 m) and the dry season 2019 (right panel; sampling heights: 320 m, 80 m, 0 m). Included are only molecular formulae that were present in more than 75% of the samples, respectively. The size of the data points represents the signal intensity of the corresponding peak. The four subgroups are distinguished with different colors. Compounds located on the black dashed line have an average carbon oxidation state of 0 ($OS_c = 0$). The labels A – F correspond to the most intense signals further characterized in Table 2.3.

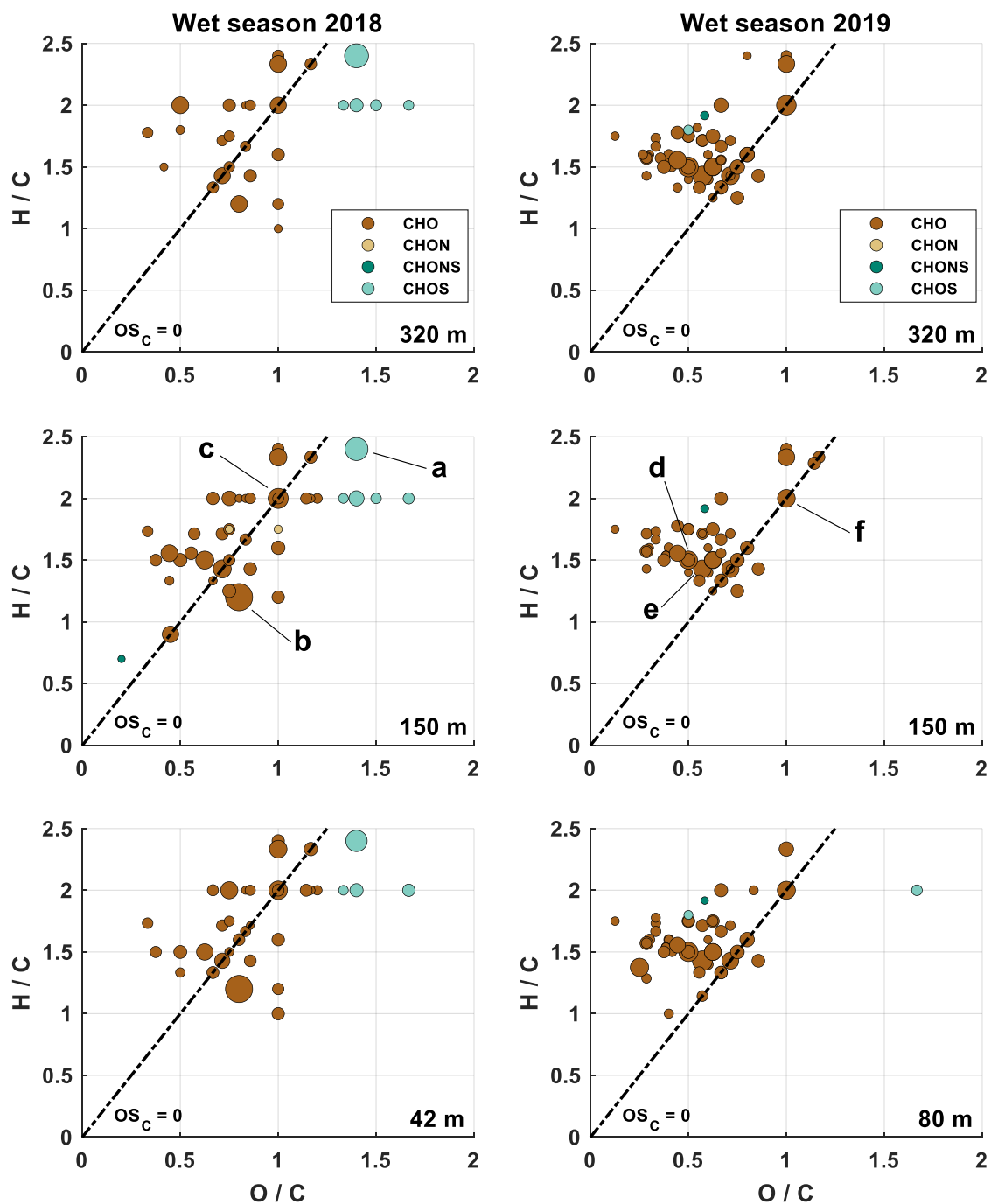


Figure 2.4: Van Krevelen plots from the wet season 2018 (left panel; sampling heights: 320 m, 150 m, 42 m) and the wet season 2019 (right panel; sampling heights: 320 m, 150 m, 80 m). Included are only molecular formulae that were present in more than 75% of the samples, respectively. The size of the data points represents the signal intensity of the corresponding peak. The four subgroups are distinguished with different colors. Compounds located on the black dashed line have an average carbon oxidation state of 0 ($OS_C = 0$). The labels a – f correspond to the most intense signals further characterized in Table 2.3.

Table 2.3: Possible identities and precursors for the most intense signals from the background ions for the different seasons.

Season	ID ¹	Formula	<i>m/z</i>	OS _C	Possible identity	Precursor	Reference
WS18	a	C ₅ H ₁₂ O ₇ S	215.0231	-	IEPOX-OS	Isoprene	(Worton et al., 2013) (Kourtchev et al., 2016)
	b	C ₅ H ₆ O ₄	129.0194	0.4	Dicarboxylic acid / Peroxy acid	Methylfuran	(Joo et al., 2019)
	c	C ₅ H ₁₀ O ₅	149.0455	0.0	Carbonyl-tetrol / Epoxy-tetrol / Carboxyl-triol	Isoprene	(Krechmer et al., 2015) (Chen et al., 2020)
DS18	A	C ₅ H ₁₀ O ₅	149.0455	0.0		See ID c	
	B	C ₄ H ₆ O ₄	117.0193	0.5	Succinic acid	-	(Wang et al., 2017)
	C	C ₇ H ₁₀ O ₅	173.0454	0.0	3-acetylpentane-dioic acid	α-pinene	(Chen et al., 2020) (Kleindienst et al., 2007)
WS19	d	C ₈ H ₁₂ O ₄	171.0662	-0.5	Ketolimonic acid / Terpenylic acid	Limonene / α-pinene	(Hammes et al., 2019) (Eddingsaas et al., 2012)
	e	C ₇ H ₁₀ O ₄	157.0506	-0.3	Carboxylic acid	Limonene	(Hammes et al., 2019)
	f	C ₅ H ₁₀ O ₅	149.0455	0.0		See ID c	
DS19	D	C ₅ H ₁₀ O ₅	149.0455	0.0		See ID c	
	E	C ₄ H ₆ O ₅	133.0142	1.0	Malic acid	Isoprene	(Nguyen et al., 2010)
	F	C ₇ H ₁₀ O ₅	173.0454	0.0		See ID C	

¹ IDs correspond to the labels illustrated in Figure 2.3 and Figure 2.4.

² Isoprene epoxydiol organosulfate ester (2-methyltetrol sulfate ester).

The more complex chemical background of the dry seasons is clearly illustrated in the VK diagram in Figure 2.3. Especially the dry season 2018 was characterized by a high abundance of signals with H/C ratios ≥ 1.5 and O/C ratios ≤ 0.5 . These compounds are commonly attributed to aliphatic species, which can be related to both biogenic and anthropogenic sources. Simultaneously, several compounds with low elemental ratios (H/C ≤ 1.0 and O/C ≤ 0.5) were identified as background ions, typically associated with aromatic hydrocarbons (Wozniak et al., 2008; Mazzoleni et al., 2012). Species within this region in the VK diagram were exclusively observed during the dry season 2018, where the highest particle concentrations were detected. All detected ions were classified by their aromaticity equivalent X_c according to Yassine et al. (2014), in order to identify mono- and polycyclic aromatic species. While monocyclic structures such as benzene and functionalized derivatives are indicated by values of X_c ≥ 2.50 , condensed polycyclic aromatic compounds are described by X_c ≥ 2.71 . Naphthalene is the smallest polycyclic structure meeting this criterion (Yassine et al., 2014; Wang et al., 2017). The dry season 2018 was characterized by several aromatic species with X_c values ≥ 2.50 (Figure S9). The most intense signals correspond to the ions at *m/z* 149.0243 (C₈H₆O₃), *m/z* 164.0353 (C₈H₇NO₃), *m/z* 193.0505 (C₁₀H₁₀O₄), and *m/z* 207.0298 (C₁₀H₈O₅) each with DBE values ≥ 6 . These compounds

were already identified as relevant components of biomass burning activities. Kautzman et al. (2010) and Chhabra et al. (2015) observed $C_8H_6O_3$ and $C_{10}H_8O_5$ during naphthalene photooxidation experiments in a chamber study. Naphthalene and other polycyclic aromatic hydrocarbons (PAH) have been related to wood combustion processes in the literature and are considered to impact human health (Schauer et al., 2001; Chan et al., 2009; Samburova et al., 2016). Similarly, $C_{10}H_{10}O_4$ might be a product formed during the degradation of cellulose and lignin, two important biopolymers (Kong et al., 2021). The MS^2 spectrum (Figure S10) revealed two fragments of CO_2 and $C_3H_4O_2$ (acrylic acid), leading to a tentative structure of ferulic acid. Details can be found in the supporting information. $C_8H_7NO_3$ was assigned to a nitro-phenolic structure, which can be formed during biomass pyrolysis. This compound class is a major contributor to brown carbon (BrC) (Lin et al., 2016) and has been detected earlier in SOA samples from the Amazon rainforest (Claeys et al., 2012). Another intense background ion was 4-nitrocatechol at m/z 154.0146 ($C_6H_5NO_4$), which has been previously considered as a marker compound for biomass burning OA (Iinuma et al., 2010; Claeys et al., 2012; Kourtchev et al., 2016). However, it should be emphasized that the corresponding X_c value for 4-nitrocatechol is 2.33, leading to the assumption that the number of aromatic species might have been underestimated (Wang et al., 2017). All samples collected during the dry season 2018 revealed high ion signals for 4-nitrocatechol, suggesting that biomass burning significantly contributed to SOA. As expected, the concentrations were lower in daytime samples, presumably due to the rapid photolysis of NO_2 and NO_3 radicals during the day (Monks, 2005; Seinfeld and Pandis, 2016). The dry season campaigns were accompanied by an increased number of active fires and biomass burning, as can be seen in Table S2. Consequently, the detected aromatic hydrocarbons are mainly attributed to anthropogenic sources (Henze et al., 2008). Surprisingly, the background analysis of the dry season 2019 revealed solely two different aromatic compounds although the number of registered forest fires in the Amazon region was nearly twofold. The ion at m/z 164.0353 ($C_8H_7NO_3$) appeared in almost every sample in high intensities, suggesting this compound to be an important biomass burning marker in this study. The second ion at m/z 219.0455 ($C_{15}H_8O_2$) has already been reported by Bruns et al. (2015). The authors identified this compound as an oxygenated PAH produced during wood combustion with a pyrene core structure, which seems reasonable according to the increased X_c Value of 2.82 and 12 DBE.

To further characterize the chemical background composition the average carbon oxidation state (OS_C) has been calculated for each detected molecular CHO formula. This metric was introduced by Kroll et al. (2011) and can be used to describe complex mixtures of organic aerosols. Various chemical processes in the atmosphere are determined by the oxidation state of organic components. Highly oxidized molecules (HOM) with sufficiently low volatilities are able to nucleate, resulting in new particle formation and subsequent particle growth and aging (Bianchi et al., 2016; Molteni et al., 2016).

Organic species with $OS_C = 0$ are indicated by the dashed line in Figure 2.3 and Figure 2.4. According to Tu et al. (2016), HOMs are defined as molecules with $O/C \geq 0.6$ and/or $OS_C \geq 0$ and are consequently located on the right side of the dashed line in the VK diagrams. It is clearly visible that samples from the dry season 2018 revealed the highest number of highly oxygenated and oxidized ions, accounting for approximately 30% of the total number of compounds. The average molecular formula for the HOMs during the dry season 2018 was $C_{6.5}H_{8.6}O_{5.1}$ with C4 – C10 backbones, indicating isoprene and monoterpene precursor as the main source for HOMs in the Amazon. The dry season 2019 revealed a less oxidized effective molecular formula of $C_{6.7}H_{10.2}O_{5.7}$. However, it should be noted that the number of highly oxygenated compounds might have been underestimated in this study since very polar species were not separated sufficiently with the LC-method (Figure S11).

Figure 2.5 and Figure 2.6 illustrate the OS_C depending on the carbon number for each CHO compound, with OS_C values ranging from -1.5 to $+1.2$ for the dry seasons and -1.1 to $+1.0$ for the wet seasons. This result is consistent with other studies in remote environments (Kourtchev et al., 2013; Kourtchev et al., 2016). Molecules with OS_C between -0.5 and -1.5 and carbon numbers greater than seven are considered as biomass burning organic aerosol (BBOA), which is primarily emitted in the atmosphere. In contrast, molecules with OS_C between -0.5 and $+1.0$ with less than 13 carbon atoms are generally associated with semivolatile and low-volatility oxygenated organic aerosol (SV-OOA and LW-OOA) (Kroll et al., 2011; Wang et al., 2017). These compounds are formed by multiple oxidation reactions and are commonly attributed to fresh and aged SOA, respectively (Zhang et al., 2007; Jimenez et al., 2009). The chemical background composition during the dry seasons revealed several compounds attributed to LV-OOA, indicating more aged SOA compared to the wet seasons. Long-range transportation due to less precipitation might be responsible for that observation. Additionally, the abundance of species related to BBOA suggests forest fires as a key contributor to SOA loadings in the Amazon rainforest during the dry periods. In contrast, the majority of the background compounds during the wet seasons are associated with SV-OOA, indicating that local biogenic emissions are the main source for freshly formed SOA. Interestingly, the contribution of BBOA related compounds was significantly higher for the wet season 2019, presumably because of the increased number of active fires for this period.

The background analysis revealed major differences in the chemical composition between the two seasons in the Amazon rainforest. However, we could not observe significant variations at different heights. It is assumed that characteristic background compounds are well mixed in the atmosphere at ATTO and their attendance is independent of short-time events occurring at individual heights.

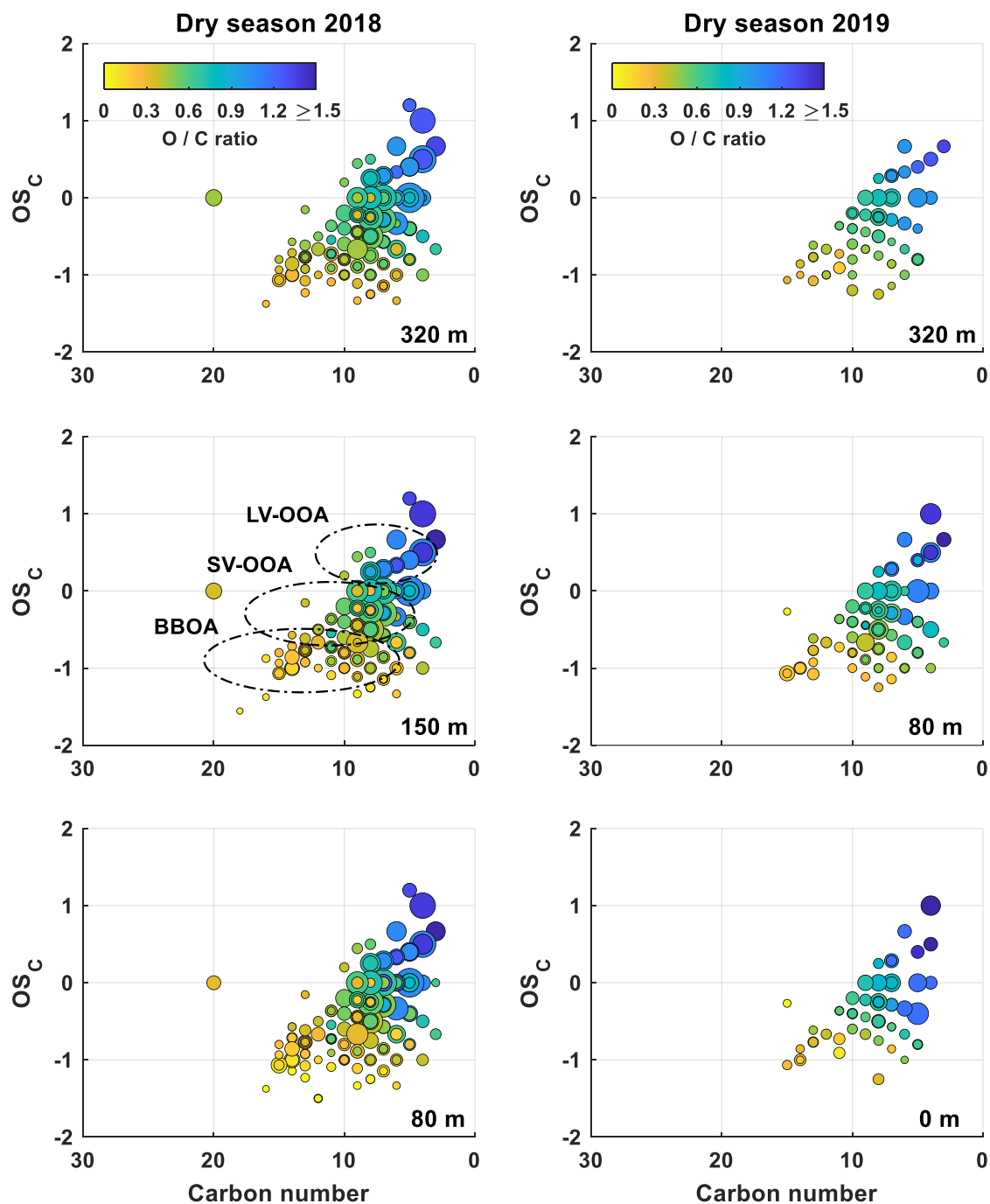


Figure 2.5: Carbon oxidation state (OS_C) plots for all detected CHO species during the dry season 2018 (left) and dry season 2019 (right). Only background ions are included. The size of the data points represents the signal intensity of the corresponding peak. The color code illustrates the degree of oxygenation. The black dashed areas are related to low-volatility (LV-OOA) and semivolatile (SV-OOA) oxygenated organic aerosol and biomass burning organic aerosol (BBOA) (Kroll et al., 2011).

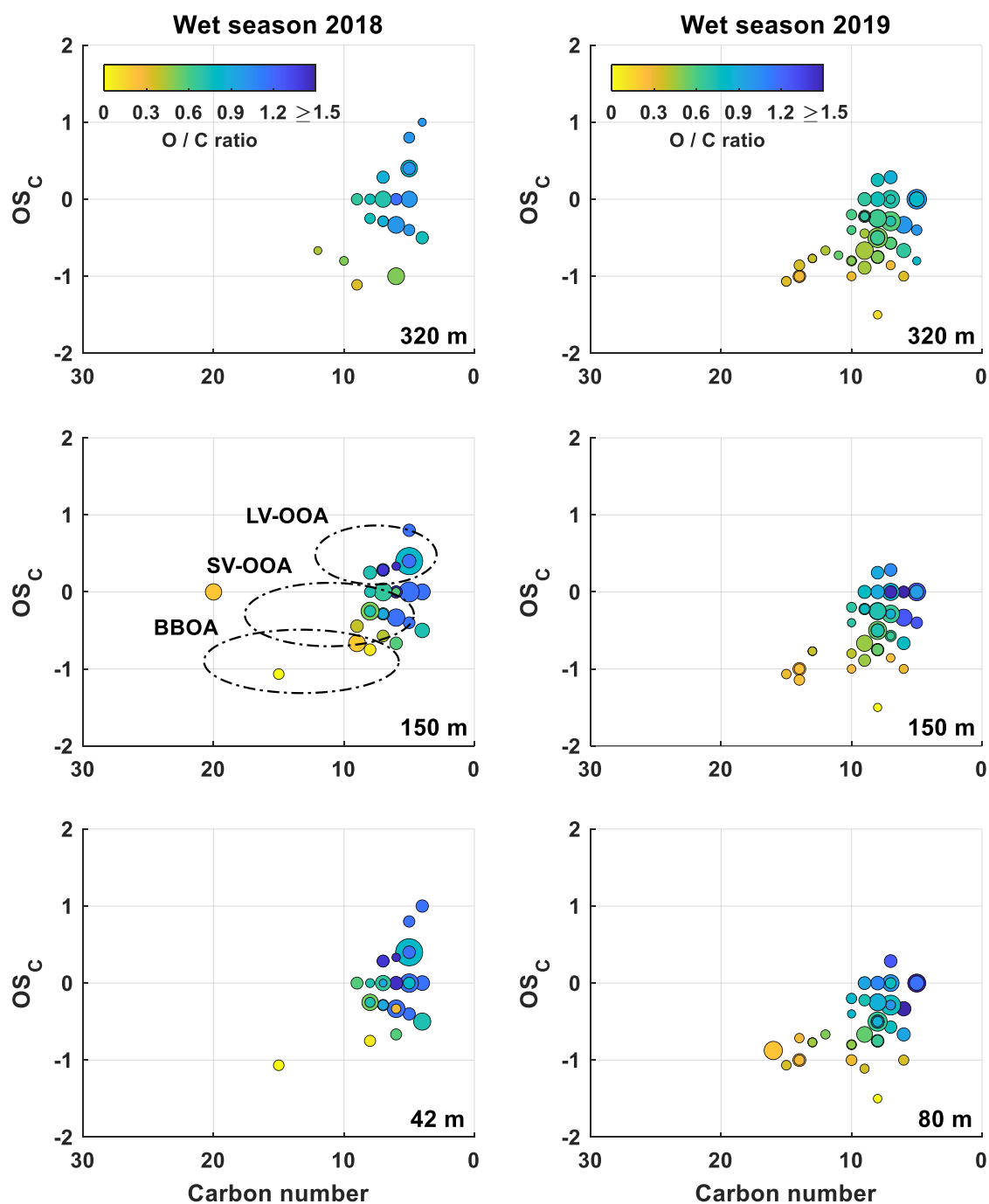


Figure 2.6: Carbon oxidation state (OS_C) plots for all detected CHO species during the wet season 2018 (left) and wet season 2019 (right). Only background ions are included. The size of the data points represents the signal intensity of the corresponding peak. The color code illustrates the degree of oxygenation. The black dashed areas are related to low-volatility (LV-OOA) and semivolatile (SV-OOA) oxygenated organic aerosol and biomass burning organic aerosol (BBOA) (Kroll et al., 2011).

2.3.2 Detailed Non-Targeted Data Evaluation

The chemical composition of SOA filter samples is getting more complex by also considering signals which are not included in the background data. These signals were attributed to irregular atmospheric events presumably caused by varying meteorological conditions. However, compounds that were only detected once in the respective data set were excluded as they were not considered representative. Additionally, the already discussed background data was subtracted in this section. The remaining signals were attributed according to the sampling time during daytime (7:00 – 17:00 local time, UTC-4h) and nighttime (17:00 – 7:00). An additional sample in the morning (7:00 – 12:00) was collected during the dry season 2019 only, while the daytime sample was collected between 12:00 and 17:00. The resulting VK diagrams are shown in Figure 2.7 and Figure 2.8 for the seasons in 2018, and Figure S12 and Figure S13 for 2019. The most complex chemical composition was observed during the dry season 2018, similar to the considerations related to the background signals. A large number of CHOS compounds have been detected. More than 85% of these molecules have $O/S \geq 4$, indicating the presence of at least one sulfate functional group. Especially, species with $O/C \geq 1$ and $H/C \geq 2$ were the most prominent (region (I) in Figure 2.7), with highly oxygenated C4 and C5 backbones. The two signals with the highest intensities were related to $C_5H_{12}O_7S$ (m/z 215.0231, IEPOX-OS) and $C_5H_{10}O_7S$ (m/z 213.0075) and were detected on filter samples from all four campaigns. Both structures were already attributed to isoprene-derived OS, indicating isoprene as the most important precursor for S-containing OA at ATTO. The mentioned compounds have been classified as background species during the wet season 2018, however, with significantly lower signal intensities. This result implies that the formation of IEPOX-OS is correlated to increased sulfate concentrations during the dry seasons, probably related to biomass and fossil fuel emissions from long-range transportation (Andreae et al., 2015). This result is supported by Kourtchev et al. (2016), who observed the highest concentrations of IEPOX-OS on filter samples impacted by a large number of surrounding forest fires. Interestingly, nighttime samples revealed the highest CHOS signal intensities for all measurement campaigns. This result has also been observed by Kourtchev et al. (2014b) and Gómez-González et al. (2012) who suggested an increased gas-to-particle partitioning at lower temperatures during the night.

Another ion at m/z 135.0663 ($C_5H_{12}O_4$) has been identified as 2-methyltetrols during each campaign with high intensities and is well established in the literature as a relevant photooxidation product of isoprene in the Amazon rainforest (Claeys et al., 2004b; Claeys et al., 2010; Kourtchev et al., 2016). Simultaneously, a high abundance of HOMs was observed during the dry seasons and the wet season 2019 (region (II) in Figure 2.7), indicating more aged organic species. This is also highlighted by an increased number of LV-OOA species in the OS_C plots, as can be seen in the supplementary information.

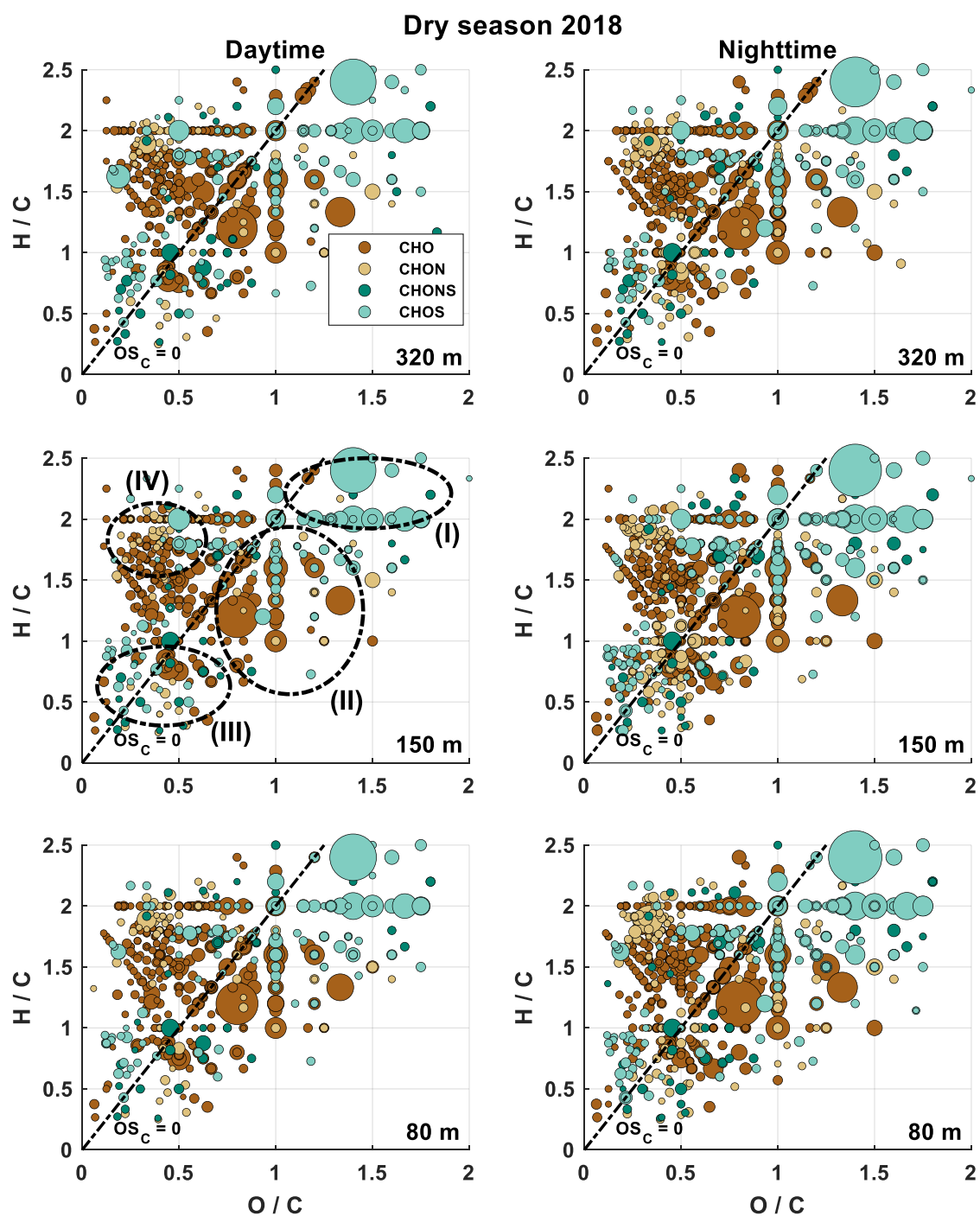


Figure 2.7: Van Krevelen plots from the dry season 2018 during daytime (left panel) and nighttime (right panel). Included are only molecular formulae that were present in more than one of the samples, respectively. The background signals are subtracted. The size of the data points represents the signal intensity of the corresponding peak. The four subgroups are distinguished with different colors. Compounds located on the black dashed line have an average carbon oxidation state of 0 ($OS_c = 0$). For the explanation of the ovals (I) – (IV) it is referred to the text.

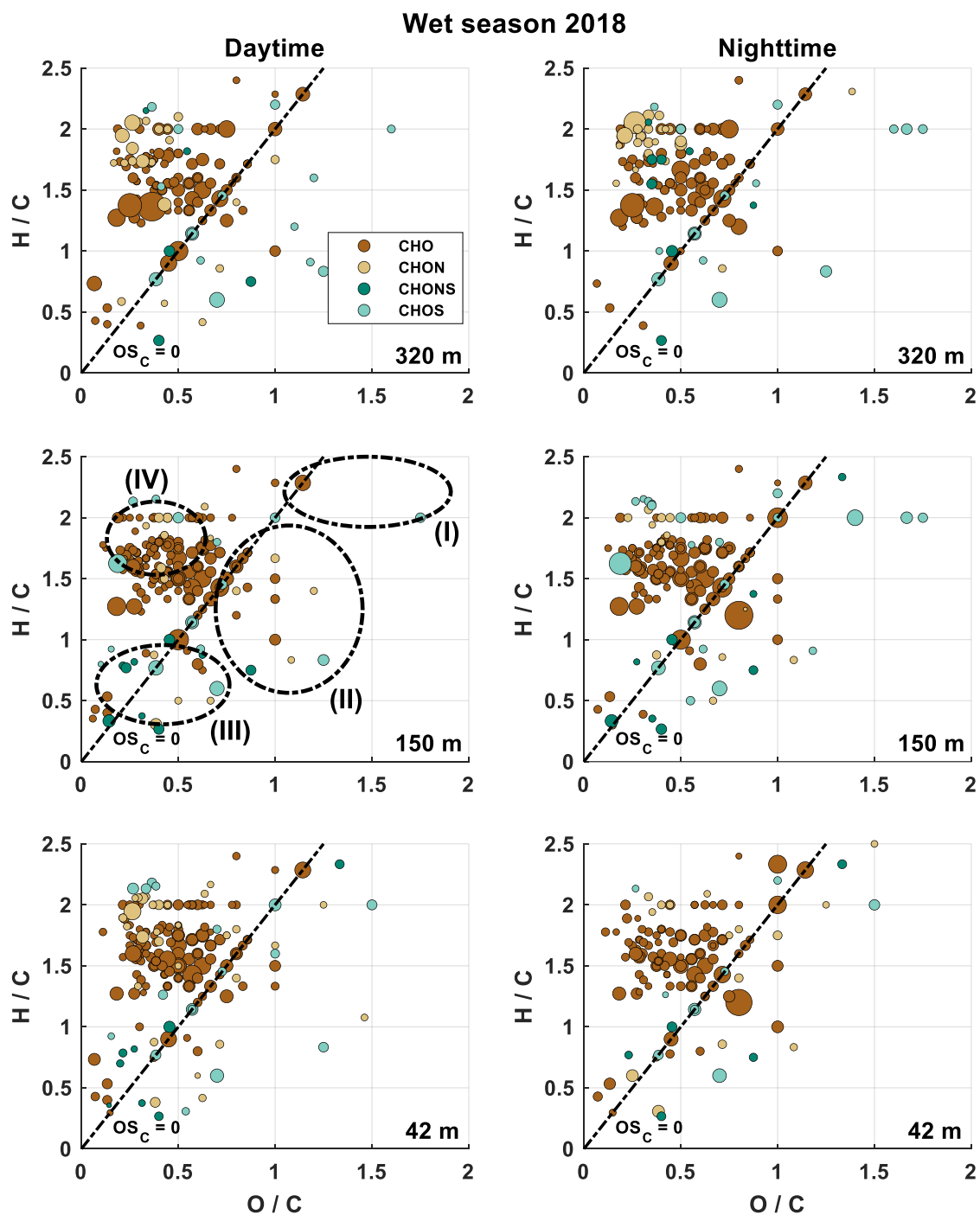


Figure 2.8: Van Krevelen plots from the wet season 2018 during daytime (left panel) and nighttime (right panel). Included are only molecular formulae that were present in more than one of the samples, respectively. The background signals are subtracted. The size of the data points represents the signal intensity of the corresponding peak. The four subgroups are distinguished with different colors. Compounds located on the black dashed line have an average carbon oxidation state of 0 ($OS_c = 0$). For the explanation of the ovals (I) – (IV) it is referred to the text.

Region (II) was dominated by m/z 129.0194 ($C_5H_6O_4$), which was earlier observed after the reaction of 3-methylfuran with NO_3 radicals to either produce an unsaturated dicarboxylic acid or a peroxy acid (Joo et al., 2019). Furans have been established as products of cellulose combustion (Mettler et al., 2012), and, consequently, are detected with higher signal intensities during the dry seasons. Additionally, the enhanced nitrate chemistry during the night led to diurnal variations with increased intensities in nighttime samples. However, $C_5H_6O_4$ was also observed in samples from the wet seasons with lower incidents of forest fires, suggesting an additional biogenic emission source. The C_5 backbone implies isoprene as a potential precursor, which formed $C_5H_6O_4$ after photooxidation experiments in chamber studies (Nguyen et al., 2011; Clark et al., 2013). Other intense ion signals correspond to m/z 161.0455 ($C_6H_{10}O_5$) and m/z 203.0562 ($C_8H_{12}O_6$). $C_6H_{10}O_5$ and $C_8H_{12}O_6$ were attributed to 1,6-anhydro- β -D-glucopyranose (levoglucosan) and 3-methyl-1,2,3-butanetricarboxylic acid (MBTCA) by authentic standard substances, respectively. Levoglucosan is a generally accepted product of cellulose pyrolysis used as a marker compound for biomass burning activities (Simoneit et al., 1999; Nolte et al., 2001). As expected, the signal intensities were significantly higher during the dry seasons with increased numbers of fires and anthropogenic emissions. In contrast, MBTCA is a well-established tracer compound for aged biogenic SOA formed by the photooxidation of α - and β -pinene (Szmigielski et al., 2007; Zhang et al., 2010), and was detected on nearly each filter sample with significant variations in the signal intensity. Similarly, two detected CHONS compounds at m/z 294.0654 ($C_{10}H_{17}O_7NS$) and m/z 296.0446 ($C_9H_{15}O_8NS$) have been related to aged SOA, which were already identified as oxidation products of α -pinene, β -pinene, and limonene (Surratt et al., 2008). The $O/(N+S)$ ratio ≥ 3.5 allows the presence of both $-OSO_3H$ and $-ONO_2$ functional groups and the assignment as nitrooxy-organosulfates (NOS). These compounds were observed on several filter samples during each campaign, indicating a substantial SOA contribution of biogenic monoterpenes. However, higher intensities of these CHONS species during the dry season suggest a strong correlation with increased NO_x and SO_2 levels, supporting the results by Kourtchev et al. (2016). The mentioned NOS species are highly oxygenated, resulting in low saturation vapor pressures C_0 . This thermodynamic parameter represents the gas-to-particle partitioning properties of organic molecules and allows their classification as VOC, intermediate-volatile organic compounds (IVOC), semi-volatile OC (SVOC), low-volatile OC (LVOC), and extremely low-volatile OC (ELVOC) (Pankow, 1994b; Odum et al., 1996; Murphy et al., 2014). The parameterization has already been applied for the characterization of organic aerosols (Shiraiwa et al., 2014; Li et al., 2016). Figure 2.9 compares the classification of organic species from the dry and wet season 2018 according to their saturation vapor pressure C_0 . It can be seen that the molecular distribution is clearly shifted towards species with lower volatilities for the dry season, indicating the more oxidized and aged character of SOA particles compared to the wet season. Increased levels of HNO_3 and SO_2 and

less removal by precipitation might favor the formation of OC with low volatilities. Besides highly oxygenated NOS several high molecular weight compounds with either C8 – C10 or C17 – C20 backbones were identified as LVOC/ELVOC, suggesting oligomeric structures based on isoprene and monoterpene precursors. These products are supposed to be low-volatile due to the incorporation of additional functional groups and the increase of the carbon number in the molecular structure (Kroll and Seinfeld, 2008; Daumit et al., 2013). Two prominent ion signals at m/z 333.0859 ($C_{10}H_{22}O_{10}S$) and m/z 357.1557 ($C_{17}H_{26}O_8$) have already been observed in chamber studies with isoprene and α -pinene (Surratt et al., 2008; Kristensen et al., 2013). The majority of the oligomers were detected on filter samples from dry season campaigns, implying a stronger contribution of oligomerization reaction to SOA during these periods.

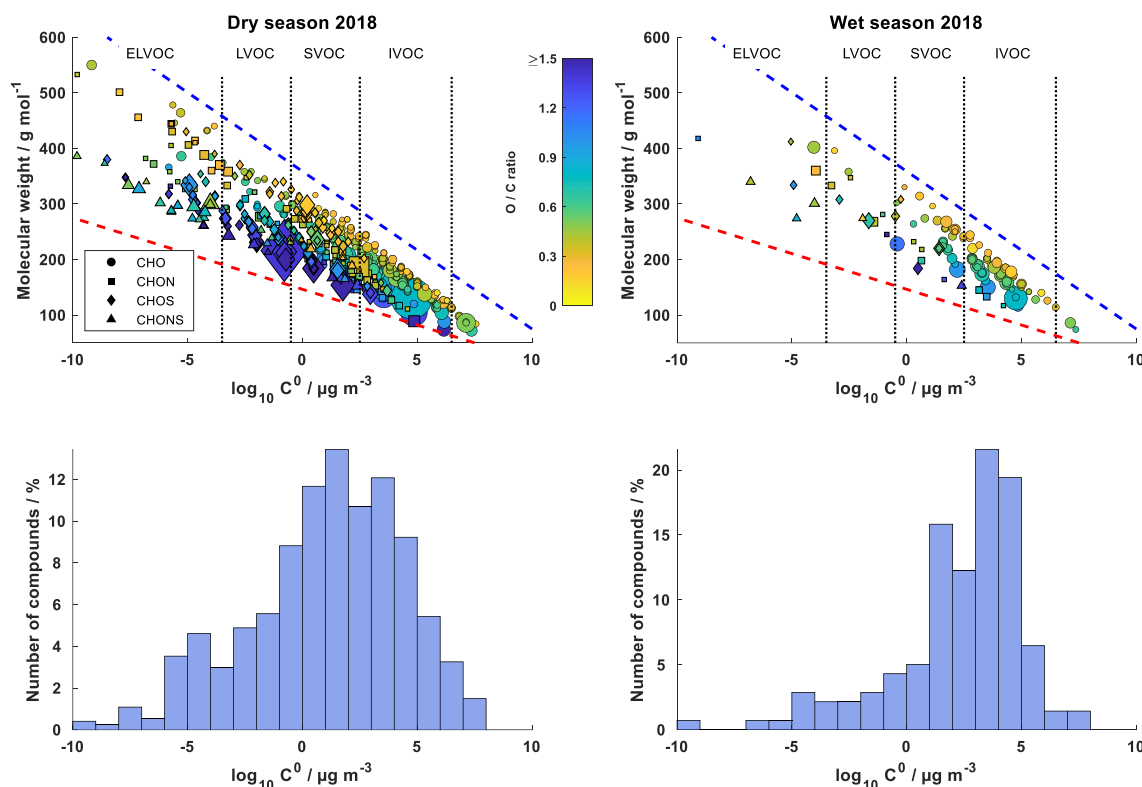


Figure 2.9: Molecular classification of organic species for the dry season 2018 (left) and the wet season 2018 (right) according to their saturation vapor pressure C_0 . The color code describes the degree of oxygenation. The blue dashed line indicates linear alkanes C_nH_{2n+2} , while the red dashed line represents sugar alcohols $C_nH_{2n+2}O_n$ according to Li et al. (2016). The lower panel shows the distribution of all detected compounds among the respective classes.

Region (III) in Figure 2.7 and Figure 2.8 is mainly characterized by unsaturated hydrocarbons with a low degree of oxygenation. Most of these compounds are classified as CHON, CHOS, and CHONS with X_c values ≥ 2.5 , indicating aromatic molecular structures. The most intense ion signals have been associated with m/z 154.0146 ($C_6H_5NO_4$, 4-nitrocatechol), m/z 168.0301 ($C_7H_7NO_4$, methyl-

nitrocatechols), and m/z 185.0457 ($C_8H_9NO_4$, dimethyl-nitrocatechols), which are generally related to biomass burning OA and anthropogenic emissions (Iinuma et al., 2010; Claeys et al., 2012; Kitanovski et al., 2012; Kahnt et al., 2013). In fact, Kourtchev et al. (2016) found increased levels of these compounds in the Amazon region during periods with high incidents of forest fires. Similar to this observation, intense ion signals of nitrocatechols have been detected in the present study during the dry seasons which were highly affected by combustion activities. In contrast, the SOA characterization for the wet season 2018 did not reveal any nitrocatechols, while moderate intensities of $C_6H_5NO_4$ and $C_7H_7NO_4$ were detected during the wet season 2019. This result coincides with a higher number of fires for the latter campaign, resulting in increased mass concentrations of black carbon (Figure S17). Accordingly, the OS_C analysis revealed a large number of compounds attributed to BBOA. However, $C_6H_5NO_4$ was the only compound identified as background species during the dry season 2018, suggesting lower SOA contributions by $C_7H_7NO_4$ and $C_8H_9NO_4$ at ATTO. While aromatic hydrocarbons in the region (III) are mainly attributed to anthropogenic emissions, the aliphatic species in the region (IV) of the VK diagrams can be attributed to mixed anthropogenic and biogenic sources (Henze et al., 2008; Kourtchev et al., 2013). A prominent ion was observed at m/z 185.0819 which was assigned to the molecular formula of $C_9H_{14}O_4$. This compound revealed several signals in the LC analysis according to multiple isomeric structures. One signal was identified by an authentic standard compound as pinic acid (PA). The additional signals are presumably related to oxidation products of other biogenic monoterpenes, such as β -pinene, limonene, and Δ^3 -carene (Jenkin, 2004; Chen and Griffin, 2005; Hammes et al., 2019). In contrast to MBTCA, pinic acid is an early-generation oxidation product of α -pinene and can therefore be used as a tracer for freshly formed SOA. The later-generation product MBTCA was more abundant during the dry seasons, indicating more processed SOA particles, while PA was predominant during the wet periods. Furthermore, MBTCA showed generally higher contributions at the top of ATTO compared to PA. This can be explained by the larger footprint area at 320 m allowing the collection of aged aerosol particles after long-range transportation. Simultaneously, PA rather represents local biogenic emissions resulting in increased concentrations at lower sampling heights.

In contrast to the dry seasons, the wet season 2018 was characterized by clean air conditions with clearly fewer different molecules detected. This result agrees with the lowest particle mass and number concentrations observed during this campaign. The low incidents of forest fires are associated with reduced NO_x and BCe (black carbon equivalents) concentrations. Consequently, the detected compounds were mostly attributed to biogenic sources with a low influence on anthropogenic emissions. The OS_C analysis showed that most signals were associated with SV-OOA, indicating mainly fresh formed PM. Further details can be found in the supporting information.

Kendrick mass (KM) analysis is a valuable visualization tool for complex organic mixtures and was introduced by Kendrick (1963) and Hughey et al. (2001). This technique has already been applied for the characterization of organic aerosol samples (Lin et al., 2012; Rincón et al., 2012; Kourtchev et al., 2013). It allows the assignment of all signals of a homologous series if the elemental composition of one compound has been identified (Nizkorodov et al., 2011). Figure 2.10 compares the KMD_{CH_2} diagrams for the dry and wet season 2018.

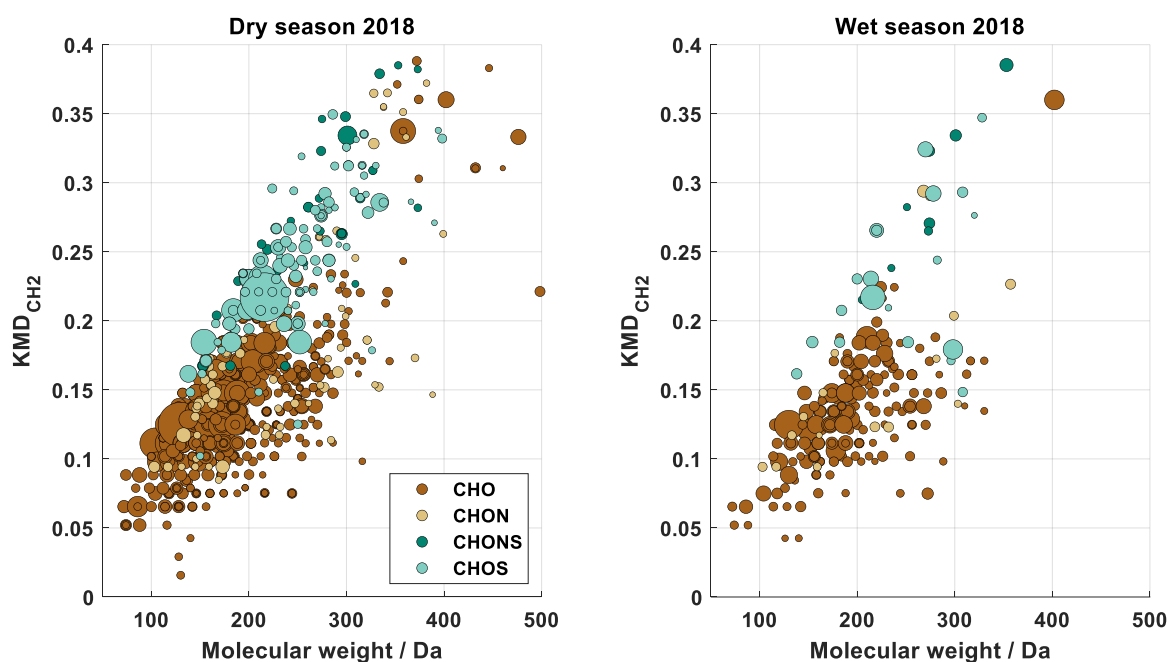


Figure 2.10: CH_2 -Kendrick diagrams for all signals detected at 150 m during the dry season 2018 (left) and the wet season 2018 (right), respectively. The size of the data points represents the signal intensity of the corresponding peak. The four subgroups are distinguished with different colors.

As discussed earlier, the dry season was characterized by biomass burning and aged OA, resulting in large-membered homologous series of CHO compounds with increased MW compared to the wet season. Compounds with $\text{KMD}_{\text{CH}_2} \leq 0.11$ appear to be unsaturated carboxylic acids with the general molecular formulae of $\text{C}_n\text{H}_{2n}\text{O}_2$, $\text{C}_n\text{H}_{2n}\text{O}_3$, $\text{C}_n\text{H}_{2n-2}\text{O}_2$, and $\text{C}_n\text{H}_{2n-2}\text{O}_4$. The elemental composition suggests fatty acids, which have been reported in SOA related studies as substantial compounds of marine and terrestrial vegetation (Stephanou and Stratigakis, 1993; Rincón et al., 2012; Kourtchev et al., 2014b). Thus, long-range transportation of marine aerosols or BBOA might explain the higher abundance of fatty acids during the dry season (Oros and Simoneit, 2001; Tervahattu et al., 2002). Additionally, a high number of CHOS compounds with $\text{KMD}_{\text{CH}_2} \geq 0.21$ were detected during the dry season exclusively. Similar results have been reported by Kourtchev et al. (2016), who found more homologous series of CHOS compounds in aerosol samples impacted by anthropogenic emissions.

These species are supposedly highly oxygenated organosulfates, presumably formed by heterogeneous reactions on acidic sulfate particles.

Another interesting ion was detected at m/z 186.1135 ($C_9H_{17}NO_3$) with high signal intensities mainly during the dry season 2018. This compound was already observed in biomass burning related chamber experiments and field measurements in the Amazon rainforest (Laskin et al., 2009; Kourtchev et al., 2016). Furthermore, Kendrick mass analysis revealed a homologous series of $C_9H_{17}NO_3$ with an altering number of CH_2 units in the present study, which is illustrated in the KMD plot in Figure 2.11. The general molecular formula can be described as $C_nH_{2n-1}NO_3$ with n ranging from 3 to up to 17 depending on the filter sample. Initially, the elemental composition suggested a nitrooxy ($-ONO_2$) functional group. However, MS^2 experiments (Figure S18) did not show the typical nitrate fragment. Instead, the observed fragments indicated the presence of a carbamate functional group ($R-NH-COOH$). Due to their zwitterionic structure, these species might be relevant for atmospheric condensed phase chemistry similar to amino acids (Mopper and Zika, 1987; Milne and Zika, 1993; McGregor and Anastasio, 2001; Barbaro et al., 2011). It should be emphasized that this result is tentative and needs further investigation.

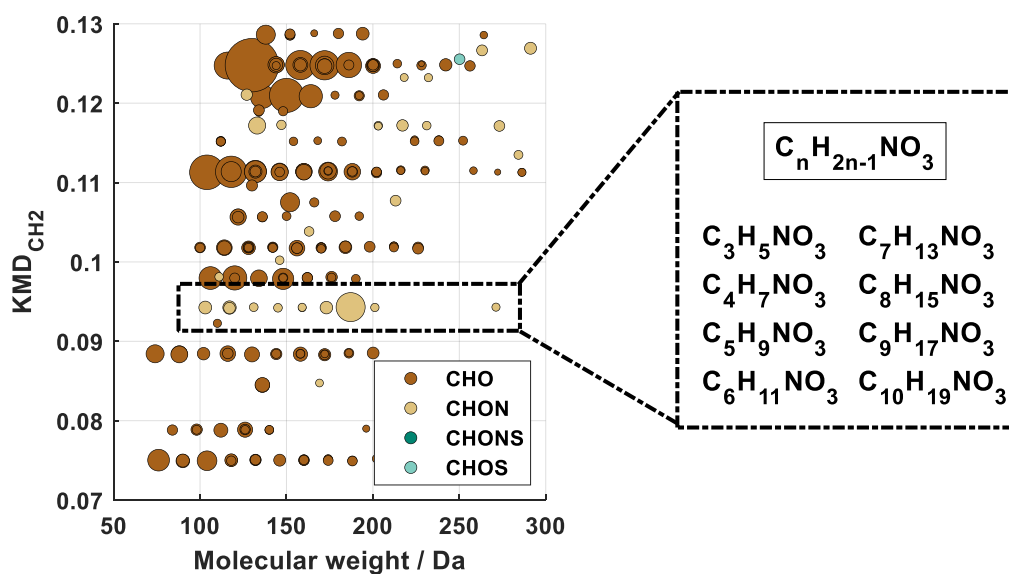


Figure 2.11: Kendrick mass defect diagram for the dry season 2018. The size of the data points represents the signal intensity of the corresponding peak. The four subgroups are distinguished with different colors. The dashed box highlights a homologous series of CHON compounds with a molecular formula of $C_nH_{2n-1}NO_3$ with $n = (3 - 17)$, potentially related to biomass burning emissions.

2.3.3 Targeted Analysis for Selected Marker Species

Non-targeted data evaluation is beneficial for complex organic mixtures of particulate matter on filter samples. It provides comprehensive information on their chemical composition, aging and transformation processes, and atmospheric and meteorological impacts. However, the accurate targeted analysis of selected organic species is still necessary to reliably identify emission sources and thus comprehend new particle formation. In this context, four individual components have been emphasized in this study, i.e., 2-methyltetrols, levoglucosan, MBTCA, and β -caryophyllinic acid ($C_{14}H_{22}O_4$, β -CA). These can act as markers for the specific sources of isoprene, biomass burning, monoterpenes, and sesquiterpenes to subsequently assess their contribution to the total OA (Simoneit et al., 1999; Jaoui et al., 2007; Claeys et al., 2010).

The four marker species were quantified on filter samples from the dry season 2018 and 2019 and the wet season 2019. The mean concentrations, as well as the minimum and maximum values, are summarized in Table 2.4. Note that the concentrations of 2-methyltetrols are the sum of 2-methylthreitol and 2-methylerythritol, which were quantified simultaneously. The time profiles for each measurement campaign are shown in the supporting information. The highest concentrations for all compounds were detected during the dry season 2018 coinciding with the highest levels of PM concentrations. As expected, levoglucosan exhibited high concentrations of $3.5 \mu\text{g m}^{-3}$ and $2.1 \mu\text{g m}^{-3}$ (mean values) for the dry seasons 2018 and 2019, respectively, which were impacted by high numbers of forest fires. Consequently, levoglucosan concentrations of up to $6.1 \mu\text{g m}^{-3}$ were observed. Similar levels were measured in Rondônia in the Amazon basin by Claeys et al. (2010) during the dry season in September 2002. The authors reported mean concentrations of $2.1 \mu\text{g m}^{-3}$ for levoglucosan, while significantly lower values of $0.06 \mu\text{g m}^{-3}$ were detected during the wet period in 2002. This result stays in contrast to the present study with levoglucosan concentrations of approximately one order of magnitude higher ($0.9 \mu\text{g m}^{-3}$), suggesting that ATTO was affected by deforestation fires not only during the dry seasons. The time profiles in the supporting information show clearly pronounced diel patterns with prevalent levoglucosan concentrations during the daytime for each campaign. These diel variations seemed reasonable because enhanced oxidative combustion activities were expected during the day. However, Claeys et al. (2010) observed the opposite trend and interpreted the higher nighttime levels of levoglucosan partly by fast atmospheric photooxidation during the day (Hoffmann et al., 2010; Hennigan et al., 2010). The inconsistency with the present study might imply that levoglucosan is affected not only by photochemical transformation and processing but also by meteorological parameters such as relative humidity and temperature. These conditions could control partitioning processes and the aqueous-phase chemistry of hydrophilic levoglucosan. Especially, the distance between the sampling location and the biomass burning source essentially determines the transportation

time and thus the photochemical depletion of levoglucosan. As indicated by de Gouw et al. (2003) acetonitrile could be used as an additional tracer species to avoid underestimations of biomass burning OA.

Table 2.4: Mean concentrations and ranges for 2-Methyltetrols, levoglucosan, MBTCA, and β -caryophyllinic acid on filter samples according to the sampling time and tower height. Note that the concentrations of levoglucosan are listed in $\mu\text{g m}^{-3}$ instead of ng m^{-3} .

	Height m	2-Methyltetrols Conc. / ng m^{-3}		Levoglucosan Conc. / $\mu\text{g m}^{-3}$		MBTCA Conc. / ng m^{-3}		β -CA Conc. / ng m^{-3}	
		Mean	Range	Mean	Range	Mean	Range	Mean	Range
DS18	80	94.3	51.1 – 142.2	3.5	1.5 – 6.1	9.3	4.8 – 13.1	2.2	1.4 – 3.5
	150	109.3	60.8 – 157.6	3.5	1.7 – 5.8	8.6	4.8 – 11.5	1.8	1.2 – 2.7
	320	103.6	55.5 – 156.1	3.5	1.6 – 5.4	7.8	4.5 – 10.6	1.3	0.6 – 1.8
WS19	80	23.5	0.4 – 79.3	0.9	<0.1 – 2.6	2.0	0.1 – 4.3	1.0	0.2 – 1.6
	150	21.5	2.0 – 46.8	0.8	<0.1 – 1.9	1.9	0.2 – 3.8	1.0	0.2 – 1.4
	320	30.4	4.1 – 56.9	1.0	<0.1 – 2.2	2.5	0.5 – 4.3	0.9	0.2 – 1.4
DS19	0	35.5	14.4 – 82.9	1.9	0.5 – 3.6	4.9	1.4 – 8.5	1.4	0.5 – 2.5
	80	78.5	31.5 – 194.6	2.6	0.8 – 5.4	5.7	1.6 – 8.0	1.7	0.8 – 2.7
	320	34.6	7.9 – 53.0	1.8	0.6 – 3.6	4.8	0.9 – 7.3	0.2	<0.1 – 0.3

The mean concentrations of MBTCA during the dry seasons were 8.6 ng m^{-3} and 5.1 ng m^{-3} , respectively. Lower levels of 2.1 ng m^{-3} were observed during the wet season 2019. This indicates the more relevant oxidative processing and aging at drier periods, which agrees with a previous study in the Amazon basin by Kourtchev et al. (2016). Additionally, effective removal by wet deposition might lead to decreased MBTCA levels. Significantly lower concentrations of $(0.03 - 0.25) \text{ ng m}^{-3}$ were detected in an urban environment (Kourtchev et al., 2014b), highlighting the important SOA contribution of monoterpenes at ATTO. The 2-methyltetrols behaved similarly to MBTCA with higher mean concentrations in the dry periods (102.4 ng m^{-3} and 50.0 ng m^{-3}), while they decreased to 25.1 ng m^{-3} during the wet season 2019. Again, wet deposition may result in the removal of the 2-methyltetrols during rainy periods. Moreover, their formation is facilitated by aerosol acidity as stated in the literature (Edney et al., 2005; Kourtchev et al., 2005; Surratt et al., 2007a). Consequently, higher SO_2 concentrations during the dry period might lead to enhanced production of 2-methyltetrols, supporting the results obtained by Claeys et al. (2010). In contrast, β -CA revealed no significant seasonal variations with mean concentrations ranging from 1.0 ng m^{-3} to 1.8 ng m^{-3} , indicating a less relevant SOA contribution of sesquiterpenes compared to monoterpenes at ATTO. It should be noted that further investigations with additional sesquiterpene tracers are needed to assess their SOA contribution in more detail.

Figure 2.12 illustrates the vertical concentration profiles of the 2-methyltetrols, MBTCA, β -CA, and levoglucosan at ATTO. The dry season vertical profiles for 2-methyltetrols, MBTCA, and β -CA exhibit a steep pattern with decreasing concentrations from lower sampling heights to the top of the tower.

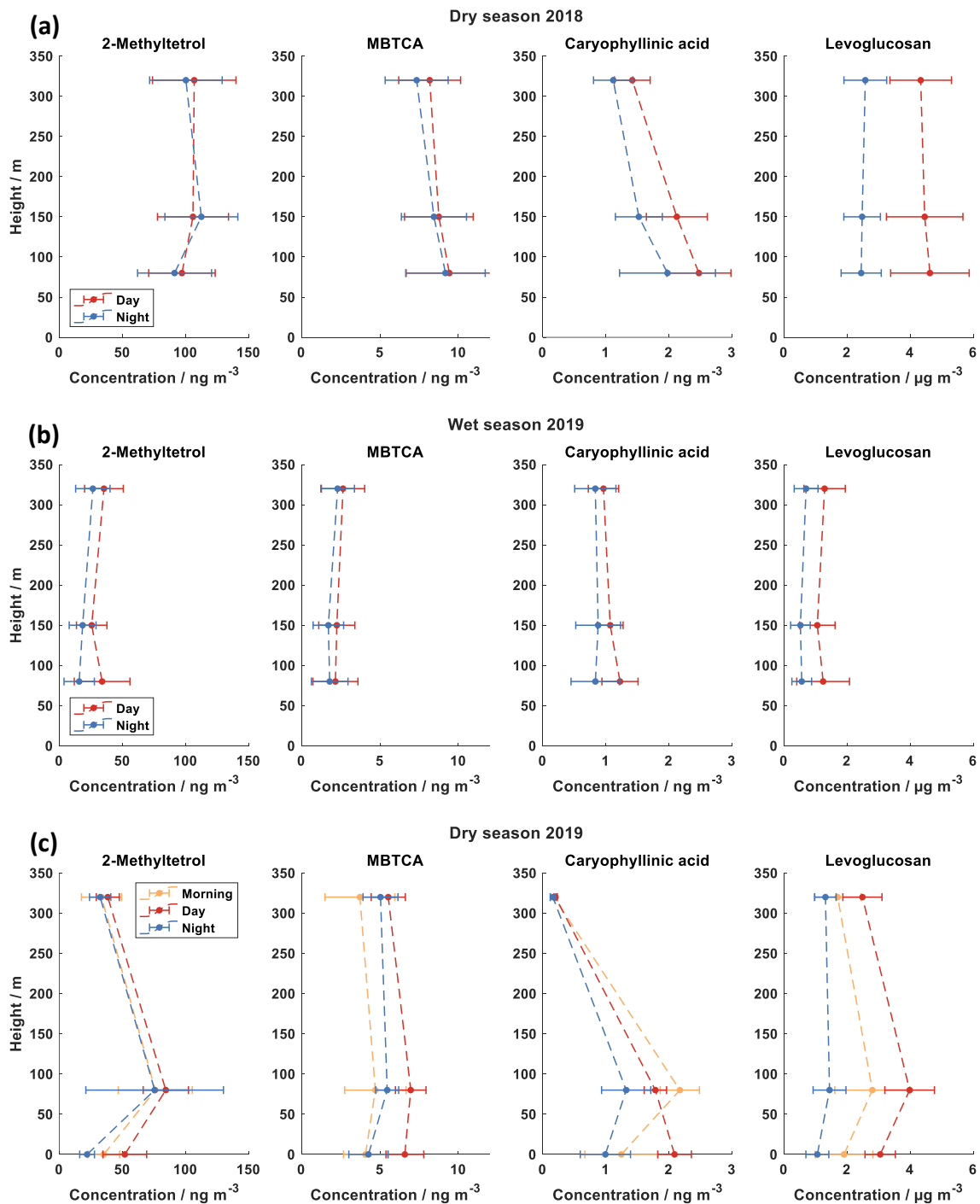


Figure 2.12: Vertical concentration profiles of 2-methyltetrol, MBTCA, β -CA, and levoglucosan during the (a) dry season 2018, (b) wet season 2019, and (c) dry season 2019. Different sampling periods are indicated by different colors. Note that the concentrations of levoglucosan are presented in $\mu\text{g m}^{-3}$.

This behavior might be explained by the strong contribution of local biogenic sources to the VOC emissions, suggesting the forest canopy as the major origin for isoprene and terpenes. This result is supported by a detailed study on isoprene and monoterpene emissions at ATTO (Yáñez-Serrano et al., 2015). At top of ATTO oxidative processing and upwards air mixing are resulting in decreased concentrations. Generally, higher concentrations were expected for the dry seasons since increased ambient temperatures and photosynthetic active radiation (PAR) facilitate the emission rates of isoprene and monoterpenes (Guenther et al., 1991; Kesselmeier and Staudt, 1999). This also affects the diel variation with prevalent concentrations during the day. The wet season vertical profiles revealed a different concentration pattern. It seems that less photochemistry due to cloud cover, enhanced wet deposition, and turbulent mixing adjusting the concentrations above the canopy (Yáñez-Serrano et al., 2015). Interestingly, the sub-canopy region appears to be decoupled from the atmosphere above indicated by the ground-level samples during the dry season 2019. The vegetation beneath the canopy is less affected by fluctuating temperatures and incoming radiation leading to slower OH radical-initiated oxidation of isoprene and terpenes. In contrast, the vertical profiles of levoglucosan exhibit almost balanced concentrations at each sampling height above the canopy. This indicates different sources for levoglucosan, presumably long-range transportation from deforestation fires and subsequent air mixing.

Besides PM_{2.5} measurements, particle size resolved MOUDI sampling was performed at the nearby 80 m triangular mast. It should be noted that a 60 m stainless steel aerosol inlet was connected to the filter. Thus, the calculated concentrations might be slightly underestimated. Additionally, the triangular mast is completely embedded in the forest structure, which could result in different emission rates than those at ATTO. Figure 2.13 shows the particle size distributions for the dry season 2018 and the wet season 2019. For both periods levoglucosan is mainly attributed to the coarse mode with significantly higher concentrations during the dry season. This might be related to primary combustion emissions. Claeys et al. (2010) also explained this behavior by a preferred condensation of levoglucosan on coarse primary PM during wet periods due to its hydrophilic character. However, levoglucosan revealed a similar particle size distribution in the dry season, suggesting this mechanism to be dominant even during drier periods at ATTO. In contrast, the distribution patterns of MBTCA and β -CA were peaking in the accumulation mode, indicating oxidative heterogeneous chemistry as the prominent source (Claeys et al., 2010). This also highlights their contribution to particle growth (Kourtchev et al., 2005). Interestingly, the 2-methyltetrols showed a distinct bimodal distribution pattern during the dry season 2018. Similar to MBTCA and β -CA high concentrations were detected in the accumulation mode, while an additional peak was observed in the coarse mode. It has been reported in the literature that 2-methyltetrols are also directly produced by vegetation (Ahmed et al., 1996; Enomoto et al., 2004;

Nozière et al., 2011). This might explain their contribution to the coarse mode, which agrees with an additional primary source of 2-methyltetrols.

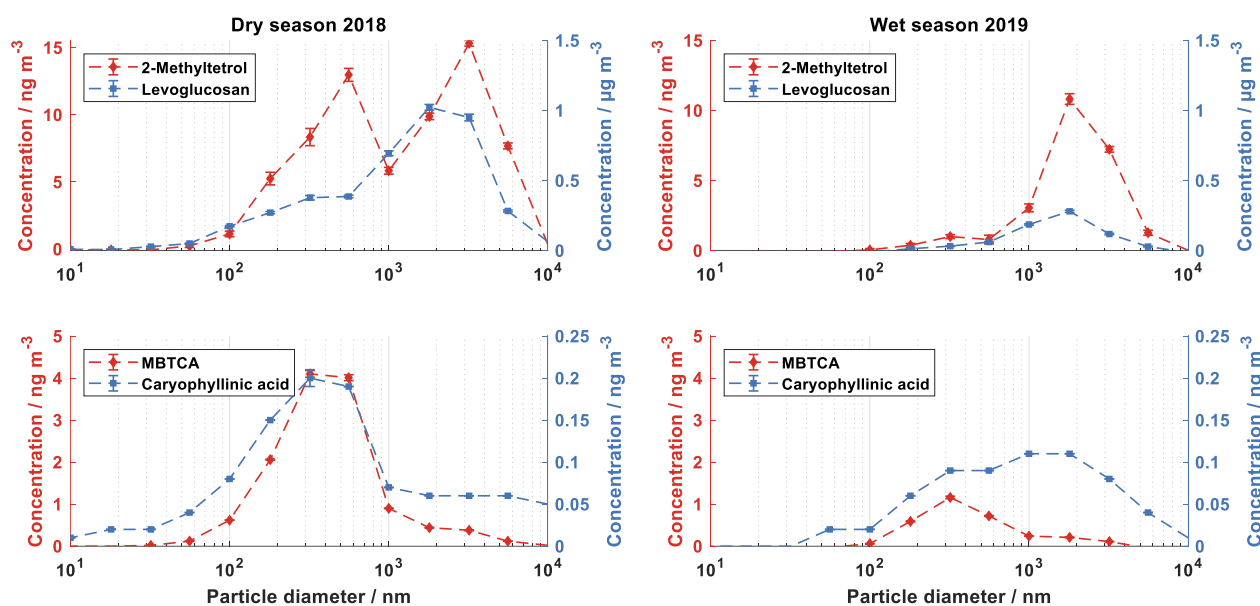


Figure 2.13: Concentration profiles of 2-methyltetrol, MBTCA, β -CA, and levoglucosan according to the particle size. The quantification of MOUDI samples was performed for the dry season 2018 and the wet season 2019. Note that the concentrations of levoglucosan are presented in $\mu\text{g m}^{-3}$.

2.4 Conclusion

The organic chemical composition of atmospheric SOA particles from the Amazon rainforest has been investigated by high-resolution MS coupled to a UHPLC system. In total, four different seasons from 2018 and 2019 have been covered, including “cleaner”, wet periods and “polluted”, dry periods. Additionally, the ATTO site allowed filter sampling throughout the boundary layer. This enabled the intercomparison of several seasons from a unique ecosystem characterized by the complex interaction of innumerable emission sources.

A large fraction of isomeric structures in each data set highlighted the requirement of the LC pre-separation technique. Furthermore, it enabled the reliable identification and semi-quantification of thousands of different molecular formulae by diminishing ion suppression. A total of 875 – 1555 formulae have been identified during the wet seasons, while the dry season filters exhibited a higher chemical complexity with 1050 – 1940 different molecular formulae. Most of the compounds have been assigned to CHO, although CHOS molecules represented a substantial fraction of the OA during each campaign. The aerosol particles were mainly consisting of compounds with $\text{MW} < 250$, while oligomeric species became more relevant at drier periods. Evaluating the complex MS data by

sophisticated techniques, such as VK diagrams, Kendrick mass defect, OS_C diagrams, etc., revealed pronounced differences between the respective seasons. Especially during the dry seasons, a significant number of HOMs with low volatilities were detected, underlining the relevance of oxidative processing and transformation compared to the wet seasons. Less removal by wet deposition might promote long-range transportation and the formation of low-volatile species. Simultaneously, a large fraction of BBOA contributed to the total SOA as indicated by high X_c values. In consequence, unsaturated and aromatic compounds such as nitrocatechols and nitrophenols were mainly attributed to deforestation fires primarily taking place in the dry periods. Interestingly, the chemical composition of SOA particles from the wet season 2019 revealed a similar SOA chemical composition compared to the dry seasons, which implies that combustion emissions in rainy periods are more relevant than expected. Fossil fuel burning in Europe or Africa could be responsible for that via long-range transportation over the Atlantic (Andreae et al., 2015). However, these results are presumably associated with individual occurring events, which are complicated to identify due to rather long sampling durations (~10 h – 14 h). This highlights the importance to determine the background chemical composition that is mostly characterized by local emission sources as well as prevalent meteorological conditions and air mass origins. The background analysis clearly showed that the SOA particles were dominated by aliphatic species with O/C ratios below 0.8, suggesting biogenic origins. Only filters from the dry season 2018 revealed an increased influence of biomass burning activities coinciding with increased particle number and NO_x concentrations.

IEPOX-OS and 2-methyltetrols have been observed on almost every filter sample with the highest signal intensities. This emphasizes the large contribution of isoprene oxidation products to the SOA loading at ATTO. It appeared that increased SO_2 and NO_x concentrations during the dry periods resulted in higher signal intensities, which is consistent with previous studies in the Amazon basin (Claeys et al., 2010; Kourtchev et al., 2016). Similarly, pinic acid and MBTCA have been observed with high signal intensities, supporting monoterpenes as relevant SOA precursors. However, the ratio of both compounds showed a distinct seasonal behavior with increased levels of MBTCA during the dry seasons indicating more processed OA, while pinic acid was prevalent on filter samples from wet seasons. In contrast, oxidation products from sesquiterpenes seemed to be less relevant for the SOA chemical composition at ATTO. Although levoglucosan has been detected in high concentrations, its fast photochemical degradation might lead to underestimations of BBOA (Hoffmann et al., 2010; Hennigan et al., 2010). Therefore, upcoming investigations will consider additional biomass burning tracer. The applied LC-MS analysis provides reliable semiquantitative results, however, a more comprehensive targeted quantification is necessary to further assess the isoprene and terpenes SOA contribution.

Additionally, the sampling duration will be reduced in the future to also capture individual plume events to reliably link varying meteorological conditions to certain chemical species. Unfortunately, this study could not reveal significant height-dependent SOA characteristics. Further sampling heights as well as statistical data evaluation techniques (e.g., hierarchical clustering) might help to determine the impact of convective mixing, local BVOC emissions, and long-range transportations.

Author contributions

Denis Leppla conducted the aerosol sampling, the sample preparation, and the measurements. Denis Leppla analyzed the data and wrote the manuscript. Nora Zannoni helped to collect the aerosol samples. Leslie Kremper, Maria Praß, Bruna Hollanda, Jonathan Williams, Florian Ditas, Christopher Pöhlker, and Stefan Wolff provided the SMPS and trace gas data. The meteorological data was provided by Marta Sá. Thorsten Hoffmann supervised the study. All authors contributed in the scientific exchange and read and revised the manuscript.

Acknowledgments

For the operation of the ATTO site, we acknowledge the support by the German Federal Ministry of Education and Research (BMBF Contract 01LK1602D) and the Brazilian Ministério da Ciência, Tecnologia e Inovação (MCTI/FINEP) as well as the Amazon State University (UEA), FAPEAM, LBA/INPA, and SDS/CEUC/RDS-Uatumã. We also acknowledge the support of the Max Planck Society and the Instituto Nacional de Pesquisas da Amazonia (INPA).

2.5 Additional Information

The following information is not part of the original manuscript. However, this section provides additional details concerning the applied LC-MS method as well as data processing.

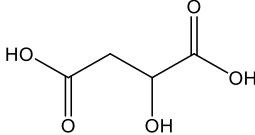
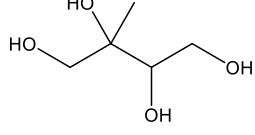
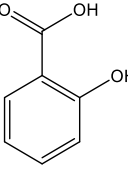
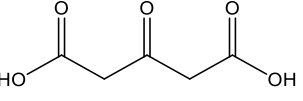
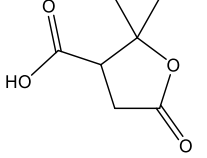
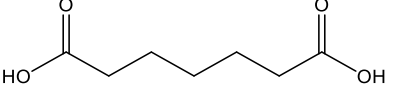
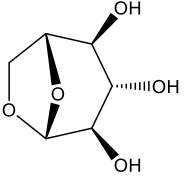
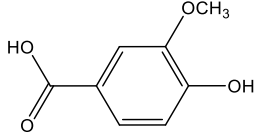
2.5.1 Method Evaluation

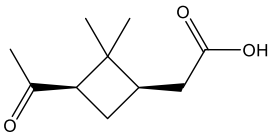
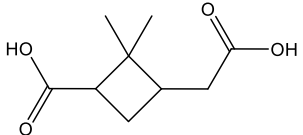
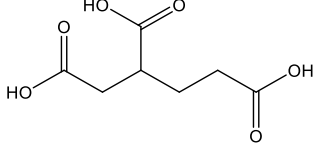
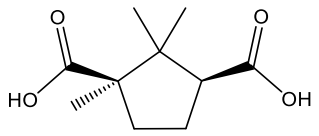
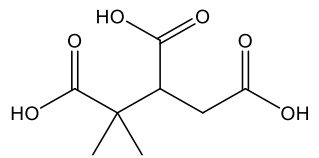
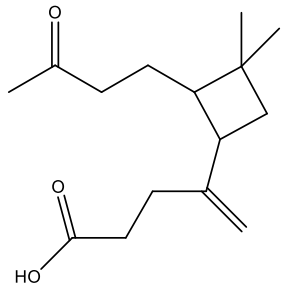
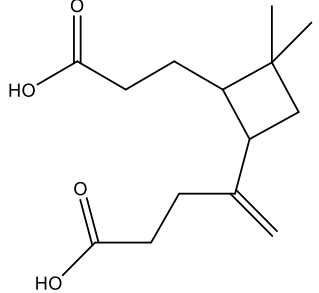
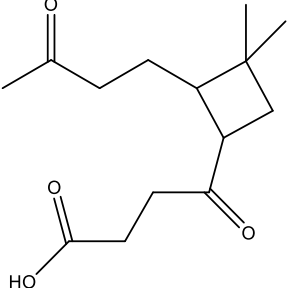
This section covers important aspects of the LC method development. This study focused on a single and sophisticated approach for the trace analysis of specific marker species on aerosol filter samples. Characteristic marker species can be used to identify emission sources for biogenic SOA or biomass burning events (Robinson et al., 2006a, 2006b). However, marker compounds must fulfill certain criteria, such as chemical stability against atmospheric oxidation and low volatility. These properties provide increased molecular lifetimes so that the marker species can also be detected after long-range transportation. For instance, levoglucosan (1,6-anhydro- β -D-glucopyranose) has been established as marker species for biomass burning activities. It is emitted into the atmosphere by the combustion of cellulose-containing wood (Simoneit et al., 1999). Biogenic SOA markers include oxidation products of isoprene, monoterpenes, and sesquiterpenes. Appropriate tracers for isoprene-derived SOA are 2-methyltetrols (Claeys et al., 2004a; Claeys et al., 2004b; Kourtchev et al., 2005). However, these compounds are highly polar due to the four hydroxyl groups, which complicates the analysis by RP-HPLC. The most important marker compound for aged biogenic SOA from monoterpenes is 3-methyl-1,2,3-butanetricarboxylic acid (MBTCA) formed by OH radical-initiated oxidation of α - and β -pinene (Szmigielski et al., 2007; Müller et al., 2012). Earlier-generation oxidation products, such as pinonic acid and pinic acid, can then be used to distinguish between freshly formed and processed SOA. Additionally, sesquiterpene oxidation products, such as β -caryophyllinic acid and β -nocaryophyllonic acid, are suitable marker species because of their low volatility (van Eijck et al., 2013).

The marker species used in this study for method development are listed in Table 2.5. Salicylic acid (99%), 3-oxoglutaric acid (96%), terebic acid (98%), pimelic acid (96%), levoglucosan (99%), *cis*-pinonic acid (98%), methyltricarballic acid ($\geq 88\%$), and camphoric acid (99%) were purchased from Sigma-Aldrich (Steinheim, Germany). D-malic acid ($\geq 99.5\%$) was obtained from Merck (Darmstadt, Germany). Vanillic acid was purchased from Alfa Aesar (Heysham, UK). Pinic acid was synthesized according to Moglioni et al. (2000). MBTCA was synthesized following the study by Dette et al. (2014). The sesquiterpene oxidation products β -caryophyllonic acid, β -caryophyllinic acid, and β -nocaryophyllonic acid were synthesized by van Eijck et al. (2013). Calibration solutions were prepared

in a mixture of water and acetonitrile (9:1) (Fisher Scientific, Optima™ grade) with concentrations ranging from 0.5 ng mL⁻¹ to 800 ng mL⁻¹. Blank solutions were prepared in the same manner.

Table 2.5: Analytes used for method development. Also listed are the molecular formulae, m/z ratios, structures, and the calculated quantification limits (LOD).

Analyte	Molecular formula	m/z [M-H] ⁻	Structure	LOD ¹ / ng mL ⁻¹
D-malic acid	C ₄ H ₆ O ₅	133.0142		9.98
2-methyltetrols	C ₅ H ₁₂ O ₄	135.0663		5.74
salicylic acid	C ₇ H ₆ O ₃	137.0244		2.11
3-oxoglutaric acid	C ₅ H ₆ O ₅	145.0142		2.71
terebic acid	C ₇ H ₁₀ O ₄	157.0506		3.09
pimelic acid	C ₇ H ₁₂ O ₄	159.0663		4.52
levoglucosan	C ₆ H ₁₀ O ₅	161.0455		29.68
vanillic acid	C ₈ H ₈ O ₄	167.0349		12.66

<i>cis</i> -pinonic acid	C ₁₀ H ₁₆ O ₃	183.1027		2.38
pinic acid	C ₉ H ₁₄ O ₄	185.0819		1.74
methyltricarballic acid	C ₇ H ₁₀ O ₆	189.0405		2.17
camphoric acid	C ₁₀ H ₁₆ O ₄	199.0976		3.32
MBTCA	C ₈ H ₁₂ O ₆	203.0561		3.25
β -caryophyllonic acid	C ₁₅ H ₂₄ O ₃	251.1653		7.87
β -caryophyllinic acid	C ₁₄ H ₂₂ O ₄	253.1445		2.67
β -nocaryophyllonic acid	C ₁₄ H ₂₂ O ₄	253.1445		3.06

¹ Instrumental detection limits calculated according to DIN 32645.

Each measurement was calibrated externally by six- to eight-point linear regression, which provided calibration functions for all analytes. The unknown concentrations of the filter samples were quantified after the determination of the signal areas and background subtraction. The limits of detection (LOD) were calculated according to DIN 32645.

Furthermore, the filter extraction method described in Section 2.2.2 was evaluated to assess the extraction efficiency. Therefore, blank filters were spiked with 50 ng mL^{-1} and 500 ng mL^{-1} of α -pinene oxidation products, i.e., pinic acid and MBTCA, respectively. The experiments were performed in triplicates. The calibration functions are illustrated in Figure 2.14. Based on the linear regression, extraction efficiencies of $(93.6 \pm 3.9)\%$ and $(92.5 \pm 5.5)\%$ were calculated for pinic acid and MBTCA, respectively. Thus, a quantitative extraction of SOA constituents from filter samples was assumed for all measurements.

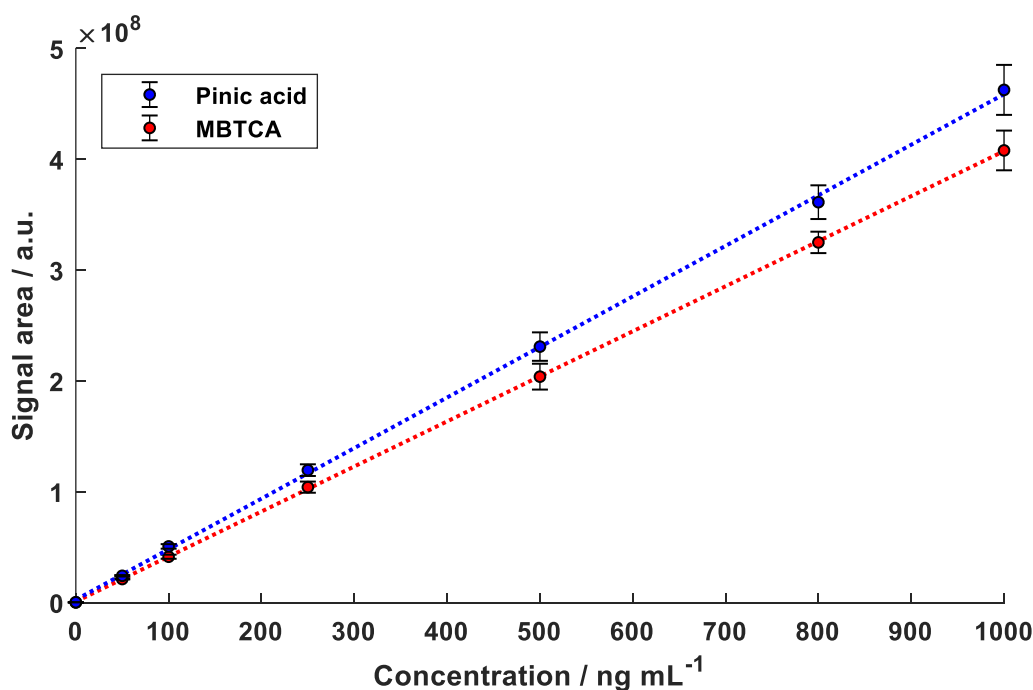


Figure 2.14: External calibration functions of pinic acid (blue) and MBTCA (red) used for the validation of filter extraction efficiencies.

2.5.2 Data Processing by MZmine 2.30

A non-targeted approach was developed and applied to the high-resolution mass spectra obtained from the analysis of each filter sample. Therefore, MZmine2.30 was used for data processing including toolboxes for peak detection, filtering for shoulder peaks and duplicates, chromatogram builder,

deconvolution and smoothing, alignment, adduct and complex search, and formula prediction (Pluskal et al., 2010; Wang et al., 2017). The following optimized parameterization was used in this study:

1. For each scan, only masses with signal intensities above 5000 were included for further processing. Signal intensities below 5000 were treated as noise and consequently not considered. Afterward, a shoulder peak filtering was applied with a mass resolution of 140 000 at m/z 200.
2. Chromatograms were built for each mass by using the ADAP Chromatogram Builder Module (Myers et al., 2017). The minimum intensity required to start a new chromatogram was set to 15 000 with a mass tolerance of 2 ppm.
3. The chromatograms were smoothed (filter width of 5) and deconvoluted by the ADAP Wavelet algorithm (Myers et al., 2017) (S/N threshold of 9; coefficient/area threshold of 110; peak duration of 0.03 – 1.00; retention time wavelet range of 0.01 – 0.17).
4. Isotopic peaks were removed (mass tolerance of 2 ppm; 0.1 min retention time tolerance; maximum charge of 1).
5. Adducts were removed (retention time tolerance of 0.1 min; mass tolerance of 2 ppm; maximum relative peak height of 50%; mass difference: m/z 41.0266 $[M-H+ACN]^-$, m/z 46.0055 $[M-H+CH_2O_2]^-$, m/z 67.9874 $[M-H+CH_2ONa]^-$). Ion complexes were also removed with the parameters mentioned above.
6. Peaks detected in different samples were aligned, based on the mass and retention time tolerances (mass tolerance of 2 ppm; weight for m/z of 5; retention time tolerance of 0.1 min; weight for retention time of 4). A minimum score of 85% for isotope patterns was required.
7. The formula prediction was based on $[M-H]^-$ ions with a mass tolerance of 2 ppm. Tentative molecular formulae with an elemental composition of CHONS were determined according to the following constraints: $C_{2-40}H_{2-100}O_{0-40}N_{0-4}S_{0-2}$; $0.1 \leq H/C \leq 6$; $N/C \leq 4$; $O/C \leq 3$; $S/C \leq 3$; multiple-element counts according to Kind and Fiehn (2007); double bond equivalents (DBE) integer and between 0 – 30. Finally, all peaks were filtered for isotope pattern with a mass tolerance of 5 ppm. Therefore, the software was used in a batch mode with decreasing minimum scores for the isotope pattern match starting at 99% to 85%.
8. Peak duplicates were removed (mass tolerance of 2 ppm; retention time tolerance of 0.1 min)

The resulting peak lists contained m/z ratios, molecular formulae, retention times, and signal areas of each detected organic species. The mass spectra of blank samples were processed accordingly. All

peak lists were further computed by Matlab R2017b (The MathWorks Inc., Natick, USA). Background subtraction was performed to only retain signals with sample-to-blank ratios ≥ 3 . Afterward, further elemental constraints were applied (H/C ratio of 0.3 – 3; N/C ratios of 0 – 0.5; S/C ratios of 0 – 0.2) to remove molecular formulae unlikely to be observed in nature (Wozniak et al., 2008; Fuller et al., 2012; Wang et al., 2017).

2.5.3 Hierarchical Cluster Analysis

The increasing applications of high-resolution mass spectrometry for the chemical investigation of organic aerosols in the past decade highlight the potential of this analytical technique. In combination with soft ionization methods and complementary measurements, HRMS has developed into a powerful tool for the analysis of highly complex environmental aerosol samples. The unambiguous identification of OA constituents requires high mass resolving power and mass accuracy to also resolve isobaric signals. Nizkorodov et al. (2011) emphasized the benefits of HRMS as can be seen in Figure 2.15. However, consistently improving mass resolving powers are leading to ever-increasing amounts of complex MS data. Especially, field campaigns with a large number of environmental OA samples can result in time-consuming data processing. Therefore, software-based procedures and statistical tools are needed for a detailed evaluation and interpretation of HRMS data.

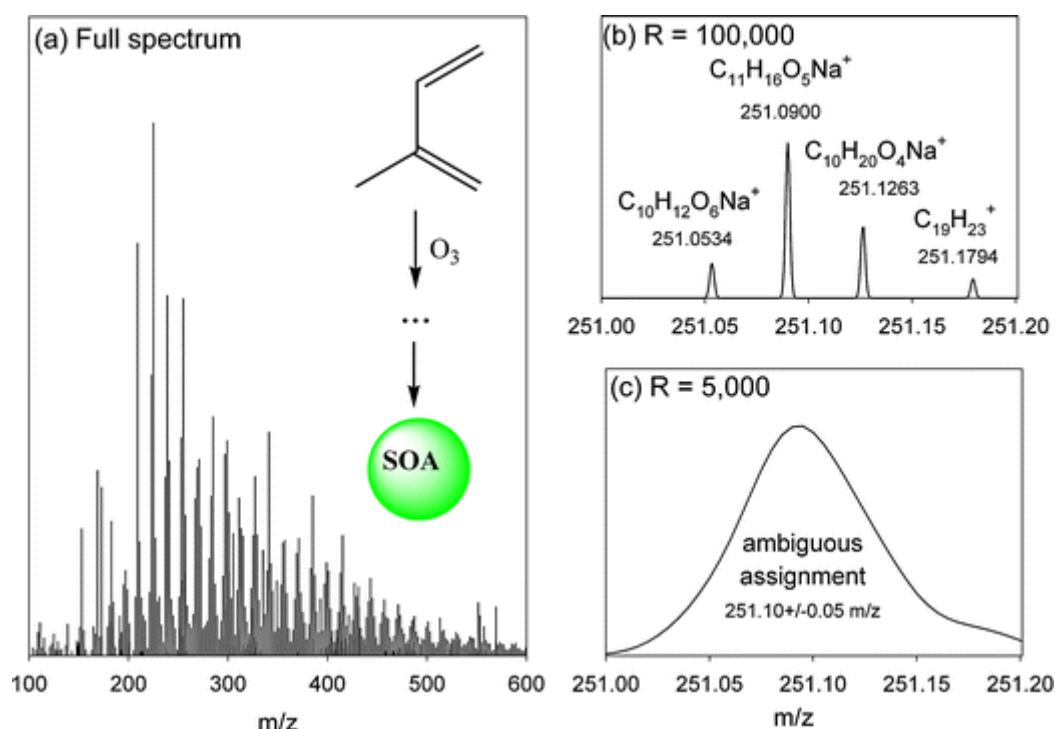


Figure 2.15: Mass spectrum of SOA particles generated by ozonolysis oxidation of isoprene in the positive mode. It also illustrates the difference of signals at m/z 251 with resolving powers of 5000 and 100 000.

Hierarchical cluster analysis (HCA) has proven to be a promising technique to process HRMS data of aerosol particles (Robinson et al., 2013; Kourtchev et al., 2014a; Crawford et al., 2014). HCA is a multivariate statistical tool, which can be used to interpret complex analytical data based on a large number of samples (Treiger et al., 1995; Bondarenko et al., 1996). Briefly, the clustering algorithm computes the distance or similarity between all objects m in a dataset leading to a matrix with $m \cdot (m - 1)/2$ pairs. Subsequently, the two most similar objects, i.e., the closest, are merged into a binary cluster. The newly generated clusters and the remaining objects in the matrix are processed again until all objects are linked in a single multi-membered hierarchical cluster or dendrogram.

HCA can be used to identify correlations between a large number of aerosol samples. Furthermore, the integration of environmental samples together with samples from smog chamber experiments in the HCA allows for source attribution. Thus, a preliminary approach for hierarchical cluster analysis of SOA filter samples was developed in this study using Matlab. In a first step, the HRMS data was organized in a matrix M_{xy} with x samples and y different detected organic compounds represented by the signal areas, respectively. Afterward, the data was normalized by z -score standardization to compensate for varying signal ranges using Equation (2.7) (Bondarenko et al., 1996; Robinson et al., 2013):

$$z = \frac{y - \mu}{\sigma} \quad (2.7)$$

where y is the signal area of a given compound, μ the mean value, and σ the standard deviation. The resulting normalized data has a mean of 0 and a standard deviation of 1. The subsequent similarity of objects was defined as the Euclidean distance, while Ward's linkage was used for the clustering (Bondarenko et al., 1996).

As a proof-of-principle, the developed HCA method was applied to selected SOA samples from field measurements and smog chamber experiments. Therefore, aerosol particles were generated by ozone-initiated oxidation of α -pinene in a 100 L chamber. Detailed experimental conditions can be found in Section 3.2.2. The HRMS data provides a unique molecular fingerprint of the oxidation products. With this approach, the origin of organic compounds on environmental samples can be determined and the contribution of certain BVOCs to the total SOA mass can be assessed. The tentative results are illustrated in Figure 2.16. Twelve samples for the dry season 2018 (X, Y, Z-samples, 10/22/2018 – 10/23/2018) and the wet season 2019 (M, N, O-Samples, 03/05/2019 – 03/06/2019) were included in the HCA, respectively. The samples were collected during daytime (D) and nighttime (N) at 80 m (X, M), 150 m (Y, N), and 320 m (Z, O). Additionally, the HCA contained one filter sample from a chamber experiment (O_3/α -pinene). Each horizontal line represents an individual detected organic

compound (1577 in total), while the presence/absence in the samples is indicated by the color scheme (z-score). Red colors simply imply high signal areas and blue colors imply low signal areas. The preliminary results highlight the potential of HCA for non-targeted approaches as differences in the molecular composition of aerosol samples can easily be visualized.

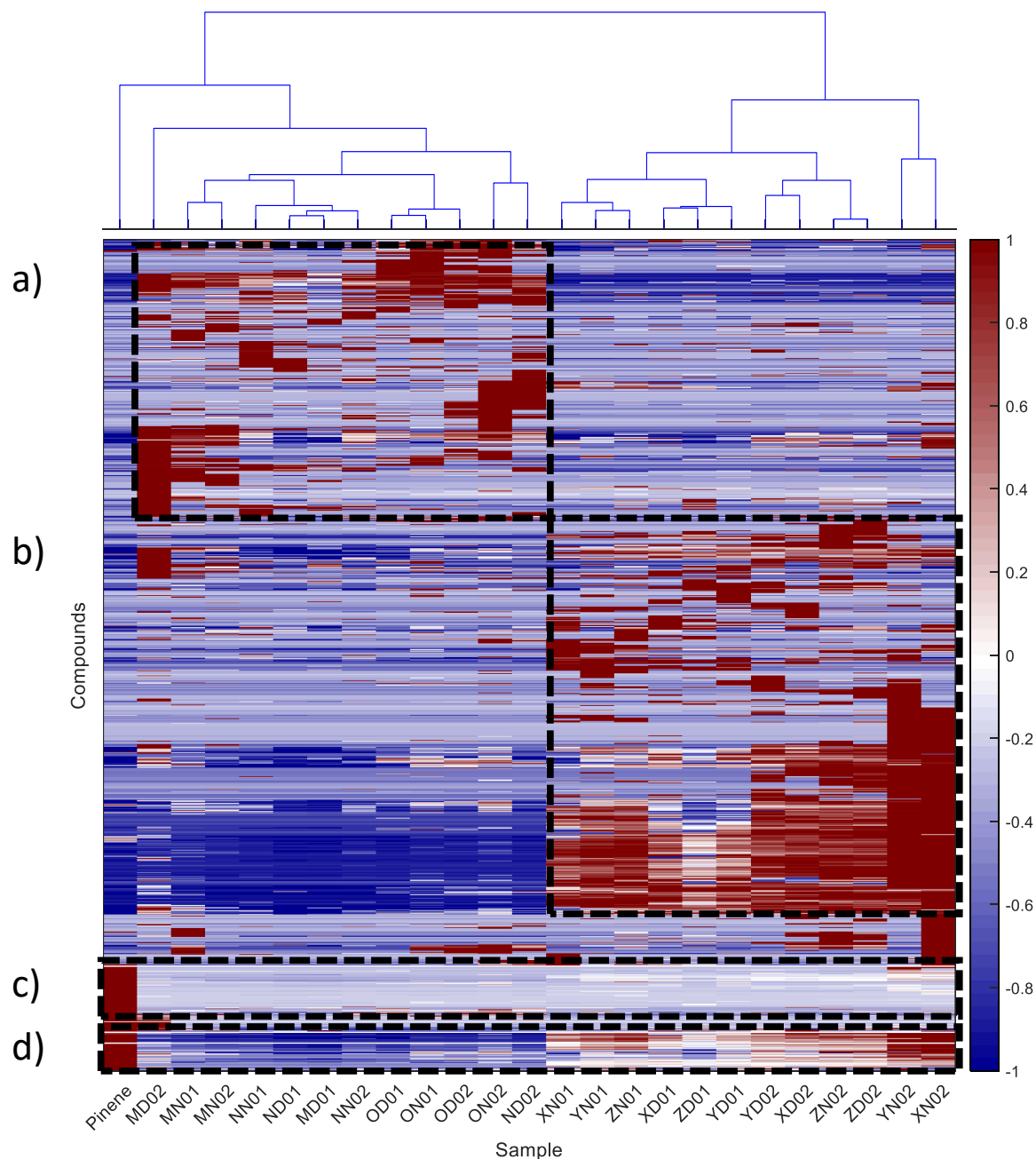


Figure 2.16: Hierarchical cluster analysis (HCA) of twelve samples from the dry season 2018 (X, Y, Z) and the wet season 2019 (M, N, O) during daytime (D) and nighttime (N). One sample from a chamber experiment (O_3/α -pinene) was also included. The z-score is defined by the color code, indicating high signal areas (red) and low signal areas (blue) for each detected organic compound (horizontal lines). Regions (a) and (b) consist of species, which are characteristic for the wet and dry season, respectively. Regions (c) and (d) represent the molecular fingerprint of α -pinene oxidation and the abundance of the corresponding oxidation products during the campaigns.

The algorithm successfully joined samples with similar chemical composition into clusters, as can be seen by the dendrogram. For instance, samples collected simultaneously at different heights (e.g., XN01, YN01, ZN01 and XD01, YD01, ZD01) exhibited high similarity in the molecular composition. As expected, large differences in the chemical characteristics were observed between the wet and dry seasons indicated by the dashed boxes (a) and (b) in Figure 2.16. The major aspects were already discussed above. More importantly, the sample with α -pinene oxidation products showed a distinct molecular fingerprint with organic species in the boxes (c) and (d). While region (c) comprises compounds detected during both the wet and dry season, compounds in the region (d) can mainly be attributed to the dry season. Well-known α -pinene oxidation products were merged in region (c), such as m/z 157.0506 ($C_7H_{10}O_4$), m/z 171.0664 ($C_8H_{12}O_4$), m/z 183.1027 ($C_{10}H_{16}O_3$), m/z 185.0819 ($C_9H_{14}O_4$), and m/z 189.0769 ($C_8H_{14}O_5$). These have already been assigned to terebic acid, terpenylic acid, pinonic acid, pinic acid, and diaterpernylic acid, respectively (Claeys et al., 2009; Yasmeen et al., 2010; Kristensen et al., 2014). Interestingly, MBTCA could be found in region (d) instead indicating an increased SOA contribution by this compound during the dry season. This result can be explained by the fact that the aerosol particles are more processed at drier periods, which facilitates the formation of the later-generation product MBTCA. Additionally, a larger number of high molecular weight (HMW) species were observed in region (d), such as m/z 337.1657 ($C_{18}H_{26}O_6$), m/z 351.1814 ($C_{19}H_{28}O_6$), m/z 357.1556 ($C_{17}H_{26}O_8$), and m/z 367.1764 ($C_{19}H_{28}O_7$). The latter two compounds were identified as dimeric species corresponding to a diaterpernylic ester and a hydroxypinonyl ester of pinic acid, respectively (Müller et al., 2008; Kahnt et al., 2018). Interestingly, these dimers were exclusively detected on filters from the dry season highlighting the relevance of oligomerization reactions for the SOA formation. The preliminary results obtained by HCA support the findings discussed above and prove that statistical data evaluation is a useful extension to common high-resolution mass spectral visualization methods. The implementation of additional VOCs can thus help to assign unknown organic compounds to relevant biogenic SOA precursor species.

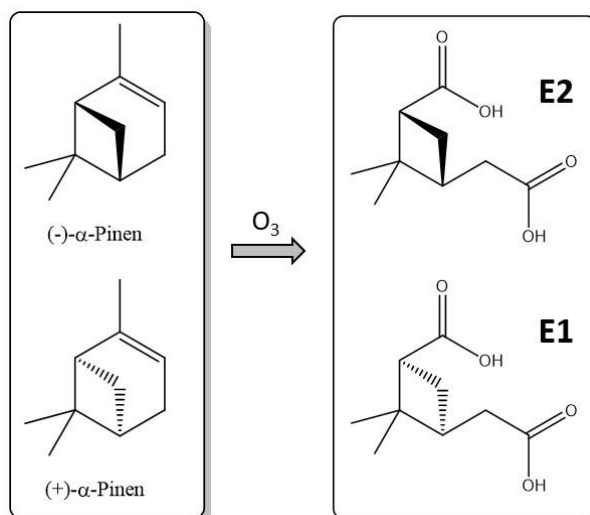
3 Chirally Specified Analysis of Pinic Acid

This chapter is a reprint of the manuscript:

Denis Leppla, Nora Zannoni, Leslie Kremper, Jonathan Williams, Christopher Pöhlker, Marta Sá,
Maria Christina Solci, Thorsten Hoffmann

Varying Chiral Ratio of Pinic Acid Enantiomers above the Amazon Rainforest

Leppla, D., Zannoni, N., Kremper, L., Williams, J., Pöhlker, C., Sá, M., Solci, M. C., and Hoffmann, T.: Varying chiral ratio of Pinic acid enantiomers above the Amazon rainforest, *Atmos. Chem. Phys. Discuss.* [preprint], <https://doi.org/10.5194/acp-2021-150>, in review, 2021.



Abstract

Chiral chemodiversity plays a crucial role in biochemical processes such as insect and plant communication. However, the vast majority of organic aerosol studies do not distinguish between enantiomeric compounds in the particle phase. Here we report chirally specified measurements of secondary organic aerosol (SOA) at the Amazon Tall Tower Observatory (ATTO) at different altitudes during three measurement campaigns at different seasons. Analysis of filter samples by liquid chromatography coupled to mass spectrometry (LC-MS) has shown that the chiral ratio of pinic acid ($C_9H_{14}O_4$) varies with increasing height above the canopy. A similar trend was recently observed for the gas-phase precursor α -pinene, but more pronounced. Nevertheless, the measurements indicate that neither the oxidation of (+/-)- α -pinene nor the incorporation of the products into the particulate phase proceeds with stereo preference and that the chiral information of the precursor molecule is merely transferred to the low-volatility product. The observation of the weaker height gradient of the present enantiomers in the particle phase at the observation site can be explained by the significant differences in the atmospheric lifetimes of reactant and product. Therefore, it is suggested that the chiral ratio of pinic acid is mainly determined by large-scale emission processes of the two precursors, while meteorological, chemical, or physicochemical processes do not play a particular role. Characteristic emissions of the chiral aerosol precursors from different forest ecosystems, in some cases even with contributions from forest related fauna, could thus provide large-scale information on the different contributions to biogenic secondary aerosols via the analytics of the chiral particle-bound degradation products.

3.1 Introduction

The Amazon Basin is one of the most pristine ecosystems on Earth and extends over a region of about 6 million km^2 in South America. Approximately 80% of this region is covered with rainforest which accounts for circa 40% of all tropical forests on the globe (Goulding and Barthem, 2003; Andreae et al., 2015). Various studies estimated the total aboveground carbon content of the Amazon forest at about 86 – 108 Pg C (Saatchi et al., 2007; Baccini et al., 2012), demonstrating its crucial role in climate change and life on Earth in general. In addition to the importance of the Amazon rainforest for the global carbon cycle, its role within the hydrological cycle is one of its most important functions and responsible for the most biodiverse ecosystem on Earth (Hoorn et al., 2010; Wittmann et al., 2013). The immense biodiversity, however, is constantly threatened by deforestation and land-use change (Vieira et al., 2008; Pöhlker et al., 2019). In particular, forest fires are the primary source of pollution. One of the

consequences of these anthropogenic activities are significant seasonal variations in aerosol particle concentrations in the Amazon basin, which strongly affect the radiation budget, cloud physics, and precipitation (Martin et al., 2010; Pöschl et al., 2010; Artaxo et al., 2013). However, even without human influence an estimated 760 Tg C is released into the atmosphere annually worldwide in the form of biogenic volatile organic compounds (BVOCs) (Sindelarova et al., 2014). Rapid reactions with atmospheric reactants, such as OH radicals and ozone, lead to products with lower volatility and subsequently to the formation of secondary organic aerosols (SOAs) (Kroll and Seinfeld, 2008). Organic compounds account for up to 90% of total atmospheric particulate matter in tropical forests (Kanakidou et al., 2004), and directly and indirectly affect the Earth's climate.

Monoterpenes are considered an important fraction of BVOCs comprising a huge variety of individual chemical compounds (Guenther et al., 2012). Many of those are chiral and carry stereogenic centers, resulting in enantiomeric structures that cannot be superimposed. Although chiral molecules play a critical role in insect and plant communication (Phillips et al., 2003; Mori, 2014), they are rarely distinguished in studies regarding atmospheric chemistry. The reason for this is that enantiomers have identical physical and chemical properties in an otherwise non-chiral environment, such as boiling point, exact mass but also reaction rate with atmospheric oxidants (OH, O₃, and NO₃). However, when oligomerization based on chiral building blocks occurs, a process also relevant to secondary organic aerosol formation (Tolocka et al., 2004; Hallquist et al., 2009), changes in physicochemical properties may well occur. It has been shown that physical and chemical properties, such as melting point and water solubility, can then be determined by stereochemistry (Katsumoto et al., 2010; Baker et al., 2015; Cash et al., 2016). Thus, chirality might affect the ability of SOA formation and, consequently, influence for example the radiative forcing and cloud processing of aerosol particles.

Recently, Zannoni et al. (2020) have reported significant variances of the enantiomeric ratio of α -pinene with increasing altitude at the ATTO site in the Amazon rainforest. This unexpected result was attributed to strong local sources, such as insects, which may be responsible for changing the predominant ambient ratio of (-)- and (+)- α -pinene. Through subsequent atmospheric oxidation, the chiral information should be transferred to the particle phase since for certain oxidation reactions the stereochemical centers are retained. Pinic acid is an oxygenated product of α -pinene ozonolysis and a key product of atmospheric VOC degradation compounds identified at the molecular level (Christoffersen et al., 1998; Ma et al., 2007; Yasmeen et al., 2011; Mutzel et al., 2016). Due to its two carboxyl functions, it has a relatively low vapor pressure and thus a strong tendency to partition into the particle phase. Another important product of the α -pinene oxidation is 3-methyl-1,2,3-butanetricarboxylic acid (MBTCA) (Szmigielski et al., 2007; Yasmeen et al., 2010; Müller et al., 2012; Claeys et al., 2007), which would actually be a better marker substance for particle-bound VOC

oxidation products due to its even lower volatility. However, MBTCA has lost the original chiral information due to the breakup of the four-membered ring. Here we show that the chiral ratio of pinic acid in the Amazon rainforest exhibits an excess of one enantiomer. The results reflect the trend observed in the gas phase indicating a direct link between BVOC emissions and SOA concentrations through chirality.

3.2 Experimental Section

3.2.1 Measurement Campaigns and Filter Sampling

Ambient aerosol particles were collected during three campaigns (10/22/2018 – 10/31/2018, 03/04/2019 – 03/14/2019, 09/20/2019 – 09/26/2019) in the Amazon rainforest at the Amazon Tall Tower Observatory (ATTO) station. The research site is already well described by Andreae et al. (2015). Briefly, ATTO is located about 150 km northeast of Manaus, Brazil, and about 12 km northeast of the Uatumã River within the Uatumã Sustainable Development Reserve (UDSR). The site is located on a plateau ~120 m above sea level and is surrounded by dense, non-flooded upland forest (terra firme) with a maximum tree canopy height of approximately 40 m. The area between the river and the plateau is primarily characterized by floodplain forests and white-sandy soil ecosystems of the savanna (campinas) and forest (campinarana) types. The seasonal shift of the Intertropical Convergence Zone (ITCZ) influences meteorological characteristics at the ATTO with clean and wet conditions from February to May and polluted and dry conditions from August to November (Pöhlker et al., 2019) (more details can be found in the supporting information). Key meteorological parameters, trace gas concentrations, and particle concentrations are continuously recorded at the station.

PM_{2.5} filter samples were collected from the 80 m, 150 m, and 320 m platforms of the ATTO tower (coordinates: S 02°08.752' W 59°00.335') during the 2018 dry season and 2019 wet season. During the 2019 dry season, an instrument was moved from the 150 m platform to the ground. Aerosol particles were collected on filters consisting of borosilicate glass microfibers bonded with PTFE (Pallflex® Emfab, 70 mm diameter). To exclude particles with aerodynamic diameters larger than 2.5 μm, a pre-separator (Digitel, DPM2.3) was installed upstream of the filter holder. The flow rate was kept constant at 38 L min⁻¹. In order to distinguish between day and nighttime, the sampling time was 12 h on average. This also ensured sufficient aerosol mass on the filter. Additionally, particle size resolved filter samples were collected at the smaller 80 m triangular mast (coordinates: S 02°08.602' W 59°00.033'). For this purpose, an aerosol inlet at a height of 60 m was connected to a micro-orifice uniform deposit impactor (MOUDI) (TSI, 125R), which allowed sampling of 13 different stages with particle diameters between

10 μm and 10 nm. The flow rate was kept constant at 10 L min^{-1} . The filter samples were stored in a freezer at $-25\text{ }^{\circ}\text{C}$ until analysis. A total of 203 filter samples were collected and analyzed.

3.2.2 Chamber Experiments

We performed ozonolysis experiments with enantiomerically pure (–)- and (+)- α -pinene (Sigma Aldrich, 99%, optical purity ee: 97%) to identify the resulting pinic acid enantiomers. For this purpose, we used a 100 L glass reaction chamber that was completely darkened. Prior to an experiment, the chamber was purged with synthetic air overnight to remove residual particles and reactants from the gas phase. In addition, an activated carbon trap was used to eliminate all organic compounds in the air stream. For each experiment, the chamber was flushed with humidified synthetic air at a constant rate of 6 L min^{-1} , resulting in a relative humidity of 50%. Ozone was generated using the calibration system of an ozone analyzer (Dasibi, 1008-RS) and then introduced into the chamber at a flow rate of 3 L min^{-1} . The ozone concentration stabilized at about 800 ppb. The VOC precursor compound was placed in a diffusion test gas source maintained at 40 $^{\circ}\text{C}$ (Thorenz et al., 2012). A flow rate of 1 L min^{-1} was set to transport the VOCs into the reaction chamber. On average, an α -pinene concentration of 200 ppb was present in the chamber. The particle size distribution for diameters between 10 – 800 nm was recorded using a Scanning Mobility Particle Sizer (SMPS) (GRIMM, Advanced CPC 5.416). Details can be found in the supporting information (Figure S22, Figure S23).

3.2.3 Sample Preparation and LC-MS Analysis

One half of each filter was extracted three times with 1.5 mL in a 9:1 mixture of methanol and water (Fisher Scientific, Optima™ grade) on a laboratory shaker for 30 min. The resulting extracts were combined and filtered through 0.2 μm PTFE syringe filters (Carl Roth, Rotilabo® KC94.1) to remove undissolved material. The solvent was then completely evaporated under a gentle N_2 stream and 700 μL of a 9:1 mixture of water and acetonitrile (Fisher Scientific, Optima™ grade) was added to the remaining residue. All samples were analyzed using an ultra-high performance liquid chromatograph (UHPLC) (ThermoFisher Scientific, UltiMate 3000) coupled to an Orbitrap mass spectrometer (MS) (ThermoFisher Scientific, Q Exactive™). The instrument was equipped with an electrospray ionization (ESI) source and operated in the negative mode. The MS system was regularly calibrated with a negative ion calibration solution (Fisher Scientific, Pierce™). The mass resolution was 140 000 at m/z 200 with mass accuracies less than 1 ppm. To obtain sufficient ion signal intensities, the following ESI-MS parameters were applied: Spray voltage -3.2 kV ; capillary temperature 300 $^{\circ}\text{C}$; auxiliary gas flow 10;

sheath gas flow 30; S-lens RF level 50%. Chiral separation was performed on an amylose-based tris(3-chloro-5-methylphenylcarbamate) column (150 × 2.1 mm ID, 5 μm, Daicel, CHIRALPAK® IG). Eluent A (water with 2% acetonitrile and 0.04% formic acid) and eluent B (acetonitrile with 2% water) were used for isocratic separation (80:20) at a constant flow of 200 μL min⁻¹. The column temperature was maintained at 25 °C. To ensure the identification of pinic acid in the collected aerosol samples, a standard compound was synthesized according to Moglioni et al. (2000). Seven-point calibration curves were generated with concentrations of pinic acid ranging from 0.5 ng mL⁻¹ to 500 ng mL⁻¹.

3.3 Results and Discussion

To identify the two enantiomers of pinic acid, a synthesized reference standard was analyzed by HPLC-MS. The LC method was optimized to ensure baseline separation of the two stereoisomers. The corresponding chromatogram is shown in Figure 3.1, upper panel (a).

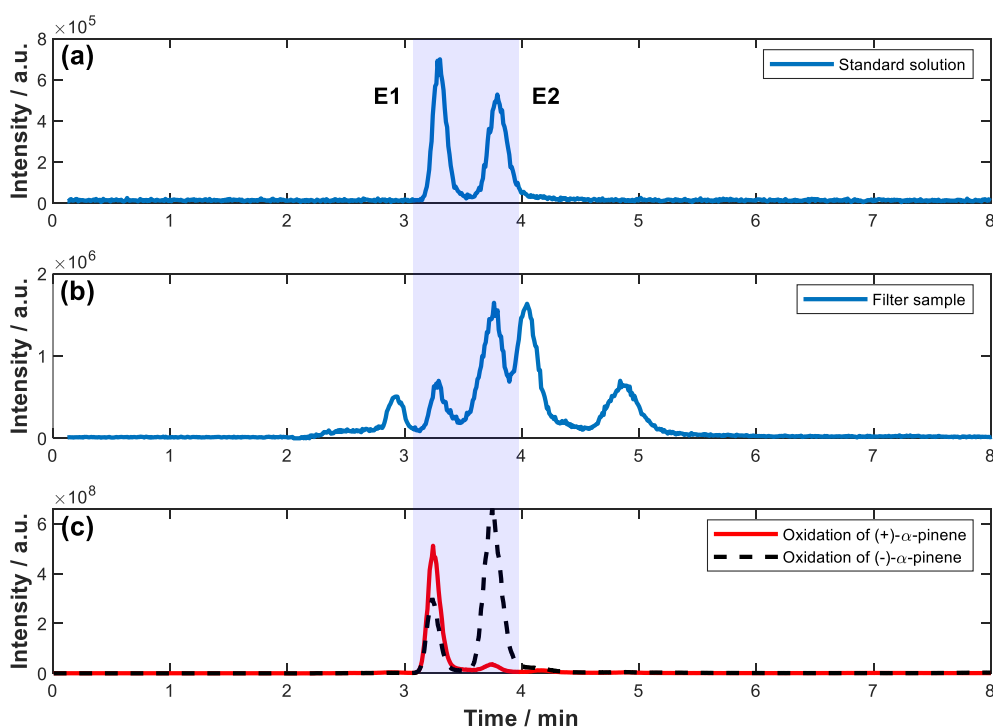


Figure 3.1: Typical chromatograms of pinic acid C₉H₁₄O₄ ([M-H]⁻ *m/z* 185.0819). Both stereoisomers are baseline separated in a reference standard aqueous solution (a). Integration resulted in equal areas, which indicates a racemic mixture. The middle panel (b) illustrates an exemplary analysis of a filter sample. These experiments revealed additional signals at *m/z* 185.0819, a typical mass for monoterpene oxidation products. The lower panel (c) highlights the results of the chamber experiments to distinguish between both stereoisomers of pinic acid (E1 in red results from the ozonolysis of (+)-α-pinene, E2 in dashed black results from the ozonolysis of (-)-α-pinene).

Integration of the reference standard resulted in almost equal signal areas, indicating a racemic standard compound. As confirmed by chamber experiments (lower panel, (c)), the first signal (red line) can be assigned to the oxidation product of enantiomerically pure (+)- α -pinene. It is referred to as E1 in this study. In the subsequent experiment, enantiomerically pure (-)- α -pinene was oxidized. Accordingly, the later eluting second signal resulted from the ozonolysis of pure (-)- α -pinene and is designated E2. As can be seen in the bottom panel (c) of Figure 3.1, E1 was also detected after oxidation of (-)- α -pinene. This was caused by memory effects from the previous chamber experiment with (+)- α -pinene, a common observation in SOA experiments caused by pinic acid condensation on the chamber walls and revolatilization in subsequent experiments. This was also confirmed by the observation of a steady decrease in this carryover in further experiments. However, these results allowed the unambiguous identification and quantification of both pinic acid stereoisomers in the measurements of filter samples from the Amazon rainforest. Since the particular molecular formula $C_9H_{14}O_4$ (m/z 185.0819) is common for oxidation products of various monoterpenes (Kourtchev et al., 2015), for example also for the products of the oxidation of Δ^3 -carene and sabinene, i.e. sabinic and 3-caric acid (Larsen et al., 2001), additional signals were observed in the measurements at the ATTO tower besides those formed by the α -pinene oxidation (middle panel (b)). No further assignment of these signals was made in this study.

3.3.1 Vertical Concentration Gradients of Pinic Acid on PM_{2.5} Filter Samples

Zannoni et al. (2020) showed with measurements made at the ATTO tower that the enantiomeric ratio of α -pinene varies with (+)- α -pinene dominating at canopy level and (-)- α -pinene at the top level of the tower. The ratio was observed to be independent of wind direction and speed and the authors suggest the presence of a potent uncharacterized local (+)- α -pinene rich source, possibly linked to herbivory and termites. Here, we report similar observations for the chiral ratio of pinic acid enantiomers in the particle phase. Figure 3.2 illustrates the atmospheric concentrations of both stereoisomers in $ng\ m^{-3}$ measured at different heights at ATTO during the dry season in October 2018 (denoted as DS18), the wet season in March 2019 (WS19), and the dry season in September 2019 (DS19). The displayed data corresponds to the calculated mean values for the respective campaign in the morning hours (07:00 – 12:00 local time only for DS19), during daytime (07:00 – 17:00 local time for DS18 and WS 19, 12:00 – 17:00 local time for DS19), and during nighttime (17:00 – 07:00 local time). The instrumental detection limits were sufficiently low for both pinic acid stereoisomers (Figure S24), which enabled the reliable quantification of most atmospheric concentrations. However, some samples revealed concentrations of E1 below the detection limit. This occurred mainly for samples taken during

the wet season with generally lower particle concentrations (see supporting information) and for measurements at 320 m during DS19. Nevertheless, these values were included in the calculation of the chiral ratio, as they still represent the trend.

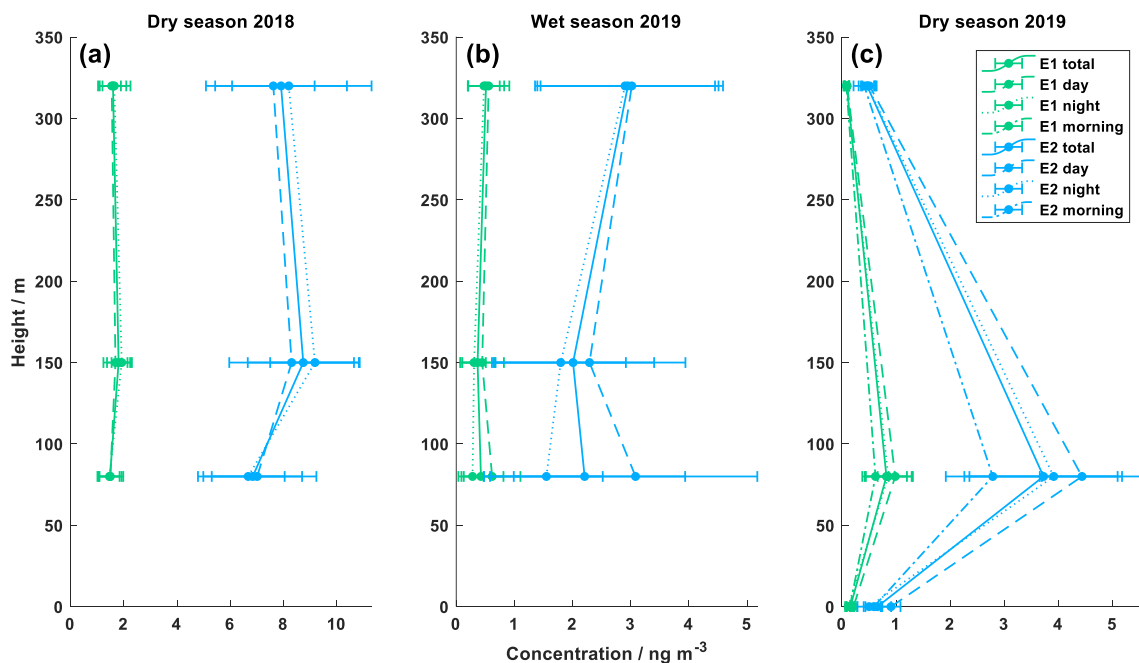


Figure 3.2: Vertical concentration profiles of the pinic acid enantiomers E1 and E2 during three different campaigns ((a) dry season 2018 = October 2018, (b) wet season 2019 = March 2019, (c) dry season 2019 = September 2019). Aerosol filter samples were collected at 80 m, 150 m, and 320 m for the Dry season 2018 and the Wet season 2019. For the Dry season 2019, the instrument at 150 m was moved to the ground level at 0 m. Daytime refers to 7:00 – 17:00, nighttime refers to 17:00 – 7:00 during the first two campaigns. For the third campaign, the time resolution was improved with morning time between 7:00 – 12:00, daytime between 12:00 – 17:00, and nighttime between 17:00 – 7:00. All times are local times. The data points correspond to the mean values of all measurements.

As can be seen in Figure 3.2, all samples had higher concentrations of E2 than E1 with maximum values at 80 m and 150 m for the dry seasons. The higher concentrations of the E2 precursor (α -pinene) could be an explanation for this observation. The highest average concentrations of E2 were measured during DS18 at 150 m with $(9 \pm 2) \text{ ng m}^{-3}$ (errors are represented by one standard deviation of the data sets), while the lowest average concentrations of $(0.09 \pm 0.04) \text{ ng m}^{-3}$ were recorded during DS19 at 320 m. All values are listed in Table 3.1. Contrary to expectations, the concentrations at 320 m during DS19 were significantly lower than during DS18 and below the values of WS19. However, during this period (DS19), significantly lower total particle masses were also observed (see SMPS data in Figure S7). This may have caused the significantly lower pinic acid concentrations on the top of the sampling platform. During the DS19 campaign, the aerosol collector was moved from 150 m to the ground level to include chemistry below the canopy in our observations. Concentrations for pinic acid were lower below the canopy, which was also reported by Plewka et al. (2006) during measurements in

a coniferous forest in Germany. They concluded that increased actinic radiation above the canopy could be the reason for this observation. However, the significantly lower ozone concentrations below the canopy and particle sinks due to dry deposition also fit this observation. Thus, the measured concentration profiles suggest photochemical processes and oxidation chemistry above the forest. Additionally, as recently reported by Bourtsoukidis et al. (2018), soil can be excluded as a potentially effective monoterpene source at ATTO. Consequently, lower ground level concentrations of pinic acid are expected. The α -pinene emissions exhibit a pronounced day-night cycle and reach their maximum together with photosynthetically active radiation (PAR) and temperature at about 11:00 to 14:00 local time (Zannoni et al., 2020). In comparison, a temporal shift of the diel concentration maxima is expected for the particulate phase, caused by mixing and chemical aging. As assumed, the mean concentrations of the measured VOC oxidation products were higher during the daytime in each campaign, except for 80 m and 320 m during DS18 (Figure 3.2). But, of course, the coarse temporal resolution of the present measurements prevents the determination of more detailed diel concentration profiles.

Table 3.1: Average concentration values for E1 and E2 at different heights during three measurement campaigns. Errors are represented as standard deviations of the dataset. Additionally, the calculated enantiomeric ratio, ER, is listed.

	Height / m	avg. c(E1) / ng m ⁻³	avg. c(E2) / ng m ⁻³	avg. ER (E2 / E1)
DS18	80	1.48 ± 0.43	6.84 ± 1.85	4.62 ± 0.11
	150	1.81 ± 0.43	8.74 ± 2.08	4.84 ± 0.10
	320	1.60 ± 0.49	7.91 ± 2.47	4.95 ± 0.12
WS19	80	0.42 ± 0.39	2.21 ± 1.73	5.20 ± 0.19
	150	0.37 ± 0.30	2.01 ± 1.39	5.48 ± 0.15
	320	0.51 ± 0.31	2.95 ± 1.56	5.77 ± 0.12
DS19	0	0.15 ± 0.07	0.65 ± 0.25	4.23 ± 0.11
	80	0.82 ± 0.38	3.72 ± 1.37	4.54 ± 0.12
	320	0.09 ± 0.04	0.46 ± 0.16	5.30 ± 0.09

Figure 3.3 shows the calculated enantiomer ratios for both stereoisomers of pinic acid, E2 / E1. The most remarkable result is that the ratio increases consistently with tower height over all measurement periods. Although the absolute concentrations of the pinic acid enantiomers vary considerably between campaigns, the chiral ratios are always in the range 4 – 6. The dry seasons are characterized by ratios of about 4.6 ± 0.1 and 4.5 ± 0.1 at 80 m, while the wet season shows elevated values of 5.2 ± 0.2 . At 320 m, the E2 enantiomer resulting from (-)- α -pinene oxidation is even more dominant, leading to ratios of 4.9 ± 0.1 and 5.30 ± 0.09 during the dry seasons and 5.8 ± 0.1 during the wet season, respectively. Compared to the vertical concentration gradients of pinic acid in Figure 3.2, the enantiomeric ratios

increase with tower height regardless of the absolute concentrations. This fits very well with the observations of Zannoni et al. (2020), as they described similar results for the chiral ratio of $(-)\text{-}\alpha\text{-pinene}$ / $(+)\text{-}\alpha\text{-pinene}$, i.e., the precursors of the analytes measured here. Increasing values from 0.38 to 6.5 (40 m and 320 m, respectively) were reported, with $(-)\text{-}\alpha\text{-pinene}$ being the dominant species in the gas phase at the top of ATTO. The chamber experiments performed (Figure 3.1) showed that E2 is the oxidation product of $(-)\text{-}\alpha\text{-pinene}$. Therefore, as shown in Figure 3.3, the chiral ratio in the particulate phase behaves similarly to that in the gas phase but is much less pronounced. It ranges from 4.2 ± 0.1 near the ground to 5.8 ± 0.1 at 320 m altitude. Remarkably, as reported by Zannoni et al. (2020), there was little variation in the two $\alpha\text{-pinene}$ enantiomers in the gas phase during the 2018 wet season. This finding is not consistent with the results from the particulate phase as shown in Figure 3.3, at least when compared to the 2019 results. Similar to the dry seasons, the chiral ratio of pinic acid also shows steady growth with increasing tower height during the wet season.

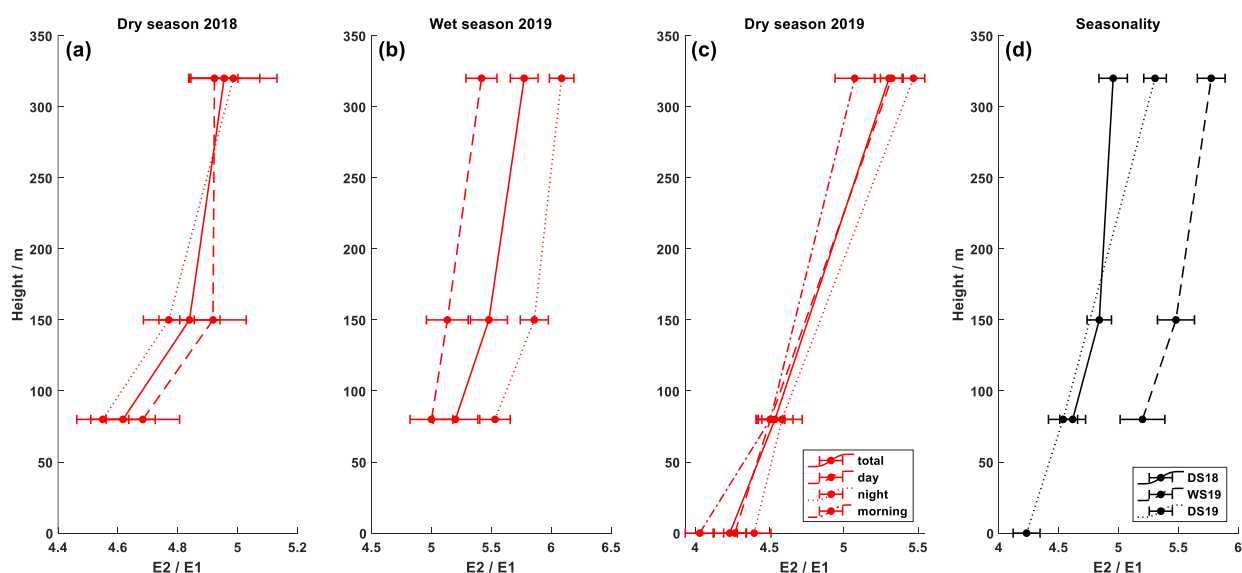


Figure 3.3: Vertical profiles of the enantiomeric ratio E2 / E1 (a – c). The local times correspond to those shown in Figure 3.2. Additionally, the comparison for all campaigns is shown in panel (d) (DS = dry season, WS = wet season). There is a constant increase of E2 compared to E1 with increasing altitude. All values are in the same magnitude. However, the wet season was characterized by slightly larger ratios.

The emission of $\alpha\text{-pinene}$ and the ratio of enantiomers released is determined by the vegetation and thus, for ecosystem measurement sites such as ATTO, by the local flora, possibly with additional contributions from the local fauna, such as termites (Zannoni et al., 2020). Measurements at different altitudes in the present study, thus first reflect differences in releases from the different source regions, which, after all, depend on the effective measurement altitude (Arriga et al., 2017). Thereby, the measurements reflect local sources at the lower levels and regional influences at the upper levels

(Bakwin et al., 1998; Andrews et al., 2014). Due to the high reactivity of biogenic VOCs toward OH radicals and ozone, the mean tropospheric lifetime of α -pinene is on average only 2.6 h and 4.6 h, respectively (Atkinson, 1997, 2000; Kesselmeier and Staudt, 1999). Thus, strong local sources such as insects can alter the enantiomeric distributions in the gas phase. Consequently, the chiral ratio for α -pinene at ATTO varies strongly with increasing tower height. However, the oxidative formation and especially depletion of pinic acid occur on different time scales with estimated lifetimes of several days (Rogge et al., 1993; Rudich et al., 2007; Schauer et al., 1996). The difference in the two enantiomers is therefore much less pronounced for the chiral oxidation products, but also reflects the different footprint regions.

3.3.2 Daily Variations of Pinic Acid Concentrations

Figure 3.4 shows the absolute concentrations for E1 and E2 of pinic acid near the ground (blue), at 80 m (dark green), 150 m (green), and 320 m (light green) for the three measurement campaigns. In general, absolute concentrations at the respective tower heights vary rather slightly within each campaign, with the greatest variation just above the canopy on the 80 m platform.

It is clear that the 80 m values are more influenced by local sources than the 150 m and 320 m heights. This is evident for both the DS19 and WS19 campaigns. In particular, the daytime samples (03/06/2019, 03/07/2019, and 03/09/2019) show different concentration trends at 80 m height compared to the higher tower levels. An obvious explanation is characterized by an effective coupling between the forest canopy and the superjacent atmosphere caused by strong turbulent activity during the daytime (Andreae et al., 2015). Measurements within this roughness sublayer (RSL) are expected to be strongly influenced by the various roughness elements. In general, the RSL is thought to extend to approximately 2 to 3 times the canopy height of about 40 m (Raupach et al., 1996; Williams et al., 2007; Chor et al., 2017). In addition, according to Dias-Júnior et al. (2019), the RSL merges directly into the adjacent convective mixed layer. Thus, similar conditions exist for both 150 m and 320 m heights, resulting in decoupled concentration profiles compared to 80 m.

The proportions of the two enantiomers showed almost constant ratios both for the different sampling heights and within each measurement campaign (see Figure 3.4b, d, f). However, as indicated above, the ratios were also quite similar between the different campaigns. A certain trend can be seen in the dry season of 2019 (Figure 3.4f), as here the relative concentration of E2 increased over time at all observation heights. All these observations supported the idea that the chiral ratio is determined by mixing and transport processes rather than by the preferential formation of a particular enantiomer.

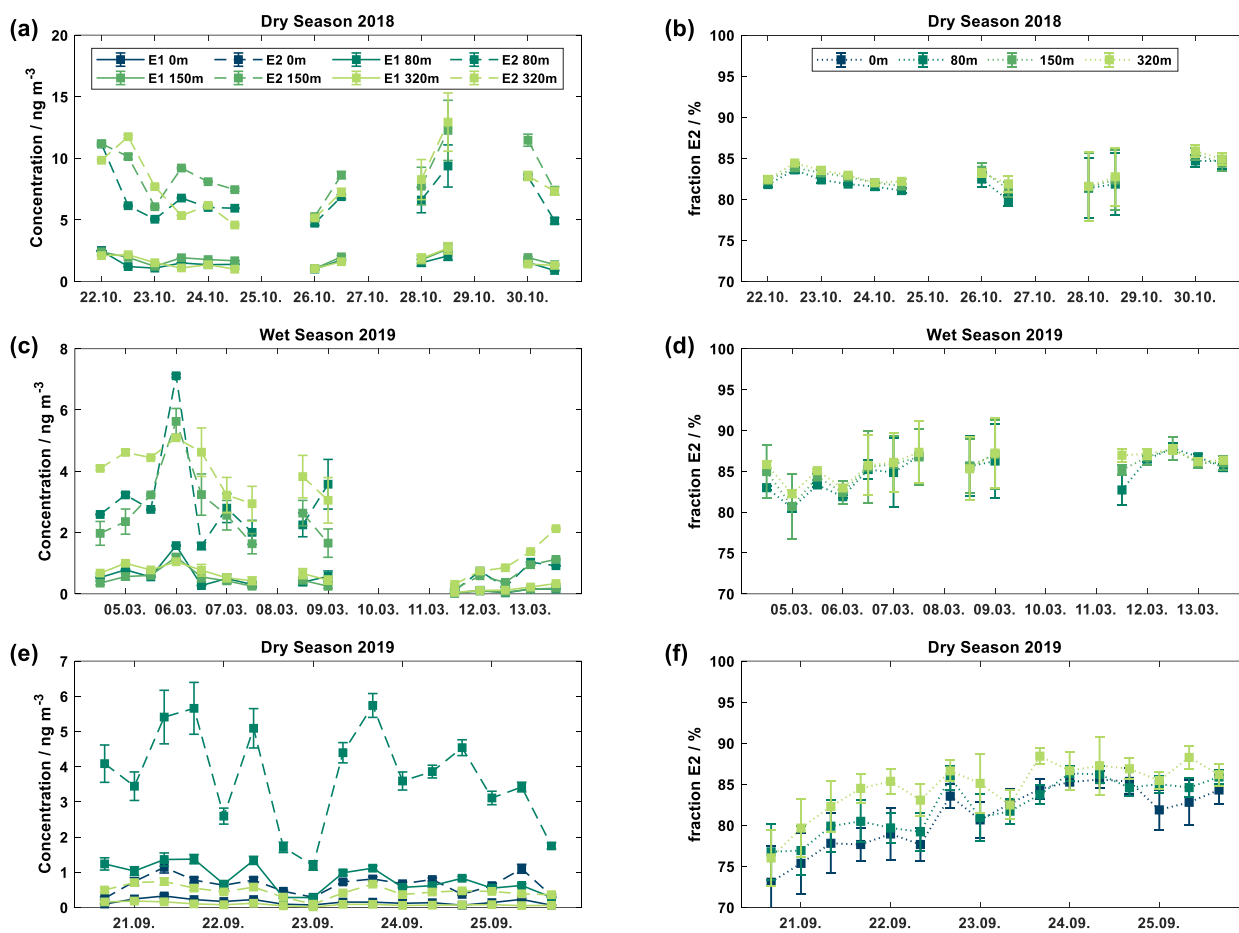


Figure 3.4: Absolute concentrations of E1 and E2 at different heights at ATTO are displayed in (a), (c), and (e) for three different measurement campaigns, respectively. The resulting chiral relative abundance of E2 is illustrated in (b), (d), and (f). Each data point corresponds to a sample collected at ATTO. The analysis of aerosol samples at ground level (0 m) was only performed during the dry season 2019.

3.3.3 Particle Size Resolved Measurements at the Triangular Mast

In addition to the PM_{2.5} filter samples, MOUDI measurements were carried out to investigate the chiral ratio of pinic acid at different particle diameters. Size resolved samples were collected at the 60 m inlet of the triangular mast during each campaign. Figure 3.5 shows the concentration of E1 and E2 in the different particle fractions. Similar to the PM_{2.5} samples, all MOUDI samples were dominated by the E2 enantiomer. However, especially in the size range with small particles (diameter ≤ 100 nm) and large particles (diameter ≥ 1000 nm), low total particle mass concentrations were measured (see Figure S25), resulting partly in concentrations of the dicarboxylic acid below the detection limit. Nevertheless, these values were included in the figure as they illustrate the general trend. All measurements showed elevated concentrations of pinic acid for the particle size range between 180 nm and 560 nm diameter. Maximum concentrations of (0.027 ± 0.002) ng m^{-3} for E1 and (0.113 ± 0.023) ng m^{-3} for E2 were

determined in both dry seasons. The rainy season reached maximum concentrations of (0.026 ± 0.020) ng m⁻³ for E1 and (0.077 ± 0.059) ng m⁻³ for E2. It should be noted that these results are mean concentrations that include four and two MOUDI measurements, respectively. This is due to the fact that the sampling time was significantly extended to ensure sufficient aerosol mass loadings on the filters.

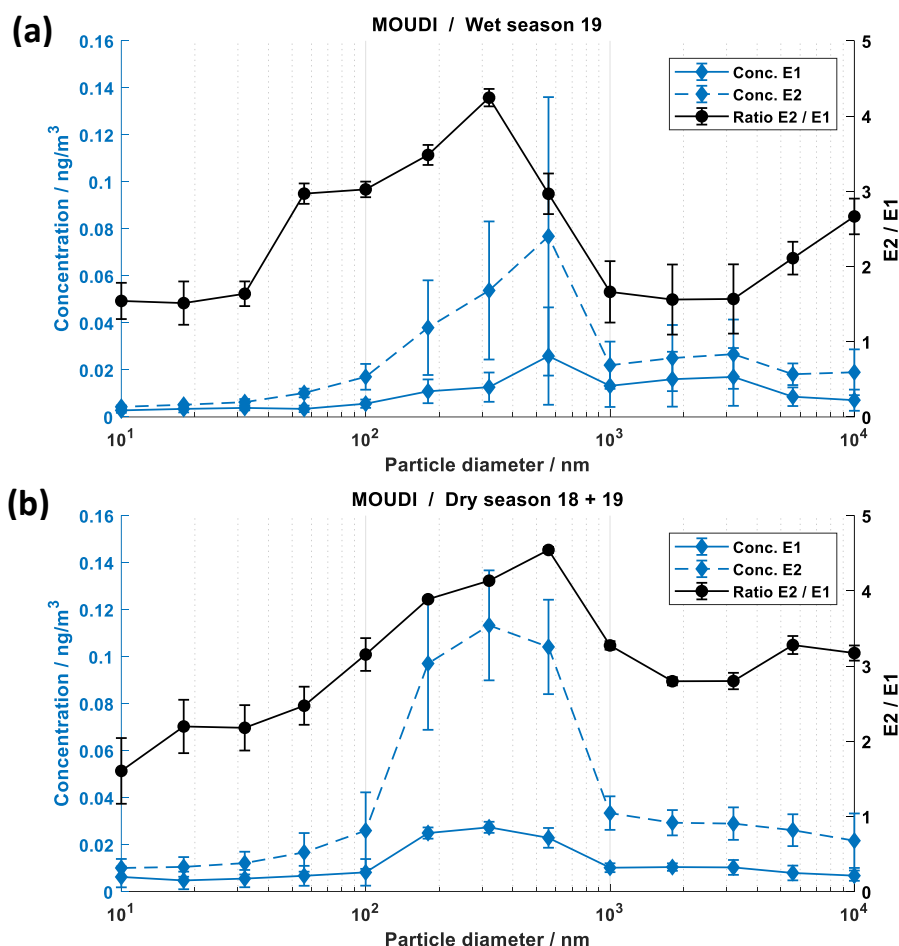


Figure 3.5: Particle size resolved MOUDI measurements of pinic acid at the triangular mast (60 m) (dry season = (a), wet season = (b)). The concentrations of E1 and E2 are illustrated together with the resulting chiral ratio. Both seasons revealed elevated concentrations in the particle size range between 180 – 560 nm diameters. The concentrations for small particle diameters (< 56 nm) were partially below the limit of detection. The respective values are still shown to illustrate the trend. The data points correspond to the mean values of all measurements.

The concentrations of E1 and E2 showed essentially similar size distributions as the particle size distribution measured with SMPS systems during the respective measurement periods (see Figure S25). Accordingly, the highest concentrations of pinic acid are found in particles with diameters between 100 nm and 600 nm, which represents the accumulation mode of the particle size distribution. In fact, the absolute concentrations are slightly lower compared to the samples collected at ATTO, which could have two reasons. First, the MOUDI samples were collected with a 60 m inlet, which may result in

particle losses in the inlet lines. Second, the sampling time was extended to several days, which could obviously favor sampling artifacts such as evaporation/decomposition of the target analyte during sampling. Consequently, lower concentrations of pinic acid are found. The resulting chiral ratios between E2 and E1 tend to be lower, with average values of 4.2 and 3.6 for the dry and wet seasons, respectively, but still quite similar to the measurements presented previously at ATTO. The observed shape of the size distribution of the ratio of the two enantiomers, also shown in Figure 3.5, is interesting but not easily explained. The comparatively high relative contributions of E1 (E2 / E1 value ratios between 1.5 and 3) in the particularly small (< 100 nm) and particularly large particles (> 1000 nm) are striking. As discussed above, such behavior could be caused by an aerosol matrix that is also chiral, meaning that, for example, the E1 enantiomer is preferentially incorporated into the particle phase. Although such behavior can certainly not be ruled out by our measurements, there are other possible explanations. In principle, the particle size is also related to the different ages of the aerosol particles. The very small particle fractions are comparatively young because after particle formation (whether released as small primary particles or newly formed by gas-particle conversion) condensation processes from the gas phase (or coagulation) cause the particles to grow so that they transition to larger particle regions with increasing age. Thus, a different ratio of the two enantiomers could be explained by the fact that the chiral precursors of the particles formed in the immediate vicinity of the measurement site have a different ratio here than in a more spacious environment. Indeed, Zannoni et al. (2020) was able to measure higher (+)- α -pinene concentrations (i.e., the precursor of E1) closer to the measurement site than far above the ground. However, the again relatively small E2 / E1 ratios of particles larger than 1000 nm do not fit such an interpretation. Finally, the cause could be an analytical artifact that simply shows small but constant additive effects at lower concentrations (e.g., due to additive cross-interference from coeluting substances). Future measurements will have to show which of the possible explanations really explains the observations made.

Figure 3.6 again compares the results at the two different sites and the different measurement heights with respect to the relative abundances of E1 and E2. Unlike the ATTO tower, the triangular mast is fully integrated into the forest structure without any clearing and therefore may better represent the local emission signature at low altitudes. Zannoni et al. (2020) suggested that insects could be a potential source to alter the chiral ratio of monoterpenes. In particular, termites have shown (+)- α -pinene enriched emissions. Apparently, their contribution can shift the chiral ratio from locally dominant (-)- α -pinene to (+)- α -pinene.

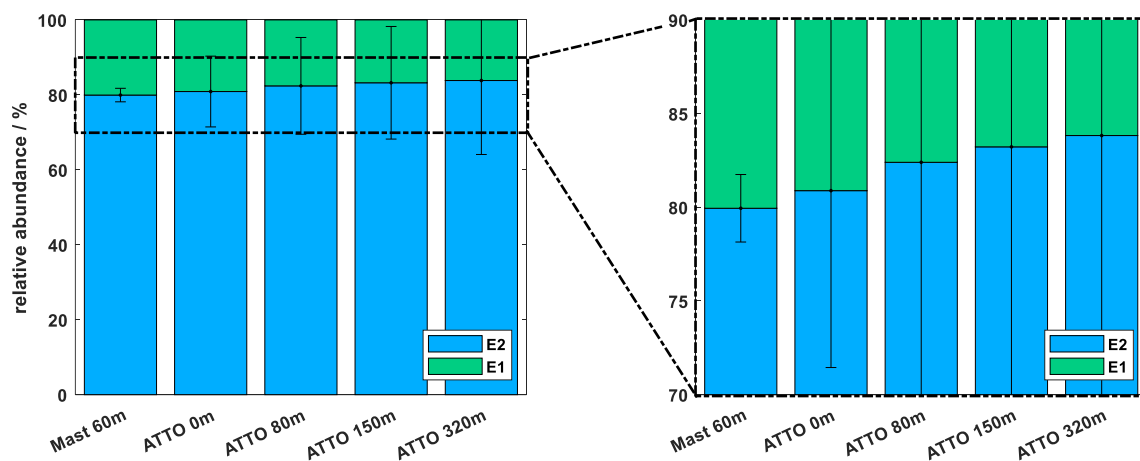


Figure 3.6: The average relative abundance is illustrated for five different sampling locations at the triangular mast and ATTO tower. The right panel shows an enlarged version to highlight the increasing fraction of E2 with tower height. Apparently, the triangular mast exhibits a different local emission signature caused by the dense inclusion into the forest structure.

3.4 Conclusion

The present study reports the concentrations and ratios of the two enantiomers of pinic acid within and above the Amazon rainforest at the ATTO site. In all samples, the enantiomer from the oxidation of (–)- α -pinene dominated, confirming the results of precursor measurements at the same site. Similar to the gas-phase, a gradient in the ratios of the two enantiomers with increasing tower height was also evident in the particle phase. This observation was consistent over three measurement campaigns from October 2018 to September 2019. The measurements shown at different heights suggest that the results reflect differences in the releases of the chiral precursors, which do depend on the effective measurement height. Thus, local sources influence the results at lower levels and regional sources influence those at higher levels. Somewhat different patterns were observed at 80 m sampling height than at the higher levels, which again indicates that for measurements at 80 m the local emission conditions have a greater influence on the results. The results obtained from the triangular mast support this assumption.

Overall, the presented results show that the chiral relationship of the biogenic precursor compound α -pinene is preserved in the oxidation products studied here and can thus be used to interpret the biogenic emission sources. However, due to the different lifetimes of the precursor VOC and the particle-bound oxidation products, using the chiral ratios of the longer-lived compound provides a larger-scale picture of precursor emissions, while also revealing local and regional influences. However, it should also be mentioned that further improvements in the analytical methods would be useful. The molecular formula $C_9H_{14}O_4$ of pinic acid can be formed by a number of other monoterpenes, making reliable quantification at very low concentrations difficult. Therefore, additional chamber experiments with other relevant

BVOCs would certainly be helpful to identify and assign the additional LC signals observed. This could potentially provide further helpful information on large-scale biogenic VOC releases and their contributions to the atmospheric particulate phase.

Author contributions

Denis Leppla conducted the aerosol sampling, the sample preparation, and the measurements. Denis Leppla analyzed the data and wrote the manuscript. Nora Zannoni helped to collect the aerosol samples. Denis Leppla and Leslie Kremper were responsible for the chamber experiments. Leslie Kremper and Christopher Pöhlker provided the SMPS data. The meteorological data was provided by Marta Sá. Thorsten Hoffmann supervised the study. All authors contributed to the scientific exchange and read and revised the manuscript.

Acknowledgments

For the operation of the ATTO site, we acknowledge the support by the German Federal Ministry of Education and Research (BMBF Contract 01LK1602D) and the Brazilian Ministério da Ciência, Tecnologia e Inovação (MCTI/FINEP) as well as the Amazon State University (UEA), FAPEAM, LBA/INPA, and SDS/CEUC/RDS-Uatumã. We also acknowledge the support of the Max Planck Society and the Instituto Nacional de Pesquisas da Amazonia (INPA).

4 Conclusions and Outlook

In the present study ultrahigh-resolution mass spectrometry (UHRMS) was proven a suitable and versatile analytical technique for the investigation of aerosol particles. A non-targeted approach was developed and successfully applied to filter samples from several field campaigns in the Amazon rainforest. The combination with a soft ionization method by ESI in the negative mode enabled the analysis of organic aerosol compounds on a molecular level without fragmentation. To complement the qualitative information obtained, the MS system was coupled with an HPLC device allowing simultaneous quantification of specific marker species. Additionally, a large fraction of isomeric compounds were detected on all filter samples making the chromatographic pre-separation an essential tool for high-resolution mass spectral experiments.

The complex mass spectral data obtained by UHRMS requires software-based processing methods for reliable evaluation. Therefore, a sophisticated non-targeted screening approach was developed to identify more than 4000 distinct organic species. According to the elemental composition, they were classified as CHO, CHON, CHOS, and CHONS compounds. Comprehensive visualization techniques for UHRMS data (e.g., Van Krevelen, Kendrick mass defect) were applied to compare the SOA chemical composition of filter samples from different seasons and heights at ATTO. The largest number of compounds was assigned to the CHO category, although the CHOS class represented a substantial fraction for each season. These classes mainly contained carboxylic acids, as confirmed by the neutral loss of CO₂ in MS² experiments. Furthermore, most of the CHOS compounds exhibited O/S ratios ≥ 4 , indicating organosulfates. Semiquantification revealed higher signal intensities for CHOS compounds during the dry seasons, suggesting a strong contribution of anthropogenic SO₂ emissions to the SOA formation. Moreover, the dry seasons are highly affected by deforestation fires resulting in an increased number of unsaturated and aromatic compounds such as nitrophenols and nitrocatechols. However, similar observations were made during the wet season 2019, which could arise from higher incidents of forest fires compared to the wet season 2018. A larger number of highly oxidized and oxygenated molecules were detected during the dry seasons indicated by increased carbon oxidation states (OS_C). More processed aerosol might be the result of less removal by wet deposition. However, certain oxidative processes (e.g., OH radical-initiated photooxidation, ozonolysis) might be enhanced during drier and hotter periods producing more oxidized SOA. This hypothesis needs to be addressed in upcoming studies. All four field campaigns were characterized by high signal intensities of IEPOX-OS, 2-methyltetrols, pinic acid, and MBTCA. This result proves that isoprene and monoterpenes are the major precursor compounds for SOA formation in the Amazon. Height-resolved measurements suggested the forest canopy as the predominant BVOC emission source. Sesquiterpenes appeared to be

less relevant for the SOA formation. Lower LC-MS sensitivity towards sesquiterpene oxidation products might cause this observation. Authentic standard compounds could help to improve the analytical method. Additionally, particle size resolved MOUDI measurements were presented in this study. MBTCA and β -caryophyllinic acid revealed increased concentrations in the accumulation mode, indicating SOA formation through heterogeneous chemistry. In contrast, levoglucosan was mainly attributed to the coarse mode. Primary combustion emissions might be responsible for that observation. Interestingly, 2-methyltetrols showed increased concentrations in both the accumulation mode and the coarse mode, suggesting primary and secondary formation processes.

Also, an LC method based on an amylose stationary phase was developed to perform chirally specified measurements of SOA samples. This study successfully separated the two enantiomeric structures of pinic acid, which are oxidation products from (+/-)- α -pinene. Enantiopure ozonolysis reactions in a smog chamber were performed and enabled the assignment of a chiral gas-phase precursor to one pinic acid enantiomer. The analysis of filter samples has shown that the chiral ratio of pinic acid varied with increasing sampling height. Previously, a similar trend was observed for the gas-phase precursors at the ATTO site. This result indicated that the chiral information is transferred from the gas- to the particle phase, while local sources affect the chiral ratio at lower altitudes and regional sources influence higher levels. The chiral analysis of the long-lived pinic acid will thus be useful to receive large-scale pictures of the precursor emissions including local and regional information. However, additional chamber experiments with other relevant BVOCs are necessary to identify all isomeric structures with the molecular formula $C_9H_{14}O_4$.

Generally, the application of HPLC-UHRMS to filter samples from the ATTO station has proven to be a powerful analytical technique to investigate the highly complex chemical composition of SOA. Non-targeted and targeted approaches were demonstrated to attribute SOA fingerprints to biogenic and anthropogenic emission sources. However, further improvements are necessary to reliably assess large-scale BVOC emissions and their contribution to the particle-phase. Especially, the rather low sampling time resolution prevents the analysis of individual plume events. Nevertheless, a compromise must be found between collection time and sufficient aerosol mass on the filter predefined by the analytical system. An automated sampling device could be useful for simultaneous sampling at several heights at ATTO for future campaigns. This setup allows the collection of aerosols from short-timed events, such as photooxidation in the morning, starting nucleation processes, the influence of heavy rain, *etc.* Another advanced application relies on the utilization of particle-into-liquid sampler (PILS). This technique enables constant aqueous extraction of SOA constituents into several sample vials. Water-soluble organic carbon (WSOC), i.e. polar and hydrophilic oxidation products of isoprene (e.g., 2-methyltetrols) and monoterpenes (e.g., pinic acid), and anhydrosugars (e.g., levoglucosan), is collected and stored with

PILS. In combination with hydrophilic interaction liquid chromatography (HILIC), a large fraction of so far coeluting polar compounds would be accessible. A 2D-LC approach (HILIC \times C18 / CHIRAL \times C18) will be applied in upcoming experiments to extend the analytical information. Moreover, the used LC-MS technique should be enhanced by complementary instruments, such as GC or AMS, to cover a larger fraction of SOA constituents. Besides technical improvements, the software-based evaluation of complex UHRMS data should be optimized. Advancing codes and algorithms for non-targeted data processing will help to visualize and interpret detailed SOA chemical compositions.

5 References

- Ahmed, A. A., Abd el-Razek, M. H., Abu Mostafa, E. A., Williams, H. J., Scott, A. I., Reibenspies, J. H., and Mabry, T. J.: A new derivative of glucose and 2-C-methyl-D-erythritol from *Ferula sinaica*, *Journal of natural products*, 59, 1171–1173, <https://doi.org/10.1021/np9603434>, 1996.
- Alfarra, M. R., Coe, H., Allan, J. D., Bower, K. N., Boudries, H., Canagaratna, M. R., Jimenez, J. L., Jayne, J. T., Garforth, A. A., Li, S.-M., and Worsnop, D. R.: Characterization of urban and rural organic particulate in the Lower Fraser Valley using two Aerodyne Aerosol Mass Spectrometers, *Atmospheric Environment*, 38, 5745–5758, <https://doi.org/10.1016/j.atmosenv.2004.01.054>, 2004.
- Aljawhary, D., Zhao, R., Lee, A. K. Y., Wang, C., and Abbatt, J. P. D.: Kinetics, Mechanism, and Secondary Organic Aerosol Yield of Aqueous Phase Photo-oxidation of α -Pinene Oxidation Products, *The journal of physical chemistry. A*, 120, 1395–1407, <https://doi.org/10.1021/acs.jpca.5b06237>, 2016.
- Allen, C. W.: *Astrophysical quantities*, 3rd ed., Athlone, London, 310 pp., 1991.
- Andrade, F. J., Shelley, J. T., Wetzel, W. C., Webb, M. R., Gamez, G., Ray, S. J., and Hieftje, G. M.: Atmospheric pressure chemical ionization source. 1. Ionization of compounds in the gas phase, *Analytical chemistry*, 80, 2646–2653, <https://doi.org/10.1021/ac800156y>, 2008.
- Andreae, M. O. and Rosenfeld, D.: Aerosol–cloud–precipitation interactions. Part 1. The nature and sources of cloud-active aerosols, *Earth-Science Reviews*, 89, 13–41, <https://doi.org/10.1016/j.earscirev.2008.03.001>, 2008.
- Andreae, M. O. and Crutzen, P. J.: Atmospheric Aerosols: Biogeochemical Sources and Role in Atmospheric Chemistry, *Science (New York, N.Y.)*, 276, 1052–1058, <https://doi.org/10.1126/science.276.5315.1052>, 1997.
- Andreae, M. O., Acevedo, O. C., Araùjo, A., Artaxo, P., Barbosa, C. G. G., Barbosa, H. M. J., Brito, J., Carbone, S., Chi, X., Cintra, B. B. L., da Silva, N. F., Dias, N. L., Dias-Júnior, C. Q., Ditas, F., Ditz, R., Godoi, A. F. L., Godoi, R. H. M., Heimann, M., Hoffmann, T., Kesselmeier, J., Könemann, T., Krüger, M. L., Lavric, J. V., Manzi, A. O., Lopes, A. P., Martins, D. L., Mikhailov, E. F., Moran-Zuloaga, D., Nelson, B. W., Nölscher, A. C., Santos Nogueira, D., Piedade, M. T. F., Pöhlker, C., Pöschl, U., Quesada, C. A., Rizzo, L. V., Ro, C.-U., Ruckteschler, N., Sá, L. D. A., Oliveira Sá, M. de, Sales, C. B., dos Santos, R. M. N., Saturno, J., Schöngart, J., Sörgel, M., Souza, C. M. de, Souza, R. A. F. de, Su, H., Targhetta, N., Tóta, J., Trebs, I., Trumbore, S., van Eijck, A., Walter, D., Wang, Z., Weber, B., Williams, J., Winderlich, J., Wittmann, F., Wolff, S., and Yáñez-Serrano, A. M.: The Amazon Tall Tower Observatory (ATTO): Overview of pilot measurements on ecosystem ecology, meteorology, trace gases, and aerosols, *Atmos. Chem. Phys.*, 15, 10723–10776, <https://doi.org/10.5194/acp-15-10723-2015>, 2015.
- Andreae, M. O., Rosenfeld, D., Artaxo, P., Costa, A. A., Frank, G. P., Longo, K. M., and Silva-Dias, M. A. F.: Smoking rain clouds over the Amazon, *Science (New York, N.Y.)*, 303, 1337–1342, <https://doi.org/10.1126/science.1092779>, 2004.
- Andrews, A. E., Kofler, J. D., Trudeau, M. E., Williams, J. C., Neff, D. H., Masarie, K. A., Chao, D. Y., Kitzi, D. R., Novelli, P. C., Zhao, C. L., Dlugokencky, E. J., Lang, P. M., Crotwell, M. J., Fischer, M. L., Parker, M. J., Lee, J. T., Baumann, D. D., Desai, A. R., Stanier, C. O., Wekker, S. F. J. de, Wolfe, D. E., Munger, J. W., and Tans, P. P.: CO₂, CO, and CH₄ measurements from tall towers in the NOAA Earth System Research Laboratory's Global Greenhouse Gas Reference Network: instrumentation, uncertainty analysis, and recommendations for future high-accuracy greenhouse gas monitoring efforts, *Atmos. Meas. Tech.*, 7, 647–687, <https://doi.org/10.5194/amt-7-647-2014>, 2014.
- Ardrey, R. E.: *Liquid Chromatography – Mass Spectrometry: An Introduction*, Wiley, 2003.
- Arriga, N., Rannik, Ü., Aubinet, M., Carrara, A., Vesala, T., and Papale, D.: Experimental validation of footprint models for eddy covariance CO₂ flux measurements above grassland by means of

- natural and artificial tracers, *Agricultural and Forest Meteorology*, 242, 75–84, <https://doi.org/10.1016/j.agrformet.2017.04.006>, 2017.
- Artaxo, P.: Physical and chemical properties of aerosols in the wet and dry seasons in Rondônia, Amazonia, *J. Geophys. Res.*, 107, 1052, <https://doi.org/10.1029/2001JD000666>, 2002.
- Artaxo, P., Rizzo, L. V., Brito, J. F., Barbosa, H. M. J., Arana, A., Sena, E. T., Cirino, G. G., Bastos, W., Martin, S. T., and Andreae, M. O.: Atmospheric aerosols in Amazonia and land use change: From natural biogenic to biomass burning conditions, *Faraday Discuss.*, 165, 203, <https://doi.org/10.1039/c3fd00052d>, 2013.
- Atkinson, R.: Atmospheric chemistry of VOCs and NO_x, *Atmospheric Environment*, 34, 2063–2101, [https://doi.org/10.1016/S1352-2310\(99\)00460-4](https://doi.org/10.1016/S1352-2310(99)00460-4), 2000.
- Atkinson, R.: Gas-Phase Tropospheric Chemistry of Volatile Organic Compounds: 1. Alkanes and Alkenes, *Journal of Physical and Chemical Reference Data*, 26, 215–290, <https://doi.org/10.1063/1.556012>, 1997.
- Atkinson, R., Baulch, D. L., Cox, R. A., Crowley, J. N., Hampson, R. F., Hynes, R. G., Jenkin, M. E., Rossi, M. J., and Troe, J.: Evaluated kinetic and photochemical data for atmospheric chemistry: Volume II – gas phase reactions of organic species, *Atmos. Chem. Phys.*, 6, 3625–4055, <https://doi.org/10.5194/acp-6-3625-2006>, 2006.
- Atkinson, R. and Arey, J.: Gas-phase tropospheric chemistry of biogenic volatile organic compounds: a review, *Atmospheric Environment*, 37, 197–219, [https://doi.org/10.1016/S1352-2310\(03\)00391-1](https://doi.org/10.1016/S1352-2310(03)00391-1), 2003a.
- Atkinson, R. and Arey, J.: Atmospheric degradation of volatile organic compounds, *Chemical reviews*, 103, 4605–4638, <https://doi.org/10.1021/cr0206420>, 2003b.
- Baccini, A., Goetz, S. J., Walker, W. S., Laporte, N. T., Sun, M., Sulla-Menashe, D., Hackler, J., Beck, P. S. A., Dubayah, R., Friedl, M. A., Samanta, S., and Houghton, R. A.: Estimated carbon dioxide emissions from tropical deforestation improved by carbon-density maps, *Nature Clim Change*, 2, 182–185, <https://doi.org/10.1038/nclimate1354>, 2012.
- Badertscher, M., Bischofberger, K., Munk, M. E., and Pretsch, E.: A novel formalism to characterize the degree of unsaturation of organic molecules, *Journal of chemical information and computer sciences*, 41, 889–893, <https://doi.org/10.1021/ci000135o>, 2001.
- Baker, M. B., Albertazzi, L., Voets, I. K., Leenders, C. M. A., Palmans, A. R. A., Pavan, G. M., and Meijer, E. W.: Consequences of chirality on the dynamics of a water-soluble supramolecular polymer, *Nature communications*, 6, 6234, <https://doi.org/10.1038/ncomms7234>, 2015.
- Bakwin, P. S., Tans, P. P., Hurst, D. F., and Zhao, C.: Measurements of carbon dioxide on very tall towers: results of the NOAA/CMDL program, *Tellus B: Chemical and Physical Meteorology*, 50, 401–415, <https://doi.org/10.3402/tellusb.v50i5.16216>, 1998.
- Barbaro, E., Zangrando, R., Moret, I., Barbante, C., Cescon, P., and Gambaro, A.: Free amino acids in atmospheric particulate matter of Venice, Italy, *Atmospheric Environment*, 45, 5050–5057, <https://doi.org/10.1016/j.atmosenv.2011.01.068>, 2011.
- Barrado, A. I., García, S., Barrado, E., and Pérez, R. M.: PM_{2.5}-bound PAHs and hydroxy-PAHs in atmospheric aerosol samples: Correlations with season and with physical and chemical factors, *Atmospheric Environment*, 49, 224–232, <https://doi.org/10.1016/j.atmosenv.2011.11.056>, 2012.
- Barsanti, K. C. and Pankow, J. F.: Thermodynamics of the formation of atmospheric organic particulate matter by accretion reactions—Part 3: Carboxylic and dicarboxylic acids, *Atmospheric Environment*, 40, 6676–6686, <https://doi.org/10.1016/j.atmosenv.2006.03.013>, 2006.
- Bateman, A. P., Walser, M. L., Desyaterik, Y., Laskin, J., Laskin, A., and Nizkorodov, S. A.: The effect of solvent on the analysis of secondary organic aerosol using electrospray ionization mass spectrometry, *Environ. Sci. Technol.*, 42, 7341–7346, <https://doi.org/10.1021/es801226w>, 2008.
- Bates, K. H. and Jacob, D. J.: A new model mechanism for atmospheric oxidation of isoprene: global effects on oxidants, nitrogen oxides, organic products, and secondary organic aerosol, *Atmos. Chem. Phys.*, 19, 9613–9640, <https://doi.org/10.5194/acp-19-9613-2019>, 2019.

- Beck, M. and Hoffmann, T.: A detailed MS n study for the molecular identification of a dimer formed from oxidation of pinene, *Atmospheric Environment*, 130, 120–126, <https://doi.org/10.1016/j.atmosenv.2015.09.012>, 2016.
- Bianchi, F., Tröstl, J., Junninen, H., Frege, C., Henne, S., Hoyle, C. R., Molteni, U., Herrmann, E., Adamov, A., Bukowiecki, N., Chen, X., Duplissy, J., Gysel, M., Hutterli, M., Kangasluoma, J., Kontkanen, J., Kürten, A., Manninen, H. E., Münch, S., Peräkylä, O., Petäjä, T., Rondo, L., Williamson, C., Weingartner, E., Curtius, J., Worsnop, D. R., Kulmala, M., Dommen, J., and Baltensperger, U.: New particle formation in the free troposphere: A question of chemistry and timing, *Science (New York, N.Y.)*, 352, 1109–1112, <https://doi.org/10.1126/science.aad5456>, 2016.
- Bondarenko, I., Treiger, B., van Grieken, R., and van Espen, P.: IDAS: a Windows based software package for cluster analysis, *Spectrochimica Acta Part B: Atomic Spectroscopy*, 51, 441–456, [https://doi.org/10.1016/0584-8547\(95\)01448-9](https://doi.org/10.1016/0584-8547(95)01448-9), 1996.
- Boucher, O. and Lohmann, U.: The sulfate-CCN-cloud albedo effect, *Tellus B: Chemical and Physical Meteorology*, 47, 281–300, <https://doi.org/10.3402/tellusb.v47i3.16048>, 1995.
- Bourtsoukidis, E., Behrendt, T., Yañez-Serrano, A. M., Hellén, H., Diamantopoulos, E., Catão, E., Ashworth, K., Pozzer, A., Quesada, C. A., Martins, D. L., Sá, M., Araujo, A., Brito, J., Artaxo, P., Kesselmeier, J., Lelieveld, J., and Williams, J.: Strong sesquiterpene emissions from Amazonian soils, *Nature communications*, 9, 2226, <https://doi.org/10.1038/s41467-018-04658-y>, 2018.
- Bruns, E. A., Krapf, M., Orasche, J., Huang, Y., Zimmermann, R., Drinovec, L., Močnik, G., El-Haddad, I., Slowik, J. G., Dommen, J., Baltensperger, U., and Prévôt, A. S. H.: Characterization of primary and secondary wood combustion products generated under different burner loads, *Atmos. Chem. Phys.*, 15, 2825–2841, <https://doi.org/10.5194/acp-15-2825-2015>, 2015.
- Canagaratna, M. R., Jayne, J. T., Jimenez, J. L., Allan, J. D., Alfarra, M. R., Zhang, Q., Onasch, T. B., Drewnick, F., Coe, H., Middlebrook, A., Delia, A., Williams, L. R., Trimborn, A. M., Northway, M. J., DeCarlo, P. F., Kolb, C. E., Davidovits, P., and Worsnop, D. R.: Chemical and microphysical characterization of ambient aerosols with the aerodyne aerosol mass spectrometer, *Mass spectrometry reviews*, 26, 185–222, <https://doi.org/10.1002/mas.20115>, 2007.
- Carlton, A. G., Wiedinmyer, C., and Kroll, J. H.: A review of Secondary Organic Aerosol (SOA) formation from isoprene, *Atmos. Chem. Phys.*, 9, 4987–5005, <https://doi.org/10.5194/acp-9-4987-2009>, 2009.
- Cash, J. M., Heal, M. R., Langford, B., and Drewer, J.: A review of stereochemical implications in the generation of secondary organic aerosol from isoprene oxidation, *Environmental science. Processes & impacts*, 18, 1369–1380, <https://doi.org/10.1039/c6em00354k>, 2016.
- Cech, N. B. and Enke, C. G.: Practical implications of some recent studies in electrospray ionization fundamentals, *Mass spectrometry reviews*, 20, 362–387, <https://doi.org/10.1002/mas.10008>, 2001.
- Chan, A. W. H., Kautzman, K. E., Chhabra, P. S., Surratt, J. D., Chan, M. N., Crouse, J. D., Kürten, A., Wennberg, P. O., Flagan, R. C., and Seinfeld, J. H.: Secondary organic aerosol formation from photooxidation of naphthalene and alkylnaphthalenes: implications for oxidation of intermediate volatility organic compounds (IVOCs), *Atmos. Chem. Phys.*, 9, 3049–3060, <https://doi.org/10.5194/acp-9-3049-2009>, 2009.
- Chen, J. and Griffin, R.: Modeling secondary organic aerosol formation from oxidation of α -pinene, β -pinene, and γ -limonene, *Atmospheric Environment*, 39, 7731–7744, <https://doi.org/10.1016/j.atmosenv.2005.05.049>, 2005.
- Chen, Y., Takeuchi, M., Nah, T., Xu, L., Canagaratna, M. R., Stark, H., Baumann, K., Canonaco, F., Prévôt, A. S. H., Huey, L. G., Weber, R. J., and Ng, N. L.: Chemical characterization of secondary organic aerosol at a rural site in the southeastern US: insights from simultaneous high-resolution time-of-flight aerosol mass spectrometer (HR-ToF-AMS) and FIGAERO chemical ionization mass spectrometer (CIMS) measurements, *Atmos. Chem. Phys.*, 20, 8421–8440, <https://doi.org/10.5194/acp-20-8421-2020>, 2020.

- Chhabra, P. S., Lambe, A. T., Canagaratna, M. R., Stark, H., Jayne, J. T., Onasch, T. B., Davidovits, P., Kimmel, J. R., and Worsnop, D. R.: Application of high-resolution time-of-flight chemical ionization mass spectrometry measurements to estimate volatility distributions of α -pinene and naphthalene oxidation products, *Atmos. Meas. Tech.*, 8, 1–18, <https://doi.org/10.5194/amt-8-1-2015>, 2015.
- Chor, T. L., Dias, N. L., Araújo, A., Wolff, S., Zahn, E., Manzi, A., Trebs, I., Sá, M. O., Teixeira, P. R., and Sörgel, M.: Flux-variance and flux-gradient relationships in the roughness sublayer over the Amazon forest, *Agricultural and Forest Meteorology*, 239, 213–222, <https://doi.org/10.1016/j.agrformet.2017.03.009>, 2017.
- Christoffersen, T.S., Hjorth, J., Horie, O., Jensen, N.R., Kotzias, D., Molander, L.L., Neeb, P., Ruppert, L., Winterhalter, R., Virkkula, A., Wirtz, K., and Larsen, B.R.: cis-pinic acid, a possible precursor for organic aerosol formation from ozonolysis of α -pinene, *Atmospheric Environment*, 32, 1657–1661, [https://doi.org/10.1016/S1352-2310\(97\)00448-2](https://doi.org/10.1016/S1352-2310(97)00448-2), 1998.
- Chung, S. H.: Global distribution and climate forcing of carbonaceous aerosols, *J. Geophys. Res.*, 107, 13,791, <https://doi.org/10.1029/2001JD001397>, 2002.
- Claeys, M., Kourtchev, I., Pashynska, V., Vas, G., Vermeylen, R., Wang, W., Cafmeyer, J., Chi, X., Artaxo, P., Andreae, M. O., and Maenhaut, W.: Polar organic marker compounds in atmospheric aerosols during the LBA-SMOCC 2002 biomass burning experiment in Rondônia, Brazil: sources and source processes, time series, diel variations and size distributions, *Atmos. Chem. Phys.*, 10, 9319–9331, <https://doi.org/10.5194/acp-10-9319-2010>, 2010.
- Claeys, M., Vermeylen, R., Yasmeen, F., Gómez-González, Y., Chi, X., Maenhaut, W., Mészáros, T., and Salma, I.: Chemical characterisation of humic-like substances from urban, rural and tropical biomass burning environments using liquid chromatography with UV/vis photodiode array detection and electrospray ionisation mass spectrometry, *Environ. Chem.*, 9, 273, <https://doi.org/10.1071/EN11163>, 2012.
- Claeys, M., Iinuma, Y., Szmigielski, R., Surratt, J. D., Blockhuys, F., van Alsenoy, C., Böge, O., Sierau, B., Gómez-González, Y., Vermeylen, R., van der Veken, P., Shahgholi, M., Chan, A. W. H., Herrmann, H., Seinfeld, J. H., and Maenhaut, W.: Terpenylic acid and related compounds from the oxidation of alpha-pinene: implications for new particle formation and growth above forests, *Environ. Sci. Technol.*, 43, 6976–6982, <https://doi.org/10.1021/es9007596>, 2009.
- Claeys, M., Szmigielski, R., Kourtchev, I., van der Veken, P., Vermeylen, R., Maenhaut, W., Jaoui, M., Kleindienst, T. E., Lewandowski, M., Offenberg, J. H., and Edney, E. O.: Hydroxydicarboxylic acids: markers for secondary organic aerosol from the photooxidation of alpha-pinene, *Environ. Sci. Technol.*, 41, 1628–1634, <https://doi.org/10.1021/es0620181>, 2007.
- Claeys, M., Wang, W., Ion, A. C., Kourtchev, I., Gelencsér, A., and Maenhaut, W.: Formation of secondary organic aerosols from isoprene and its gas-phase oxidation products through reaction with hydrogen peroxide, *Atmospheric Environment*, 38, 4093–4098, <https://doi.org/10.1016/j.atmosenv.2004.06.001>, 2004a.
- Claeys, M., Graham, B., Vas, G., Wang, W., Vermeylen, R., Pashynska, V., Cafmeyer, J., Guyon, P., Andreae, M. O., Artaxo, P., and Maenhaut, W.: Formation of secondary organic aerosols through photooxidation of isoprene, *Science (New York, N.Y.)*, 303, 1173–1176, <https://doi.org/10.1126/science.1092805>, 2004b.
- Clark, C. H., Nakao, S., Asa-Awuku, A., Sato, K., and Cocker, D. R.: Real-Time Study of Particle-Phase Products from α -Pinene Ozonolysis and Isoprene Photooxidation Using Particle into Liquid Sampling Directly Coupled to a Time-of-Flight Mass Spectrometer (PILS-ToF), *Aerosol Science and Technology*, 47, 1374–1382, <https://doi.org/10.1080/02786826.2013.844333>, 2013.
- Crawford, I., Robinson, N. H., Flynn, M. J., Foot, V. E., Gallagher, M. W., Huffman, J. A., Stanley, W. R., and Kaye, P. H.: Characterisation of bioaerosol emissions from a Colorado pine forest: results from the BEACHON-RoMBAS experiment, *Atmos. Chem. Phys.*, 14, 8559–8578, <https://doi.org/10.5194/acp-14-8559-2014>, 2014.

- Dall'Osto, M., Ceburnis, D., Monahan, C., Worsnop, D. R., Bialek, J., Kulmala, M., Kurtén, T., Ehn, M., Wenger, J., Sodeau, J., Healy, R., and O'Dowd, C.: Nitrogenated and aliphatic organic vapors as possible drivers for marine secondary organic aerosol growth, *J. Geophys. Res.*, 117, n/a-n/a, <https://doi.org/10.1029/2012JD017522>, 2012.
- Daumit, K. E., Kessler, S. H., and Kroll, J. H.: Average chemical properties and potential formation pathways of highly oxidized organic aerosol, *Faraday Discuss.*, 165, 181–202, <https://doi.org/10.1039/c3fd00045a>, 2013.
- Davis, E. M. and Croteau, R.: Cyclization Enzymes in the Biosynthesis of Monoterpenes, Sesquiterpenes, and Diterpenes, in: *Biosynthesis*, edited by: Meijere, A. de, Kessler, H., Ley, S. V., Thiem, J., Vögtle, F., Houk, K. N., Lehn, J.-M., Schreiber, S. L., Trost, B. M., Yamamoto, H., Leeper, F. J., and Vederas, J. C., Springer Berlin Heidelberg, Berlin, Heidelberg, 53–95, https://doi.org/10.1007/3-540-48146-X_2, 2000.
- de Gouw, J. A.: Budget of organic carbon in a polluted atmosphere: Results from the New England Air Quality Study in 2002, *J. Geophys. Res.*, 110, 5745, <https://doi.org/10.1029/2004JD005623>, 2005.
- de Gouw, J. A., Warneke, C., Parrish, D. D., Holloway, J. S., Trainer, M., and Fehsenfeld, F. C.: Emission sources and ocean uptake of acetonitrile (CH₃CN) in the atmosphere, *J. Geophys. Res.*, 108, <https://doi.org/10.1029/2002JD002897>, 2003.
- DeCarlo, P. F., Kimmel, J. R., Trimborn, A., Northway, M. J., Jayne, J. T., Aiken, A. C., Gonin, M., Fuhrer, K., Horvath, T., Docherty, K. S., Worsnop, D. R., and Jimenez, J. L.: Field-deployable, high-resolution, time-of-flight aerosol mass spectrometer, *Anal. Chem.*, 78, 8281–8289, <https://doi.org/10.1021/ac061249n>, 2006.
- Detle, H. P., Qi, M., Schröder, D. C., Godt, A., and Koop, T.: Glass-forming properties of 3-methylbutane-1,2,3-tricarboxylic acid and its mixtures with water and pinonic acid, *The journal of physical chemistry. A*, 118, 7024–7033, <https://doi.org/10.1021/jp505910w>, 2014.
- Dias-Júnior, C. Q., Dias, N. L., Santos, R. M. N., Sörgel, M., Araújo, A., Tsokankunku, A., Ditas, F., Santana, R. A., Randow, C., Sá, M., Pöhlker, C., Toledo Machado, L. A., Sá, L. D., Moran-Zuloaga, D., Janssen, R., Acevedo, O., Oliveira, P., Fisch, G., Chor, T., and Manzi, A.: Is There a Classical Inertial Sublayer Over the Amazon Forest?, *Geophys. Res. Lett.*, 46, 5614–5622, <https://doi.org/10.1029/2019GL083237>, 2019.
- DIN 32645: Deutsches Institut für Normierung e.V.: 2008-11, *Chemische Analytik - Nachweis-, Erfassungs- und Bestimmungsgrenze unter Wiederholbedingungen - Begriffe, Verfahren, Auswertung*, Beuth Verlag GmbH, Berlin, <https://doi.org/10.31030/1465413>.
- Donahue, N. M., Epstein, S. A., Pandis, S. N., and Robinson, A. L.: A two-dimensional volatility basis set: 1. organic-aerosol mixing thermodynamics, *Atmos. Chem. Phys.*, 11, 3303–3318, <https://doi.org/10.5194/acp-11-3303-2011>, 2011.
- Donahue, N. M., Robinson, A. L., Stanier, C. O., and Pandis, S. N.: Coupled partitioning, dilution, and chemical aging of semivolatile organics, *Environ. Sci. Technol.*, 40, 2635–2643, <https://doi.org/10.1021/es052297c>, 2006.
- Dusek, U., Frank, G. P., Hildebrandt, L., Curtius, J., Schneider, J., Walter, S., Chand, D., Drewnick, F., Hings, S., Jung, D., Borrmann, S., and Andreae, M. O.: Size matters more than chemistry for cloud-nucleating ability of aerosol particles, *Science (New York, N.Y.)*, 312, 1375–1378, <https://doi.org/10.1126/science.1125261>, 2006.
- Dzidic, I., Carroll, D. I., Stillwell, R. N., and Horning, E. C.: Comparison of positive ions formed in nickel-63 and corona discharge ion sources using nitrogen, argon, isobutane, ammonia and nitric oxide as reagents in atmospheric pressure ionization mass spectrometry, *Anal. Chem.*, 48, 1763–1768, <https://doi.org/10.1021/ac50006a035>, 1976.
- Eddingsaas, N. C., Loza, C. L., Yee, L. D., Chan, M., Schilling, K. A., Chhabra, P. S., Seinfeld, J. H., and Wennberg, P. O.: α -pinene photooxidation under controlled chemical conditions – Part 2: SOA yield and composition in low- and high-NO_x environments, *Atmos. Chem. Phys.*, 12, 7413–7427, <https://doi.org/10.5194/acp-12-7413-2012>, 2012.

- Edney, E. O., Kleindienst, T. E., Jaoui, M., Lewandowski, M., Offenberg, J. H., Wang, W., and Claeys, M.: Formation of 2-methyl tetrols and 2-methylglyceric acid in secondary organic aerosol from laboratory irradiated isoprene/NOX/SO₂/air mixtures and their detection in ambient PM_{2.5} samples collected in the eastern United States, *Atmospheric Environment*, 39, 5281–5289, <https://doi.org/10.1016/j.atmosenv.2005.05.031>, 2005.
- Ehn, M., Kleist, E., Junninen, H., Petäjä, T., Lönn, G., Schobesberger, S., Dal Maso, M., Trimborn, A., Kulmala, M., Worsnop, D. R., Wahner, A., Wildt, J., and Mentel, T. F.: Gas phase formation of extremely oxidized pinene reaction products in chamber and ambient air, *Atmos. Chem. Phys.*, 12, 5113–5127, <https://doi.org/10.5194/acp-12-5113-2012>, 2012.
- Ehn, M., Thornton, J. A., Kleist, E., Sipila, M., Junninen, H., Pullinen, I., Springer, M., Rubach, F., Tillmann, R., Lee, B., Lopez-Hilfiker, F., Andres, S., Acir, I.-H., Rissanen, M., Jokinen, T., Schobesberger, S., Kangasluoma, J., Kontkanen, J., Nieminen, T., Kurten, T., Nielsen, L. B., Jorgensen, S., Kjaergaard, H. G., Canagaratna, M., Maso, M. D., Berndt, T., Petaja, T., Wahner, A., Kerminen, V.-M., Kulmala, M., Worsnop, D. R., Wildt, J., and Mentel, T. F.: A large source of low-volatility secondary organic aerosol, *Nature*, 506, 476–479, <https://doi.org/10.1038/nature13032>, 2014.
- Enomoto, H., Kohata, K., Nakayama, M., Yamaguchi, Y., and Ichimura, K.: 2-C-methyl-D-erythritol is a major carbohydrate in petals of *Phlox subulata* possibly involved in flower development, *Journal of plant physiology*, 161, 977–980, <https://doi.org/10.1016/j.jplph.2004.01.009>, 2004.
- Facchini, M. C., Fuzzi, S., Zappoli, S., Andracchio, A., Gelencsér, A., Kiss, G., Krivácsy, Z., Mészáros, E., Hansson, H.-C., Alsberg, T., and Zebühr, Y.: Partitioning of the organic aerosol component between fog droplets and interstitial air, *J. Geophys. Res.*, 104, 26821–26832, <https://doi.org/10.1029/1999JD900349>, 1999.
- Fall, R. and Monson, R. K.: Isoprene emission rate and intercellular isoprene concentration as influenced by stomatal distribution and conductance, *Plant physiology*, 100, 987–992, <https://doi.org/10.1104/pp.100.2.987>, 1992.
- Farmer, D. K. and Jimenez, J. L.: Real-time atmospheric chemistry field instrumentation, *Analytical chemistry*, 82, 7879–7884, <https://doi.org/10.1021/ac1010603>, 2010.
- Finlayson-Pitts, B. J. and Pitts, J. N.: Overview of the Chemistry of Polluted and Remote Atmospheres, in: *Chemistry of the Upper and Lower Atmosphere*, Elsevier, 1–14, <https://doi.org/10.1016/B978-012257060-5/50003-4>, 2000.
- Forster, P., Ramaswamy, V., Artaxo, P., Berntsen, T., Betts, R., Fahey, D. W., Haywood, J., Lean, J., Lowe, D. C., Myhre, G., Nganga, J., Prinn, R., Raga, G., Schulz, M., van Dorland, R., and Miller, H. L.: Changes in Atmospheric Constituents and in Radiative Forcing Chapter 2. In: *Climate Change 2007: The Physical Science Basis. Contribution of Working Group I to the Fourth Assessment Report of the Intergovernmental Panel on Climate Change* [Solomon, S., D. Qin, M. Manning, Z. Chen, M. Marquis, K.B. Averyt, M. Tignor and H.L. Miller (eds.)], Cambridge University Press, Cambridge, United Kingdom, 1 CD-ROM (12 cm), 2007.
- Fuller, S. J., Zhao, Y., Cliff, S. S., Wexler, A. S., and Kalberer, M.: Direct surface analysis of time-resolved aerosol impactor samples with ultrahigh-resolution mass spectrometry, *Analytical chemistry*, 84, 9858–9864, <https://doi.org/10.1021/ac3020615>, 2012.
- Gershenson, J. and Dudareva, N.: The function of terpene natural products in the natural world, *Nature chemical biology*, 3, 408–414, <https://doi.org/10.1038/nchembio.2007.5>, 2007.
- Goldstein, A. H. and Galbally, I. E.: Known and unknown organic constituents in the Earth's atmosphere, *Environ. Sci. Technol.*, 41, 1514–1521, <https://doi.org/10.1021/es072476p>, 2007.
- Gómez-González, Y., Wang, W., Vermeylen, R., Chi, X., Neiryck, J., Janssens, I. A., Maenhaut, W., and Claeys, M.: Chemical characterisation of atmospheric aerosols during a 2007 summer field campaign at Brasschaat, Belgium: sources and source processes of biogenic secondary organic aerosol, *Atmos. Chem. Phys.*, 12, 125–138, <https://doi.org/10.5194/acp-12-125-2012>, 2012.
- Goulding, M. and Barthelm, R.: *The Smithsonian atlas of the Amazon*, Smithsonian Institution; Combined Academic, Washington, D.C., Chesham, 325 pp., 2003.

- Graedel, T. E. and Crutzen, P. J.: *Chemie der Atmosphäre: Bedeutung für Klima und Umwelt, Spektrum-Lehrbuch*, Spektrum, Akad. Verl., Heidelberg, Berlin, Oxford, 511 pp., 1994.
- Greenberg, J. P., Guenther, A. B., Pétron, G., Wiedinmyer, C., Vega, O., Gatti, L. V., Tota, J., and Fisch, G.: Biogenic VOC emissions from forested Amazonian landscapes, *Global Change Biology*, 10, 651–662, <https://doi.org/10.1111/j.1365-2486.2004.00758.x>, 2004.
- Gross, J. H.: *Mass Spectrometry: A Textbook*, 2. ed., Springer-Verlag Berlin Heidelberg, Berlin, Heidelberg, Online-Ressource, 2011.
- Guenther, A., Karl, T., Harley, P., Wiedinmyer, C., Palmer, P. I., and Geron, C.: Estimates of global terrestrial isoprene emissions using MEGAN (Model of Emissions of Gases and Aerosols from Nature), *Atmos. Chem. Phys.*, 6, 3181–3210, <https://doi.org/10.5194/acp-6-3181-2006>, 2006.
- Guenther, A. B., Jiang, X., Heald, C. L., Sakulyanontvittaya, T., Duhl, T., Emmons, L. K., and Wang, X.: The Model of Emissions of Gases and Aerosols from Nature version 2.1 (MEGAN2.1): an extended and updated framework for modeling biogenic emissions, *Geosci. Model Dev.*, 5, 1471–1492, <https://doi.org/10.5194/gmd-5-1471-2012>, 2012.
- Guenther, A., Hewitt, C. N., Erickson, D., Fall, R., Geron, C., Graedel, T., Harley, P., Klinger, L., Lerdau, M., McKay, W. A., Pierce, T., Scholes, B., Steinbrecher, R., Tallamraju, R., Taylor, J., and Zimmerman, P.: A global model of natural volatile organic compound emissions, *J. Geophys. Res.*, 100, 8873, <https://doi.org/10.1029/94JD02950>, 1995.
- Guenther, A. B., Monson, R. K., and Fall, R.: Isoprene and monoterpene emission rate variability: Observations with eucalyptus and emission rate algorithm development, *J. Geophys. Res.*, 96, 10799, <https://doi.org/10.1029/91JD00960>, 1991.
- Hallquist, M., Wenger, J. C., Baltensperger, U., Rudich, Y., Simpson, D., Claeys, M., Dommen, J., Donahue, N. M., George, C., Goldstein, A. H., Hamilton, J. F., Herrmann, H., Hoffmann, T., Iinuma, Y., Jang, M., Jenkin, M. E., Jimenez, J. L., Kiendler-Scharr, A., Maenhaut, W., McFiggans, G., Mentel, T. F., Monod, A., Prévôt, A. S. H., Seinfeld, J. H., Surratt, J. D., Szmigielski, R., and Wildt, J.: The formation, properties and impact of secondary organic aerosol: current and emerging issues, *Atmos. Chem. Phys.*, 9, 5155–5236, <https://doi.org/10.5194/acp-9-5155-2009>, 2009.
- Hammes, J., Lutz, A., Mentel, T., Faxon, C., and Hallquist, M.: Carboxylic acids from limonene oxidation by ozone and hydroxyl radicals: insights into mechanisms derived using a FIGAERO-CIMS, *Atmos. Chem. Phys.*, 19, 13037–13052, <https://doi.org/10.5194/acp-19-13037-2019>, 2019.
- Harris, D. C.: *Lehrbuch der quantitativen Analyse*, 8. Auflage, Lehrbuch, Springer Spektrum, Berlin, Heidelberg, 955 pp., 2014.
- Haywood, J.: Atmospheric Aerosols and Their Role in Climate Change, in: *Climate Change (Second Edition)*, edited by: Trevor Letcher, Elsevier, 449–463, <https://doi.org/10.1016/B978-0-444-63524-2.00027-0>, 2016.
- Heald, C. L., Jacob, D. J., Park, R. J., Russell, L. M., Huebert, B. J., Seinfeld, J. H., Liao, H., and Weber, R. J.: A large organic aerosol source in the free troposphere missing from current models, *Geophys. Res. Lett.*, 32, n/a-n/a, <https://doi.org/10.1029/2005GL023831>, 2005.
- Hennigan, C. J., Sullivan, A. P., Collett, J. L., and Robinson, A. L.: Levoglucosan stability in biomass burning particles exposed to hydroxyl radicals, *Geophys. Res. Lett.*, 37, n/a-n/a, <https://doi.org/10.1029/2010GL043088>, 2010.
- Henze, D. K., Seinfeld, J. H., Ng, N. L., Kroll, J. H., Fu, T.-M., Jacob, D. J., and Heald, C. L.: Global modeling of secondary organic aerosol formation from aromatic hydrocarbons: high- vs. low-yield pathways, *Atmos. Chem. Phys.*, 8, 2405–2420, <https://doi.org/10.5194/acp-8-2405-2008>, 2008.
- Hinds, W. C.: *Aerosol technology: Properties, behavior, and measurement of airborne particles*, 2nd ed., Wiley, New York, Chichester, 483 pp., 1999.
- Hitzenberger, R.: Surface tension of Rax cloud water and its relation to the concentration of organic material, *J. Geophys. Res.*, 107, 91, <https://doi.org/10.1029/2002JD002506>, 2002.

- Hoffmann, D., Tilgner, A., Iinuma, Y., and Herrmann, H.: Atmospheric stability of levoglucosan: a detailed laboratory and modeling study, *Environ. Sci. Technol.*, 44, 694–699, <https://doi.org/10.1021/es902476f>, 2010.
- Hoffmann, T. and Klockow, D.: Atmosphärenchemie biogener Kohlenwasserstoffe, *Chemie in unserer Zeit*, 32, 182–191, <https://doi.org/10.1002/ciuz.19980320403>, 1998.
- Hoffmann, T., Huang, R.-J., and Kalberer, M.: Atmospheric analytical chemistry, *Analytical chemistry*, 83, 4649–4664, <https://doi.org/10.1021/ac2010718>, 2011.
- Hoffmann, T., Bandur, R., Hoffmann, S., and Warscheid, B.: On-line characterization of gaseous and particulate organic analytes using atmospheric pressure chemical ionization mass spectrometry, *Spectrochimica Acta Part B: Atomic Spectroscopy*, 57, 1635–1647, [https://doi.org/10.1016/S0584-8547\(02\)00111-8](https://doi.org/10.1016/S0584-8547(02)00111-8), 2002.
- Hoorn, C., Wesselingh, F. P., ter Steege, H., Bermudez, M. A., Mora, A., Sevink, J., Sanmartín, I., Sanchez-Meseguer, A., Anderson, C. L., Figueiredo, J. P., Jaramillo, C., Riff, D., Negri, F. R., Hooghiemstra, H., Lundberg, J., Stadler, T., Särkinen, T., and Antonelli, A.: Amazonia through time: Andean uplift, climate change, landscape evolution, and biodiversity, *Science (New York, N.Y.)*, 330, 927–931, <https://doi.org/10.1126/science.1194585>, 2010.
- Horning, E. C., Horning, M. G., Carroll, D. I., Dzidic, I., and Stillwell, R. N.: New picogram detection system based on a mass spectrometer with an external ionization source at atmospheric pressure, *Anal. Chem.*, 45, 936–943, <https://doi.org/10.1021/ac60328a035>, 1973.
- Houghton, R. A., Lawrence, K. T., Hackler, J. L., and Brown, S.: The spatial distribution of forest biomass in the Brazilian Amazon: a comparison of estimates, *Global Change Biology*, 7, 731–746, <https://doi.org/10.1111/j.1365-2486.2001.00426.x>, 2001.
- Hudson, J. G.: Variability of the relationship between particle size and cloud-nucleating ability, *Geophys. Res. Lett.*, 34, 126, <https://doi.org/10.1029/2006GL028850>, 2007.
- Hughey, C. A., Hendrickson, C. L., Rodgers, R. P., Marshall, A. G., and Qian, K.: Kendrick Mass Defect Spectrum: A Compact Visual Analysis for Ultrahigh-Resolution Broadband Mass Spectra, *Anal. Chem.*, 73, 4676–4681, <https://doi.org/10.1021/ac010560w>, 2001.
- Iinuma, Y., Böge, O., Gräfe, R., and Herrmann, H.: Methyl-nitrocatechols: atmospheric tracer compounds for biomass burning secondary organic aerosols, *Environmental science & technology*, 44, 8453–8459, <https://doi.org/10.1021/es102938a>, 2010.
- INPE - Instituto Nacional de Pesquisas Espaciais, 2020: Portal do Monitoramento de Queimadas e Incêndios Florestais, Programa Queimadas, <http://www.inpe.br/queimadas>, last access: 14 December 2020.
- IPCC: Climate change 2014: Synthesis Report: Contribution of Working Groups I, II and III to the Fifth Assessment Report of the Intergovernmental Panel on Climate Change, Pachauri, R. K. and Meyer, L. A. (Eds.), IPCC, Geneva, Switzerland, 151 pp., 2014.
- IPCC: Climate Change 2013: The Physical Science Basis. Contribution of Working Group I to the Fifth Assessment Report of the Intergovernmental Panel on Climate Change., Stocker, T.F., D. Qin, G.-K. Plattner, M. Tignor, S.K. Allen, J. Boschung, A. Nauels, Y. Xia, and V. Bex and P.M. Midgley (Eds.), Cambridge University Press, Cambridge, United Kingdom and New York, NY, USA, 2013.
- Jaoui, M., Szmigielski, R., Nestorowicz, K., Kolodziejczyk, A., Sarang, K., Rudzinski, K. J., Konopka, A., Bulska, E., Lewandowski, M., and Kleindienst, T. E.: Organic Hydroxy Acids as Highly Oxygenated Molecular (HOM) Tracers for Aged Isoprene Aerosol, *Environmental science & technology*, 53, 14516–14527, <https://doi.org/10.1021/acs.est.9b05075>, 2019.
- Jaoui, M., Lewandowski, M., Kleindienst, T. E., Offenberg, J. H., and Edney, E. O.: β -caryophyllinic acid: An atmospheric tracer for β -caryophyllene secondary organic aerosol, *Geophys. Res. Lett.*, 34, <https://doi.org/10.1029/2006GL028827>, 2007.
- Jenkin, M. E.: Modelling the formation and composition of secondary organic aerosol from α - and β -pinene ozonolysis using MCM v3, *Atmos. Chem. Phys.*, 4, 1741–1757, <https://doi.org/10.5194/acp-4-1741-2004>, 2004.

- Jenkin, M. E., Shallcross, D. E., and Harvey, J. N.: Development and application of a possible mechanism for the generation of cis-pinic acid from the ozonolysis of α - and β -pinene, *Atmospheric Environment*, 34, 2837–2850, [https://doi.org/10.1016/S1352-2310\(00\)00087-X](https://doi.org/10.1016/S1352-2310(00)00087-X), 2000.
- Jimenez, J. L., Canagaratna, M. R., Donahue, N. M., Prevot, A. S. H., Zhang, Q., Kroll, J. H., DeCarlo, P. F., Allan, J. D., Coe, H., Ng, N. L., Aiken, A. C., Docherty, K. S., Ulbrich, I. M., Grieshop, A. P., Robinson, A. L., Duplissy, J., Smith, J. D., Wilson, K. R., Lanz, V. A., Hueglin, C., Sun, Y. L., Tian, J., Laaksonen, A., Raatikainen, T., Rautiainen, J., Vaattovaara, P., Ehn, M., Kulmala, M., Tomlinson, J. M., Collins, D. R., Cubison, M. J., Dunlea, E. J., Huffman, J. A., Onasch, T. B., Alfarra, M. R., Williams, P. I., Bower, K., Kondo, Y., Schneider, J., Drewnick, F., Borrmann, S., Weimer, S., Demerjian, K., Salcedo, D., Cottrell, L., Griffin, R., Takami, A., Miyoshi, T., Hatakeyama, S., Shimono, A., Sun, J. Y., Zhang, Y. M., Dzepina, K., Kimmel, J. R., Sueper, D., Jayne, J. T., Herndon, S. C., Trimborn, A. M., Williams, L. R., Wood, E. C., Middlebrook, A. M., Kolb, C. E., Baltensperger, U., and Worsnop, D. R.: Evolution of organic aerosols in the atmosphere, *Science (New York, N.Y.)*, 326, 1525–1529, <https://doi.org/10.1126/science.1180353>, 2009.
- Johnston, M. V. and Kerecman, D. E.: Molecular Characterization of Atmospheric Organic Aerosol by Mass Spectrometry, *Annual review of analytical chemistry (Palo Alto, Calif.)*, 12, 247–274, <https://doi.org/10.1146/annurev-anchem-061516-045135>, 2019.
- Joo, T., Rivera-Rios, J. C., Takeuchi, M., Alvarado, M. J., and Ng, N. L.: Secondary Organic Aerosol Formation from Reaction of 3-Methylfuran with Nitrate Radicals, *ACS Earth Space Chem.*, 3, 922–934, <https://doi.org/10.1021/acsearthspacechem.9b00068>, 2019.
- Jorgenson, J. W.: Capillary liquid chromatography at ultrahigh pressures, *Annual review of analytical chemistry (Palo Alto, Calif.)*, 3, 129–150, <https://doi.org/10.1146/annurev.anchem.1.031207.113014>, 2010.
- Kahnt, A., Vermeylen, R., Iinuma, Y., Safi Shalamzari, M., Maenhaut, W., and Claeys, M.: High-molecular-weight esters in α -pinene ozonolysis secondary organic aerosol: structural characterization and mechanistic proposal for their formation from highly oxygenated molecules, *Atmos. Chem. Phys.*, 18, 8453–8467, <https://doi.org/10.5194/acp-18-8453-2018>, 2018.
- Kahnt, A., Behrouzi, S., Vermeylen, R., Safi Shalamzari, M., Vercauteren, J., Roekens, E., Claeys, M., and Maenhaut, W.: One-year study of nitro-organic compounds and their relation to wood burning in PM10 aerosol from a rural site in Belgium, *Atmospheric Environment*, 81, 561–568, <https://doi.org/10.1016/j.atmosenv.2013.09.041>, 2013.
- Kanakidou, M., Seinfeld, J. H., Pandis, S. N., Barnes, I., Dentener, F. J., Facchini, M. C., van Dingenen, R., Ervens, B., Nenes, A., Nielsen, C. J., Swietlicki, E., Putaud, J. P., Balkanski, Y., Fuzzi, S., Horth, J., Moortgat, G. K., Winterhalter, R., Myhre, C. E. L., Tsigaridis, K., Vignati, E., Stephanou, E. G., and Wilson, J.: Organic aerosol and global climate modelling: a review, *Atmos. Chem. Phys.*, 5, 1053–1123, <https://doi.org/10.5194/acp-5-1053-2005>, 2005.
- Kanakidou, M., Seinfeld, J. H., Pandis, S. N., Barnes, I., Dentener, F. J., Facchini, M. C., van Dingenen, R., Ervens, B., Nenes, A., Nielsen, C. J., Swietlicki, E., Putaud, J. P., Balkanski, Y., Fuzzi, S., Horth, J., Moortgat, G. K., Winterhalter, R., Myhre, C. E. L., Tsigaridis, K., Vignati, E., Stephanou, E. G., and Wilson, J.: Organic aerosol and global climate modelling: A review, *Atmos. Chem. Phys. Discuss.*, 4, 5855–6024, <https://doi.org/10.5194/acpd-4-5855-2004>, 2004.
- Katsumoto, Y., Kubosaki, N., and Miyata, T.: Molecular approach to understand the tacticity effects on the hydrophilicity of poly(N-isopropylacrylamide): solubility of dimer model compounds in water, *The journal of physical chemistry. B*, 114, 13312–13318, <https://doi.org/10.1021/jp107442h>, 2010.
- Kautzman, K. E., Surratt, J. D., Chan, M. N., Chan, A. W. H., Hersey, S. P., Chhabra, P. S., Dalleska, N. F., Wennberg, P. O., Flagan, R. C., and Seinfeld, J. H.: Chemical composition of gas- and aerosol-phase products from the photooxidation of naphthalene, *The journal of physical chemistry. A*, 114, 913–934, <https://doi.org/10.1021/jp908530s>, 2010.

- Kebarle, P. and Verkerk, U. H.: Electrospray: from ions in solution to ions in the gas phase, what we know now, *Mass spectrometry reviews*, 28, 898–917, <https://doi.org/10.1002/mas.20247>, 2009.
- Kendrick, E.: A Mass Scale Based on $CH_2 = 14.0000$ for High Resolution Mass Spectrometry of Organic Compounds, *Anal. Chem.*, 35, 2146–2154, <https://doi.org/10.1021/ac60206a048>, 1963.
- Kesselmeier, J. and Staudt, M.: Biogenic Volatile Organic Compounds (VOC): An Overview on Emission, Physiology and Ecology, *Journal of Atmospheric Chemistry*, 33, 23–88, <https://doi.org/10.1023/A:1006127516791>, 1999.
- Kind, T. and Fiehn, O.: Seven Golden Rules for heuristic filtering of molecular formulas obtained by accurate mass spectrometry, *BMC bioinformatics*, 8, 105, <https://doi.org/10.1186/1471-2105-8-105>, 2007.
- Kirkby, J., Duplissy, J., Sengupta, K., Frege, C., Gordon, H., Williamson, C., Heinritzi, M., Simon, M., Yan, C., Almeida, J., Tröstl, J., Nieminen, T., Ortega, I. K., Wagner, R., Adamov, A., Amorim, A., Bernhammer, A.-K., Bianchi, F., Breitenlechner, M., Brilke, S., Chen, X., Craven, J., Dias, A., Ehrhart, S., Flagan, R. C., Franchin, A., Fuchs, C., Guida, R., Hakala, J., Hoyle, C. R., Jokinen, T., Junninen, H., Kangasluoma, J., Kim, J., Krapf, M., Kürten, A., Laaksonen, A., Lehtipalo, K., Makhmutov, V., Mathot, S., Molteni, U., Onnela, A., Peräkylä, O., Piel, F., Petäjä, T., Praplan, A. P., Pringle, K., Rap, A., Richards, N. A. D., Riipinen, I., Rissanen, M. P., Rondo, L., Sarnela, N., Schobesberger, S., Scott, C. E., Seinfeld, J. H., Sipilä, M., Steiner, G., Stozhkov, Y., Stratmann, F., Tomé, A., Virtanen, A., Vogel, A. L., Wagner, A. C., Wagner, P. E., Weingartner, E., Wimmer, D., Winkler, P. M., Ye, P., Zhang, X., Hansel, A., Dommen, J., Donahue, N. M., Worsnop, D. R., Baltensperger, U., Kulmala, M., Carslaw, K. S., and Curtius, J.: Ion-induced nucleation of pure biogenic particles, *Nature*, 533, 521–526, <https://doi.org/10.1038/nature17953>, 2016.
- Kirk-Davidoff, D.: The Greenhouse Effect, Aerosols, and Climate Change, in: *Green Chemistry*, Elsevier, 211–234, <https://doi.org/10.1016/B978-0-12-809270-5.00009-1>, 2018.
- Kitanovski, Z., Grgić, I., Yasmeen, F., Claeys, M., and Cusak, A.: Development of a liquid chromatographic method based on ultraviolet-visible and electrospray ionization mass spectrometric detection for the identification of nitrocatechols and related tracers in biomass burning atmospheric organic aerosol, *Rapid communications in mass spectrometry RCM*, 26, 793–804, <https://doi.org/10.1002/rcm.6170>, 2012.
- Kleindienst, T. E., Lewandowski, M., Offenberg, J. H., Jaoui, M., and Edney, E. O.: The formation of secondary organic aerosol from the isoprene + OH reaction in the absence of NO_x , *Atmos. Chem. Phys.*, 9, 6541–6558, <https://doi.org/10.5194/acp-9-6541-2009>, 2009.
- Kleindienst, T. E., Jaoui, M., Lewandowski, M., Offenberg, J. H., Lewis, C. W., Bhave, P. V., and Edney, E. O.: Estimates of the contributions of biogenic and anthropogenic hydrocarbons to secondary organic aerosol at a southeastern US location, *Atmospheric Environment*, 41, 8288–8300, <https://doi.org/10.1016/j.atmosenv.2007.06.045>, 2007.
- Köhler, H.: The nucleus in and the growth of hygroscopic droplets, *Trans. Faraday Soc.*, 32, 1152–1161, <https://doi.org/10.1039/TF9363201152>, 1936.
- Konermann, L., Ahadi, E., Rodriguez, A. D., and Vahidi, S.: Unraveling the mechanism of electrospray ionization, *Analytical chemistry*, 85, 2–9, <https://doi.org/10.1021/ac302789c>, 2013.
- Kong, X., Salvador, C. M., Carlsson, S., Pathak, R., Davidsson, K. O., Le Breton, M., Gaita, S. M., Mitra, K., Hallquist, Å. M., Hallquist, M., and Pettersson, J. B. C.: Molecular characterization and optical properties of primary emissions from a residential wood burning boiler, *The Science of the total environment*, 754, 142143, <https://doi.org/10.1016/j.scitotenv.2020.142143>, 2021.
- Kourtchev, I., Godoi, R. H. M., Connors, S., Levine, J. G., Archibald, A., Godoi, A. F. L., Paralovo, S., Barbosa, C. G. G., Souza, R. A. F., Manzi, A. O., Seco, R., Sjostedt, S., Park, J.-H., Guenther, A., Kim, S., Smith, J., Martin, S. T., and Kalberer, M.: Molecular composition of organic aerosols in central Amazonia: An ultra-high resolution mass spectrometry study, *Atmos. Chem. Phys.*, 16, 11899–11913, <https://doi.org/10.5194/acp-16-11899-2016>, 2016.

- Kourtchev, I., Doussin, J.-F., Giorio, C., Mahon, B., Wilson, E. M., Maurin, N., Pangui, E., Venables, D. S., Wenger, J. C., and Kalberer, M.: Molecular composition of fresh and aged secondary organic aerosol from a mixture of biogenic volatile compounds: a high-resolution mass spectrometry study, *Atmos. Chem. Phys.*, 15, 5683–5695, <https://doi.org/10.5194/acp-15-5683-2015>, 2015.
- Kourtchev, I., Fuller, S. J., Giorio, C., Healy, R. M., Wilson, E., O'Connor, I., Wenger, J. C., McLeod, M., Aalto, J., Ruuskanen, T. M., Maenhaut, W., Jones, R., Venables, D. S., Sodeau, J. R., Kulmala, M., and Kalberer, M.: Molecular composition of biogenic secondary organic aerosols using ultrahigh-resolution mass spectrometry: Comparing laboratory and field studies, *Atmos. Chem. Phys.*, 14, 2155–2167, <https://doi.org/10.5194/acp-14-2155-2014>, 2014a.
- Kourtchev, I., O'Connor, I. P., Giorio, C., Fuller, S. J., Kristensen, K., Maenhaut, W., Wenger, J. C., Sodeau, J. R., Glasius, M., and Kalberer, M.: Effects of anthropogenic emissions on the molecular composition of urban organic aerosols: An ultrahigh resolution mass spectrometry study, *Atmospheric Environment*, 89, 525–532, <https://doi.org/10.1016/j.atmosenv.2014.02.051>, 2014b.
- Kourtchev, I., Ruuskanen, T., Maenhaut, W., Kulmala, M., and Claeys, M.: Observation of 2-methyltetrols and related photo-oxidation products of isoprene in boreal forest aerosols from Hyytiälä, Finland, *Atmos. Chem. Phys.*, 5, 2761–2770, <https://doi.org/10.5194/acp-5-2761-2005>, 2005.
- Kourtchev, I., Fuller, S., Aalto, J., Ruuskanen, T. M., McLeod, M. W., Maenhaut, W., Jones, R., Kulmala, M., and Kalberer, M.: Molecular composition of boreal forest aerosol from Hyytiälä, Finland, using ultrahigh resolution mass spectrometry, *Environmental science & technology*, 47, 4069–4079, <https://doi.org/10.1021/es3051636>, 2013.
- Krechmer, J. E., Coggon, M. M., Massoli, P., Nguyen, T. B., Crouse, J. D., Hu, W., Day, D. A., Tyndall, G. S., Henze, D. K., Rivera-Rios, J. C., Nowak, J. B., Kimmel, J. R., Mauldin, R. L., Stark, H., Jayne, J. T., Sipilä, M., Junninen, H., Clair, J. M. S., Zhang, X., Feiner, P. A., Zhang, L., Miller, D. O., Brune, W. H., Keutsch, F. N., Wennberg, P. O., Seinfeld, J. H., Worsnop, D. R., Jimenez, J. L., and Canagaratna, M. R.: Formation of Low Volatility Organic Compounds and Secondary Organic Aerosol from Isoprene Hydroxyhydroperoxide Low-NO Oxidation, *Environmental science & technology*, 49, 10330–10339, <https://doi.org/10.1021/acs.est.5b02031>, 2015.
- Kristensen, K., Cui, T., Zhang, H., Gold, A., Glasius, M., and Surratt, J. D.: Dimers in α -pinene secondary organic aerosol: effect of hydroxyl radical, ozone, relative humidity and aerosol acidity, *Atmos. Chem. Phys.*, 14, 4201–4218, <https://doi.org/10.5194/acp-14-4201-2014>, 2014.
- Kristensen, K., Enggrob, K. L., King, S. M., Worton, D. R., Platt, S. M., Mortensen, R., Rosenoern, T., Surratt, J. D., Bilde, M., Goldstein, A. H., and Glasius, M.: Formation and occurrence of dimer esters of pinene oxidation products in atmospheric aerosols, *Atmos. Chem. Phys.*, 13, 3763–3776, <https://doi.org/10.5194/acp-13-3763-2013>, 2013.
- Kroll, J. H. and Seinfeld, J. H.: Chemistry of secondary organic aerosol: Formation and evolution of low-volatility organics in the atmosphere, *Atmospheric Environment*, 42, 3593–3624, <https://doi.org/10.1016/j.atmosenv.2008.01.003>, 2008.
- Kroll, J. H., Donahue, N. M., Jimenez, J. L., Kessler, S. H., Canagaratna, M. R., Wilson, K. R., Altieri, K. E., Mazzoleni, L. R., Wozniak, A. S., Bluhm, H., Mysak, E. R., Smith, J. D., Kolb, C. E., and Worsnop, D. R.: Carbon oxidation state as a metric for describing the chemistry of atmospheric organic aerosol, *Nature chemistry*, 3, 133–139, <https://doi.org/10.1038/nchem.948>, 2011.
- Kroll, J. H., Ng, N. L., Murphy, S. M., Flagan, R. C., and Seinfeld, J. H.: Secondary Organic Aerosol Formation from Isoprene Photooxidation, *Environ. Sci. Technol.*, 40, 1869–1877, <https://doi.org/10.1021/es0524301>, 2006.
- Kroll, J. H., Ng, N. L., Murphy, S. M., Varutbangkul, V., Flagan, R. C., and Seinfeld, J. H.: Chamber studies of secondary organic aerosol growth by reactive uptake of simple carbonyl compounds, *J. Geophys. Res.*, 110, 909, <https://doi.org/10.1029/2005JD006004>, 2005.

- Kückelmann, U., Warscheid, B., and Hoffmann, T.: On-line characterization of organic aerosols formed from biogenic precursors using atmospheric pressure chemical ionization mass spectrometry, *Anal. Chem.*, 72, 1905–1912, <https://doi.org/10.1021/ac991178a>, 2000.
- Kuhn, U.: Isoprene and monoterpene emissions of Amazônian tree species during the wet season: Direct and indirect investigations on controlling environmental functions, *J. Geophys. Res.*, 107, <https://doi.org/10.1029/2001JD000978>, 2002.
- Kulkarni, P., Baron, P. A., and Willeke, K. (Eds.): *Aerosol Measurement*, John Wiley & Sons, Inc, Hoboken, NJ, USA, 2011.
- Kulmala, M., Kontkanen, J., Junninen, H., Lehtipalo, K., Manninen, H. E., Nieminen, T., Petäjä, T., Sipilä, M., Schobesberger, S., Rantala, P., Franchin, A., Jokinen, T., Järvinen, E., Äijälä, M., Kangasluoma, J., Hakala, J., Aalto, P. P., Paasonen, P., Mikkilä, J., Vanhanen, J., Aalto, J., Hakola, H., Makkonen, U., Ruuskanen, T., Mauldin, R. L., Duplissy, J., Vehkamäki, H., Bäck, J., Kortelainen, A., Riipinen, I., Kurtén, T., Johnston, M. V., Smith, J. N., Ehn, M., Mentel, T. F., Lehtinen, K. E. J., Laaksonen, A., Kerminen, V.-M., and Worsnop, D. R.: Direct observations of atmospheric aerosol nucleation, *Science (New York, N.Y.)*, 339, 943–946, <https://doi.org/10.1126/science.1227385>, 2013.
- Kundu, S., Fisseha, R., Putman, A. L., Rahn, T. A., and Mazzoleni, L. R.: High molecular weight SOA formation during limonene ozonolysis: insights from ultrahigh-resolution FT-ICR mass spectrometry characterization, *Atmos. Chem. Phys.*, 12, 5523–5536, <https://doi.org/10.5194/acp-12-5523-2012>, 2012.
- Larsen, B. R., Di Bella, D., Glasius, M., Winterhalter, R., Jensen, N. R., and Hjorth, J.: Gas-Phase OH Oxidation of Monoterpenes: Gaseous and Particulate Products., *J Atmos Chem*, 38, 231–276, <https://doi.org/10.1023/A:1006487530903>, 2001.
- Laskin, A., Smith, J. S., and Laskin, J.: Molecular characterization of nitrogen-containing organic compounds in biomass burning aerosols using high-resolution mass spectrometry, *Environ. Sci. Technol.*, 43, 3764–3771, <https://doi.org/10.1021/es803456n>, 2009.
- Lelieveld, J., Evans, J. S., Fnais, M., Giannadaki, D., and Pozzer, A.: The contribution of outdoor air pollution sources to premature mortality on a global scale, *Nature*, 525, 367–371, <https://doi.org/10.1038/nature15371>, 2015.
- Li, Y., Pöschl, U., and Shiraiwa, M.: Molecular corridors and parameterizations of volatility in the chemical evolution of organic aerosols, *Atmos. Chem. Phys.*, 16, 3327–3344, <https://doi.org/10.5194/acp-16-3327-2016>, 2016.
- Lin, J. C., Matsui, T., Pielke, R. A., and Kummerow, C.: Effects of biomass-burning-derived aerosols on precipitation and clouds in the Amazon Basin: a satellite-based empirical study, *J. Geophys. Res.*, 111, 32141, <https://doi.org/10.1029/2005JD006884>, 2006.
- Lin, P., Aiona, P. K., Li, Y., Shiraiwa, M., Laskin, J., Nizkorodov, S. A., and Laskin, A.: Molecular Characterization of Brown Carbon in Biomass Burning Aerosol Particles, *Environmental science & technology*, 50, 11815–11824, <https://doi.org/10.1021/acs.est.6b03024>, 2016.
- Lin, P., Rincon, A. G., Kalberer, M., and Yu, J. Z.: Elemental composition of HULIS in the Pearl River Delta Region, China: results inferred from positive and negative electrospray high resolution mass spectrometric data, *Environmental science & technology*, 46, 7454–7462, <https://doi.org/10.1021/es300285d>, 2012.
- Lin, Y.-H., Knipping, E. M., Edgerton, E. S., Shaw, S. L., and Surratt, J. D.: Investigating the influences of SO₂ and NH₃ levels on isoprene-derived secondary organic aerosol formation using conditional sampling approaches, *Atmos. Chem. Phys.*, 13, 8457–8470, <https://doi.org/10.5194/acp-13-8457-2013>, 2013.
- Liu, S. and Liang, X.-Z.: Observed Diurnal Cycle Climatology of Planetary Boundary Layer Height, *Journal of Climate*, 23, 5790–5809, <https://doi.org/10.1175/2010JCLI3552.1>, 2010.
- Lukács, H., Gelencsér, A., Hoffer, A., Kiss, G., Horváth, K., and Hartyáni, Z.: Quantitative assessment of organosulfates in size-segregated rural fine aerosol, *Atmos. Chem. Phys.*, 9, 231–238, <https://doi.org/10.5194/acp-9-231-2009>, 2009.

- Ma, Y., Russell, A. T., and Marston, G.: Mechanisms for the formation of secondary organic aerosol components from the gas-phase ozonolysis of alpha-pinene, *Physical chemistry chemical physics* PCCP, 10, 4294–4312, <https://doi.org/10.1039/b803283a>, 2008.
- Ma, Y., Willcox, T. R., Russell, A. T., and Marston, G.: Pinic and pinonic acid formation in the reaction of ozone with alpha-pinene, *Chemical communications* (Cambridge, England), 1328–1330, <https://doi.org/10.1039/B617130C>, 2007.
- Makarov: Electrostatic axially harmonic orbital trapping: a high-performance technique of mass analysis, *Analytical chemistry*, 72, 1156–1162, <https://doi.org/10.1021/ac991131p>, 2000.
- Marple, V. A. and Olson, B. A.: Sampling and Measurement Using Inertial, Gravitational, Centrifugal, and Thermal Techniques, in: *Aerosol Measurement*, edited by: Kulkarni, P., Baron, P. A., and Willeke, K., John Wiley & Sons, Inc, Hoboken, NJ, USA, 129–151, <https://doi.org/10.1002/9781118001684.ch8>, 2011.
- Marple, V. A., Rubow, K. L., and Behm, S. M.: A Microorifice Uniform Deposit Impactor (MOUDI): Description, Calibration, and Use, *Aerosol Science and Technology*, 14, 434–446, <https://doi.org/10.1080/02786829108959504>, 1991.
- Martin, S. T., Andreae, M. O., Artaxo, P., Baumgardner, D., Chen, Q., Goldstein, A. H., Guenther, A., Heald, C. L., Mayol-Bracero, O. L., McMurry, P. H., Pauliquevis, T., Pöschl, U., Prather, K. A., Roberts, G. C., Saleska, S. R., Silva Dias, M. A., Spracklen, D. V., Swietlicki, E., and Trebs, I.: Sources and properties of Amazonian aerosol particles, *Rev. Geophys.*, 48, 486, <https://doi.org/10.1029/2008RG000280>, 2010.
- Mazzoleni, L. R., Saranjampour, P., Dalbec, M. M., Samburova, V., Hallar, A. G., Zielinska, B., Lowenthal, D. H., and Kohl, S.: Identification of water-soluble organic carbon in non-urban aerosols using ultrahigh-resolution FT-ICR mass spectrometry: organic anions, *Environ. Chem.*, 9, 285, <https://doi.org/10.1071/EN11167>, 2012.
- McGarvey, D. J. and Croteau, R.: Terpenoid metabolism, *The Plant cell*, 7, 1015–1026, <https://doi.org/10.1105/tpc.7.7.1015>, 1995.
- McGregor, K. G. and Anastasio, C.: Chemistry of fog waters in California's Central Valley: 2. Photochemical transformations of amino acids and alkyl amines, *Atmospheric Environment*, 35, 1091–1104, [https://doi.org/10.1016/S1352-2310\(00\)00282-X](https://doi.org/10.1016/S1352-2310(00)00282-X), 2001.
- McMurry, P.: A review of atmospheric aerosol measurements, *Atmospheric Environment*, 34, 1959–1999, [https://doi.org/10.1016/S1352-2310\(99\)00455-0](https://doi.org/10.1016/S1352-2310(99)00455-0), 2000.
- Mentel, T. F., Springer, M., Ehn, M., Kleist, E., Pullinen, I., Kurtén, T., Rissanen, M., Wahner, A., and Wildt, J.: Formation of highly oxidized multifunctional compounds: autoxidation of peroxy radicals formed in the ozonolysis of alkenes – deduced from structure–product relationships, *Atmos. Chem. Phys.*, 15, 6745–6765, <https://doi.org/10.5194/acp-15-6745-2015>, 2015.
- Mettler, M. S., Mushrif, S. H., Paulsen, A. D., Javadekar, A. D., Vlachos, D. G., and Dauenhauer, P. J.: Revealing pyrolysis chemistry for biofuels production: Conversion of cellulose to furans and small oxygenates, *Energy Environ. Sci.*, 5, 5414–5424, <https://doi.org/10.1039/C1EE02743C>, 2012.
- Meyer, V. R.: *Praxis der Hochleistungs-Flüssigchromatographie*, 10., vollständig überarbeitete und erweiterte Auflage, Wiley-VCH Verlag GmbH & Co. KGaA, Weinheim, 382 pp., 2009.
- Milne, P. J. and Zika, R. G.: Amino acid nitrogen in atmospheric aerosols: Occurrence, sources and photochemical modification, *J Atmos Chem*, 16, 361–398, <https://doi.org/10.1007/BF01032631>, 1993.
- Mitchell, R. I. and Pilcher, J. M.: Improved Cascade Impactor for Measuring Aerosol Particle Sizes, *Ind. Eng. Chem.*, 51, 1039–1042, <https://doi.org/10.1021/ie51396a041>, 1959.
- Moglioni, A. G., García-Expósito, E., Aguado, G. P., Parella, T., Branchadell, V., Moltrasio, G. Y., and Ortuño, R. M.: Divergent routes to chiral cyclobutane synthons from (-)-alpha-pinene and their use in the stereoselective synthesis of dehydro amino acids, *The Journal of organic chemistry*, 65, 3934–3940, <https://doi.org/10.1021/jo991773c>, 2000.

- Molteni, U., Bianchi, F., Klein, F., El Haddad, I., Frege, C., Rossi, M. J., Dommen, J., and Baltensperger, U.: Formation of highly oxygenated organic molecules from aromatic compounds, 2016.
- Monks, P. S.: Gas-phase radical chemistry in the troposphere, *Chemical Society reviews*, 34, 376–395, <https://doi.org/10.1039/b307982c>, 2005.
- Monson, R. K. and Fall, R.: Isoprene emission from aspen leaves influence of environment and relation to photosynthesis and photorespiration, *Plant physiology*, 90, 267–274, <https://doi.org/10.1104/pp.90.1.267>, 1989.
- Mopper, K. and Zika, R. G.: Free amino acids in marine rains: evidence for oxidation and potential role in nitrogen cycling, *Nature*, 325, 246–249, <https://doi.org/10.1038/325246a0>, 1987.
- Mori, K.: Stereochemical studies on pheromonal communications, *Proceedings of the Japan Academy. Series B, Physical and biological sciences*, 90, 373–388, <https://doi.org/10.2183/pjab.90.373>, 2014.
- Müller, L., Reinnig, M.-C., Naumann, K. H., Saathoff, H., Mentel, T. F., Donahue, N. M., and Hoffmann, T.: Formation of 3-methyl-1,2,3-butanetricarboxylic acid via gas phase oxidation of pinonic acid – a mass spectrometric study of SOA aging, *Atmos. Chem. Phys.*, 12, 1483–1496, <https://doi.org/10.5194/acp-12-1483-2012>, 2012.
- Müller, L., Reinnig, M.-C., Warnke, J., and Hoffmann, T.: Unambiguous identification of esters as oligomers in secondary organic aerosol formed from cyclohexene and cyclohexene/ α -pinene ozonolysis, *Atmos. Chem. Phys.*, 8, 1423–1433, <https://doi.org/10.5194/acp-8-1423-2008>, 2008.
- Murphy, B. N., Donahue, N. M., Robinson, A. L., and Pandis, S. N.: A naming convention for atmospheric organic aerosol, *Atmos. Chem. Phys.*, 14, 5825–5839, <https://doi.org/10.5194/acp-14-5825-2014>, 2014.
- Mutzel, A., Rodigast, M., Iinuma, Y., B?ge, O., and Herrmann, H.: Monoterpene SOA: Contribution of first-generation oxidation products to formation and chemical composition, *Atmospheric Environment*, 130, 136–144, <https://doi.org/10.1016/j.atmosenv.2015.10.080>, 2016.
- Myers, O. D., Sumner, S. J., Li, S., Barnes, S., and Du, X.: One Step Forward for Reducing False Positive and False Negative Compound Identifications from Mass Spectrometry Metabolomics Data: New Algorithms for Constructing Extracted Ion Chromatograms and Detecting Chromatographic Peaks, *Analytical chemistry*, 89, 8696–8703, <https://doi.org/10.1021/acs.analchem.7b00947>, 2017.
- Nagori, J., Janssen, R. H. H., Fry, J. L., Krol, M., Jimenez, J. L., Hu, W., and Vilà-Guerau de Arellano, J.: Biogenic emissions and land–atmosphere interactions as drivers of the daytime evolution of secondary organic aerosol in the southeastern US, *Atmos. Chem. Phys.*, 19, 701–729, <https://doi.org/10.5194/acp-19-701-2019>, 2019.
- NASA: Global Climate Change: Evidence., National Aeronautics and Space Administration NASA, <https://climate.nasa.gov/evidence/>, last access: 23 June 2020, 2020.
- National Research Council: Radiative Forcing of Climate Change: Expanding the Concept and Addressing Uncertainties, National Academies Press, Washington, D.C., 2005.
- Nguyen, T. B., Roach, P. J., Laskin, J., Laskin, A., and Nizkorodov, S. A.: Effect of humidity on the composition of isoprene photooxidation secondary organic aerosol, *Atmos. Chem. Phys.*, 11, 6931–6944, <https://doi.org/10.5194/acp-11-6931-2011>, 2011.
- Nguyen, T. B., Bateman, A. P., Bones, D. L., Nizkorodov, S. A., Laskin, J., and Laskin, A.: High-resolution mass spectrometry analysis of secondary organic aerosol generated by ozonolysis of isoprene, *Atmospheric Environment*, 44, 1032–1042, <https://doi.org/10.1016/j.atmosenv.2009.12.019>, 2010.
- Nizkorodov, S. A., Laskin, J., and Laskin, A.: Molecular chemistry of organic aerosols through the application of high resolution mass spectrometry, *Physical chemistry chemical physics PCCP*, 13, 3612–3629, <https://doi.org/10.1039/C0CP02032J>, 2011.

- Nolte, C. G., Schauer, J. J., Cass, G. R., and Simoneit, B. R.: Highly polar organic compounds present in wood smoke and in the ambient atmosphere, *Environ. Sci. Technol.*, 35, 1912–1919, <https://doi.org/10.1021/es001420r>, 2001.
- Nozière, B., Kalberer, M., Claeys, M., Allan, J., D'Anna, B., Decesari, S., Finessi, E., Glasius, M., Grgić, I., Hamilton, J. F., Hoffmann, T., Iinuma, Y., Jaoui, M., Kahnt, A., Kampf, C. J., Kourtchev, I., Maenhaut, W., Marsden, N., Saarikoski, S., Schnelle-Kreis, J., Surratt, J. D., Szidat, S., Szmigielski, R., and Wisthaler, A.: The molecular identification of organic compounds in the atmosphere: state of the art and challenges, *Chemical reviews*, 115, 3919–3983, <https://doi.org/10.1021/cr5003485>, 2015.
- Nozière, B., González, N. J.D., Borg-Karlson, A.-K., Pei, Y., Redeby, J. P., Krejci, R., Dommen, J., Prevot, A. S. H., and Anthonsen, T.: Atmospheric chemistry in stereo: A new look at secondary organic aerosols from isoprene, *Geophys. Res. Lett.*, 38, n/a-n/a, <https://doi.org/10.1029/2011GL047323>, 2011.
- Odum, J. R., Hoffmann, T., Bowman, F., Collins, D. R., Flagan, R. C., and Seinfeld, J. H.: Gas/Particle Partitioning and Secondary Organic Aerosol Yields, *Environ. Sci. Technol.*, 30, 2580–2585, <https://doi.org/10.1021/es950943+>, 1996.
- Oliveira, P. H. F., Artaxo, P., Pires, C., Lucca, S. de, Procópio, A., Holben, B., Schafer, J., Cardoso, L. F., Wofsy, S. C., and Rocha, H. R.: The effects of biomass burning aerosols and clouds on the CO₂ flux in Amazonia, *Tellus B: Chemical and Physical Meteorology*, 59, 338–349, <https://doi.org/10.1111/j.1600-0889.2007.00270.x>, 2007.
- Oros, D. R. and Simoneit, B. R.T.: Identification and emission factors of molecular tracers in organic aerosols from biomass burning Part 1. Temperate climate conifers, *Applied Geochemistry*, 16, 1513–1544, [https://doi.org/10.1016/S0883-2927\(01\)00021-X](https://doi.org/10.1016/S0883-2927(01)00021-X), 2001.
- Pandis, S. N., Harley, R. A., Cass, G. R., and Seinfeld, J. H.: Secondary organic aerosol formation and transport, *Atmospheric Environment. Part A. General Topics*, 26, 2269–2282, [https://doi.org/10.1016/0960-1686\(92\)90358-R](https://doi.org/10.1016/0960-1686(92)90358-R), 1992.
- Pandis, S. N., Paulson, S. E., Seinfeld, J. H., and Flagan, R. C.: Aerosol formation in the photooxidation of isoprene and β -pinene, *Atmospheric Environment. Part A. General Topics*, 25, 997–1008, [https://doi.org/10.1016/0960-1686\(91\)90141-S](https://doi.org/10.1016/0960-1686(91)90141-S), 1991.
- Pankow, J. F., Seinfeld, J. H., Asher, W. E., and Erdakos, G. B.: Modeling the formation of secondary organic aerosol. 1. Application of theoretical principles to measurements obtained in the alpha-pinene/, beta-pinene/, sabinene/, delta3-carene/, and cyclohexane/ozone systems, *Environ. Sci. Technol.*, 35, 1164–1172, <https://doi.org/10.1021/es001321d>, 2001.
- Pankow, J. F.: An absorption model of gas/particle partitioning of organic compounds in the atmosphere, *Atmospheric Environment*, 28, 185–188, [https://doi.org/10.1016/1352-2310\(94\)90093-0](https://doi.org/10.1016/1352-2310(94)90093-0), 1994a.
- Pankow, J. F.: An absorption model of the gas/aerosol partitioning involved in the formation of secondary organic aerosol, *Atmospheric Environment*, 28, 189–193, [https://doi.org/10.1016/1352-2310\(94\)90094-9](https://doi.org/10.1016/1352-2310(94)90094-9), 1994b.
- Parshintsev, J., Hartonen, K., and Riekkola, M.-L.: Environmental analysis: Atmospheric samples, in: *Liquid Chromatography*, Elsevier, 769–798, <https://doi.org/10.1016/B978-0-12-805392-8.00024-4>, 2017.
- Paulot, F., Crouse, J. D., Kjaergaard, H. G., Kroll, J. H., Seinfeld, J. H., and Wennberg, P. O.: Isoprene photooxidation: New insights into the production of acids and organic nitrates, *Atmos. Chem. Phys.*, 9, 1479–1501, <https://doi.org/10.5194/acp-9-1479-2009>, 2009a.
- Paulot, F., Crouse, J. D., Kjaergaard, H. G., Kurten, A., St Clair, J. M., Seinfeld, J. H., and Wennberg, P. O.: Unexpected epoxide formation in the gas-phase photooxidation of isoprene, *Science (New York, N.Y.)*, 325, 730–733, <https://doi.org/10.1126/science.1172910>, 2009b.
- Peeters, J., Vereecken, L., and Fantechi, G.: The detailed mechanism of the OH-initiated atmospheric oxidation of α -pinene: a theoretical, *Physical chemistry chemical physics PCCP*, 3, 5489–5504, <https://doi.org/10.1039/b106555f>, 2001.

- Perry, R. H., Cooks, R. G., and Noll, R. J.: Orbitrap mass spectrometry: instrumentation, ion motion and applications, *Mass spectrometry reviews*, 27, 661–699, <https://doi.org/10.1002/mas.20186>, 2008.
- Petters, M. D. and Kreidenweis, S. M.: A single parameter representation of hygroscopic growth and cloud condensation nucleus activity, *Atmos. Chem. Phys.*, 7, 1961–1971, <https://doi.org/10.5194/acp-7-1961-2007>, 2007.
- Phillips, M. A., Wildung, M. R., Williams, D. C., Hyatt, D. C., and Croteau, R.: cDNA isolation, functional expression, and characterization of (+)- α -pinene synthase and (–)- α -pinene synthase from loblolly pine (*Pinus taeda*): Stereocontrol in pinene biosynthesis, *Archives of Biochemistry and Biophysics*, 411, 267–276, [https://doi.org/10.1016/S0003-9861\(02\)00746-4](https://doi.org/10.1016/S0003-9861(02)00746-4), 2003.
- Plewka, A., Gnauk, T., Brüggemann, E., and Herrmann, H.: Biogenic contributions to the chemical composition of airborne particles in a coniferous forest in Germany, *Atmospheric Environment*, 40, 103–115, <https://doi.org/10.1016/j.atmosenv.2005.09.090>, 2006.
- Pluskal, T., Castillo, S., Villar-Briones, A., and Oresic, M.: MZmine 2: modular framework for processing, visualizing, and analyzing mass spectrometry-based molecular profile data, *BMC bioinformatics*, 11, 395, <https://doi.org/10.1186/1471-2105-11-395>, 2010.
- Pöhlker, C., Walter, D., Paulsen, H., Könemann, T., Rodríguez-Caballero, E., Moran-Zuloaga, D., Brito, J., Carbone, S., Degrendele, C., Després, V. R., Ditas, F., Holanda, B. A., Kaiser, J. W., Lammel, G., Lavrič, J. V., Ming, J., Pickersgill, D., Pöhlker, M. L., Praß, M., Löbs, N., Saturno, J., Sörgel, M., Wang, Q., Weber, B., Wolff, S., Artaxo, P., Pöschl, U., and Andreae, M. O.: Land cover and its transformation in the backward trajectory footprint region of the Amazon Tall Tower Observatory, *Atmos. Chem. Phys.*, 19, 8425–8470, <https://doi.org/10.5194/acp-19-8425-2019>, 2019.
- Pope, C. A.: Epidemiology of fine particulate air pollution and human health: biologic mechanisms and who's at risk?, *Environmental health perspectives*, 108 Suppl 4, 713–723, <https://doi.org/10.1289/ehp.108-1637679>, 2000.
- Pöschl, U., Martin, S. T., Sinha, B., Chen, Q., Gunthe, S. S., Huffman, J. A., Borrmann, S., Farmer, D. K., Garland, R. M., Helas, G., Jimenez, J. L., King, S. M., Manzi, A., Mikhailov, E., Pauliquevis, T., Petters, M. D., Prenni, A. J., Roldin, P., Rose, D., Schneider, J., Su, H., Zorn, S. R., Artaxo, P., and Andreae, M. O.: Rainforest aerosols as biogenic nuclei of clouds and precipitation in the Amazon, *Science (New York, N.Y.)*, 329, 1513–1516, <https://doi.org/10.1126/science.1191056>, 2010.
- Pöschl, U.: Atmospheric aerosols: composition, transformation, climate and health effects, *Angewandte Chemie (International ed. in English)*, 44, 7520–7540, <https://doi.org/10.1002/anie.200501122>, 2005.
- Praplan, A. P., Schobesberger, S., Bianchi, F., Rissanen, M. P., Ehn, M., Jokinen, T., Junninen, H., Adamov, A., Amorim, A., Dommen, J., Duplissy, J., Hakala, J., Hansel, A., Heinritzi, M., Kangasluoma, J., Kirkby, J., Krapf, M., Kürten, A., Lehtipalo, K., Riccobono, F., Rondo, L., Sarnela, N., Simon, M., Tomé, A., Tröstl, J., Winkler, P. M., Williamson, C., Ye, P., Curtius, J., Baltensperger, U., Donahue, N. M., Kulmala, M., and Worsnop, D. R.: Elemental composition and clustering behaviour of α -pinene oxidation products for different oxidation conditions, *Atmos. Chem. Phys.*, 15, 4145–4159, <https://doi.org/10.5194/acp-15-4145-2015>, 2015.
- Pratt, K. A. and Prather, K. A.: Mass spectrometry of atmospheric aerosols--recent developments and applications. Part I: Off-line mass spectrometry techniques, *Mass spectrometry reviews*, 31, 1–16, <https://doi.org/10.1002/mas.20322>, 2012a.
- Pratt, K. A. and Prather, K. A.: Mass spectrometry of atmospheric aerosols--recent developments and applications. Part II: On-line mass spectrometry techniques, *Mass spectrometry reviews*, 31, 17–48, <https://doi.org/10.1002/mas.20330>, 2012b.
- Presto, A. A., Hartz, K. E. H., and Donahue, N. M.: Secondary organic aerosol production from terpene ozonolysis. 1. Effect of UV radiation, *Environ. Sci. Technol.*, 39, 7036–7045, <https://doi.org/10.1021/es050174m>, 2005a.

- Presto, A. A., Hartz, K. E. H., and Donahue, N. M.: Secondary organic aerosol production from terpene ozonolysis. 2. Effect of NO_x concentration, *Environ. Sci. Technol.*, 39, 7046–7054, <https://doi.org/10.1021/es050400s>, 2005b.
- Putaud, J.-P., van Dingenen, R., Dell'Acqua, A., Raes, F., Matta, E., Decesari, S., Facchini, M. C., and Fuzzi, S.: Size-segregated aerosol mass closure and chemical composition in Monte Cimone (I) during MINATROC, *Atmos. Chem. Phys.*, 4, 889–902, <https://doi.org/10.5194/acp-4-889-2004>, 2004.
- Putman, A. L., Offenberg, J. H., Fisseha, R., Kundu, S., Rahn, T. A., and Mazzoleni, L. R.: Ultrahigh-resolution FT-ICR mass spectrometry characterization of α -pinene ozonolysis SOA, *Atmospheric Environment*, 46, 164–172, <https://doi.org/10.1016/j.atmosenv.2011.10.003>, 2012.
- Ramanathan, V., Crutzen, P. J., Kiehl, J. T., and Rosenfeld, D.: Aerosols, climate, and the hydrological cycle, *Science (New York, N.Y.)*, 294, 2119–2124, <https://doi.org/10.1126/science.1064034>, 2001.
- Raupach, M. R., Finnigan, J. J., and Brunei, Y.: Coherent eddies and turbulence in vegetation canopies: The mixing-layer analogy, *Boundary-Layer Meteorol.*, 78, 351–382, <https://doi.org/10.1007/BF00120941>, 1996.
- Ravishankara, A. R.: Heterogeneous and Multiphase Chemistry in the Troposphere, *Science (New York, N.Y.)*, 276, 1058–1065, <https://doi.org/10.1126/science.276.5315.1058>, 1997.
- Raynor, P. C., Leith, D., Lee, K. W., and Mukund, R.: Sampling and Analysis Using Filters, in: *Aerosol Measurement*, edited by: Kulkarni, P., Baron, P. A., and Willeke, K., John Wiley & Sons, Inc, Hoboken, NJ, USA, 107–128, <https://doi.org/10.1002/9781118001684.ch7>, 2011.
- Reinhardt, A., Emmenegger, C., Gerrits, B., Panse, C., Dommen, J., Baltensperger, U., Zenobi, R., and Kalberer, M.: Ultrahigh mass resolution and accurate mass measurements as a tool to characterize oligomers in secondary organic aerosols, *Anal. Chem.*, 79, 4074–4082, <https://doi.org/10.1021/ac062425v>, 2007.
- Rincón, A. G., Calvo, A. I., Dietzel, M., and Kalberer, M.: Seasonal differences of urban organic aerosol composition – an ultra-high resolution mass spectrometry study, *Environ. Chem.*, 9, 298, <https://doi.org/10.1071/EN12016>, 2012.
- Robinson, A. L., Donahue, N. M., Shrivastava, M. K., Weitkamp, E. A., Sage, A. M., Grieshop, A. P., Lane, T. E., Pierce, J. R., and Pandis, S. N.: Rethinking organic aerosols: semivolatile emissions and photochemical aging, *Science (New York, N.Y.)*, 315, 1259–1262, <https://doi.org/10.1126/science.1133061>, 2007.
- Robinson, A. L., Subramanian, R., Donahue, N. M., Bernardo-Bricker, A., and Rogge, W. F.: Source apportionment of molecular markers and organic aerosol. 2. Biomass smoke, *Environ. Sci. Technol.*, 40, 7811–7819, <https://doi.org/10.1021/es060782h>, 2006a.
- Robinson, A. L., Subramanian, R., Donahue, N. M., Bernardo-Bricker, A., and Rogge, W. F.: Source apportionment of molecular markers and organic aerosol--1. Polycyclic aromatic hydrocarbons and methodology for data visualization, *Environ. Sci. Technol.*, 40, 7803–7810, <https://doi.org/10.1021/es0510414>, 2006b.
- Robinson, N. H., Allan, J. D., Huffman, J. A., Kaye, P. H., Foot, V. E., and Gallagher, M.: Cluster analysis of WBS single-particle bioaerosol data, *Atmos. Meas. Tech.*, 6, 337–347, <https://doi.org/10.5194/amt-6-337-2013>, 2013.
- Rogge, W. F., Mazurek, M. A., Hildemann, L. M., Cass, G. R., and Simoneit, B. R.T.: Quantification of urban organic aerosols at a molecular level: Identification, abundance and seasonal variation, *Atmospheric Environment. Part A. General Topics*, 27, 1309–1330, [https://doi.org/10.1016/0960-1686\(93\)90257-Y](https://doi.org/10.1016/0960-1686(93)90257-Y), 1993.
- Rolph, G., Stein, A., and Stunder, B.: Real-time Environmental Applications and Display sYstem: READY, *Environmental Modelling & Software*, 95, 210–228, <https://doi.org/10.1016/j.envsoft.2017.06.025>, 2017.

- Rudich, Y., Donahue, N. M., and Mentel, T. F.: Aging of organic aerosol: bridging the gap between laboratory and field studies, *Annual review of physical chemistry*, 58, 321–352, <https://doi.org/10.1146/annurev.physchem.58.032806.104432>, 2007.
- Saatchi, S. S., Houghton, R. A., Dos Santos Alvala, R. C., Soares, J. V., and Yu, Y.: Distribution of aboveground live biomass in the Amazon basin, *Global Change Biology*, 13, 816–837, <https://doi.org/10.1111/j.1365-2486.2007.01323.x>, 2007.
- Samburova, V., Connolly, J., Gyawali, M., Yatavelli, R. L. N., Watts, A. C., Chakrabarty, R. K., Zielinska, B., Moosmüller, H., and Khlystov, A.: Polycyclic aromatic hydrocarbons in biomass-burning emissions and their contribution to light absorption and aerosol toxicity, *The Science of the total environment*, 568, 391–401, <https://doi.org/10.1016/j.scitotenv.2016.06.026>, 2016.
- Satheesh, S. K. and Moorthy, K.: Radiative effects of natural aerosols: A review, *Atmospheric Environment*, 39, 2089–2110, <https://doi.org/10.1016/j.atmosenv.2004.12.029>, 2005.
- Saxena, P. and Hildemann, L. M.: Water-soluble organics in atmospheric particles: A critical review of the literature and application of thermodynamics to identify candidate compounds, *J Atmos Chem*, 24, 57–109, <https://doi.org/10.1007/BF00053823>, 1996.
- Schafer, J. S.: Atmospheric effects on insolation in the Brazilian Amazon: Observed modification of solar radiation by clouds and smoke and derived single scattering albedo of fire aerosols, *J. Geophys. Res.*, 107, 33, <https://doi.org/10.1029/2001JD000428>, 2002.
- Schauer, J. J., Kleeman, M. J., Cass, G. R., and Simoneit, B. R.: Measurement of emissions from air pollution sources. 3. C1-C29 organic compounds from fireplace combustion of wood, *Environ. Sci. Technol.*, 35, 1716–1728, <https://doi.org/10.1021/es001331e>, 2001.
- Schauer, J. J., Rogge, W. F., Hildemann, L. M., Mazurek, M. A., Cass, G. R., and Simoneit, B. R.T.: Source apportionment of airborne particulate matter using organic compounds as tracers, *Atmospheric Environment*, 30, 3837–3855, [https://doi.org/10.1016/1352-2310\(96\)00085-4](https://doi.org/10.1016/1352-2310(96)00085-4), 1996.
- Schmeling, M. and Klockow, D.: Sample collection and preparation for analysis of airborne particulate matter by total reflection X-ray fluorescence spectrometry, *Analytica Chimica Acta*, 346, 121–126, [https://doi.org/10.1016/S0003-2670\(97\)00022-6](https://doi.org/10.1016/S0003-2670(97)00022-6), 1997.
- Schwantes, R. H., Charan, S. M., Bates, K. H., Huang, Y., Nguyen, T. B., Mai, H., Kong, W., Flagan, R. C., and Seinfeld, J. H.: Low-volatility compounds contribute significantly to isoprene secondary organic aerosol (SOA) under high-NO_x conditions, *Atmos. Chem. Phys.*, 19, 7255–7278, <https://doi.org/10.5194/acp-19-7255-2019>, 2019.
- Schwartz, S. E.: The whitehouse effect—Shortwave radiative forcing of climate by anthropogenic aerosols: an overview, *Journal of Aerosol Science*, 27, 359–382, [https://doi.org/10.1016/0021-8502\(95\)00533-1](https://doi.org/10.1016/0021-8502(95)00533-1), 1996.
- Scigelova, M. and Makarov, A.: Orbitrap mass analyzer—overview and applications in proteomics, *Proteomics*, 6 Suppl 2, 16–21, <https://doi.org/10.1002/pmhc.200600528>, 2006.
- Seinfeld, J. H. and Pandis, S. N.: *Atmospheric Chemistry and Physics: From Air Pollution to Climate Change*, 3rd ed., John Wiley & Sons, 944 s, 2016.
- Seinfeld, J. H. and Pankow, J. F.: Organic atmospheric particulate material, *Annual review of physical chemistry*, 54, 121–140, <https://doi.org/10.1146/annurev.physchem.54.011002.103756>, 2003.
- Shiraiwa, M., Berkemeier, T., Schilling-Fahnestock, K. A., Seinfeld, J. H., and Pöschl, U.: Molecular corridors and kinetic regimes in the multiphase chemical evolution of secondary organic aerosol, *Atmos. Chem. Phys.*, 14, 8323–8341, <https://doi.org/10.5194/acp-14-8323-2014>, 2014.
- Shrivastava, M. K., Lipsky, E. M., Stanier, C. O., and Robinson, A. L.: Modeling semivolatile organic aerosol mass emissions from combustion systems, *Environ. Sci. Technol.*, 40, 2671–2677, <https://doi.org/10.1021/es0522231>, 2006.
- Simoneit, B.R.T., Schauer, J. J., Nolte, C. G., Oros, D. R., Elias, V. O., Fraser, M. P., Rogge, W. F., and Cass, G. R.: Levoglucosan, a tracer for cellulose in biomass burning and atmospheric particles, *Atmospheric Environment*, 33, 173–182, [https://doi.org/10.1016/S1352-2310\(98\)00145-9](https://doi.org/10.1016/S1352-2310(98)00145-9), 1999.
- Sindelarova, K., Granier, C., Bouarar, I., Guenther, A., Tilmes, S., Stavrou, T., Müller, J.-F., Kuhn, U., Stefani, P., and Knorr, W.: Global data set of biogenic VOC emissions calculated by the

- MEGAN model over the last 30 years, *Atmos. Chem. Phys.*, 14, 9317–9341, <https://doi.org/10.5194/acp-14-9317-2014>, 2014.
- Skoog, D. A. and Leary, J. J.: *Instrumentelle Analytik*, Springer Berlin Heidelberg, Berlin, Heidelberg, 1996.
- Song, C., Zaveri, R. A., Alexander, M. L., Thornton, J. A., Madronich, S., Ortega, J. V., Zelenyuk, A., Yu, X.-Y., Laskin, A., and Maughan, D. A.: Effect of hydrophobic primary organic aerosols on secondary organic aerosol formation from ozonolysis of α -pinene, *Geophys. Res. Lett.*, 34, 555, <https://doi.org/10.1029/2007GL030720>, 2007.
- Stein, A. F., Draxler, R. R., Rolph, G. D., Stunder, B. J. B., Cohen, M. D., and Ngan, F.: NOAA's HYSPLIT Atmospheric Transport and Dispersion Modeling System, *Bulletin of the American Meteorological Society*, 96, 2059–2077, <https://doi.org/10.1175/BAMS-D-14-00110.1>, 2015.
- Stephanou, E. G. and Stratigaklis, N.: Oxocarboxylic and α,ω -dicarboxylic acids: photooxidation products of biogenic unsaturated fatty acids present in urban aerosols, *Environ. Sci. Technol.*, 27, 1403–1407, <https://doi.org/10.1021/es00044a016>, 1993.
- Sullivan, R. C. and Prather, K. A.: Recent advances in our understanding of atmospheric chemistry and climate made possible by on-line aerosol analysis instrumentation, *Anal. Chem.*, 77, 3861–3885, <https://doi.org/10.1021/ac050716i>, 2005.
- Surratt, J. D., Chan, A. W. H., Eddingsaas, N. C., Chan, M., Loza, C. L., Kwan, A. J., Hersey, S. P., Flagan, R. C., Wennberg, P. O., and Seinfeld, J. H.: Reactive intermediates revealed in secondary organic aerosol formation from isoprene, *Proceedings of the National Academy of Sciences of the United States of America*, 107, 6640–6645, <https://doi.org/10.1073/pnas.0911114107>, 2010.
- Surratt, J. D., Gómez-González, Y., Chan, A. W. H., Vermeylen, R., Shahgholi, M., Kleindienst, T. E., Edney, E. O., Offenberg, J. H., Lewandowski, M., Jaoui, M., Maenhaut, W., Claeys, M., Flagan, R. C., and Seinfeld, J. H.: Organosulfate formation in biogenic secondary organic aerosol, *The journal of physical chemistry. A*, 112, 8345–8378, <https://doi.org/10.1021/jp802310p>, 2008.
- Surratt, J. D., Lewandowski, M., Offenberg, J. H., Jaoui, M., Kleindienst, T. E., Edney, E. O., and Seinfeld, J. H.: Effect of acidity on secondary organic aerosol formation from isoprene, *Environ. Sci. Technol.*, 41, 5363–5369, <https://doi.org/10.1021/es0704176>, 2007a.
- Surratt, J. D., Kroll, J. H., Kleindienst, T. E., Edney, E. O., Claeys, M., Sorooshian, A., Ng, N. L., Offenberg, J. H., Lewandowski, M., Jaoui, M., Flagan, R. C., and Seinfeld, J. H.: Evidence for Organosulfates in Secondary Organic Aerosol, *Environ. Sci. Technol.*, 41, 517–527, <https://doi.org/10.1021/es062081q>, 2007b.
- Surratt, J. D., Murphy, S. M., Kroll, J. H., Ng, N. L., Hildebrandt, L., Sorooshian, A., Szmigielski, R., Vermeylen, R., Maenhaut, W., Claeys, M., Flagan, R. C., and Seinfeld, J. H.: Chemical composition of secondary organic aerosol formed from the photooxidation of isoprene, *The journal of physical chemistry. A*, 110, 9665–9690, <https://doi.org/10.1021/jp061734m>, 2006.
- Szmigielski, R., Surratt, J. D., Gómez-González, Y., van der Veken, P., Kourtchev, I., Vermeylen, R., Blockhuys, F., Jaoui, M., Kleindienst, T. E., Lewandowski, M., Offenberg, J. H., Edney, E. O., Seinfeld, J. H., Maenhaut, W., and Claeys, M.: 3-methyl-1,2,3-butanetricarboxylic acid: An atmospheric tracer for terpene secondary organic aerosol, *Geophys. Res. Lett.*, 34, D16312, <https://doi.org/10.1029/2007GL031338>, 2007.
- Tervahattu, H., Juhanoja, J., and Kupiainen, K.: Identification of an organic coating on marine aerosol particles by TOF-SIMS, *J. Geophys. Res.*, 107, <https://doi.org/10.1029/2001JD001403>, 2002.
- Thermo Fisher Scientific: Thermo Scientific Q Exactive, Benchtop Quadrupole-Orbitrap Mass Spectrometer: Product Specifications, 2011.
- Thorenz, U. R., Kundel, M., Müller, L., and Hoffmann, T.: Generation of standard gas mixtures of halogenated, aliphatic, and aromatic compounds and prediction of the individual output rates based on molecular formula and boiling point, *Analytical and bioanalytical chemistry*, 404, 2177–2183, <https://doi.org/10.1007/s00216-012-6202-5>, 2012.

- Tolocka, M. P., Jang, M., Ginter, J. M., Cox, F. J., Kamens, R. M., and Johnston, M. V.: Formation of Oligomers in Secondary Organic Aerosol, *Environ. Sci. Technol.*, 38, 1428–1434, <https://doi.org/10.1021/es035030r>, 2004.
- Tong, H., Kourchev, I., Pant, P., Keyte, I. J., O'Connor, I. P., Wenger, J. C., Pope, F. D., Harrison, R. M., and Kalberer, M.: Molecular composition of organic aerosols at urban background and road tunnel sites using ultra-high resolution mass spectrometry, *Faraday Discuss.*, 189, 51–68, <https://doi.org/10.1039/c5fd00206k>, 2016.
- Treiger, B., Bondarenko, I., van Malderen, H., and van Grieken, R.: Elucidating the composition of atmospheric aerosols through the combined hierarchical, non-hierarchical and fuzzy clustering of large electron probe microanalysis data sets, *Analytica Chimica Acta*, 317, 33–51, [https://doi.org/10.1016/0003-2670\(95\)00405-X](https://doi.org/10.1016/0003-2670(95)00405-X), 1995.
- Tu, P., Hall, W. A., and Johnston, M. V.: Characterization of Highly Oxidized Molecules in Fresh and Aged Biogenic Secondary Organic Aerosol, *Analytical chemistry*, 88, 4495–4501, <https://doi.org/10.1021/acs.analchem.6b00378>, 2016.
- van Berkel, G. J. and Kertesz, V.: Using the electrochemistry of the electrospray ion source, *Anal. Chem.*, 79, 5510–5520, <https://doi.org/10.1021/ac071944a>, 2007.
- van Eijck, A., Opatz, T., Taraborrelli, D., Sander, R., and Hoffmann, T.: New tracer compounds for secondary organic aerosol formation from β -caryophyllene oxidation, *Atmospheric Environment*, 80, 122–130, <https://doi.org/10.1016/j.atmosenv.2013.07.060>, 2013.
- Vickers, C. E., Gershenzon, J., Lerdau, M. T., and Loreto, F.: A unified mechanism of action for volatile isoprenoids in plant abiotic stress, *Nature chemical biology*, 5, 283–291, <https://doi.org/10.1038/nchembio.158>, 2009.
- Vieira, I. C. G., Toledo, P. M., Silva, J. M. C., and Higuchi, H.: Deforestation and threats to the biodiversity of Amazonia, *Brazilian journal of biology = Revista brasleira de biologia*, 68, 949–956, <https://doi.org/10.1590/s1519-69842008000500004>, 2008.
- Vogel, A. L., Äijälä, M., Brüggemann, M., Ehn, M., Junninen, H., Petäjä, T., Worsnop, D. R., Kulmala, M., Williams, J., and Hoffmann, T.: Online atmospheric pressure chemical ionization ion trap mass spectrometry (APCI-IT-MSⁿ) for measuring organic acids in concentrated bulk aerosol – a laboratory and field study, *Atmos. Meas. Tech.*, 6, 431–443, <https://doi.org/10.5194/amt-6-431-2013>, 2013.
- Volkamer, R., Ziemann, P. J., and Molina, M. J.: Secondary Organic Aerosol Formation from Acetylene (C₂H₂): seed effect on SOA yields due to organic photochemistry in the aerosol aqueous phase, *Atmos. Chem. Phys.*, 9, 1907–1928, <https://doi.org/10.5194/acp-9-1907-2009>, 2009.
- Volkamer, R., Jimenez, J. L., San Martini, F., Dzepina, K., Zhang, Q., Salcedo, D., Molina, L. T., Worsnop, D. R., and Molina, M. J.: Secondary organic aerosol formation from anthropogenic air pollution: Rapid and higher than expected, *Geophys. Res. Lett.*, 33, 4407, <https://doi.org/10.1029/2006GL026899>, 2006.
- Wang, K.-Y. and Shallcross, D.E.: Modelling terrestrial biogenic isoprene fluxes and their potential impact on global chemical species using a coupled LSM–CTM model, *Atmospheric Environment*, 34, 2909–2925, [https://doi.org/10.1016/S1352-2310\(99\)00525-7](https://doi.org/10.1016/S1352-2310(99)00525-7), 2000.
- Wang, X., Hayeck, N., Brüggemann, M., Yao, L., Chen, H., Zhang, C., Emmelin, C., Chen, J., George, C., and Wang, L.: Chemical Characteristics of Organic Aerosols in Shanghai: A Study by Ultrahigh-Performance Liquid Chromatography Coupled With Orbitrap Mass Spectrometry, *J. Geophys. Res.*, 122, 11,703–11,722, <https://doi.org/10.1002/2017JD026930>, 2017.
- Wang, X., Piao, S., Ciais, P., Friedlingstein, P., Myneni, R. B., Cox, P., Heimann, M., Miller, J., Peng, S., Wang, T., Yang, H., and Chen, A.: A two-fold increase of carbon cycle sensitivity to tropical temperature variations, *Nature*, 506, 212–215, <https://doi.org/10.1038/nature12915>, 2014.
- Warneck, P.: Chemistry of the natural atmosphere, 2nd ed., This is volume 71 in the International geophysics series, Academic Press, San Diego, 927 pp., 2000.
- Wennberg, P. O., Bates, K. H., Crounse, J. D., Dodson, L. G., McVay, R. C., Mertens, L. A., Nguyen, T. B., Praske, E., Schwantes, R. H., Smarte, M. D., St Clair, J. M., Teng, A. P., Zhang, X., and

- Seinfeld, J. H.: Gas-Phase Reactions of Isoprene and Its Major Oxidation Products, *Chemical reviews*, 118, 3337–3390, <https://doi.org/10.1021/acs.chemrev.7b00439>, 2018.
- Went, F. W.: Blue Hazes in the Atmosphere, *Nature*, 187, 641–643, <https://doi.org/10.1038/187641a0>, 1960.
- Wex, H., Stratmann, F., Topping, D., and McFiggans, G.: The Kelvin versus the Raoult Term in the Köhler Equation, *Journal of the Atmospheric Sciences*, 65, 4004–4016, <https://doi.org/10.1175/2008JAS2720.1>, 2008.
- Whitby, K. T.: The physical characteristics of sulfur aerosols, *Atmospheric Environment (1967)*, 12, 135–159, [https://doi.org/10.1016/0004-6981\(78\)90196-8](https://doi.org/10.1016/0004-6981(78)90196-8), 1978.
- Williams, C. A., Scanlon, T. M., and Albertson, J. D.: Influence of surface heterogeneity on scalar dissimilarity in the roughness sublayer, *Boundary-Layer Meteorol*, 122, 149–165, <https://doi.org/10.1007/s10546-006-9097-x>, 2007.
- Williams, J., Reus, M. de, Krejci, R., Fischer, H., and Ström, J.: Application of the variability-size relationship to atmospheric aerosol studies: estimating aerosol lifetimes and ages, *Atmos. Chem. Phys.*, 2, 133–145, <https://doi.org/10.5194/acp-2-133-2002>, 2002.
- Wittmann, F., Householder, E., Piedade, M. T. F., Assis, R. L. de, Schöngart, J., Parolin, P., and Junk, W. J.: Habitat specificity, endemism and the neotropical distribution of Amazonian white-water floodplain trees, *Ecography*, 36, 690–707, <https://doi.org/10.1111/j.1600-0587.2012.07723.x>, 2013.
- Worton, D. R., Surratt, J. D., Lafranchi, B. W., Chan, A. W. H., Zhao, Y., Weber, R. J., Park, J.-H., Gilman, J. B., Gouw, J. de, Park, C., Schade, G., Beaver, M., Clair, J. M. S., Crouse, J., Wennberg, P., Wolfe, G. M., Harrold, S., Thornton, J. A., Farmer, D. K., Docherty, K. S., Cubison, M. J., Jimenez, J.-L., Frossard, A. A., Russell, L. M., Kristensen, K., Glasius, M., Mao, J., Ren, X., Brune, W., Browne, E. C., Pusede, S. E., Cohen, R. C., Seinfeld, J. H., and Goldstein, A. H.: Observational insights into aerosol formation from isoprene, *Environmental science & technology*, 47, 11403–11413, <https://doi.org/10.1021/es4011064>, 2013.
- Wozniak, A. S., Bauer, J. E., Sleighter, R. L., Dickhut, R. M., and Hatcher, P. G.: Technical Note: Molecular characterization of aerosol-derived water soluble organic carbon using ultrahigh resolution electrospray ionization Fourier transform ion cyclotron resonance mass spectrometry, *Atmos. Chem. Phys.*, 8, 5099–5111, <https://doi.org/10.5194/acp-8-5099-2008>, 2008.
- Yáñez-Serrano, A. M., Nölscher, A. C., Williams, J., Wolff, S., Alves, E., Martins, G. A., Bourtsoukidis, E., Brito, J., Jardine, K., Artaxo, P., and Kesselmeier, J.: Diel and seasonal changes of biogenic volatile organic compounds within and above an Amazonian rainforest, *Atmos. Chem. Phys.*, 15, 3359–3378, <https://doi.org/10.5194/acp-15-3359-2015>, 2015.
- Yáñez-Serrano, A. M., Nölscher, A. C., Bourtsoukidis, E., Gomes Alves, E., Ganzeveld, L., Bonn, B., Wolff, S., Sa, M., Yamasoe, M., Williams, J., Andreae, M. O., and Kesselmeier, J.: Monoterpene chemical speciation in a tropical rainforest: variation with season, height, and time of day at the Amazon Tall Tower Observatory (ATTO), *Atmos. Chem. Phys.*, 18, 3403–3418, <https://doi.org/10.5194/acp-18-3403-2018>, 2018.
- Yasmeen, F., Vermeylen, R., Szmigielski, R., Iinuma, Y., Böge, O., Herrmann, H., Maenhaut, W., and Claeys, M.: Terpenylic acid and related compounds: precursors for dimers in secondary organic aerosol from the ozonolysis of α - and β -pinene, *Atmos. Chem. Phys.*, 10, 9383–9392, <https://doi.org/10.5194/acp-10-9383-2010>, 2010.
- Yasmeen, F., Szmigielski, R., Vermeylen, R., Gómez-González, Y., Surratt, J. D., Chan, A. W. H., Seinfeld, J. H., Maenhaut, W., and Claeys, M.: Mass spectrometric characterization of isomeric terpenoic acids from the oxidation of α -pinene, β -pinene, d-limonene, and Δ^3 -carene in fine forest aerosol, *Journal of mass spectrometry JMS*, 46, 425–442, <https://doi.org/10.1002/jms.1911>, 2011.
- Yassine, M. M., Harir, M., Dabek-Zlotorzynska, E., and Schmitt-Kopplin, P.: Structural characterization of organic aerosol using Fourier transform ion cyclotron resonance mass spectrometry: aromaticity equivalent approach, *Rapid communications in mass spectrometry RCM*, 28, 2445–2454, <https://doi.org/10.1002/rcm.7038>, 2014.

- Zannoni, N., Leppla, D., Lembo Silveira de Assis, P. I., Hoffmann, T., Sá, M., Araújo, A., and Williams, J.: Surprising chiral composition changes over the Amazon rainforest with height, time and season, *Commun. Earth Environ. (Communications Earth & Environment)*, 1, 9317, <https://doi.org/10.1038/s43247-020-0007-9>, 2020.
- Zeri, M., Sá, L. D. A., Manzi, A. O., Araújo, A. C., Aguiar, R. G., Randow, C. von, Sampaio, G., Cardoso, F. L., and Nobre, C. A.: Variability of carbon and water fluxes following climate extremes over a tropical forest in southwestern Amazonia, *PloS one*, 9, e88130, <https://doi.org/10.1371/journal.pone.0088130>, 2014.
- Zhang, Q., Jimenez, J. L., Canagaratna, M. R., Allan, J. D., Coe, H., Ulbrich, I., Alfarra, M. R., Takami, A., Middlebrook, A. M., Sun, Y. L., Dzepina, K., Dunlea, E., Docherty, K., DeCarlo, P. F., Salcedo, D., Onasch, T., Jayne, J. T., Miyoshi, T., Shimojo, A., Hatakeyama, S., Takegawa, N., Kondo, Y., Schneider, J., Drewnick, F., Borrmann, S., Weimer, S., Demerjian, K., Williams, P., Bower, K., Bahreini, R., Cottrell, L., Griffin, R. J., Rautiainen, J., Sun, J. Y., Zhang, Y. M., and Worsnop, D. R.: Ubiquity and dominance of oxygenated species in organic aerosols in anthropogenically-influenced Northern Hemisphere midlatitudes, *Geophys. Res. Lett.*, 34, n/a-n/a, <https://doi.org/10.1029/2007GL029979>, 2007.
- Zhang, Y. J., Tang, L. L., Wang, Z., Yu, H. X., Sun, Y. L., Liu, D., Qin, W., Canonaco, F., Prévôt, A. S. H., Zhang, H. L., and Zhou, H. C.: Insights into characteristics, sources, and evolution of submicron aerosols during harvest seasons in the Yangtze River delta region, China, *Atmos. Chem. Phys.*, 15, 1331–1349, <https://doi.org/10.5194/acp-15-1331-2015>, 2015.
- Zhang, Y. Y., Müller, L., Winterhalter, R., Moortgat, G. K., Hoffmann, T., and Pöschl, U.: Seasonal cycle and temperature dependence of pinene oxidation products, dicarboxylic acids and nitrophenols in fine and coarse air particulate matter, *Atmos. Chem. Phys.*, 10, 7859–7873, <https://doi.org/10.5194/acp-10-7859-2010>, 2010.
- Zhao, D. F., Kaminski, M., Schlag, P., Fuchs, H., Acir, I.-H., Bohn, B., Häseler, R., Kiendler-Scharr, A., Rohrer, F., Tillmann, R., Wang, M. J., Wegener, R., Wildt, J., Wahner, A., and Mentel, T. F.: Secondary organic aerosol formation from hydroxyl radical oxidation and ozonolysis of monoterpenes, *Atmos. Chem. Phys.*, 15, 991–1012, <https://doi.org/10.5194/acp-15-991-2015>, 2015.
- Zubarev, R. A. and Makarov, A.: Orbitrap mass spectrometry, *Analytical chemistry*, 85, 5288–5296, <https://doi.org/10.1021/ac4001223>, 2013.

6 Appendix

The following sections contain supplementary figures and tables with information about meteorological data, additional measurements, and comprehensive lists with all detected ions from the MS analysis of SOA filter samples from the ATTO station.

6.1 Supporting Information to Chapter 2

Table S1: Values of n_C^0 and b according to the compound class to calculate C_0 . The parameterization is obtained from the detailed study by Li et al. (2016).

Compound class	n_C^0	b_C	b_O	b_{CO}	b_N	b_S
CHO	22.66	0.4481	1.656	-0.7790		
CHON	24.13	0.3667	0.7732	-0.0779	1.114	
CHOS	24.06	0.3637	1.327	-0.3988		0.7579
CHONS	28.50	0.3848	1.011	0.2921	1.053	1.3160

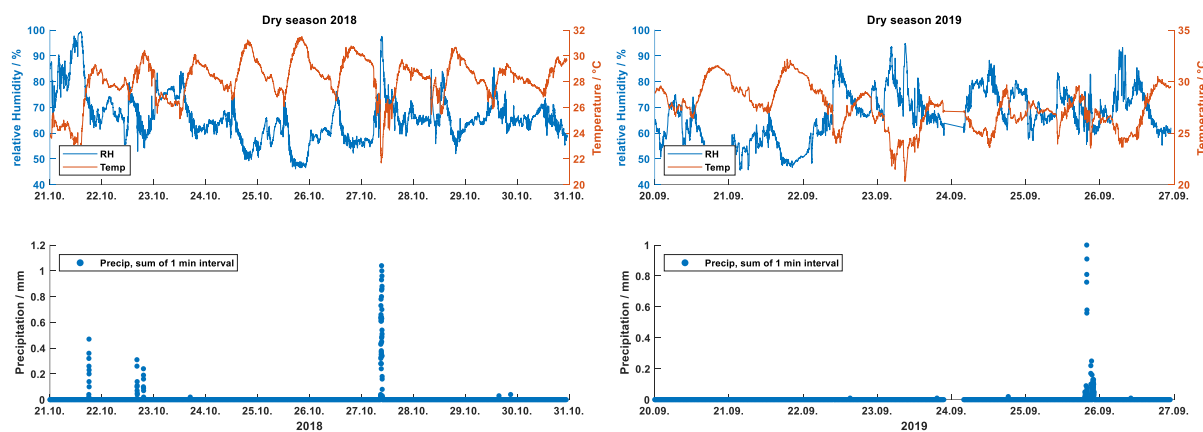


Figure S1: The upper panel illustrates the relative humidity and temperature at ATTO for the dry season 2018 (left) and the dry season 2019 (right), respectively. The lower panel shows the precipitation as a sum of 1 min intervals. The instrument was located at 325 m.

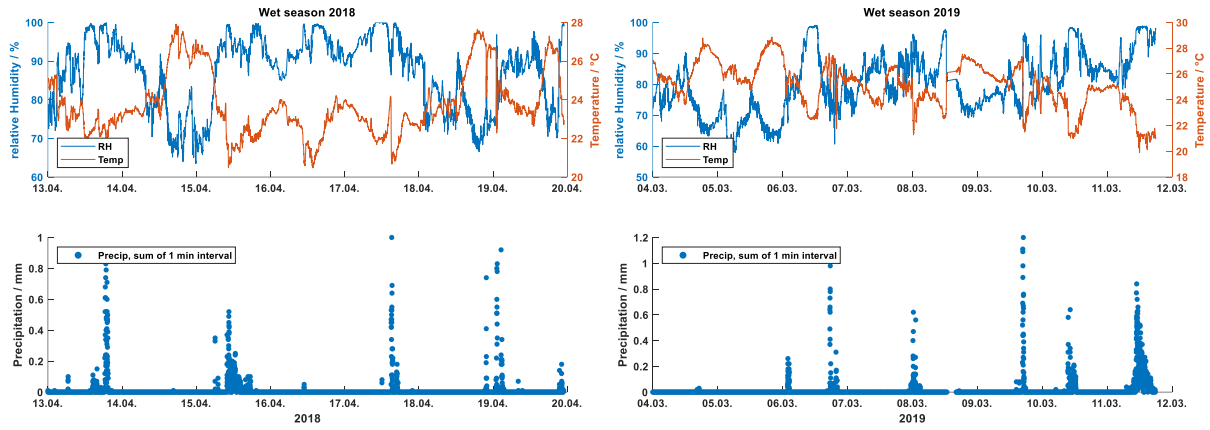


Figure S2: The upper panel illustrates the relative humidity and temperature at ATTO for the wet season 2018 (left) and the wet season 2019 (right), respectively. The lower panel shows the precipitation as a sum of 1 min intervals. The instrument was located at 325 m.

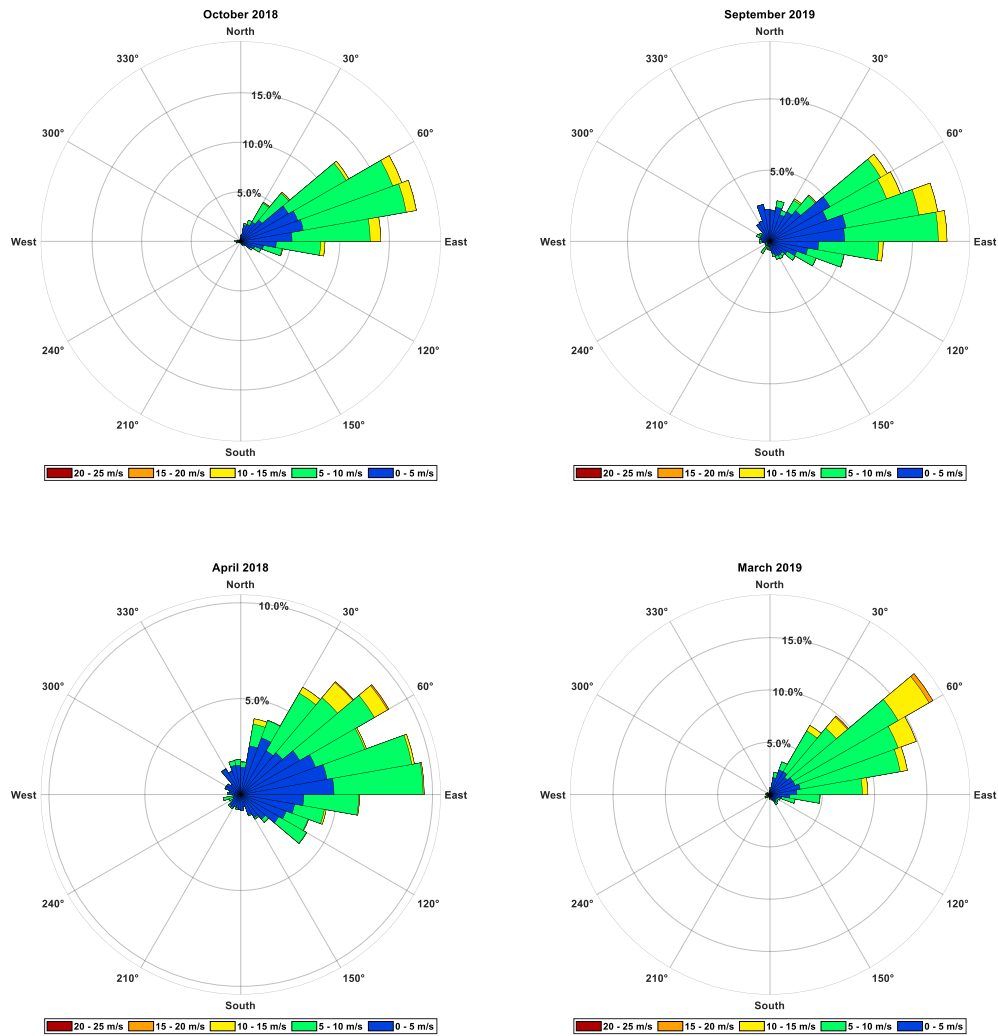


Figure S3: Wind roses for the sampling period during the dry seasons in October 2018 September 2019 (upper part) and during the wet seasons in April 2018 and March 2019 (lower part).

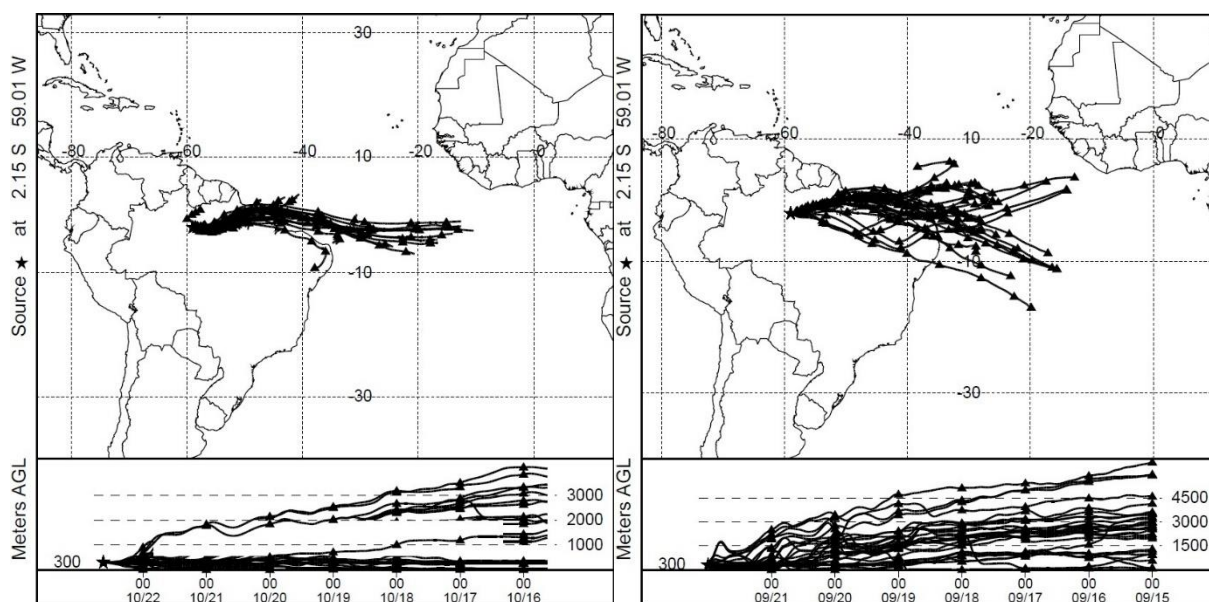


Figure S4: The 7 d HYSPLIT backward trajectory ensembles starting at 300 m above ground level for the dry season 2018 (left) and dry season 2019 (right) (Stein et al., 2015).

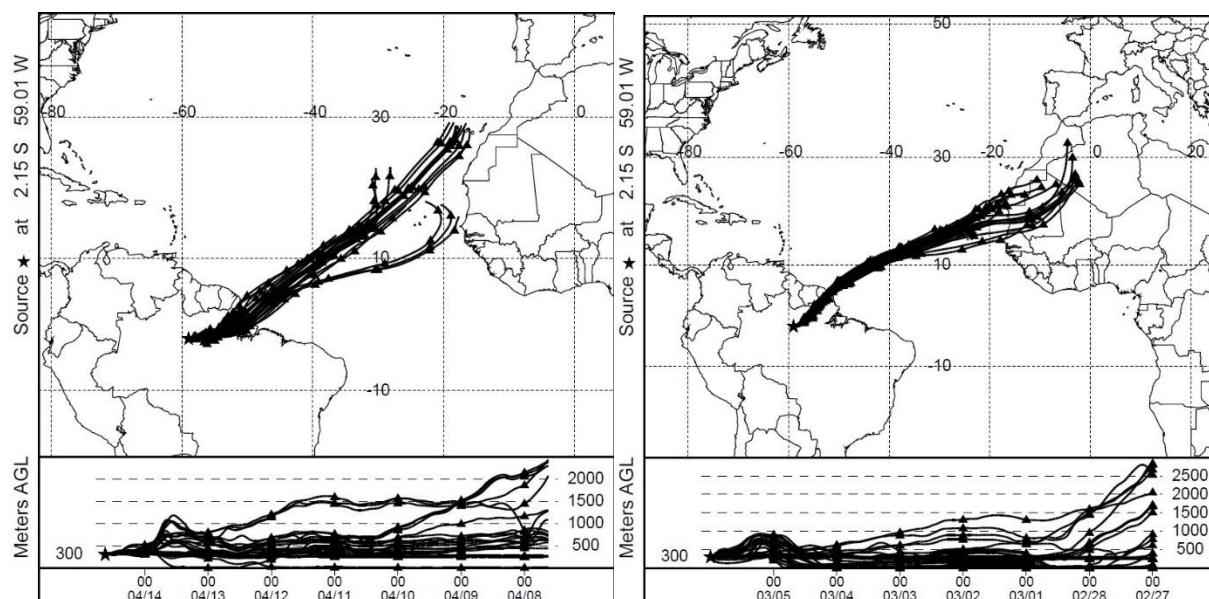


Figure S5: The 7 d HYSPLIT backward trajectory ensembles starting at 300 m above ground level for the wet season 2018 (left) and the wet season 2019 (right) (Stein et al., 2015).

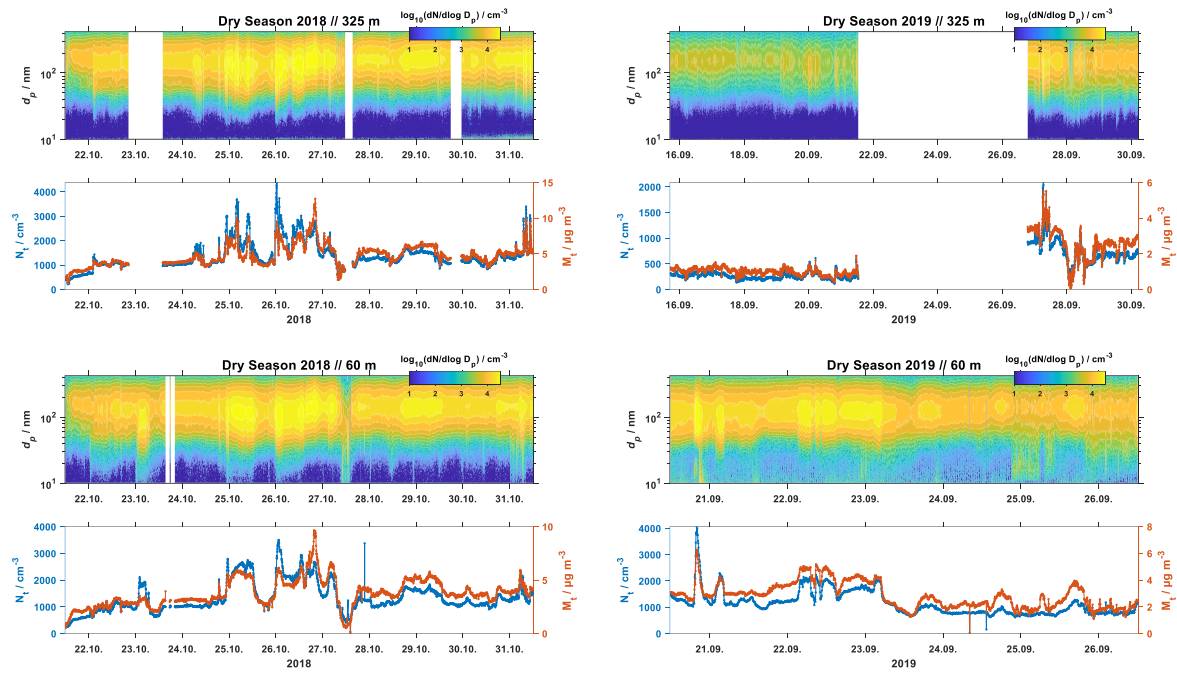


Figure S6: SMPS data for the dry season 2018 and 2019 at 60 m and 325 m altitude. The calculated total particle numbers and total particle masses are illustrated in the lower panels, respectively. The instruments did not work during the 23., 27., and 30.10.2018 and during the 21.09.2019 and 27.09.2019. Thus, a longer period is displayed.

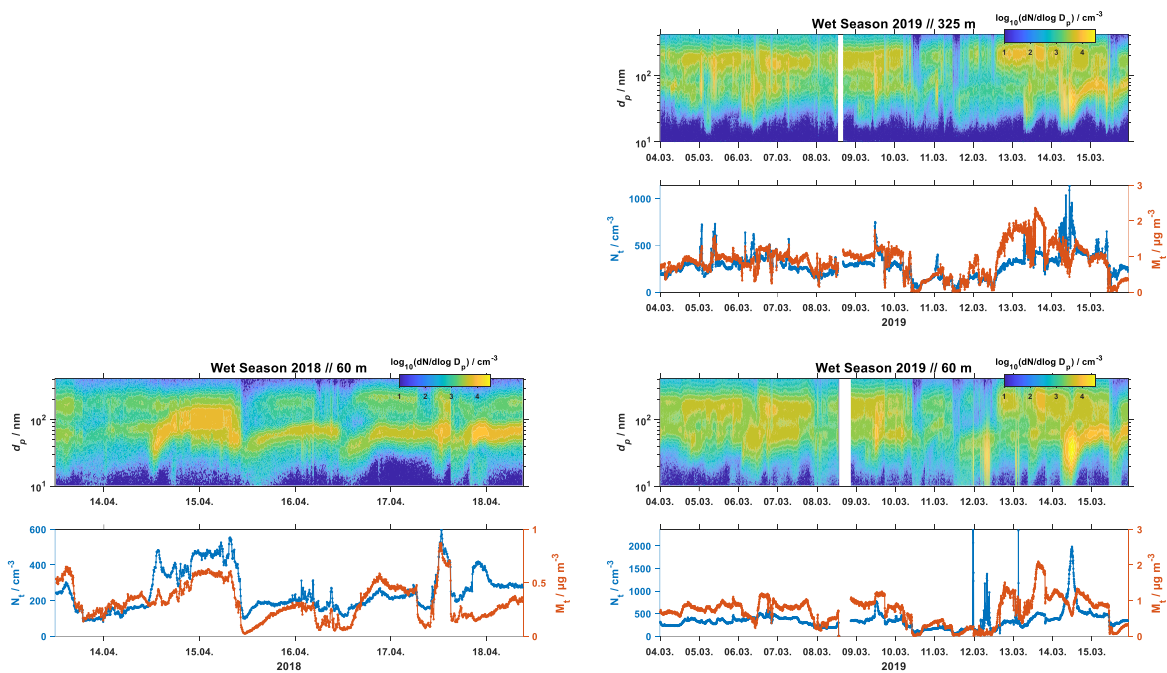


Figure S7: SMPS data for the wet season 2018 and 2019 at 60 m and 325 m altitude. The calculated total particle numbers and total particle masses are illustrated in the lower panels, respectively. No data were collected at 325 m during the wet season 2018.

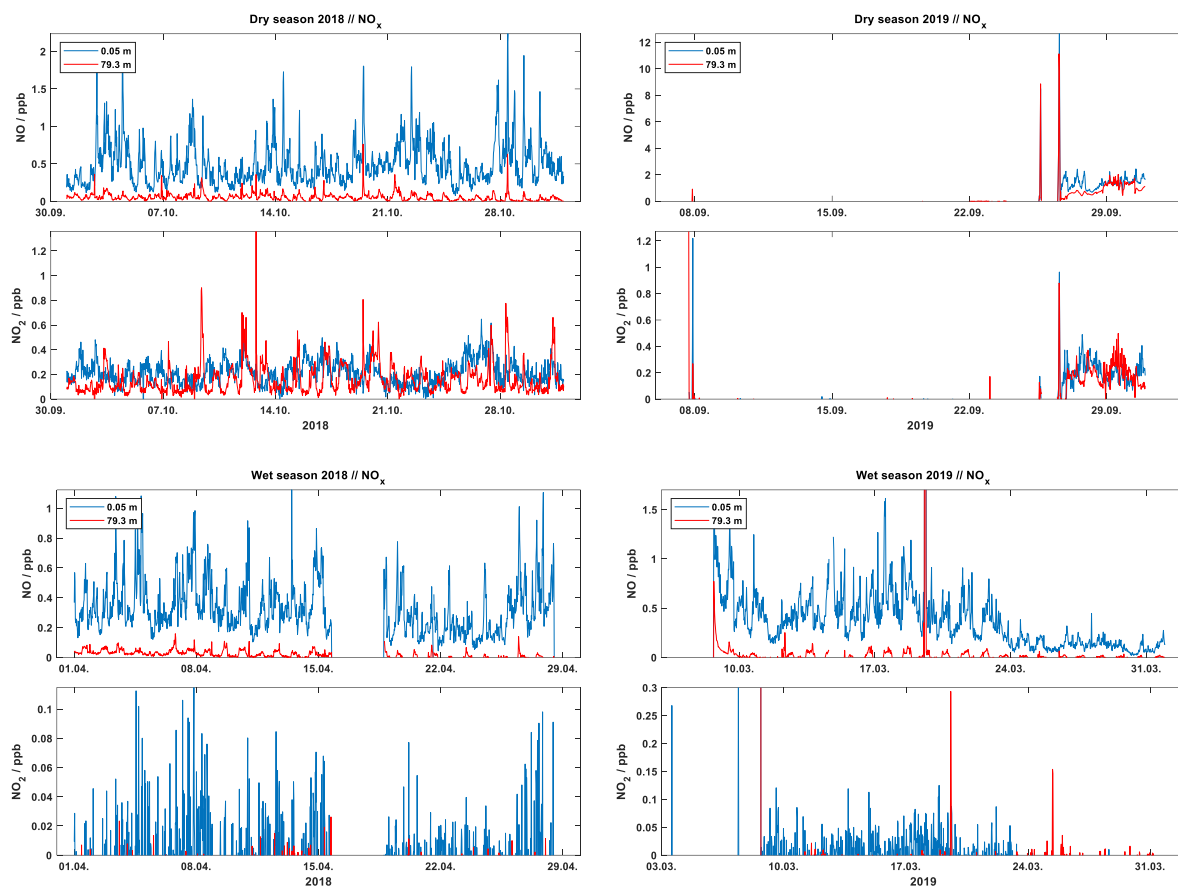


Figure S8: NO and NO₂ concentrations at 0.05 m and 79.3 m height during the dry seasons 2018 and 2019 (upper part). The instrument was malfunctioning during the dry season 2019 resulting in few datapoints. The NO_x concentration for the wet seasons 2018 and 2019 are illustrated in the lower part.

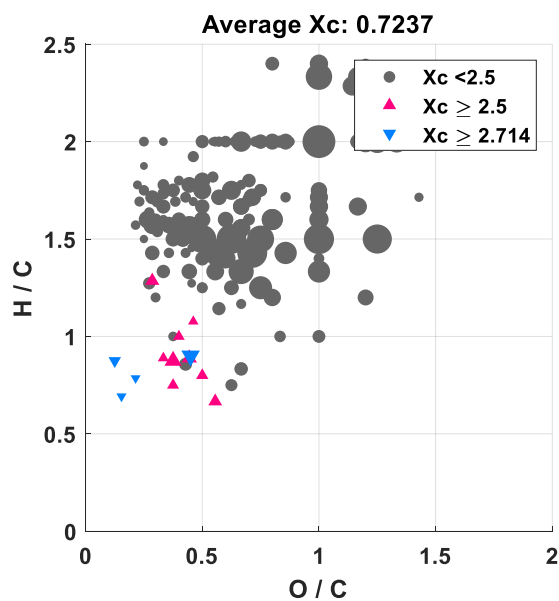


Figure S9: Van Krevelen diagram illustrating the chemical background ions during the dry season 2018 at 80 m height. According to Yassine et al. (2014), all compounds were classified by the aromaticity equivalent X_c, highlighting unsaturated mono- and polycyclic structures.

Table S2: Number of active fires each month in the Amazon region since 1998 until 2020. The sampling periods are highlighted in yellow. Data retrieved by INPE - Instituto Nacional de Pesquisas Espaciais, 2020 (Portal do Monitoramento de Queimadas e Incêndios Florestais, <http://www.inpe.br/queimadas>).

Year	Jan	Feb	Mar	Apr	May	Jun	Jul	Aug	Sep	Oct	Nov	Dec
1998	-	-	-	-	-	1549	3192	20075	19214	8777	3833	2547
1999	160	358	130	70	449	1439	3675	21525	16106	12794	4449	1703
2000	87	182	405	92	930	3211	1510	12791	10062	10226	5497	3175
2001	165	699	1134	617	916	4227	1816	17679	15528	14292	8346	4256
2002	590	667	901	405	1490	5702	7529	43484	48549	27110	23660	9174
2003	3704	1573	1997	1038	1983	6848	15918	34765	47789	25341	19631	13813
2004	2178	805	1035	1012	3131	9179	19179	43320	71522	23928	26424	16924
2005	4314	1048	758	832	1746	2954	19364	63764	68560	26624	16790	6966
2006	1973	879	903	709	843	2522	6995	34208	51028	18309	17474	8579
2007	1918	1761	1431	760	1176	3519	6196	46385	73141	28731	16025	5437
2008	938	527	860	569	383	1248	5901	21445	26469	23518	15450	6145
2009	1095	354	584	435	673	1023	2327	9732	20527	19323	19104	6505
2010	1697	1147	1176	633	1026	1911	5868	45018	43933	14798	12167	5240
2011	771	271	427	465	528	1083	2445	8002	16987	9760	9815	7632
2012	1203	438	484	473	855	1875	3095	20687	24067	14814	13259	5469
2013	1181	374	738	518	796	1450	2531	9444	16786	10242	6615	8013
2014	1573	473	1010	632	673	1628	2766	20113	20522	13222	12169	7773
2015	2042	1047	572	762	407	1287	2817	20471	29326	19469	16935	11303
2016	4657	1559	2024	1075	895	1663	6120	18340	20460	14234	11610	5124
2017	796	379	736	618	805	1759	7986	21244	36569	14457	14105	7985
2018	1444	888	1359	513	772	1980	4788	10421	24803	10654	8881	1842
2019	1419	1368	3383	1702	854	1880	5318	30900	19925	7855	11297	3275
2020	1200	1196	1641	789	829	2248	6803	29307	32017	17326	6321	2498

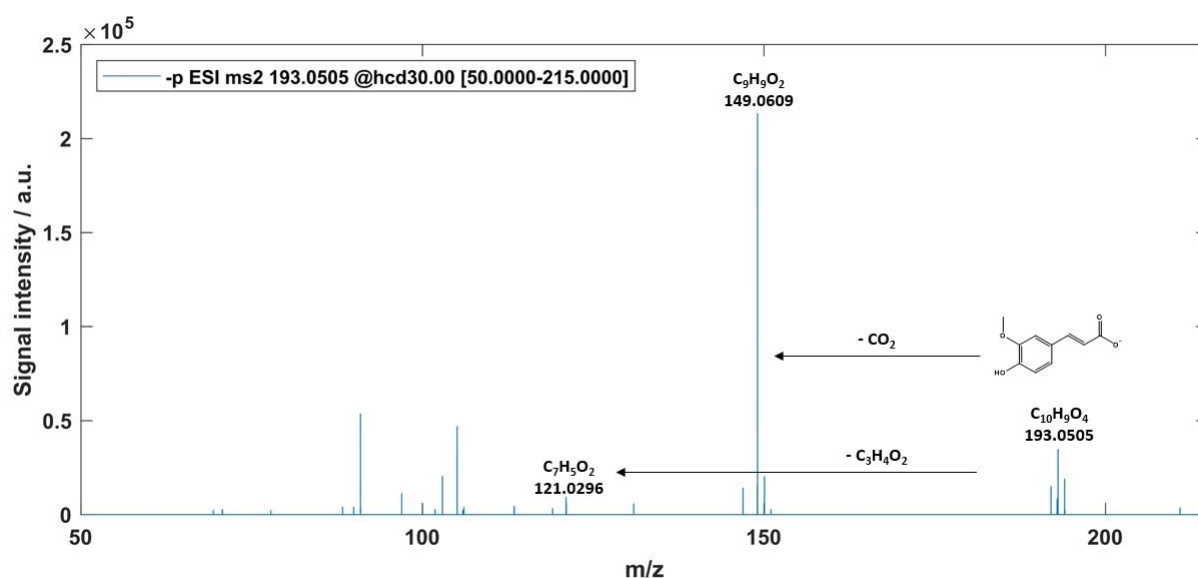


Figure S10: MS² of the background aromatic species with the molecular formula $C_{10}H_{10}O_4$ (m/z 193.0505) during the dry season 2018. Presumably, the detected ion might be ferulic acid according to the characteristic losses of carbon dioxide and acrylic acid.

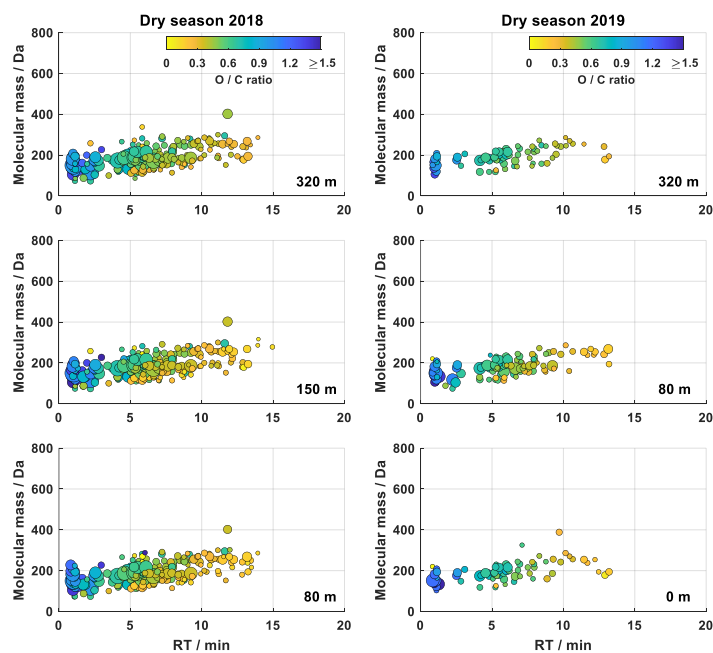


Figure S11: Background formulae for the dry season 2018 (left) and dry season 2019 (right) according to their retention time. Highly oxygenated and polar compounds are highlighted in blue color, which illustrates the need to improve the LC separation.

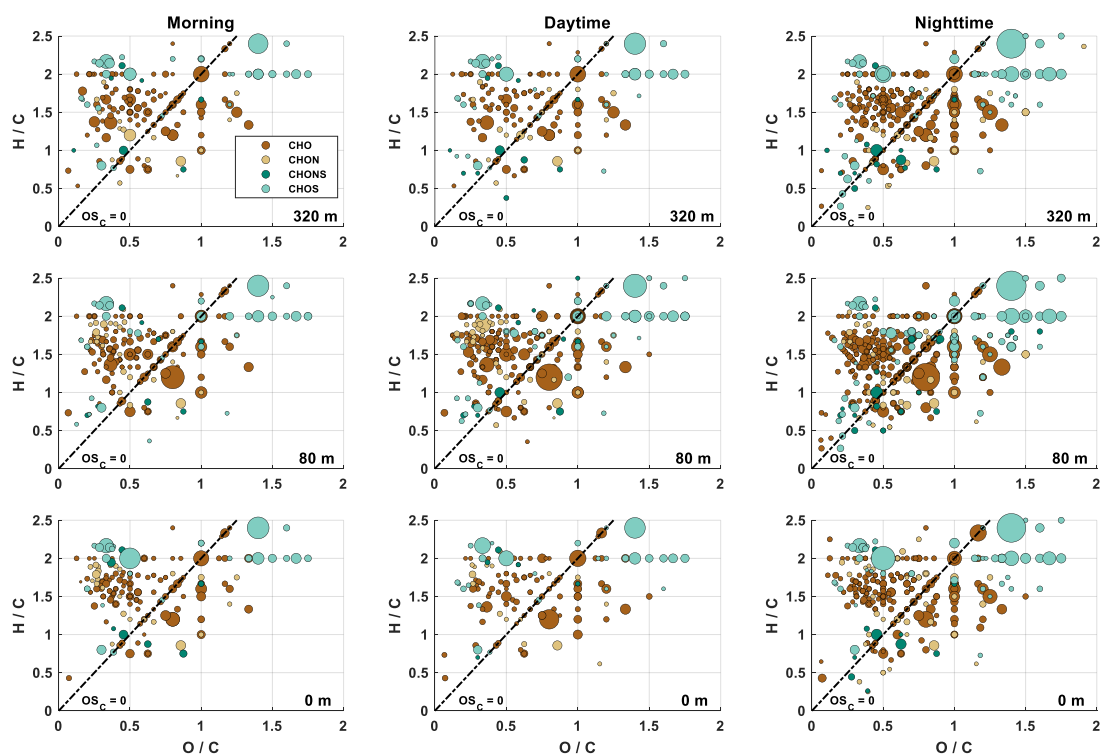


Figure S12: Van Krevelen plots from the dry season 2019 during the morning (left panel), daytime (middle panel), and nighttime (right panel). Included are only molecular formulae that were present in more than one of the samples, respectively. The background signals are subtracted. The size of the data points represents the signal intensity of the corresponding peak. The four subgroups are distinguished with different colors. Compounds located on the black dashed line have an average carbon oxidation state of 0 ($OS_C = 0$).

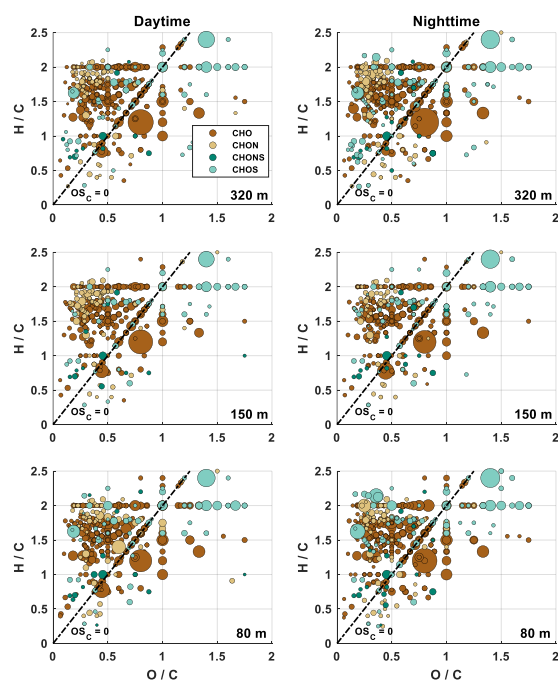


Figure S13: Van Krevelen plots from the wet season 2019 during daytime (left panel) and nighttime (right panel). Included are only molecular formulae that were present in more than one of the samples, respectively. The background signals are subtracted. The size of the data points represents the signal intensity of the corresponding peak. The four subgroups are distinguished with different colors. Compounds located on the black dashed line have an average carbon oxidation state of 0 ($OS_C = 0$).

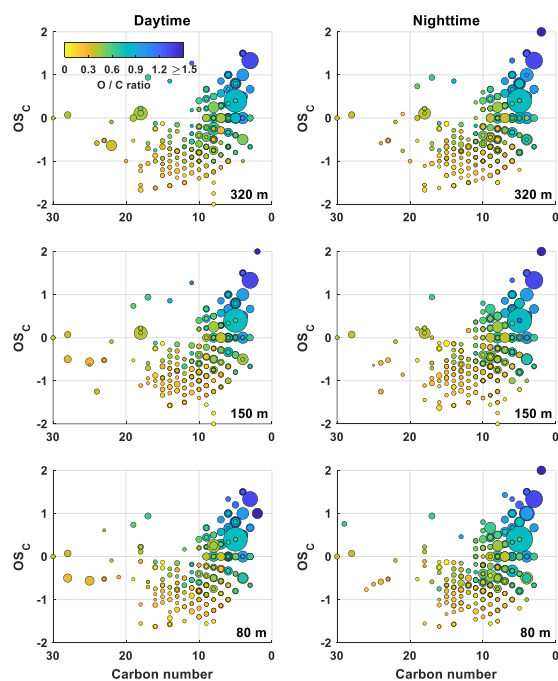


Figure S14: Carbon oxidation state (OS_C) plots for all detected CHO species during the dry season 2018 at daytime (left) and nighttime (right). Included are only molecular formulae that were present in more than one of the samples, respectively. The background signals are subtracted. The size of the data points represents the signal intensity of the corresponding peak. The color code illustrates the degree of oxygenation.

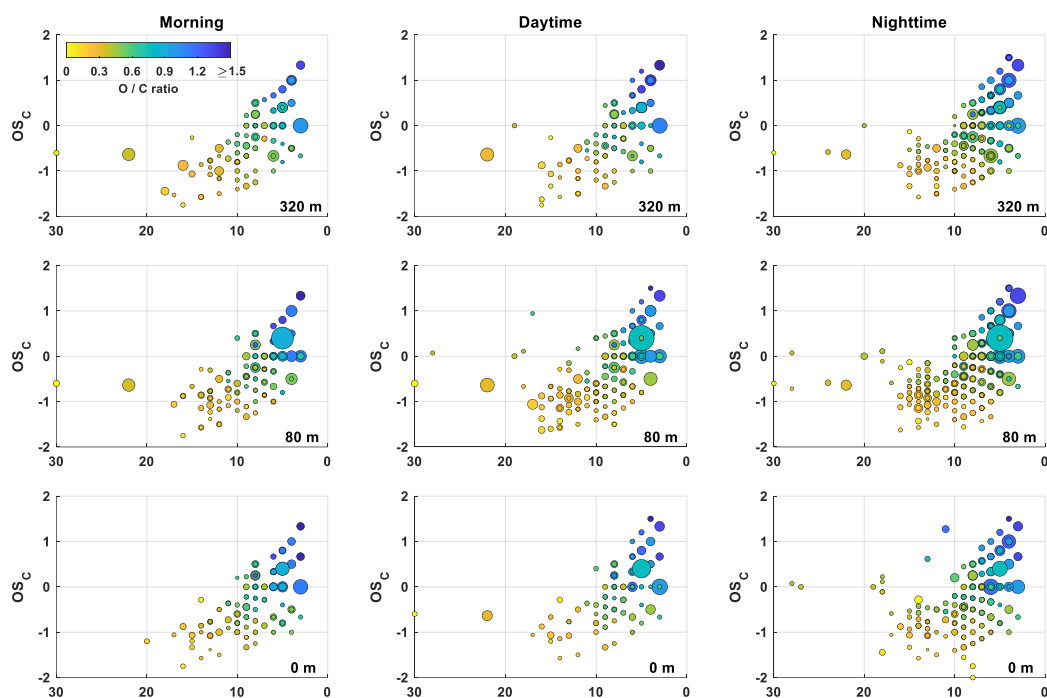


Figure S15: Carbon oxidation state (OS_C) plots for all detected CHO species during the dry season 2019 at morning (left), daytime (middle), and nighttime (right). Included are only molecular formulae that were present in more than one of the samples, respectively. The background signals are subtracted. The size of the data points represents the signal intensity of the corresponding peak. The color code illustrates the degree of oxygenation.

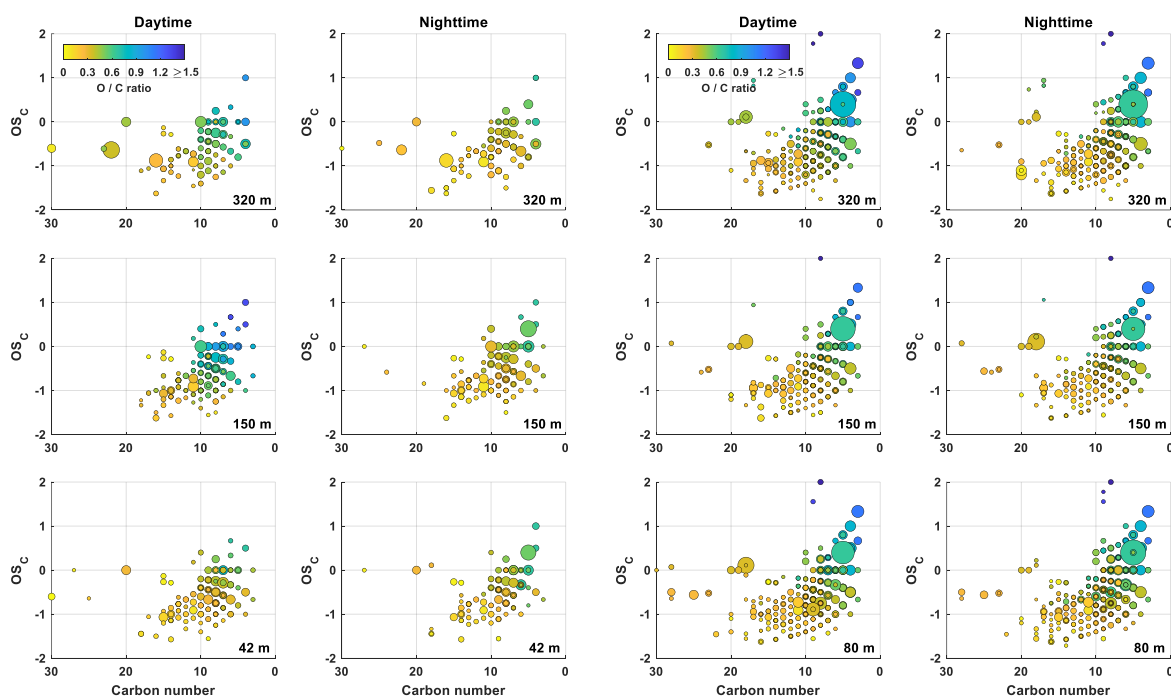


Figure S16: Carbon oxidation state (OS_C) plots for all detected CHO species during the wet season 2018 (left) and wet season 2019 for the daytime and nighttime, respectively. Included are only molecular formulae that were present in more than one of the samples, respectively. The background signals are subtracted. The size of the data points represents the signal intensity of the corresponding peak. The color code illustrates the degree of oxygenation.

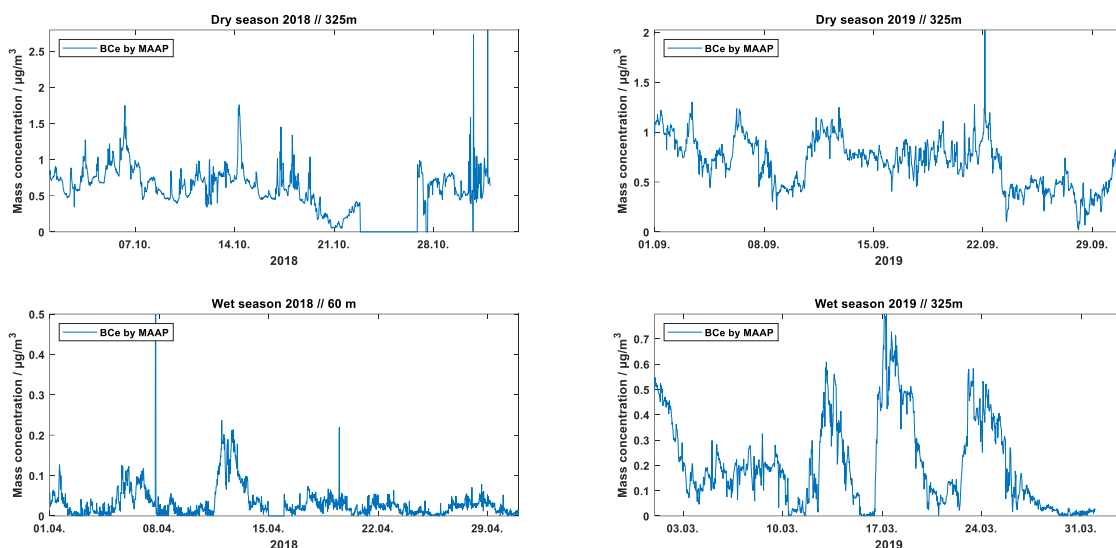


Figure S17: Black carbon equivalent (BCe) mass concentrations during dry season 2018 and 2019 (upper part) and during the wet seasons 2018 and 2019 (lower part), respectively. Higher incidents of forest fires during the wet season 2019 are presumably responsible for increased BCe mass concentrations.

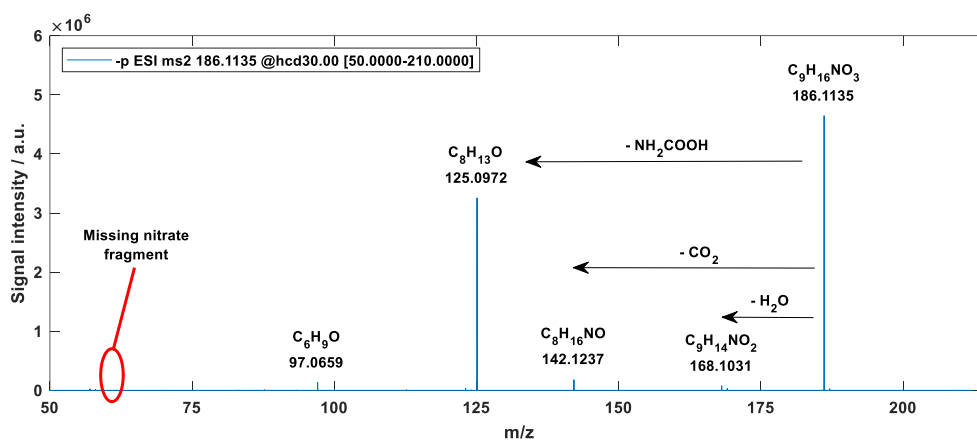


Figure S18: MS² of m/z 186.1135 ($C_9H_{17}NO_3$). A typical nitrate fragment was not observed. Consequently, a nitrooxy-species can be excluded. In contrast, the observed fragments indicate an amide and a hydroxy-functional group within the molecular structure.

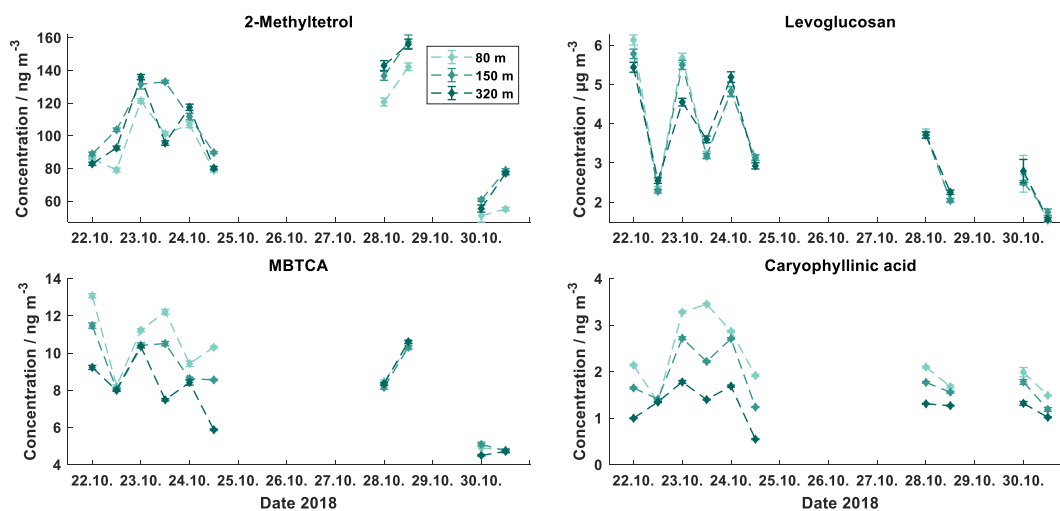


Figure S19: Time profiles for 2-methyltetrols, levoglucosan, MBTCA, and β -caryophyllinic acid during the dry season 2018. The various sampling heights are indicated by different colors.

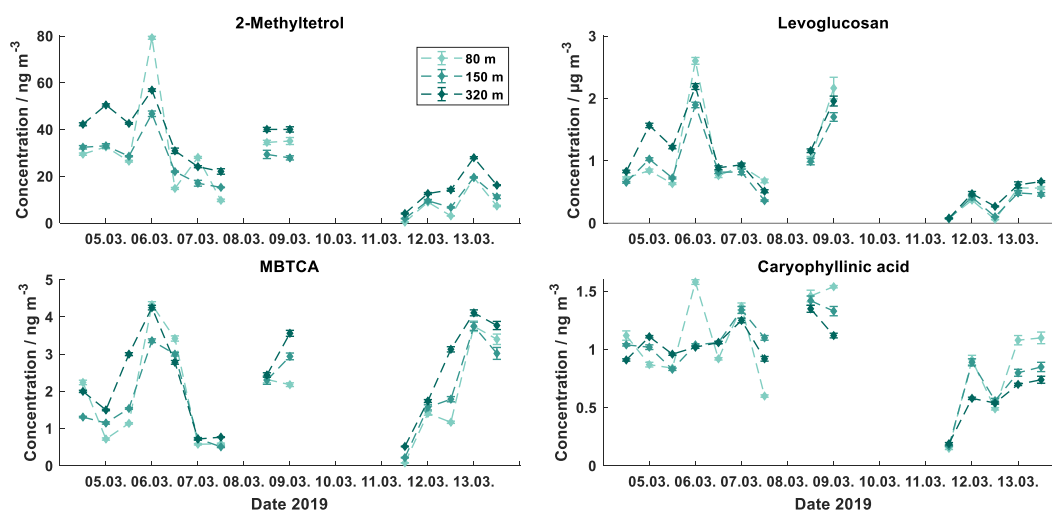


Figure S20: Time profiles for 2-methyltetrols, levoglucosan, MBTCA, and β -caryophyllinic acid during the wet season 2019. The various sampling heights are indicated by different colors.

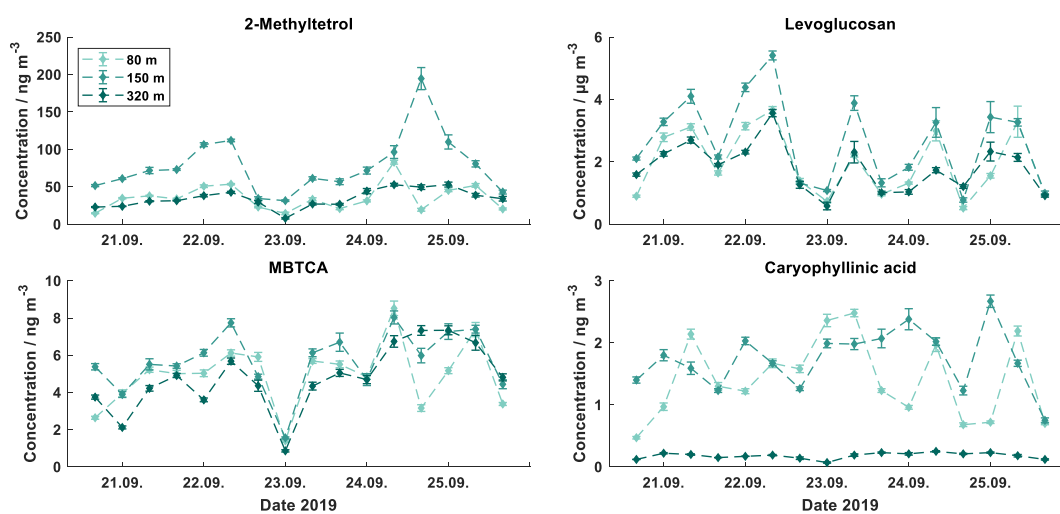


Figure S21: Time profiles for 2-methyltetrols, levoglucosan, MBTCA, and β -caryophyllinic acid during the dry season 2019. The various sampling heights are indicated by different colors.

6.2 Supporting Information to Chapter 3

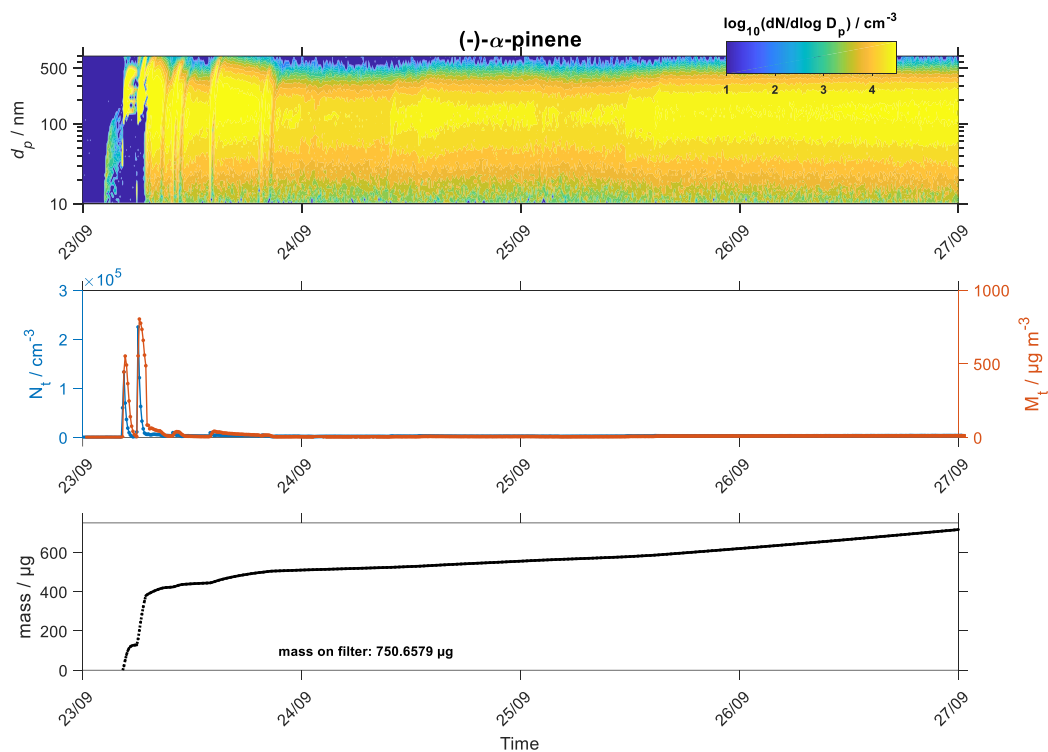


Figure S22: SMPS data of the chamber experiment of (-)- α -pinene and ozone. Additionally, the total particle number (N_t) and total particle mass (M_t) are displayed as well as the collected aerosol mass on the filter.

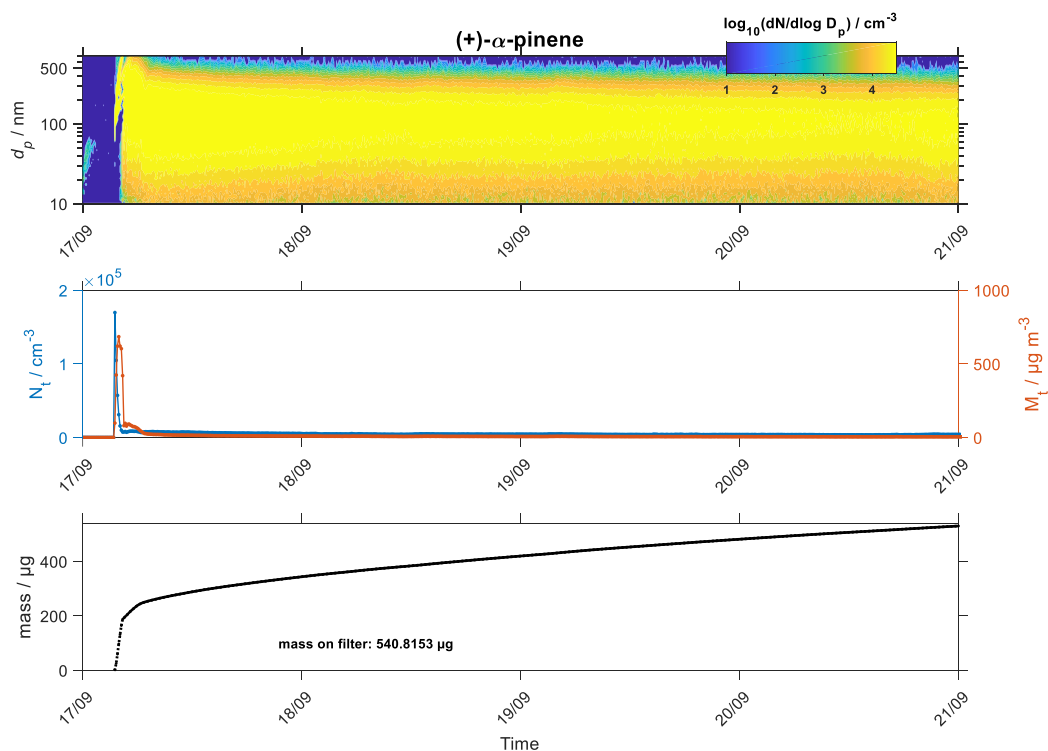


Figure S23: SMPS data of the chamber experiment of (+)- α -pinene and ozone. Additionally, the total particle number (N_t) and total particle mass (M_t) are displayed as well as the collected aerosol mass on the filter.

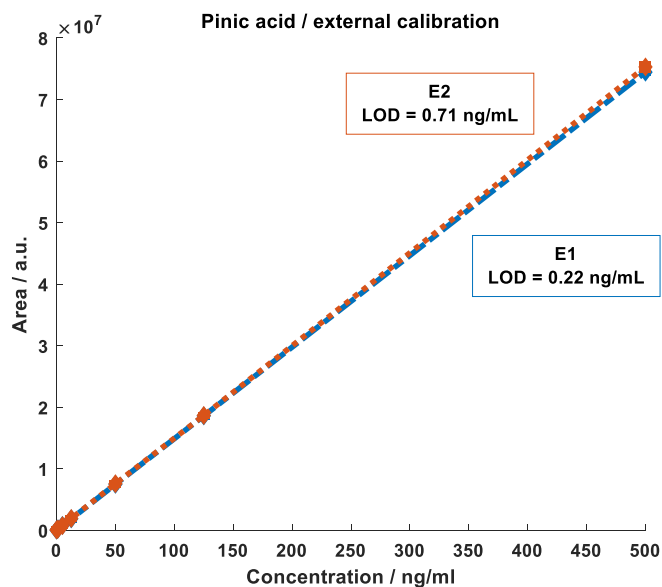


Figure S24: External calibration for the pinic acid enantiomers. Both structures show similar signal areas for increasing standard concentrations. The calculated limit of detection is below 1 ng mL^{-1} for both stereoisomers.

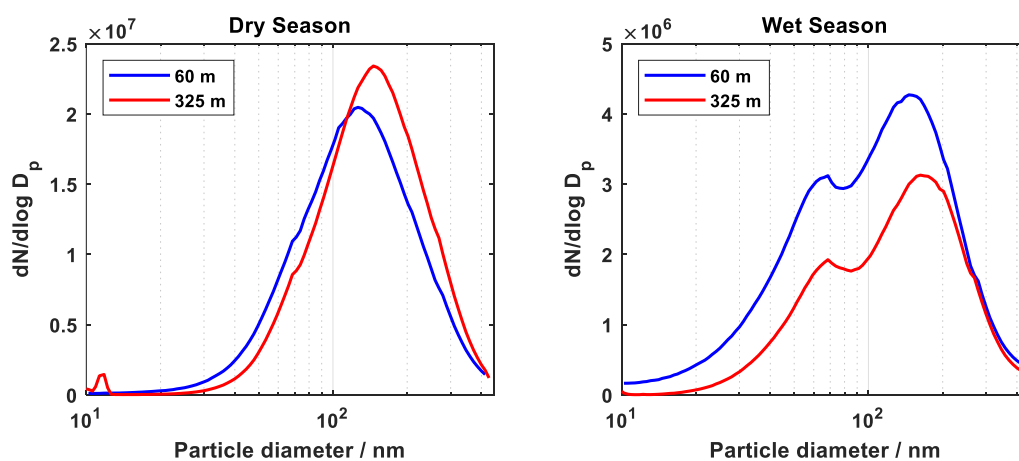


Figure S25: Typical median particle number size distributions for the dry season (left) and wet season (right). The wet season is characterized by a bimodal distribution with two maxima at roughly 70 nm and 150 nm particle diameter.

6.3 UHRMS Data

Table S3: Negative ESI mode UHRMS data for all detected CHO compounds on SOA filter samples from the ATTO site. Compounds, which were detected only once, are excluded.

m/z [M-H] ⁻	Elemental composition	O/C	H/C	m/z [M-H] ⁻	Elemental composition	O/C	H/C
71.0138	C3H4O2	0.67	1.33	271.2279	C16H32O3	0.19	2.00
73.0295	C3H6O2	0.67	2.00	273.0342	C21H6O	0.05	0.29
75.0088	C2H4O3	1.50	2.00	273.0619	C11H14O8	0.73	1.27
83.0139	C4H4O2	0.50	1.00	273.1343	C13H22O6	0.46	1.69
83.0503	C5H8O	0.20	1.60	273.1495	C17H22O3	0.18	1.29
85.0295	C4H6O2	0.50	1.50	273.1708	C14H26O5	0.36	1.86
87.0452	C4H8O2	0.50	2.00	273.2070	C15H30O4	0.27	2.00
89.0245	C3H6O3	1.00	2.00	275.0926	C15H16O5	0.33	1.07
91.0193	C6H4O	0.17	0.67	275.1137	C12H20O7	0.58	1.67
93.0345	C6H6O	0.17	1.00	275.1500	C13H24O6	0.46	1.85
97.0295	C5H6O2	0.40	1.20	275.1652	C17H24O3	0.18	1.41
97.0658	C6H10O	0.17	1.67	277.0928	C11H18O8	0.73	1.64
99.0088	C4H4O3	0.75	1.00	277.1079	C15H18O5	0.33	1.20
99.0452	C5H8O2	0.40	1.60	277.1293	C12H22O7	0.58	1.83
101.0608	C5H10O2	0.40	2.00	277.1445	C16H22O4	0.25	1.38
103.0037	C3H4O4	1.33	1.33	277.1808	C17H26O3	0.18	1.53
103.0400	C4H8O3	0.75	2.00	278.9939	C15H4O6	0.40	0.27
105.0193	C3H6O4	1.33	2.00	279.0149	C12H8O8	0.67	0.67
109.0294	C6H6O2	0.33	1.00	279.1084	C11H20O8	0.73	1.82
111.0088	C5H4O3	0.60	0.80	279.1237	C15H20O5	0.33	1.33
111.0452	C6H8O2	0.33	1.33	279.1598	C16H24O4	0.25	1.50
111.0816	C7H12O	0.14	1.71	279.2326	C18H32O2	0.11	1.78
113.0244	C5H6O3	0.60	1.20	281.0666	C13H14O7	0.54	1.08
113.0608	C6H10O2	0.33	1.67	281.1239	C11H22O8	0.73	2.00
115.0036	C4H4O4	1.00	1.00	281.1396	C15H22O5	0.33	1.47
115.0764	C6H12O2	0.33	2.00	281.1758	C16H26O4	0.25	1.63
117.0193	C4H6O4	1.00	1.50	281.2486	C18H34O2	0.11	1.89
117.0348	C8H6O	0.13	0.75	283.0608	C16H12O5	0.31	0.75
117.0557	C5H10O3	0.60	2.00	283.0675	C9H16O10	1.11	1.78
118.9987	C3H4O5	1.67	1.33	283.0826	C13H16O7	0.54	1.23
119.0350	C4H8O4	1.00	2.00	283.1188	C14H20O6	0.43	1.43
119.0502	C8H8O	0.13	1.00	283.1553	C15H24O5	0.33	1.60
121.0294	C7H6O2	0.29	0.86	283.1914	C16H28O4	0.25	1.75
125.0608	C7H10O2	0.29	1.43	284.9892	C10H6O10	1.00	0.60
125.0972	C8H14O	0.13	1.75	285.0403	C15H10O6	0.40	0.67
127.0037	C5H4O4	0.80	0.80	285.0617	C12H14O8	0.67	1.17
127.0401	C6H8O3	0.50	1.33	285.0983	C13H18O7	0.54	1.38
127.0765	C7H12O2	0.29	1.71	285.1344	C14H22O6	0.43	1.57
129.0193	C5H6O4	0.80	1.20	285.2069	C16H30O4	0.25	1.88
129.0342	C9H6O	0.11	0.67	285.2433	C17H34O3	0.18	2.00
129.0920	C7H14O2	0.29	2.00	287.1499	C14H24O6	0.43	1.71

129.1285	C8H18O	0.13	2.25	287.1861	C15H28O5	0.33	1.87
131.0349	C5H8O4	0.80	1.60	287.2227	C16H32O4	0.25	2.00
131.0713	C6H12O3	0.50	2.00	289.1293	C13H22O7	0.54	1.69
133.0143	C4H6O5	1.25	1.50	289.1441	C17H22O4	0.24	1.29
133.0298	C8H6O2	0.25	0.75	289.1655	C14H26O6	0.43	1.86
133.0506	C5H10O4	0.80	2.00	291.1030	C19H16O3	0.16	0.84
135.0298	C4H8O5	1.25	2.00	291.1086	C12H20O8	0.67	1.67
135.0452	C8H8O2	0.25	1.00	291.1239	C16H20O5	0.31	1.25
135.0662	C5H12O4	0.80	2.40	291.1451	C13H24O7	0.54	1.85
135.0816	C9H12O	0.11	1.33	291.1602	C17H24O4	0.24	1.41
137.0243	C7H6O3	0.43	0.86	293.0875	C11H18O9	0.82	1.64
139.0036	C6H4O4	0.67	0.67	293.1394	C16H22O5	0.31	1.38
139.0764	C8H12O2	0.25	1.50	293.1761	C17H26O4	0.24	1.53
139.1127	C9H16O	0.11	1.78	293.2123	C18H30O3	0.17	1.67
141.0193	C6H6O4	0.67	1.00	295.0101	C12H8O9	0.75	0.67
141.0558	C7H10O3	0.43	1.43	295.0667	C10H16O10	1.00	1.60
141.0921	C8H14O2	0.25	1.75	295.1037	C11H20O9	0.82	1.82
142.9986	C5H4O5	1.00	0.80	295.1184	C15H20O6	0.40	1.33
143.0348	C6H8O4	0.67	1.33	295.1395	C12H24O8	0.67	2.00
143.1077	C8H16O2	0.25	2.00	295.1550	C16H24O5	0.31	1.50
145.0507	C6H10O4	0.67	1.67	295.2277	C18H32O3	0.17	1.78
145.0870	C7H14O3	0.43	2.00	297.0469	C9H14O11	1.22	1.56
147.0299	C5H8O5	1.00	1.60	297.0978	C14H18O7	0.50	1.29
147.0452	C9H8O2	0.22	0.89	297.1340	C15H22O6	0.40	1.47
147.0662	C6H12O4	0.67	2.00	297.1702	C16H26O5	0.31	1.63
149.0091	C4H6O6	1.50	1.50	297.1856	C20H26O2	0.10	1.30
149.0243	C8H6O3	0.38	0.75	297.2068	C17H30O4	0.24	1.76
149.0455	C5H10O5	1.00	2.00	299.0560	C16H12O6	0.38	0.75
149.0606	C9H10O2	0.22	1.11	299.1134	C14H20O7	0.50	1.43
151.0399	C8H8O3	0.38	1.00	299.1345	C11H24O9	0.82	2.18
151.0612	C5H12O5	1.00	2.40	299.1497	C15H24O6	0.40	1.60
153.0193	C7H6O4	0.57	0.86	299.1652	C19H24O3	0.16	1.26
153.0557	C8H10O3	0.38	1.25	299.2012	C20H28O2	0.10	1.40
153.0921	C9H14O2	0.22	1.56	299.2224	C17H32O4	0.24	1.88
153.1284	C10H18O	0.10	1.80	299.2590	C18H36O3	0.17	2.00
154.9986	C6H4O5	0.83	0.67	301.1655	C15H26O6	0.40	1.73
155.0350	C7H8O4	0.57	1.14	301.1806	C19H26O3	0.16	1.37
155.0714	C8H12O3	0.38	1.50	301.2021	C16H30O5	0.31	1.88
155.1077	C9H16O2	0.22	1.78	301.2172	C20H30O2	0.10	1.50
157.0142	C6H6O5	0.83	1.00	301.2382	C17H34O4	0.24	2.00
157.0505	C7H10O4	0.57	1.43	303.1447	C14H24O7	0.50	1.71
157.1231	C9H18O2	0.22	2.00	303.1809	C15H28O6	0.40	1.87
159.0663	C7H12O4	0.57	1.71	303.1966	C19H28O3	0.16	1.47
159.1025	C8H16O3	0.38	2.00	305.0001	C6H10O14	2.33	1.67
161.0091	C5H6O6	1.20	1.20	305.0309	C14H10O8	0.57	0.71
161.0245	C9H6O3	0.33	0.67	305.1238	C13H22O8	0.62	1.69
161.0455	C6H10O5	0.83	1.67	305.1755	C18H26O4	0.22	1.44
161.0818	C7H14O4	0.57	2.00	307.0465	C14H12O8	0.57	0.86
163.0248	C5H8O6	1.20	1.60	307.1399	C13H24O8	0.62	1.85

163.0401	C9H8O3	0.33	0.89	307.1550	C17H24O5	0.29	1.41
163.0611	C6H12O5	0.83	2.00	307.1914	C18H28O4	0.22	1.56
163.0763	C10H12O2	0.20	1.20	309.1188	C12H22O9	0.75	1.83
165.0192	C8H6O4	0.50	0.75	309.1706	C17H26O5	0.29	1.53
165.0404	C5H10O6	1.20	2.00	309.2067	C18H30O4	0.22	1.67
165.0556	C9H10O3	0.33	1.11	310.9895	C8H8O13	1.63	1.00
165.0767	C6H14O5	0.83	2.33	311.1497	C16H24O6	0.38	1.50
167.0349	C8H8O4	0.50	1.00	311.1649	C20H24O3	0.15	1.20
167.0562	C5H12O6	1.20	2.40	311.1861	C17H28O5	0.29	1.65
167.0713	C9H12O3	0.33	1.33	311.2226	C18H32O4	0.22	1.78
167.1077	C10H16O2	0.20	1.60	313.0716	C17H14O6	0.35	0.82
169.0142	C7H6O5	0.71	0.86	313.1291	C15H22O7	0.47	1.47
169.0505	C8H10O4	0.50	1.25	313.1656	C16H26O6	0.38	1.63
169.0868	C9H14O3	0.33	1.56	313.1807	C20H26O3	0.15	1.30
169.1233	C10H18O2	0.20	1.80	313.2380	C18H34O4	0.22	1.89
171.0298	C7H8O5	0.71	1.14	315.0508	C16H12O7	0.44	0.75
171.0452	C11H8O2	0.18	0.73	315.1596	C19H24O4	0.21	1.26
171.0662	C8H12O4	0.50	1.50	315.1811	C16H28O6	0.38	1.75
171.1390	C10H20O2	0.20	2.00	315.1963	C20H28O3	0.15	1.40
173.0092	C6H6O6	1.00	1.00	315.2172	C17H32O5	0.29	1.88
173.0818	C8H14O4	0.50	1.75	315.2540	C18H36O4	0.22	2.00
173.1183	C9H18O3	0.33	2.00	317.0664	C16H14O7	0.44	0.88
175.0247	C6H8O6	1.00	1.33	317.1394	C18H22O5	0.28	1.22
175.0612	C7H12O5	0.71	1.71	317.1758	C19H26O4	0.21	1.37
175.0976	C8H16O4	0.50	2.00	317.2119	C20H30O3	0.15	1.50
177.0193	C9H6O4	0.44	0.67	319.0521	C8H16O13	1.63	2.00
177.0405	C6H10O6	1.00	1.67	319.1912	C19H28O4	0.21	1.47
177.0557	C10H10O3	0.30	1.00	321.0563	C22H10O3	0.14	0.45
177.0768	C7H14O5	0.71	2.00	321.1192	C13H22O9	0.69	1.69
177.0920	C11H14O2	0.18	1.27	321.2068	C19H30O4	0.21	1.58
179.0195	C5H8O7	1.40	1.60	321.2432	C20H34O3	0.15	1.70
179.0350	C9H8O4	0.44	0.89	323.0107	C6H12O15	2.50	2.00
179.0560	C6H12O6	1.00	2.00	323.1501	C17H24O6	0.35	1.41
179.0713	C10H12O3	0.30	1.20	323.1864	C18H28O5	0.28	1.56
181.0142	C8H6O5	0.63	0.75	323.2229	C19H32O4	0.21	1.68
181.0508	C9H10O4	0.44	1.11	323.2590	C20H36O3	0.15	1.80
181.0717	C6H14O6	1.00	2.33	325.0206	C13H10O10	0.77	0.77
181.0870	C10H14O3	0.30	1.40	325.1660	C17H26O6	0.35	1.53
181.1233	C11H18O2	0.18	1.64	325.2018	C18H30O5	0.28	1.67
183.0298	C8H8O5	0.63	1.00	327.0000	C12H8O11	0.92	0.67
183.0662	C9H12O4	0.44	1.33	327.0363	C13H12O10	0.77	0.92
183.1025	C10H16O3	0.30	1.60	327.2537	C19H36O4	0.21	1.89
183.1388	C11H20O2	0.18	1.82	328.9944	C15H6O9	0.60	0.40
185.0091	C7H6O6	0.86	0.86	329.0664	C17H14O7	0.41	0.82
185.0454	C8H10O5	0.63	1.25	329.1756	C20H26O4	0.20	1.30
185.0818	C9H14O4	0.44	1.56	329.1968	C17H30O6	0.35	1.76
187.0192	C14H4O	0.07	0.29	329.2329	C18H34O5	0.28	1.89
187.0248	C7H8O6	0.86	1.14	330.9794	C7H8O15	2.14	1.14
187.0975	C9H16O4	0.44	1.78	331.0157	C8H12O14	1.75	1.50

187.1338	C10H20O3	0.30	2.00	331.1909	C20H28O4	0.20	1.40
189.0349	C14H6O	0.07	0.43	331.2487	C18H36O5	0.28	2.00
189.0404	C7H10O6	0.86	1.43	333.0976	C17H18O7	0.41	1.06
189.0769	C8H14O5	0.63	1.75	333.1191	C14H22O9	0.64	1.57
189.1131	C9H18O4	0.44	2.00	333.1284	C25H18O	0.04	0.72
190.9987	C9H4O5	0.56	0.44	333.1706	C19H26O5	0.26	1.37
191.0198	C6H8O7	1.17	1.33	333.2070	C20H30O4	0.20	1.50
191.0350	C10H8O4	0.40	0.80	335.0262	C11H12O12	1.09	1.09
191.0562	C7H12O6	0.86	1.71	335.1348	C14H24O9	0.64	1.71
191.0925	C8H16O5	0.63	2.00	335.1499	C18H24O6	0.33	1.33
191.1077	C12H16O2	0.17	1.33	335.1865	C19H28O5	0.26	1.47
193.0141	C9H6O5	0.56	0.67	335.2228	C20H32O4	0.20	1.60
193.0352	C6H10O7	1.17	1.67	337.0143	C21H6O5	0.24	0.29
193.0507	C10H10O4	0.40	1.00	337.0512	C22H10O4	0.18	0.45
193.0718	C7H14O6	0.86	2.00	337.1866	C15H30O8	0.53	2.00
193.0868	C11H14O3	0.27	1.27	337.2017	C19H30O5	0.26	1.58
195.0300	C9H8O5	0.56	0.89	338.9842	C9H8O14	1.56	0.89
195.0450	C13H8O2	0.15	0.62	339.0294	C21H8O5	0.24	0.38
195.0509	C6H12O7	1.17	2.00	339.1659	C14H28O9	0.64	2.00
195.0663	C10H12O4	0.40	1.20	339.2172	C19H32O5	0.26	1.68
195.1027	C11H16O3	0.27	1.45	339.2539	C20H36O4	0.20	1.80
195.1388	C12H20O2	0.17	1.67	341.0156	C13H10O11	0.85	0.77
197.0091	C8H6O6	0.75	0.75	341.0299	C17H10O8	0.47	0.59
197.0455	C9H10O5	0.56	1.11	341.1242	C16H22O8	0.50	1.38
197.0666	C6H14O7	1.17	2.33	341.1606	C17H26O7	0.41	1.53
197.0819	C10H14O4	0.40	1.40	341.1968	C18H30O6	0.33	1.67
197.1182	C11H18O3	0.27	1.64	341.3059	C21H42O3	0.14	2.00
198.9885	C7H4O7	1.00	0.57	343.0618	C21H12O5	0.24	0.57
199.0192	C15H4O	0.07	0.27	343.0822	C18H16O7	0.39	0.89
199.0248	C8H8O6	0.75	1.00	343.1034	C15H20O9	0.60	1.33
199.0610	C9H12O5	0.56	1.33	343.1396	C16H24O8	0.50	1.50
199.0975	C10H16O4	0.40	1.60	343.1546	C20H24O5	0.25	1.20
201.0349	C15H6O	0.07	0.40	343.2126	C18H32O6	0.33	1.78
201.0403	C8H10O6	0.75	1.25	343.2486	C19H36O5	0.26	1.89
201.1132	C10H18O4	0.40	1.80	345.0314	C9H14O14	1.56	1.56
201.1496	C11H22O3	0.27	2.00	345.0980	C18H18O7	0.39	1.00
203.0141	C14H4O2	0.14	0.29	345.1552	C16H26O8	0.50	1.63
203.0561	C8H12O6	0.75	1.50	345.1918	C17H30O7	0.41	1.76
203.0925	C9H16O5	0.56	1.78	347.0771	C17H16O8	0.47	0.94
203.1287	C10H20O4	0.40	2.00	347.1342	C15H24O9	0.60	1.60
205.0139	C10H6O5	0.50	0.60	347.1712	C16H28O8	0.50	1.75
205.0353	C7H10O7	1.00	1.43	347.1862	C20H28O5	0.25	1.40
205.0505	C11H10O4	0.36	0.91	349.1505	C15H26O9	0.60	1.73
205.0717	C8H14O6	0.75	1.75	349.1655	C19H26O6	0.32	1.37
205.0870	C12H14O3	0.25	1.17	349.2015	C20H30O5	0.25	1.50
205.1081	C9H18O5	0.56	2.00	351.0211	C11H12O13	1.18	1.09
207.0298	C10H8O5	0.50	0.80	351.0574	C12H16O12	1.00	1.33
207.0510	C7H12O7	1.00	1.71	351.1298	C14H24O10	0.71	1.71
207.0661	C11H12O4	0.36	1.09	351.1808	C19H28O6	0.32	1.47

207.0873	C8H16O6	0.75	2.00	351.2175	C20H32O5	0.25	1.60
207.1389	C13H20O2	0.15	1.54	351.2900	C22H40O3	0.14	1.82
209.0092	C9H6O6	0.67	0.67	353.1094	C13H22O11	0.85	1.69
209.0454	C10H10O5	0.50	1.00	353.1453	C14H26O10	0.71	1.86
209.0666	C7H14O7	1.00	2.00	353.1605	C18H26O7	0.39	1.44
209.1182	C12H18O3	0.25	1.50	353.1968	C19H30O6	0.32	1.58
209.1545	C13H22O2	0.15	1.69	353.2330	C20H34O5	0.25	1.70
211.0193	C16H4O	0.06	0.25	355.1394	C17H24O8	0.47	1.41
211.0247	C9H8O6	0.67	0.89	357.0469	C14H14O11	0.79	1.00
211.0612	C10H12O5	0.50	1.20	357.0612	C18H14O8	0.44	0.78
211.0821	C7H16O7	1.00	2.29	357.0677	C11H18O13	1.18	1.64
211.0974	C11H16O4	0.36	1.45	357.1557	C17H26O8	0.47	1.53
211.1337	C12H20O3	0.25	1.67	357.2278	C19H34O6	0.32	1.79
213.0192	C12H6O4	0.33	0.50	357.2645	C20H38O5	0.25	1.90
213.0256	C5H10O9	1.80	2.00	359.1131	C19H20O7	0.37	1.05
213.0349	C16H6O	0.06	0.38	359.1496	C20H24O6	0.30	1.20
213.0403	C9H10O6	0.67	1.11	359.2438	C19H36O6	0.32	1.89
213.0768	C10H14O5	0.50	1.40	361.0263	C9H14O15	1.67	1.56
213.1132	C11H18O4	0.36	1.64	361.0722	C21H14O6	0.29	0.67
215.0349	C12H8O4	0.33	0.67	361.1657	C20H26O6	0.30	1.30
215.0505	C16H8O	0.06	0.50	363.2021	C17H32O8	0.47	1.88
215.0561	C9H12O6	0.67	1.33	363.2180	C21H32O5	0.24	1.52
215.1286	C11H20O4	0.36	1.82	365.0728	C13H18O12	0.92	1.38
215.1652	C12H24O3	0.25	2.00	365.1399	C22H22O5	0.23	1.00
217.0297	C15H6O2	0.13	0.40	365.1965	C20H30O6	0.30	1.50
217.0716	C9H14O6	0.67	1.56	365.2178	C17H34O8	0.47	2.00
217.1082	C10H18O5	0.50	1.80	367.0311	C15H12O11	0.73	0.80
217.1442	C11H22O4	0.36	2.00	367.1760	C19H28O7	0.37	1.47
219.0297	C11H8O5	0.45	0.73	367.2125	C20H32O6	0.30	1.60
219.0454	C15H8O2	0.13	0.53	369.1915	C19H30O7	0.37	1.58
219.0509	C8H12O7	0.88	1.50	371.0261	C14H12O12	0.86	0.86
219.0872	C9H16O6	0.67	1.78	371.0403	C18H12O9	0.50	0.67
219.1026	C13H16O3	0.23	1.23	371.0771	C19H16O8	0.42	0.84
219.1239	C10H20O5	0.50	2.00	371.2439	C20H36O6	0.30	1.80
221.0091	C10H6O6	0.60	0.60	373.0564	C18H14O9	0.50	0.78
221.0453	C11H10O5	0.45	0.91	373.0927	C19H18O8	0.42	0.95
221.0666	C8H14O7	0.88	1.75	373.1141	C16H22O10	0.63	1.38
221.0818	C12H14O4	0.33	1.17	373.1293	C20H22O7	0.35	1.10
221.1547	C14H22O2	0.14	1.57	373.1864	C18H30O8	0.44	1.67
223.0248	C10H8O6	0.60	0.80	375.1657	C17H28O9	0.53	1.65
223.0399	C14H8O3	0.21	0.57	375.1807	C21H28O6	0.29	1.33
223.0459	C7H12O8	1.14	1.71	375.2749	C20H40O6	0.30	2.00
223.0612	C11H12O5	0.45	1.09	379.0460	C20H12O8	0.40	0.60
223.0824	C8H16O7	0.88	2.00	379.1556	C23H24O5	0.22	1.04
223.0975	C12H16O4	0.33	1.33	379.2124	C21H32O6	0.29	1.52
223.1337	C13H20O3	0.23	1.54	379.2336	C18H36O8	0.44	2.00
223.1703	C14H24O2	0.14	1.71	381.1918	C20H30O7	0.35	1.50
225.0348	C17H6O	0.06	0.35	381.2280	C21H34O6	0.29	1.62
225.0404	C10H10O6	0.60	1.00	383.0107	C11H12O15	1.36	1.09

225.0556	C14H10O3	0.21	0.71	383.1707	C19H28O8	0.42	1.47
225.0616	C7H14O8	1.14	2.00	383.1920	C16H32O10	0.63	2.00
225.0768	C11H14O5	0.45	1.27	383.2069	C20H32O7	0.35	1.60
225.1130	C12H18O4	0.33	1.50	384.9841	C17H6O11	0.65	0.35
225.1497	C13H22O3	0.23	1.69	385.0561	C19H14O9	0.47	0.74
225.1859	C14H26O2	0.14	1.86	387.1447	C21H24O7	0.33	1.14
227.0141	C16H4O2	0.13	0.25	387.2018	C19H32O8	0.42	1.68
227.0565	C10H12O6	0.60	1.20	387.2750	C21H40O6	0.29	1.90
227.0772	C7H16O8	1.14	2.29	389.0874	C19H18O9	0.47	0.95
227.0926	C11H16O5	0.45	1.45	389.1455	C17H26O10	0.59	1.53
227.1287	C12H20O4	0.33	1.67	389.1605	C21H26O7	0.33	1.24
227.2015	C14H28O2	0.14	2.00	391.2336	C19H36O8	0.42	1.89
229.0298	C16H6O2	0.13	0.38	393.0621	C21H14O8	0.38	0.67
229.0716	C10H14O6	0.60	1.40	393.1043	C15H22O12	0.80	1.47
229.1444	C12H22O4	0.33	1.83	393.1705	C24H26O5	0.21	1.08
229.1806	C13H26O3	0.23	2.00	393.1765	C17H30O10	0.59	1.76
231.0453	C16H8O2	0.13	0.50	393.2489	C19H38O8	0.42	2.00
231.0874	C10H16O6	0.60	1.60	395.0348	C27H8O4	0.15	0.30
231.1239	C11H20O5	0.45	1.82	395.0980	C18H20O10	0.56	1.11
231.1603	C12H24O4	0.33	2.00	395.2072	C21H32O7	0.33	1.52
233.0668	C9H14O7	0.78	1.56	399.1656	C19H28O9	0.47	1.47
233.1030	C10H18O6	0.60	1.80	399.2536	C25H36O4	0.16	1.44
233.1546	C15H22O2	0.13	1.47	401.0877	C20H18O9	0.45	0.90
235.0248	C11H8O6	0.55	0.73	403.1761	C22H28O7	0.32	1.27
235.0822	C9H16O7	0.78	1.78	403.3059	C22H44O6	0.27	2.00
235.0976	C13H16O4	0.31	1.23	405.0094	C17H10O12	0.71	0.59
235.1703	C15H24O2	0.13	1.60	406.9886	C16H8O13	0.81	0.50
237.0040	C10H6O7	0.70	0.60	407.1707	C21H28O8	0.38	1.33
237.0405	C11H10O6	0.55	0.91	410.9990	C19H8O11	0.58	0.42
237.0616	C8H14O8	1.00	1.75	411.2597	C19H40O9	0.47	2.11
237.0769	C12H14O5	0.42	1.17	413.1546	C30H22O2	0.07	0.73
237.0980	C9H18O7	0.78	2.00	413.2178	C21H34O8	0.38	1.62
237.1130	C13H18O4	0.31	1.38	415.1028	C21H20O9	0.43	0.95
237.1493	C14H22O3	0.21	1.57	415.1608	C19H28O10	0.53	1.47
239.0505	C18H8O	0.06	0.44	415.1757	C23H28O7	0.30	1.22
239.0560	C11H12O6	0.55	1.09	415.2337	C21H36O8	0.38	1.71
239.0773	C8H16O8	1.00	2.00	417.0617	C23H14O8	0.35	0.61
239.0925	C12H16O5	0.42	1.33	417.2284	C24H34O6	0.25	1.42
239.1286	C13H20O4	0.31	1.54	419.3008	C22H44O7	0.32	2.00
239.1650	C14H24O3	0.21	1.71	421.1871	C22H30O8	0.36	1.36
239.2016	C15H28O2	0.13	1.87	421.2014	C26H30O5	0.19	1.15
241.0506	C14H10O4	0.29	0.71	423.1393	C31H20O2	0.06	0.65
241.0718	C11H14O6	0.55	1.27	425.0976	C33H14O	0.03	0.42
241.1082	C12H18O5	0.42	1.50	425.1088	C19H22O11	0.58	1.16
241.1445	C13H22O4	0.31	1.69	425.1600	C24H26O7	0.29	1.08
241.2170	C15H30O2	0.13	2.00	429.1551	C23H26O8	0.35	1.13
243.0874	C11H16O6	0.55	1.45	431.1712	C23H28O8	0.35	1.22
243.1600	C13H24O4	0.31	1.85	431.2282	C21H36O9	0.43	1.71
243.1965	C14H28O3	0.21	2.00	433.0930	C24H18O8	0.33	0.75

245.1030	C11H18O6	0.55	1.64	433.2079	C20H34O10	0.50	1.70
245.1393	C12H22O5	0.42	1.83	435.0721	C23H16O9	0.39	0.70
245.1756	C13H26O4	0.31	2.00	435.0809	C34H12O	0.03	0.35
247.0460	C9H12O8	0.89	1.33	435.2960	C22H44O8	0.36	2.00
247.0822	C10H16O7	0.70	1.60	436.9990	C17H10O14	0.82	0.59
247.1186	C11H20O6	0.55	1.82	439.1602	C21H28O10	0.48	1.33
249.0616	C9H14O8	0.89	1.56	439.2119	C26H32O6	0.23	1.23
249.0769	C13H14O5	0.38	1.08	441.1496	C31H22O3	0.10	0.71
249.0980	C10H18O7	0.70	1.80	441.2134	C22H34O9	0.41	1.55
249.1133	C14H18O4	0.29	1.29	443.0249	C20H12O12	0.60	0.60
249.1341	C11H22O6	0.55	2.00	445.1139	C22H22O10	0.45	1.00
251.0200	C11H8O7	0.64	0.73	449.0357	C19H14O13	0.68	0.74
251.0560	C12H12O6	0.50	1.00	449.1553	C33H22O2	0.06	0.67
251.0773	C9H16O8	0.89	1.78	457.1864	C25H30O8	0.32	1.20
251.1137	C10H20O7	0.70	2.00	459.2017	C25H32O8	0.32	1.28
251.1290	C14H20O4	0.29	1.43	463.1972	C24H32O9	0.38	1.33
251.1652	C15H24O3	0.20	1.60	465.2124	C24H34O9	0.38	1.42
253.0718	C12H14O6	0.50	1.17	469.1863	C26H30O8	0.31	1.15
253.1081	C13H18O5	0.38	1.38	469.2086	C23H34O10	0.43	1.48
253.1293	C10H22O7	0.70	2.20	469.3018	C22H46O10	0.45	2.09
253.1446	C14H22O4	0.29	1.57	471.3324	C26H48O7	0.27	1.85
253.1807	C15H26O3	0.20	1.73	475.1397	C27H24O8	0.30	0.89
253.2173	C16H30O2	0.13	1.88	475.1971	C25H32O9	0.36	1.28
255.0511	C11H12O7	0.64	1.09	477.0102	C23H10O12	0.52	0.43
255.0664	C15H12O4	0.27	0.80	477.1909	C28H30O7	0.25	1.07
255.0725	C8H16O9	1.13	2.00	477.2130	C25H34O9	0.36	1.36
255.0878	C12H16O6	0.50	1.33	487.1602	C25H28O10	0.40	1.12
255.1238	C13H20O5	0.38	1.54	489.3016	C32H42O4	0.13	1.31
255.1602	C14H24O4	0.29	1.71	491.1918	C25H32O10	0.40	1.28
255.2332	C16H32O2	0.13	2.00	495.2231	C25H36O10	0.40	1.44
256.9941	C9H6O9	1.00	0.67	497.3341	C24H50O10	0.42	2.08
257.0878	C8H18O9	1.13	2.25	499.2332	C28H36O8	0.29	1.29
257.1031	C12H18O6	0.50	1.50	499.3013	C37H40O	0.03	1.08
257.1756	C14H26O4	0.29	1.86	515.1862	C34H28O5	0.15	0.82
257.2123	C15H30O3	0.20	2.00	515.2429	C32H36O6	0.19	1.13
259.1186	C12H20O6	0.50	1.67	517.2437	C28H38O9	0.32	1.36
259.1550	C13H24O5	0.38	1.85	527.3427	C25H52O11	0.44	2.08
259.1914	C14H28O4	0.29	2.00	529.2076	C28H34O10	0.36	1.21
261.0616	C10H14O8	0.80	1.40	529.3486	C39H46O	0.03	1.18
261.0977	C11H18O7	0.64	1.64	533.2385	C28H38O10	0.36	1.36
261.1342	C12H22O6	0.50	1.83	539.1194	C27H24O12	0.44	0.89
263.0041	C8H8O10	1.25	1.00	541.0048	C27H10O13	0.48	0.37
263.0772	C10H16O8	0.80	1.60	541.2436	C30H38O9	0.30	1.27
263.1138	C11H20O7	0.64	1.82	543.3638	C40H48O	0.03	1.20
263.1286	C15H20O4	0.27	1.33	547.2180	C28H36O11	0.39	1.29
263.1653	C16H24O3	0.19	1.50	549.1029	C28H22O12	0.43	0.79
265.0720	C13H14O6	0.46	1.08	549.3065	C30H46O9	0.30	1.53
265.0929	C10H18O8	0.80	1.80	565.2815	C33H42O8	0.24	1.27
265.1084	C14H18O5	0.36	1.29	569.3263	C37H46O5	0.14	1.24

265.1295	C11H22O7	0.64	2.00	585.3851	C28H58O12	0.43	2.07
265.1447	C15H22O4	0.27	1.47	593.0058	C23H14O19	0.83	0.61
265.2172	C17H30O2	0.12	1.76	593.1290	C30H26O13	0.43	0.87
267.0510	C12H12O7	0.58	1.00	593.1511	C27H30O15	0.56	1.11
267.0722	C9H16O9	1.00	1.78	597.3867	C29H58O12	0.41	2.00
267.1085	C10H20O8	0.80	2.00	601.2279	C31H38O12	0.39	1.23
267.1239	C14H20O5	0.36	1.43	601.2645	C32H42O11	0.34	1.31
267.1601	C15H24O4	0.27	1.60	613.3952	C33H58O10	0.30	1.76
267.1965	C16H28O3	0.19	1.75	621.0455	C36H14O11	0.31	0.39
269.0456	C15H10O5	0.33	0.67	639.0253	C28H16O18	0.64	0.57
269.1031	C13H18O6	0.46	1.38	645.2910	C34H46O12	0.35	1.35
269.1395	C14H22O5	0.36	1.57	685.0305	C29H18O20	0.69	0.62
269.1759	C15H26O4	0.27	1.73	691.0480	C21H24O26	1.24	1.14
271.0978	C16H16O4	0.25	1.00	699.3018	C37H48O13	0.35	1.30
271.1187	C13H20O6	0.46	1.54	705.3272	C40H50O11	0.28	1.25
271.1916	C15H28O4	0.27	1.87				

Table S4: Negative ESI mode UHRMS data for all detected CHON compounds on SOA filter samples from the ATTO site. Compounds, which were detected only once, are excluded.

<i>m/z</i> [M-H] ⁻	Elemental composition	O/C	H/C	<i>m/z</i> [M-H] ⁻	Elemental composition	O/C	H/C
84.0091	C3H3NO2	0.67	1.00	339.0006	C14H4N4O7	0.50	0.29
98.0247	C4H5NO2	0.50	1.25	339.0370	C15H8N4O6	0.40	0.53
100.0041	C3H3NO3	1.00	1.00	339.2287	C18H32N2O4	0.22	1.78
104.0354	C3H7NO3	1.00	2.33	339.2649	C19H36N2O3	0.16	1.89
110.0247	C5H5NO2	0.40	1.00	340.2127	C18H31NO5	0.28	1.72
112.0404	C5H7NO2	0.40	1.40	340.2488	C19H35NO4	0.21	1.84
114.0196	C4H5NO3	0.75	1.25	341.0168	C14H6N4O7	0.50	0.43
115.9990	C3H3NO4	1.33	1.00	341.2079	C17H30N2O5	0.29	1.76
118.0147	C3H5NO4	1.33	1.67	342.1707	C20H25NO4	0.20	1.25
118.0510	C4H9NO3	0.75	2.25	342.1920	C17H29NO6	0.35	1.71
126.0197	C5H5NO3	0.60	1.00	342.2647	C19H37NO4	0.21	1.95
126.0561	C6H9NO2	0.33	1.50	343.2966	C19H40N2O3	0.16	2.11
128.0353	C5H7NO3	0.60	1.40	344.2077	C17H31NO6	0.35	1.82
129.0306	C4H6N2O3	0.75	1.50	344.2439	C18H35NO5	0.28	1.94
130.0145	C4H5NO4	1.00	1.25	345.0311	C22H6N2O3	0.14	0.27
132.0302	C4H7NO4	1.00	1.75	345.2026	C16H30N2O6	0.38	1.88
134.0095	C3H5NO5	1.67	1.67	346.2233	C17H33NO6	0.35	1.94
136.0403	C7H7NO2	0.29	1.00	346.2596	C18H37NO5	0.28	2.06
138.0196	C6H5NO3	0.50	0.83	348.2392	C17H35NO6	0.35	2.06
139.0149	C5H4N2O3	0.60	0.80	349.0378	C7H14N2O14	2.00	2.00
142.0509	C6H9NO3	0.50	1.50	350.1252	C17H21NO7	0.41	1.24
143.0098	C4H4N2O4	1.00	1.00	350.1818	C15H29NO8	0.53	1.93
144.0302	C5H7NO4	0.80	1.40	351.0212	C12H8N4O9	0.75	0.67
145.0254	C4H6N2O4	1.00	1.50	351.0372	C16H8N4O6	0.38	0.50
146.0247	C8H5NO2	0.25	0.63	351.1771	C14H28N2O8	0.57	2.00
146.0458	C5H9NO4	0.80	1.80	351.2285	C19H32N2O4	0.21	1.68
148.0251	C4H7NO5	1.25	1.75	351.2499	C16H36N2O6	0.38	2.25

152.0352	C7H7NO3	0.43	1.00	352.0100	C17H7NO8	0.47	0.41
153.0305	C6H6N2O3	0.50	1.00	352.1766	C18H27NO6	0.33	1.50
154.0146	C6H5NO4	0.67	0.83	352.2125	C19H31NO5	0.26	1.63
154.0510	C7H9NO3	0.43	1.29	353.0163	C15H6N4O7	0.47	0.40
156.0303	C6H7NO4	0.67	1.17	353.0530	C16H10N4O6	0.38	0.63
156.1028	C8H15NO2	0.25	1.88	353.1096	C14H18N4O7	0.50	1.29
157.0254	C5H6N2O4	0.80	1.20	353.1311	C11H22N4O9	0.82	2.00
157.0618	C6H10N2O3	0.50	1.67	354.1916	C18H29NO6	0.33	1.61
158.0094	C5H5NO5	1.00	1.00	354.2286	C19H33NO5	0.26	1.74
158.0458	C6H9NO4	0.67	1.50	355.0324	C15H8N4O7	0.47	0.53
159.0047	C4H4N2O5	1.25	1.00	355.2235	C18H32N2O5	0.28	1.78
159.0411	C5H8N2O4	0.80	1.60	355.2601	C19H36N2O4	0.21	1.89
160.0615	C6H11NO4	0.67	1.83	356.1712	C17H27NO7	0.41	1.59
162.0196	C8H5NO3	0.38	0.63	356.2077	C18H31NO6	0.33	1.72
162.0409	C5H9NO5	1.00	1.80	357.0309	C23H6N2O3	0.13	0.26
162.0771	C6H13NO4	0.67	2.17	357.0470	C15H10N4O7	0.47	0.67
163.0360	C4H8N2O5	1.25	2.00	357.0541	C8H14N4O12	1.50	1.75
164.0201	C4H7NO6	1.50	1.75	357.2032	C17H30N2O6	0.35	1.76
164.0354	C8H7NO3	0.38	0.88	357.2758	C19H38N2O4	0.21	2.00
166.0145	C7H5NO4	0.57	0.71	358.1505	C16H25NO8	0.50	1.56
166.0508	C8H9NO3	0.38	1.13	358.2233	C18H33NO6	0.33	1.83
166.0872	C9H13NO2	0.22	1.44	358.2596	C19H37NO5	0.26	1.95
167.0098	C6H4N2O4	0.67	0.67	359.0668	C20H12N2O5	0.25	0.60
168.0301	C7H7NO4	0.57	1.00	359.2184	C17H32N2O6	0.35	1.88
168.0665	C8H11NO3	0.38	1.38	359.2546	C18H36N2O5	0.28	2.00
168.1029	C9H15NO2	0.22	1.67	360.0689	C12H15N3O10	0.83	1.25
170.0094	C6H5NO5	0.83	0.83	360.0788	C10H19NO13	1.30	1.90
170.0458	C7H9NO4	0.57	1.29	360.2389	C18H35NO6	0.33	1.94
170.0822	C8H13NO3	0.38	1.63	360.2754	C19H39NO5	0.26	2.05
170.1186	C9H17NO2	0.22	1.89	361.0062	C13H6N4O9	0.69	0.46
171.0776	C7H12N2O3	0.43	1.71	361.0165	C11H10N2O12	1.09	0.91
172.0252	C6H7NO5	0.83	1.17	361.0261	C22H6N2O4	0.18	0.27
172.0615	C7H11NO4	0.57	1.57	361.0267	C10H10N4O11	1.10	1.00
173.0203	C5H6N2O5	1.00	1.20	361.9948	C18H5NO8	0.44	0.28
173.0567	C6H10N2O4	0.67	1.67	362.1975	C20H29NO5	0.25	1.45
174.0043	C5H5NO6	1.20	1.00	362.2549	C18H37NO6	0.33	2.06
174.0771	C7H13NO4	0.57	1.86	364.2130	C20H31NO5	0.25	1.55
176.0200	C5H7NO6	1.20	1.40	365.0732	C14H14N4O8	0.57	1.00
176.0353	C9H7NO3	0.33	0.78	367.0322	C16H8N4O7	0.44	0.50
177.0304	C8H6N2O3	0.38	0.75	367.1873	C18H28N2O6	0.33	1.56
178.0145	C8H5NO4	0.50	0.63	368.2073	C19H31NO6	0.32	1.63
178.0358	C5H9NO6	1.20	1.80	368.2441	C20H35NO5	0.25	1.75
178.0509	C9H9NO3	0.33	1.00	369.0114	C15H6N4O8	0.53	0.40
180.0303	C8H7NO4	0.50	0.88	369.0478	C16H10N4O7	0.44	0.63
180.0666	C9H11NO3	0.33	1.22	369.2392	C19H34N2O5	0.26	1.79
181.0254	C7H6N2O4	0.57	0.86	370.2231	C19H33NO6	0.32	1.74
182.0095	C7H5NO5	0.71	0.71	370.2345	C18H33N3O5	0.28	1.83
182.0457	C8H9NO4	0.50	1.13	371.0263	C15H8N4O8	0.53	0.53
183.0047	C6H4N2O5	0.83	0.67	371.2187	C18H32N2O6	0.33	1.78

184.0251	C7H7NO5	0.71	1.00	372.0328	C12H11N3O11	0.92	0.92
184.0615	C8H11NO4	0.50	1.38	372.2386	C19H35NO6	0.32	1.84
184.0978	C9H15NO3	0.33	1.67	372.2750	C20H39NO5	0.25	1.95
185.0564	C7H10N2O4	0.57	1.43	373.2344	C18H34N2O6	0.33	1.89
186.0772	C8H13NO4	0.50	1.63	374.2545	C19H37NO6	0.32	1.95
186.1134	C9H17NO3	0.33	1.89	375.0221	C14H8N4O9	0.64	0.57
187.0362	C6H8N2O5	0.83	1.33	375.0370	C18H8N4O6	0.33	0.44
188.0201	C6H7NO6	1.00	1.17	375.2497	C18H36N2O6	0.33	2.00
188.0352	C10H7NO3	0.30	0.70	376.2339	C18H35NO7	0.39	1.94
188.0928	C8H15NO4	0.50	1.88	376.2699	C19H39NO6	0.32	2.05
189.0882	C7H14N2O4	0.57	2.00	377.2287	C17H34N2O7	0.41	2.00
190.0356	C6H9NO6	1.00	1.50	377.2651	C18H38N2O6	0.33	2.11
191.0461	C9H8N2O3	0.33	0.89	378.1501	C26H21NO2	0.08	0.81
192.0303	C9H7NO4	0.44	0.78	378.1923	C20H29NO6	0.30	1.45
192.0512	C6H11NO6	1.00	1.83	378.2648	C22H37NO4	0.18	1.68
192.0667	C10H11NO3	0.30	1.10	380.2802	C22H39NO4	0.18	1.77
194.0095	C8H5NO5	0.63	0.63	381.0109	C16H6N4O8	0.50	0.38
194.0305	C5H9NO7	1.40	1.80	381.0477	C17H10N4O7	0.41	0.59
194.0458	C9H9NO4	0.44	1.00	381.0543	C10H14N4O12	1.20	1.40
194.0820	C10H13NO3	0.30	1.30	382.0933	C20H17NO7	0.35	0.85
194.1187	C11H17NO2	0.18	1.55	382.2959	C22H41NO4	0.18	1.86
196.0250	C8H7NO5	0.63	0.88	383.0109	C12H8N4O11	0.92	0.67
196.0616	C9H11NO4	0.44	1.22	383.2549	C20H36N2O5	0.25	1.80
197.0203	C7H6N2O5	0.71	0.86	384.2388	C20H35NO6	0.30	1.75
197.0930	C9H14N2O3	0.33	1.56	385.0065	C15H6N4O9	0.60	0.40
198.0044	C7H5NO6	0.86	0.71	385.2338	C19H34N2O6	0.32	1.79
198.0159	C6H5N3O5	0.83	0.83	385.3069	C21H42N2O4	0.19	2.00
198.0408	C8H9NO5	0.63	1.13	386.2293	C18H33N3O6	0.33	1.83
198.0771	C9H13NO4	0.44	1.44	386.2542	C20H37NO6	0.30	1.85
198.1135	C10H17NO3	0.30	1.70	387.1558	C20H24N2O6	0.30	1.20
198.9998	C6H4N2O6	1.00	0.67	387.2498	C19H36N2O6	0.32	1.89
199.0723	C8H12N2O4	0.50	1.50	387.2867	C20H40N2O5	0.25	2.00
200.0564	C8H11NO5	0.63	1.38	388.1978	C18H31NO8	0.44	1.72
200.0927	C9H15NO4	0.44	1.67	388.2701	C20H39NO6	0.30	1.95
201.0154	C6H6N2O6	1.00	1.00	388.3061	C21H43NO5	0.24	2.05
201.0879	C8H14N2O4	0.50	1.75	389.2289	C18H34N2O7	0.39	1.89
202.0511	C11H9NO3	0.27	0.82	390.1673	C19H25N3O6	0.32	1.32
202.1085	C9H17NO4	0.44	1.89	390.2495	C19H37NO7	0.37	1.95
203.0310	C6H8N2O6	1.00	1.33	391.2443	C18H36N2O7	0.39	2.00
203.1038	C8H16N2O4	0.50	2.00	392.2648	C19H39NO7	0.37	2.05
204.0513	C7H11NO6	0.86	1.57	393.0106	C17H6N4O8	0.47	0.35
204.1241	C9H19NO4	0.44	2.11	393.1003	C10H22N2O14	1.40	2.20
206.0094	C9H5NO5	0.56	0.56	393.2605	C18H38N2O7	0.39	2.11
206.0458	C10H9NO4	0.40	0.90	394.2228	C21H33NO6	0.29	1.57
208.0098	C5H7NO8	1.60	1.40	395.0632	C18H12N4O7	0.39	0.67
208.0250	C9H7NO5	0.56	0.78	395.0798	C9H20N2O15	1.67	2.22
208.0613	C10H11NO4	0.40	1.10	395.1058	C12H20N4O11	0.92	1.67
210.0407	C9H9NO5	0.56	1.00	396.0325	C14H11N3O11	0.79	0.79
210.1133	C11H17NO3	0.27	1.55	396.2867	C21H39N3O4	0.19	1.86

210.1498	C12H21NO2	0.17	1.75	396.3114	C23H43NO4	0.17	1.87
211.0359	C8H8N2O5	0.63	1.00	397.0425	C17H10N4O8	0.47	0.59
212.0565	C9H11NO5	0.56	1.22	397.0783	C18H14N4O7	0.39	0.78
212.0927	C10H15NO4	0.40	1.50	397.2707	C21H38N2O5	0.24	1.81
212.1292	C11H19NO3	0.27	1.73	398.1818	C19H29NO8	0.42	1.53
213.0151	C7H6N2O6	0.86	0.86	398.2331	C24H33NO4	0.17	1.38
214.0110	C6H5N3O6	1.00	0.83	399.0218	C16H8N4O9	0.56	0.50
214.0510	C12H9NO3	0.25	0.75	399.0263	C21H8N2O7	0.33	0.38
214.0720	C9H13NO5	0.56	1.44	399.1263	C13H24N2O12	0.92	1.85
214.1084	C10H17NO4	0.40	1.70	400.3060	C22H43NO5	0.23	1.95
215.0100	C10H4N2O4	0.40	0.40	401.1420	C13H26N2O12	0.92	2.00
215.0670	C8H12N2O5	0.63	1.50	401.1864	C25H26N2O3	0.12	1.04
215.1035	C9H16N2O4	0.44	1.78	401.2654	C20H38N2O6	0.30	1.90
215.9935	C10H3NO5	0.50	0.30	402.2130	C19H33NO8	0.42	1.74
216.1241	C10H19NO4	0.40	1.90	402.2497	C20H37NO7	0.35	1.85
217.1193	C9H18N2O4	0.44	2.00	403.0048	C16H8N2O11	0.69	0.50
218.1033	C9H17NO5	0.56	1.89	403.0931	C22H16N2O6	0.27	0.73
219.0985	C8H16N2O5	0.63	2.00	403.2094	C18H32N2O8	0.44	1.78
220.0252	C10H7NO5	0.50	0.70	403.2443	C19H36N2O7	0.37	1.89
220.0614	C11H11NO4	0.36	1.00	403.2811	C20H40N2O6	0.30	2.00
220.0979	C12H15NO3	0.25	1.25	404.2402	C18H35N3O7	0.39	1.94
221.0778	C7H14N2O6	0.86	2.00	404.2650	C20H39NO7	0.35	1.95
222.0771	C11H13NO4	0.36	1.18	404.2767	C19H39N3O6	0.32	2.05
222.1133	C12H17NO3	0.25	1.42	405.0061	C12H10N2O14	1.17	0.83
224.0312	C8H7N3O5	0.63	0.88	405.0323	C15H10N4O10	0.67	0.67
224.0411	C6H11NO8	1.33	1.83	405.2236	C18H34N2O8	0.44	1.89
224.0562	C10H11NO5	0.50	1.10	405.2603	C19H38N2O7	0.37	2.00
224.0927	C11H15NO4	0.36	1.36	406.2442	C19H37NO8	0.42	1.95
224.1292	C12H19NO3	0.25	1.58	407.1002	C20H16N4O6	0.30	0.80
224.1655	C13H23NO2	0.15	1.77	408.3114	C24H43NO4	0.17	1.79
225.1092	C7H18N2O6	0.86	2.57	409.0953	C10H22N2O15	1.50	2.20
226.0357	C9H9NO6	0.67	1.00	409.2706	C22H38N2O5	0.23	1.73
226.0510	C13H9NO3	0.23	0.69	410.1612	C23H25NO6	0.26	1.09
226.0569	C6H13NO8	1.33	2.17	410.3273	C24H45NO4	0.17	1.88
226.0720	C10H13NO5	0.50	1.30	411.1111	C10H24N2O15	1.50	2.40
226.1083	C11H17NO4	0.36	1.55	412.2700	C22H39NO6	0.27	1.77
226.1449	C12H21NO3	0.25	1.75	413.2657	C21H38N2O6	0.29	1.81
227.0308	C8H8N2O6	0.75	1.00	415.0201	C21H8N2O8	0.38	0.38
227.1037	C10H16N2O4	0.40	1.60	415.2561	C19H36N4O6	0.32	1.89
228.0301	C12H7NO4	0.33	0.58	415.2812	C21H40N2O6	0.29	1.90
228.0666	C13H11NO3	0.23	0.85	415.3173	C22H44N2O5	0.23	2.00
228.0878	C10H15NO5	0.50	1.50	416.0016	C16H7N3O11	0.69	0.44
228.1240	C11H19NO4	0.36	1.73	416.2290	C20H35NO8	0.40	1.75
229.0251	C11H6N2O4	0.36	0.55	417.0173	C12H10N4O13	1.08	0.83
229.1192	C10H18N2O4	0.40	1.80	417.2603	C20H38N2O7	0.35	1.90
230.0305	C8H9NO7	0.88	1.13	418.1868	C22H29NO7	0.32	1.32
230.0457	C12H9NO4	0.33	0.75	419.1264	C11H24N4O13	1.18	2.18
230.0669	C9H13NO6	0.67	1.44	419.2393	C19H36N2O8	0.42	1.89
230.1398	C11H21NO4	0.36	1.91	419.9952	C15H7N3O12	0.80	0.47

231.0043	C10H4N2O5	0.50	0.40	421.1419	C11H26N4O13	1.18	2.36
231.1348	C10H20N2O4	0.40	2.00	421.2556	C19H38N2O8	0.42	2.00
232.1191	C10H19NO5	0.50	1.90	422.1455	C20H25NO9	0.45	1.25
233.0563	C11H10N2O4	0.36	0.91	423.0686	C17H16N2O11	0.65	0.94
234.0771	C12H13NO4	0.33	1.08	423.0733	C23H12N4O5	0.22	0.52
234.1348	C10H21NO5	0.50	2.10	423.1924	C24H28N2O5	0.21	1.17
234.1497	C14H21NO2	0.14	1.50	424.1945	C16H31N3O10	0.63	1.94
234.9993	C9H4N2O6	0.67	0.44	424.3427	C25H47NO4	0.16	1.88
235.0934	C8H16N2O6	0.75	2.00	425.3014	C23H42N2O5	0.22	1.83
236.0929	C12H15NO4	0.33	1.25	426.0124	C7H13N3O18	2.57	1.86
236.1289	C13H19NO3	0.23	1.46	427.1107	C16H20N4O10	0.63	1.25
238.0510	C14H9NO3	0.21	0.64	427.1142	C21H20N2O8	0.38	0.95
238.0568	C7H13NO8	1.14	1.86	428.0922	C28H15NO4	0.14	0.54
238.0721	C11H13NO5	0.45	1.18	429.1241	C28H18N2O3	0.11	0.64
238.1085	C12H17NO4	0.33	1.42	430.1865	C23H29NO7	0.30	1.26
239.0673	C10H12N2O5	0.50	1.20	430.9850	C13H8N2O15	1.15	0.62
240.0515	C10H11NO6	0.60	1.10	433.0006	C13H10N2O15	1.15	0.77
240.1241	C12H19NO4	0.33	1.58	434.2501	C19H37N3O8	0.42	1.95
240.1606	C13H23NO3	0.23	1.77	435.1312	C22H20N4O6	0.27	0.91
241.1195	C11H18N2O4	0.36	1.64	436.3428	C26H47NO4	0.15	1.81
241.9942	C8H5NO8	1.00	0.63	437.0012	C18H6N4O10	0.56	0.33
242.0460	C13H9NO4	0.31	0.69	437.0073	C11H10N4O15	1.36	0.91
242.0518	C6H13NO9	1.50	2.17	437.0640	C9H18N4O16	1.78	2.00
242.0822	C14H13NO3	0.21	0.93	438.1136	C30H17NO3	0.10	0.57
242.1033	C11H17NO5	0.45	1.55	438.1762	C21H29NO9	0.43	1.38
242.1399	C12H21NO4	0.33	1.75	438.3583	C26H49NO4	0.15	1.88
243.0406	C12H8N2O4	0.33	0.67	439.0174	C18H8N4O10	0.56	0.44
243.0984	C10H16N2O5	0.50	1.60	439.1527	C11H28N4O14	1.27	2.55
243.1350	C11H20N2O4	0.36	1.82	440.3738	C26H51NO4	0.15	1.96
244.0099	C8H7NO8	1.00	0.88	441.0796	C17H18N2O12	0.71	1.06
244.0675	C6H15NO9	1.50	2.50	441.1057	C20H18N4O8	0.40	0.90
244.0826	C10H15NO6	0.60	1.50	441.1481	C14H26N4O12	0.86	1.86
244.1554	C12H23NO4	0.33	1.92	441.2137	C23H30N4O5	0.22	1.30
245.0199	C11H6N2O5	0.45	0.55	442.3174	C24H45NO6	0.25	1.88
245.1507	C11H22N2O4	0.36	2.00	443.1973	C27H28N2O4	0.15	1.04
246.1346	C11H21NO5	0.45	1.91	443.3123	C23H44N2O6	0.26	1.91
246.9992	C10H4N2O6	0.60	0.40	443.3482	C24H48N2O5	0.21	2.00
247.0356	C11H8N2O5	0.45	0.73	446.1812	C23H29NO8	0.35	1.26
247.0721	C12H12N2O4	0.33	1.00	447.1573	C13H28N4O13	1.00	2.15
248.0414	C8H11NO8	1.00	1.38	447.1918	C26H28N2O5	0.19	1.08
248.1252	C9H19N3O5	0.56	2.11	447.2821	C20H40N4O7	0.35	2.00
249.1091	C9H18N2O6	0.67	2.00	448.1971	C23H31NO8	0.35	1.35
250.0569	C8H13NO8	1.00	1.63	449.0412	C25H10N2O7	0.28	0.40
250.0934	C9H17NO7	0.78	1.89	449.0589	C17H14N4O11	0.65	0.82
250.1296	C10H21NO6	0.60	2.10	449.0883	C25H14N4O5	0.20	0.56
250.1448	C14H21NO3	0.21	1.50	449.1733	C13H30N4O13	1.00	2.31
251.0306	C10H8N2O6	0.60	0.80	450.0491	C10H17N3O17	1.70	1.70
251.1249	C9H20N2O6	0.67	2.22	450.2857	C25H41NO6	0.24	1.64
252.0727	C8H15NO8	1.00	1.88	451.0200	C24H8N2O8	0.33	0.33

252.1242	C13H19NO4	0.31	1.46	452.3739	C27H51NO4	0.15	1.89
253.0829	C11H14N2O5	0.45	1.27	453.1684	C12H30N4O14	1.17	2.50
254.1399	C13H21NO4	0.31	1.62	454.9919	C8H12N2O20	2.50	1.50
254.1762	C14H25NO3	0.21	1.79	455.0310	C27H8N2O6	0.22	0.30
255.1348	C12H20N2O4	0.33	1.67	456.9858	C11H10N2O18	1.64	0.91
256.0981	C15H15NO3	0.20	1.00	457.1185	C29H18N2O4	0.14	0.62
256.1190	C12H19NO5	0.42	1.58	459.0462	C23H12N2O9	0.39	0.52
256.1554	C13H23NO4	0.31	1.77	459.0897	C17H20N2O13	0.76	1.18
257.0779	C10H14N2O6	0.60	1.40	459.1152	C20H20N4O9	0.45	1.00
257.1507	C12H22N2O4	0.33	1.83	460.3026	C22H43N3O7	0.32	1.95
258.0518	C12H9N3O4	0.33	0.75	463.2027	C30H28N2O3	0.10	0.93
258.0618	C10H13NO7	0.70	1.30	463.2038	C18H32N4O10	0.56	1.78
258.1710	C13H25NO4	0.31	1.92	464.1922	C23H31NO9	0.39	1.35
258.9992	C11H4N2O6	0.55	0.36	465.1686	C13H30N4O14	1.08	2.31
259.0356	C12H8N2O5	0.42	0.67	466.1714	C22H29NO10	0.45	1.32
259.1663	C12H24N2O4	0.33	2.00	467.0646	C11H20N2O18	1.64	1.82
260.0564	C13H11NO5	0.38	0.85	467.1109	C11H24N4O16	1.45	2.18
260.0672	C12H11N3O4	0.33	0.92	467.1404	C31H20N2O3	0.10	0.65
260.1505	C12H23NO5	0.42	1.92	469.2091	C24H30N4O6	0.25	1.25
261.0150	C11H6N2O6	0.55	0.55	469.3395	C24H46N4O5	0.21	1.92
261.1455	C11H22N2O5	0.45	2.00	470.0780	C28H13N3O5	0.18	0.46
262.1661	C12H25NO5	0.42	2.08	470.2123	C33H29NO2	0.06	0.88
263.1249	C10H20N2O6	0.60	2.00	471.2666	C18H40N4O10	0.56	2.22
264.0667	C16H11NO3	0.19	0.69	471.3797	C26H52N2O5	0.19	2.00
264.0727	C9H15NO8	0.89	1.67	473.3226	C24H46N2O7	0.29	1.92
264.1453	C11H23NO6	0.55	2.09	474.0977	C29H17NO6	0.21	0.59
265.0462	C11H10N2O6	0.55	0.91	475.1211	C18H24N2O13	0.72	1.33
265.1041	C9H18N2O7	0.78	2.00	476.0043	C26H7NO9	0.35	0.27
266.0783	C11H13N3O5	0.45	1.18	476.1106	C24H19N3O8	0.33	0.79
266.1399	C14H21NO4	0.29	1.50	477.0104	C24H6N4O8	0.33	0.25
267.0043	C13H4N2O5	0.38	0.31	479.1160	C17H24N2O14	0.82	1.41
267.0105	C6H8N2O10	1.67	1.33	481.1566	C32H22N2O3	0.09	0.69
268.0978	C16H15NO3	0.19	0.94	481.1629	C13H30N4O15	1.15	2.31
268.1553	C14H23NO4	0.29	1.64	482.1454	C25H25NO9	0.36	1.00
268.1917	C15H27NO3	0.20	1.80	483.1526	C23H24N4O8	0.35	1.04
270.1348	C13H21NO5	0.38	1.62	484.3019	C24H43N3O7	0.29	1.79
270.1711	C14H25NO4	0.29	1.79	484.3637	C27H51NO6	0.22	1.89
271.0320	C8H8N4O7	0.88	1.00	486.1989	C22H33NO11	0.50	1.50
271.0419	C6H12N2O10	1.67	2.00	487.0359	C31H8N2O5	0.16	0.26
271.1664	C13H24N2O4	0.31	1.85	487.2198	C24H32N4O7	0.29	1.33
272.0566	C14H11NO5	0.36	0.79	488.3696	C25H51N3O6	0.24	2.04
272.1869	C14H27NO4	0.29	1.93	489.0012	C14H10N4O16	1.14	0.71
273.0148	C12H6N2O6	0.50	0.50	489.1735	C20H30N2O12	0.60	1.50
273.9997	C12H5NO7	0.58	0.42	489.2023	C28H30N2O6	0.21	1.07
274.0829	C13H13N3O4	0.31	1.00	491.1209	C24H20N4O8	0.33	0.83
274.1297	C12H21NO6	0.50	1.75	492.1869	C24H31NO10	0.42	1.29
274.1661	C13H25NO5	0.38	1.92	493.1162	C27H18N4O6	0.22	0.67
275.0516	C9H12N2O8	0.89	1.33	493.1167	C14H26N2O17	1.21	1.86
275.0670	C13H12N2O5	0.38	0.92	493.1625	C26H26N2O8	0.31	1.00

276.1450	C12H23NO6	0.50	1.92	495.3794	C28H52N2O5	0.18	1.86
276.1562	C11H23N3O5	0.45	2.09	496.3277	C27H47NO7	0.26	1.74
277.1404	C11H22N2O6	0.55	2.00	497.0132	C9H14N4O20	2.22	1.56
278.0518	C9H13NO9	1.00	1.44	497.3344	C25H46N4O6	0.24	1.84
279.0984	C13H16N2O5	0.38	1.23	498.3370	C34H45NO2	0.06	1.32
279.1198	C10H20N2O7	0.70	2.00	498.3540	C26H49N3O6	0.23	1.88
280.0580	C11H11N3O6	0.55	1.00	498.3790	C28H53NO6	0.21	1.89
280.1188	C14H19NO5	0.36	1.36	499.0385	C20H12N4O12	0.60	0.60
280.1402	C11H23NO7	0.64	2.09	499.1215	C20H24N2O13	0.65	1.20
282.0732	C11H13N3O6	0.55	1.18	499.1732	C13H32N4O16	1.23	2.46
282.0980	C13H17NO6	0.46	1.31	500.0626	C26H15NO10	0.38	0.58
282.1345	C14H21NO5	0.36	1.50	500.3124	C28H43N3O5	0.18	1.54
282.1710	C15H25NO4	0.27	1.67	501.0124	C13H14N2O19	1.46	1.08
283.0678	C10H12N4O6	0.60	1.20	502.0577	C29H13NO8	0.28	0.45
283.2026	C15H28N2O3	0.20	1.87	504.1420	C26H23N3O8	0.31	0.88
284.1138	C13H19NO6	0.46	1.46	504.2093	C22H35NO12	0.55	1.59
284.1500	C14H23NO5	0.36	1.64	504.9862	C15H10N2O18	1.20	0.67
284.1867	C15H27NO4	0.27	1.80	509.0012	C24H6N4O10	0.42	0.25
285.0005	C9H6N2O9	1.00	0.67	509.0013	C11H14N2O21	1.91	1.27
285.1456	C13H22N2O5	0.38	1.69	511.0114	C18H12N2O16	0.89	0.67
286.0828	C14H13N3O4	0.29	0.93	512.3338	C26H47N3O7	0.27	1.81
286.2026	C15H29NO4	0.27	1.93	513.1887	C26H30N2O9	0.35	1.15
288.0151	C13H7NO7	0.54	0.54	513.1899	C14H34N4O16	1.14	2.43
288.1452	C13H23NO6	0.46	1.77	513.3899	C28H54N2O6	0.21	1.93
288.2182	C15H31NO4	0.27	2.07	514.3242	C23H49NO11	0.48	2.13
289.0209	C11H6N4O6	0.55	0.55	514.3865	C27H53N3O6	0.22	1.96
289.0461	C13H10N2O6	0.46	0.77	515.0063	C17H12N2O17	1.00	0.71
289.0576	C12H10N4O5	0.42	0.83	519.1784	C16H32N4O15	0.94	2.00
289.1406	C12H22N2O6	0.50	1.83	520.4118	C30H55N3O4	0.13	1.83
290.0672	C14H13NO6	0.43	0.93	524.0804	C20H19N3O14	0.70	0.95
290.1399	C16H21NO4	0.25	1.31	525.1810	C34H26N2O4	0.12	0.76
290.1610	C13H25NO6	0.46	1.92	526.3492	C27H49N3O7	0.26	1.81
290.1973	C14H29NO5	0.36	2.07	527.3328	C27H48N2O8	0.30	1.78
291.0101	C8H8N2O10	1.25	1.00	529.1483	C13H30N4O18	1.38	2.31
291.1197	C11H20N2O7	0.64	1.82	530.1999	C22H33N3O12	0.55	1.50
292.1039	C11H19NO8	0.73	1.73	530.2115	C38H29NO2	0.05	0.76
293.0257	C8H10N2O10	1.25	1.25	531.2134	C30H32N2O7	0.23	1.07
293.1354	C11H22N2O7	0.64	2.00	531.9953	C28H7NO11	0.39	0.25
293.1467	C10H22N4O6	0.60	2.20	531.9963	C16H11N3O18	1.13	0.69
294.1195	C11H21NO8	0.73	1.91	536.0220	C23H11N3O13	0.57	0.48
296.1866	C16H27NO4	0.25	1.69	537.3899	C30H54N2O6	0.20	1.80
297.1818	C15H26N2O4	0.27	1.73	538.0120	C20H13NO17	0.85	0.65
298.0110	C13H5N3O6	0.46	0.38	538.0130	C8H17N3O24	3.00	2.13
298.1295	C14H21NO6	0.43	1.50	538.0197	C31H9NO9	0.29	0.29
298.2020	C16H29NO4	0.25	1.81	539.1198	C28H20N4O8	0.29	0.71
299.1610	C14H24N2O5	0.36	1.71	540.3652	C28H51N3O7	0.25	1.82
299.1973	C15H28N2O4	0.27	1.87	541.0365	C23H14N2O14	0.61	0.61
300.0002	C10H7NO10	1.00	0.70	547.1269	C30H20N4O7	0.23	0.67
300.1237	C17H19NO4	0.24	1.12	547.1272	C17H28N2O18	1.06	1.65

300.2179	C16H31NO4	0.25	1.94	549.1026	C11H26N4O21	1.91	2.36
301.1038	C12H18N2O7	0.58	1.50	549.1042	C29H18N4O8	0.28	0.62
302.0003	C6H9NO13	2.17	1.50	549.1659	C32H26N2O7	0.22	0.81
302.0050	C12H5N3O7	0.58	0.42	549.2962	C32H42N2O6	0.19	1.31
302.0307	C14H9NO7	0.50	0.64	550.1054	C33H17N3O6	0.18	0.52
302.1607	C14H25NO6	0.43	1.79	551.1091	C30H20N2O9	0.30	0.67
302.1974	C15H29NO5	0.33	1.93	554.3446	C28H49N3O8	0.29	1.75
304.1401	C13H23NO7	0.54	1.77	554.3802	C29H53N3O7	0.24	1.83
304.1765	C14H27NO6	0.43	1.93	555.3643	C29H52N2O8	0.28	1.79
304.1877	C13H27N3O5	0.38	2.08	558.3755	C28H53N3O8	0.29	1.89
304.2128	C15H31NO5	0.33	2.07	561.1323	C20H26N4O15	0.75	1.30
305.0257	C9H10N2O10	1.11	1.11	567.1636	C16H32N4O18	1.13	2.00
305.1351	C12H22N2O7	0.58	1.83	568.3961	C30H55N3O7	0.23	1.83
306.0625	C14H13NO7	0.50	0.93	570.3274	C29H49NO10	0.34	1.69
306.1191	C12H21NO8	0.67	1.75	571.0378	C26H12N4O12	0.46	0.46
306.1557	C13H25NO7	0.54	1.92	575.1181	C13H28N4O21	1.62	2.15
306.1707	C17H25NO4	0.24	1.47	576.9879	C9H14N4O25	2.78	1.56
307.1512	C12H24N2O7	0.58	2.00	582.4114	C31H57N3O7	0.23	1.84
308.0985	C11H19NO9	0.82	1.73	583.1934	C29H32N2O11	0.38	1.10
308.1865	C17H27NO4	0.24	1.59	583.1948	C17H36N4O18	1.06	2.12
308.2231	C18H31NO3	0.17	1.72	584.3075	C29H47NO11	0.38	1.62
309.0569	C9H14N2O10	1.11	1.56	588.3612	C26H55NO13	0.50	2.12
309.0723	C13H14N2O7	0.54	1.08	593.0064	C24H10N4O15	0.63	0.42
310.1773	C15H25N3O4	0.27	1.67	593.1284	C13H30N4O22	1.69	2.31
310.2021	C17H29NO4	0.24	1.71	593.1303	C31H22N4O9	0.29	0.71
311.0060	C13H4N4O6	0.46	0.31	595.0030	C14H16N2O24	1.71	1.14
311.0516	C12H12N2O8	0.67	1.00	596.4026	C29H59NO11	0.38	2.03
312.2179	C17H31NO4	0.24	1.82	597.3872	C30H54N4O8	0.27	1.80
314.2336	C17H33NO4	0.24	1.94	598.3012	C33H45NO9	0.27	1.36
314.2699	C18H37NO3	0.17	2.06	603.0059	C29H8N4O12	0.41	0.28
315.1557	C14H24N2O6	0.43	1.71	603.0345	C19H16N4O19	1.00	0.84
316.0462	C15H11NO7	0.47	0.73	604.3184	C38H43N3O4	0.11	1.13
316.1763	C15H27NO6	0.40	1.80	605.0290	C22H14N4O17	0.77	0.64
319.0413	C10H12N2O10	1.00	1.20	605.0314	C27H14N2O15	0.56	0.52
319.2027	C18H28N2O3	0.17	1.56	606.0331	C19H17N3O20	1.05	0.89
320.0580	C6H15N3O12	2.00	2.50	608.4523	C35H63NO7	0.20	1.80
320.1715	C14H27NO7	0.50	1.93	609.3398	C31H50N2O10	0.32	1.61
321.0260	C15H6N4O5	0.33	0.40	611.0177	C24H12N4O16	0.67	0.50
322.1656	C17H25NO5	0.29	1.47	613.0136	C14H18N2O25	1.79	1.29
322.2020	C18H29NO4	0.22	1.61	621.3916	C37H54N2O6	0.16	1.46
323.0059	C14H4N4O6	0.43	0.29	622.2758	C33H41N3O9	0.27	1.24
323.2338	C18H32N2O3	0.17	1.78	625.2410	C32H38N2O11	0.34	1.19
324.2180	C18H31NO4	0.22	1.72	625.3867	C36H54N2O7	0.19	1.50
325.0217	C14H6N4O6	0.43	0.43	639.3032	C33H44N4O9	0.27	1.33
325.1766	C16H26N2O5	0.31	1.63	646.2935	C39H41N3O6	0.15	1.05
326.0159	C12H9NO10	0.83	0.75	649.0282	C21H18N2O22	1.05	0.86
326.1971	C17H29NO5	0.29	1.71	657.5048	C36H70N2O8	0.22	1.94
326.2334	C18H33NO4	0.22	1.83	661.3808	C34H54N4O9	0.26	1.59
327.0004	C13H4N4O7	0.54	0.31	669.0636	C32H18N2O15	0.47	0.56

327.0367	C14H8N4O6	0.43	0.57	671.0218	C34H12N2O14	0.41	0.35
327.1924	C16H28N2O5	0.31	1.75	685.0296	C12H22N4O29	2.42	1.83
327.2286	C17H32N2O4	0.24	1.88	691.0464	C34H16N2O15	0.44	0.47
328.1763	C16H27NO6	0.38	1.69	695.2980	C40H44N2O9	0.23	1.10
328.2490	C18H35NO4	0.22	1.94	695.5073	C35H72N2O11	0.31	2.06
329.0168	C13H6N4O7	0.54	0.46	699.3022	C38H44N4O9	0.24	1.16
330.1920	C16H29NO6	0.38	1.81	701.0022	C27H14N2O21	0.78	0.52
330.2283	C17H33NO5	0.29	1.94	701.0031	C15H18N4O28	1.87	1.20
330.9908	C6H8N2O14	2.33	1.33	704.2871	C30H47N3O16	0.53	1.57
331.2237	C16H32N2O5	0.31	2.00	713.4717	C36H66N4O10	0.28	1.83
332.1716	C15H27NO7	0.47	1.80	714.1223	C34H25N3O15	0.44	0.74
332.2187	C15H31N3O5	0.33	2.07	714.1231	C21H33NO26	1.24	1.57
332.2441	C17H35NO5	0.29	2.06	714.1240	C39H25NO13	0.33	0.64
334.0740	C7H17N3O12	1.71	2.43	714.4745	C33H69N3O13	0.39	2.09
334.1657	C18H25NO5	0.28	1.39	715.1290	C19H32N4O25	1.32	1.68
334.1873	C15H29NO7	0.47	1.93	715.4707	C32H68N4O13	0.41	2.13
335.0267	C12H8N4O8	0.67	0.67	717.1353	C38H26N2O13	0.34	0.68
335.0418	C16H8N4O5	0.31	0.50	723.5008	C36H72N2O12	0.33	2.00
336.0210	C10H11NO12	1.20	1.10	725.5075	C38H70N4O9	0.24	1.84
336.0304	C21H7NO4	0.19	0.33	726.5111	C35H73N3O12	0.34	2.09
337.0212	C15H6N4O6	0.40	0.40	729.5734	C39H78N4O8	0.21	2.00
337.1005	C10H18N4O9	0.90	1.80	738.1149	C30H29NO21	0.70	0.97
338.2334	C19H33NO4	0.21	1.74	740.4926	C35H71N3O13	0.37	2.03

Table S5: Negative ESI mode UHRMS data for all detected CHOS compounds on SOA filter samples from the ATTO site. Compounds, which were detected only once, are excluded.

<i>m/z</i> [M-H] ⁻	Elemental composition	O/C	H/C	<i>m/z</i> [M-H] ⁻	Elemental composition	O/C	H/C
105.0015	C3H6O2S	0.67	2.00	299.0083	C8H12O10S	1.25	1.50
134.9755	C3H4O4S	1.33	1.33	299.0382	C16H12O4S	0.25	0.75
136.9914	C3H6O4S	1.33	2.00	299.0440	C9H16O9S	1.00	1.78
139.0070	C3H8O4S	1.33	2.67	299.0747	C17H16O3S	0.18	0.94
142.9806	C5H4O3S	0.60	0.80	299.0805	C10H20O8S	0.80	2.00
148.9701	C7H2O2S	0.29	0.29	299.0953	C14H20O5S	0.36	1.43
149.0275	C5H10O3S	0.60	2.00	299.1324	C15H24O4S	0.27	1.60
149.0643	C6H14O2S	0.33	2.33	300.9488	C10H6O7S2	0.70	0.60
151.0069	C4H8O4S	1.00	2.00	300.9655	C10H6O9S	0.90	0.60
152.9862	C3H6O5S	1.67	2.00	301.0240	C8H14O10S	1.25	1.75
155.0020	C3H8O5S	1.67	2.67	301.0536	C16H14O4S	0.25	0.88
156.9964	C6H6O3S	0.50	1.00	301.0602	C9H18O9S	1.00	2.00
163.0434	C6H12O3S	0.50	2.00	301.0968	C10H22O8S	0.80	2.20
164.9863	C4H6O5S	1.25	1.50	301.1111	C14H22O5S	0.36	1.57
167.0018	C4H8O5S	1.25	2.00	302.9645	C10H8O7S2	0.70	0.80
167.0383	C5H12O4S	0.80	2.40	303.0397	C8H16O10S	1.25	2.00
169.0175	C4H10O5S	1.25	2.50	303.0751	C9H20O9S	1.00	2.22
170.9758	C6H4O4S	0.67	0.67	303.1996	C16H32O3S	0.19	2.00
171.0121	C7H8O3S	0.43	1.14	304.9583	C13H6O5S2	0.38	0.46
177.0227	C6H10O4S	0.67	1.67	305.0310	C15H14O3S2	0.20	0.93

177.0589	C7H14O3S	0.43	2.00	305.0641	C19H14O2S	0.11	0.74
178.9655	C4H4O6S	1.50	1.00	306.9376	C12H4O6S2	0.50	0.33
179.0020	C5H8O5S	1.00	1.60	307.0283	C14H12O6S	0.43	0.86
179.0382	C6H12O4S	0.67	2.00	307.0342	C7H16O11S	1.57	2.29
180.9812	C4H6O6S	1.50	1.50	307.0466	C15H16O3S2	0.20	1.07
181.0176	C5H10O5S	1.00	2.00	307.0499	C11H16O8S	0.73	1.45
182.9968	C4H8O6S	1.50	2.00	307.0851	C12H20O7S	0.58	1.67
183.0121	C8H8O3S	0.38	1.00	307.1582	C14H28O5S	0.36	2.00
183.0332	C5H12O5S	1.00	2.40	307.1944	C15H32O4S	0.27	2.13
185.0126	C4H10O6S	1.50	2.50	309.0138	C6H14O12S	2.00	2.33
185.0276	C8H10O3S	0.38	1.25	309.0955	C19H18O2S	0.11	0.95
186.9860	C10H4O2S	0.20	0.40	309.1739	C14H30O5S	0.36	2.14
188.9863	C6H6O5S	0.83	1.00	310.9473	C15H4O4S2	0.27	0.27
191.0748	C8H16O3S	0.38	2.00	311.0227	C13H12O7S	0.54	0.92
191.1110	C9H20O2S	0.22	2.22	311.0441	C10H16O9S	0.90	1.60
192.9812	C5H6O6S	1.20	1.20	311.1319	C16H24O4S	0.25	1.50
193.0539	C7H14O4S	0.57	2.00	311.1686	C17H28O3S	0.18	1.65
193.0902	C8H18O3S	0.38	2.25	313.0241	C9H14O10S	1.11	1.56
194.9968	C5H8O6S	1.20	1.60	313.0537	C17H14O4S	0.24	0.82
195.0156	C6H12O3S2	0.50	2.00	313.0598	C10H18O9S	0.90	1.80
195.0330	C6H12O5S	0.83	2.00	313.0783	C11H22O6S2	0.55	2.00
195.0695	C7H16O4S	0.57	2.29	313.0967	C11H22O8S	0.73	2.00
196.9762	C4H6O7S	1.75	1.50	313.1112	C15H22O5S	0.33	1.47
197.0124	C5H10O6S	1.20	2.00	313.1479	C16H26O4S	0.25	1.63
197.0489	C6H14O5S	0.83	2.33	314.9645	C11H8O7S2	0.64	0.73
198.9918	C4H8O7S	1.75	2.00	315.0396	C9H16O10S	1.11	1.78
199.0069	C8H8O4S	0.50	1.00	315.0756	C10H20O9S	0.90	2.00
199.0280	C5H12O6S	1.20	2.40	316.9590	C14H6O5S2	0.36	0.43
199.0434	C9H12O3S	0.33	1.33	317.0190	C8H14O11S	1.38	1.75
200.9862	C7H6O5S	0.71	0.86	317.0488	C16H14O5S	0.31	0.88
201.0017	C11H6O2S	0.18	0.55	317.0695	C13H18O7S	0.54	1.38
201.0074	C4H10O7S	1.75	2.50	317.0907	C10H22O9S	0.90	2.20
203.0174	C11H8O2S	0.18	0.73	317.1422	C15H26O5S	0.33	1.73
203.1108	C10H20O2S	0.20	2.00	319.0344	C8H16O11S	1.38	2.00
206.9967	C6H8O6S	1.00	1.33	319.0647	C16H16O5S	0.31	1.00
207.0120	C10H8O3S	0.30	0.80	319.0798	C20H16O2S	0.10	0.80
207.0333	C7H12O5S	0.71	1.71	319.1221	C14H24O6S	0.43	1.71
207.0696	C8H16O4S	0.50	2.00	319.1946	C16H32O4S	0.25	2.00
207.1059	C9H20O3S	0.33	2.22	321.0799	C16H18O5S	0.31	1.13
208.9372	C8H2O3S2	0.38	0.25	321.1739	C15H30O5S	0.33	2.00
208.9761	C5H6O7S	1.40	1.20	321.2105	C16H34O4S	0.25	2.13
209.0126	C6H10O6S	1.00	1.67	322.9931	C6H12O13S	2.17	2.00
209.0489	C7H14O5S	0.71	2.00	323.1107	C20H20O2S	0.10	1.00
209.0852	C8H18O4S	0.50	2.25	323.1534	C14H28O6S	0.43	2.00
210.9917	C5H8O7S	1.40	1.60	323.1893	C15H32O5S	0.33	2.13
211.0281	C6H12O6S	1.00	2.00	325.0229	C10H14O10S	1.00	1.40
211.0646	C7H16O5S	0.71	2.29	325.1111	C16H22O5S	0.31	1.38
213.0073	C5H10O7S	1.40	2.00	325.1475	C17H26O4S	0.24	1.53
213.0226	C9H10O4S	0.44	1.11	325.1686	C14H30O6S	0.43	2.14

215.0174	C12H8O2S	0.17	0.67	325.1839	C18H30O3S	0.17	1.67
215.0231	C5H12O7S	1.40	2.40	326.9599	C15H4O7S	0.47	0.27
217.0176	C8H10O5S	0.63	1.25	326.9645	C12H8O7S2	0.58	0.67
218.9789	C7H8O4S2	0.57	1.14	327.0178	C13H12O8S	0.62	0.92
221.0123	C7H10O6S	0.86	1.43	327.0364	C14H16O5S2	0.36	1.14
221.0644	C12H14O2S	0.17	1.17	327.0391	C10H16O10S	1.00	1.60
221.1215	C10H22O3S	0.30	2.20	327.0761	C11H20O9S	0.82	1.82
222.9528	C9H4O3S2	0.33	0.44	327.1268	C16H24O5S	0.31	1.50
223.0282	C7H12O6S	0.86	1.71	327.1633	C17H28O4S	0.24	1.65
223.0646	C8H16O5S	0.63	2.00	328.9946	C16H10O4S2	0.25	0.63
223.1008	C9H20O4S	0.44	2.22	329.0551	C10H18O10S	1.00	1.80
224.9686	C9H6O3S2	0.33	0.67	329.0851	C18H18O4S	0.22	1.00
225.0074	C6H10O7S	1.17	1.67	329.1425	C16H26O5S	0.31	1.63
225.0438	C7H14O6S	0.86	2.00	329.2160	C18H34O3S	0.17	1.89
225.0802	C8H18O5S	0.63	2.25	331.0342	C9H16O11S	1.22	1.78
226.9868	C5H8O8S	1.60	1.60	332.9928	C11H10O10S	0.91	0.91
227.0174	C13H8O2S	0.15	0.62	333.0224	C19H10O4S	0.21	0.53
227.0232	C6H12O7S	1.17	2.00	333.0500	C9H18O11S	1.22	2.00
227.0384	C10H12O4S	0.40	1.20	333.0589	C20H14O3S	0.15	0.70
227.0593	C7H16O6S	0.86	2.29	333.0856	C10H22O10S	1.00	2.20
228.9965	C12H6O3S	0.25	0.50	335.0177	C22H8O2S	0.09	0.36
229.0028	C5H10O8S	1.60	2.00	336.9335	C9H6O10S2	1.11	0.67
229.0328	C13H10O2S	0.15	0.77	337.0235	C11H14O10S	0.91	1.27
229.0386	C6H14O7S	1.17	2.33	337.0452	C8H18O12S	1.50	2.25
229.0540	C10H14O4S	0.40	1.40	337.0903	C20H18O3S	0.15	0.90
231.0122	C12H8O3S	0.25	0.67	337.1266	C21H22O2S	0.10	1.05
231.0181	C5H12O8S	1.60	2.40	337.1324	C14H26O7S	0.50	1.86
231.0484	C13H12O2S	0.15	0.92	337.2051	C16H34O5S	0.31	2.13
233.0489	C9H14O5S	0.56	1.56	339.0032	C10H12O11S	1.10	1.20
233.1581	C12H26O2S	0.17	2.17	339.0539	C15H16O7S	0.47	1.07
235.0646	C9H16O5S	0.56	1.78	339.0755	C12H20O9S	0.75	1.67
235.1008	C10H20O4S	0.40	2.00	339.1631	C18H28O4S	0.22	1.56
235.1374	C11H24O3S	0.27	2.18	339.1844	C15H32O6S	0.40	2.13
237.0075	C7H10O7S	1.00	1.43	339.1997	C19H32O3S	0.16	1.68
237.0440	C8H14O6S	0.75	1.75	341.0492	C18H14O5S	0.28	0.78
237.0801	C9H18O5S	0.56	2.00	341.0546	C11H18O10S	0.91	1.64
237.1166	C10H22O4S	0.40	2.20	341.1426	C17H26O5S	0.29	1.53
238.9842	C10H8O3S2	0.30	0.80	341.1792	C18H30O4S	0.22	1.67
238.9867	C6H8O8S	1.33	1.33	343.1583	C17H28O5S	0.29	1.65
239.0175	C14H8O2S	0.14	0.57	343.2313	C19H36O3S	0.16	1.89
239.0230	C7H12O7S	1.00	1.71	345.1011	C15H22O7S	0.47	1.47
239.0596	C8H16O6S	0.75	2.00	346.9389	C7H8O12S2	1.71	1.14
241.0025	C6H10O8S	1.33	1.67	347.1534	C16H28O6S	0.38	1.75
241.0331	C14H10O2S	0.14	0.71	349.0596	C13H18O9S	0.69	1.38
241.0388	C7H14O7S	1.00	2.00	349.1114	C18H22O5S	0.28	1.22
241.0541	C11H14O4S	0.36	1.27	349.1320	C15H26O7S	0.47	1.73
241.0749	C8H18O6S	0.75	2.25	350.9489	C10H8O10S2	1.00	0.80
242.9432	C8H4O5S2	0.63	0.50	351.0397	C12H16O10S	0.83	1.33
242.9815	C5H8O9S	1.80	1.60	351.1847	C16H32O6S	0.38	2.00

243.0122	C13H8O3S	0.23	0.62	351.2206	C17H36O5S	0.29	2.12
243.0179	C6H12O8S	1.33	2.00	353.0120	C18H10O6S	0.33	0.56
243.0330	C10H12O5S	0.50	1.20	353.0279	C22H10O3S	0.14	0.45
243.0486	C14H12O2S	0.14	0.86	353.0694	C16H18O7S	0.44	1.13
244.9794	C5H10O7S2	1.40	2.00	353.0915	C13H22O9S	0.69	1.69
244.9973	C5H10O9S	1.80	2.00	353.1423	C18H26O5S	0.28	1.44
245.0280	C13H10O3S	0.23	0.77	353.1789	C19H30O4S	0.21	1.58
245.0335	C6H14O8S	1.33	2.33	353.2005	C16H34O6S	0.38	2.13
245.0488	C10H14O5S	0.50	1.40	353.2150	C20H34O3S	0.15	1.70
247.0433	C13H12O3S	0.23	0.92	355.0705	C12H20O10S	0.83	1.67
247.0646	C10H16O5S	0.50	1.60	355.1578	C18H28O5S	0.28	1.56
249.0803	C10H18O5S	0.50	1.80	355.1947	C19H32O4S	0.21	1.68
249.1529	C12H26O3S	0.25	2.17	355.2317	C20H36O3S	0.15	1.80
250.9842	C11H8O3S2	0.27	0.73	357.0646	C15H18O8S	0.53	1.20
251.0175	C15H8O2S	0.13	0.53	357.1379	C17H26O6S	0.35	1.53
251.0230	C8H12O7S	0.88	1.50	357.1739	C18H30O5S	0.28	1.67
251.0595	C9H16O6S	0.67	1.78	359.0752	C22H16O3S	0.14	0.73
251.0959	C10H20O5S	0.50	2.00	359.2626	C20H40O3S	0.15	2.00
251.1321	C11H24O4S	0.36	2.18	361.0170	C20H10O5S	0.25	0.50
252.9636	C10H6O4S2	0.40	0.60	361.0448	C10H18O12S	1.20	1.80
253.0025	C7H10O8S	1.14	1.43	361.0908	C22H18O3S	0.14	0.82
253.0330	C15H10O2S	0.13	0.67	361.2053	C18H34O5S	0.28	1.89
253.0385	C8H14O7S	0.88	1.75	361.2783	C20H42O3S	0.15	2.10
253.0750	C9H18O6S	0.67	2.00	362.9644	C15H8O7S2	0.47	0.53
254.9793	C10H8O4S2	0.40	0.80	363.1479	C16H28O7S	0.44	1.75
255.0181	C7H12O8S	1.14	1.71	364.9763	C18H6O7S	0.39	0.33
255.0487	C15H12O2S	0.13	0.80	365.1215	C22H22O3S	0.14	1.00
255.0697	C12H16O4S	0.33	1.33	367.1794	C16H32O7S	0.44	2.00
255.0728	C9H20O4S2	0.44	2.22	367.2158	C17H36O6S	0.35	2.12
256.9759	C9H6O7S	0.78	0.67	369.0801	C20H18O5S	0.25	0.90
256.9974	C6H10O9S	1.50	1.67	369.0859	C13H22O10S	0.77	1.69
257.0281	C14H10O3S	0.21	0.71	373.0961	C16H22O8S	0.50	1.38
257.0337	C7H14O8S	1.14	2.00	373.1322	C17H26O7S	0.41	1.53
257.0487	C11H14O5S	0.45	1.27	373.2416	C20H38O4S	0.20	1.90
257.0644	C15H14O2S	0.13	0.93	375.1845	C18H32O6S	0.33	1.78
259.0134	C6H12O9S	1.50	2.00	377.0486	C21H14O5S	0.24	0.67
259.0492	C7H16O8S	1.14	2.29	377.0694	C18H18O7S	0.39	1.00
260.9743	C5H10O8S2	1.60	2.00	377.2003	C18H34O6S	0.33	1.89
261.0073	C9H10O7S	0.78	1.11	377.2735	C20H42O4S	0.20	2.10
261.0226	C13H10O4S	0.31	0.77	378.9611	C11H8O13S	1.18	0.73
261.0593	C14H14O3S	0.21	1.00	379.0429	C24H12O3S	0.13	0.50
262.9321	C7H4O7S2	1.00	0.57	379.0702	C14H20O10S	0.71	1.43
262.9897	C5H12O8S2	1.60	2.40	379.1583	C20H28O5S	0.25	1.40
263.0594	C10H16O6S	0.60	1.60	379.2157	C18H36O6S	0.33	2.00
263.1324	C12H24O4S	0.33	2.00	380.9764	C11H10O13S	1.18	0.91
265.0751	C10H18O6S	0.60	1.80	381.0594	C24H14O3S	0.13	0.58
265.1474	C12H26O4S	0.33	2.17	381.1735	C20H30O5S	0.25	1.50
266.9601	C10H4O7S	0.70	0.40	381.2312	C18H38O6S	0.33	2.11
267.0179	C8H12O8S	1.00	1.50	383.1019	C14H24O10S	0.71	1.71

267.0544	C9H16O7S	0.78	1.78	383.2107	C17H36O7S	0.41	2.12
267.0907	C10H20O6S	0.60	2.00	385.0452	C12H18O12S	1.00	1.50
268.9758	C10H6O7S	0.70	0.60	385.1176	C14H26O10S	0.71	1.86
269.0340	C8H14O8S	1.00	1.75	387.1121	C17H24O8S	0.47	1.41
269.0644	C16H14O2S	0.13	0.88	389.1635	C18H30O7S	0.39	1.67
269.0854	C13H18O4S	0.31	1.38	391.0134	C17H12O9S	0.53	0.71
269.1060	C10H22O6S	0.60	2.20	391.0494	C18H16O8S	0.44	0.89
271.0134	C7H12O9S	1.29	1.71	391.1065	C16H24O9S	0.56	1.50
271.0438	C15H12O3S	0.20	0.80	391.2526	C20H40O5S	0.25	2.00
271.0644	C12H16O5S	0.42	1.33	393.1010	C19H22O7S	0.37	1.16
271.1373	C14H24O3S	0.21	1.71	393.1528	C24H26O3S	0.13	1.08
272.9706	C9H6O8S	0.89	0.67	395.0800	C18H20O8S	0.44	1.11
273.0227	C14H10O4S	0.29	0.71	395.1019	C15H24O10S	0.67	1.60
273.0288	C7H14O9S	1.29	2.00	395.1892	C21H32O5S	0.24	1.52
273.0652	C8H18O8S	1.00	2.25	395.2467	C19H40O6S	0.32	2.11
273.0801	C12H18O5S	0.42	1.50	396.9712	C11H10O14S	1.27	0.91
275.0230	C10H12O7S	0.70	1.20	397.1118	C22H22O5S	0.23	1.00
275.1686	C14H28O3S	0.21	2.00	397.2262	C18H38O7S	0.39	2.11
276.9965	C16H6O3S	0.19	0.38	399.1268	C22H24O5S	0.23	1.09
277.0171	C13H10O5S	0.38	0.77	401.1487	C15H30O10S	0.67	2.00
277.0239	C6H14O10S	1.67	2.33	405.0069	C21H10O7S	0.33	0.48
277.0331	C17H10O2S	0.12	0.59	405.0651	C19H18O8S	0.42	0.95
277.1114	C12H22O5S	0.42	1.83	407.1021	C16H24O10S	0.63	1.50
277.1844	C14H30O3S	0.21	2.14	409.0178	C24H10O5S	0.21	0.42
278.9602	C11H4O7S	0.64	0.36	409.0958	C19H22O8S	0.42	1.16
278.9844	C5H12O9S2	1.80	2.40	409.1682	C21H30O6S	0.29	1.43
279.0154	C13H12O3S2	0.23	0.92	411.1114	C19H24O8S	0.42	1.26
279.0545	C10H16O7S	0.70	1.60	411.1844	C21H32O6S	0.29	1.52
279.0905	C11H20O6S	0.55	1.82	411.2418	C19H40O7S	0.37	2.11
279.1271	C12H24O5S	0.42	2.00	412.9662	C11H10O15S	1.36	0.91
279.1633	C13H28O4S	0.31	2.15	413.1491	C16H30O10S	0.63	1.88
280.9589	C11H6O5S2	0.45	0.55	414.9980	C15H12O12S	0.80	0.80
280.9946	C12H10O4S2	0.33	0.83	416.9614	C10H10O16S	1.60	1.00
281.0277	C16H10O3S	0.19	0.63	423.0698	C26H16O4S	0.15	0.62
281.0336	C9H14O8S	0.89	1.56	423.0751	C19H20O9S	0.47	1.05
281.0699	C10H18O7S	0.70	1.80	423.1335	C17H28O10S	0.59	1.65
281.1065	C11H22O6S	0.55	2.00	424.9662	C12H10O15S	1.25	0.83
281.1428	C12H26O5S	0.42	2.17	425.1432	C24H26O5S	0.21	1.08
282.9746	C11H8O5S2	0.45	0.73	425.2572	C20H42O7S	0.35	2.10
283.0130	C8H12O9S	1.13	1.50	429.1013	C22H22O7S	0.32	1.00
283.0493	C9H16O8S	0.89	1.78	429.1946	C21H34O7S	0.33	1.62
283.0678	C10H20O5S2	0.50	2.00	435.1477	C22H28O7S	0.32	1.27
283.0798	C17H16O2S	0.12	0.94	437.1640	C22H30O7S	0.32	1.36
283.0856	C10H20O7S	0.70	2.00	441.0139	C17H14O12S	0.71	0.82
283.1010	C14H20O4S	0.29	1.43	441.0800	C26H18O5S	0.19	0.69
283.1372	C15H24O3S	0.20	1.60	441.2520	C20H42O8S	0.40	2.10
284.9686	C14H6O3S2	0.21	0.43	443.1958	C18H36O10S	0.56	2.00
284.9896	C11H10O5S2	0.45	0.91	444.9720	C15H10O14S	0.93	0.67
284.9926	C7H10O10S	1.43	1.43	445.1540	C20H30O9S	0.45	1.50

285.0291	C8H14O9S	1.13	1.75	453.0347	C15H18O14S	0.93	1.20
285.0591	C16H14O3S	0.19	0.88	456.9868	C20H10O11S	0.55	0.50
285.0655	C9H18O8S	0.89	2.00	459.0903	C26H20O6S	0.23	0.77
285.0954	C17H18O2S	0.12	1.06	460.9821	C19H10O12S	0.63	0.53
285.1166	C14H22O4S	0.29	1.57	462.9972	C19H12O12S	0.63	0.63
286.9861	C10H8O8S	0.80	0.80	465.1016	C25H22O7S	0.28	0.88
287.0084	C7H12O10S	1.43	1.71	467.1745	C23H32O8S	0.35	1.39
287.0383	C15H12O4S	0.27	0.80	469.0748	C27H18O6S	0.22	0.67
287.0443	C8H16O9S	1.13	2.00	469.2835	C22H46O8S	0.36	2.09
288.9655	C9H6O9S	1.00	0.67	471.3517	C27H52O4S	0.15	1.93
289.0176	C14H10O5S	0.36	0.71	473.1482	C21H30O10S	0.48	1.43
289.0208	C11H14O5S2	0.45	1.27	473.1580	C32H26O2S	0.06	0.81
289.0541	C15H14O4S	0.27	0.93	475.1065	C23H24O9S	0.39	1.04
291.0699	C15H16O4S	0.27	1.07	479.1165	C26H24O7S	0.27	0.92
291.1268	C13H24O5S	0.38	1.85	479.1741	C24H32O8S	0.33	1.33
291.1634	C14H28O4S	0.29	2.00	485.2785	C22H46O9S	0.41	2.09
293.0190	C6H14O11S	1.83	2.33	488.9770	C20H10O13S	0.65	0.50
293.0310	C14H14O3S2	0.21	1.00	493.1169	C23H26O10S	0.43	1.13
293.1063	C12H22O6S	0.50	1.83	501.0129	C22H14O12S	0.55	0.64
293.1792	C14H30O4S	0.29	2.14	503.0503	C19H20O14S	0.74	1.05
294.9532	C15H4O3S2	0.20	0.27	513.3099	C24H50O9S	0.38	2.08
294.9744	C12H8O5S2	0.42	0.67	525.1741	C32H30O5S	0.16	0.94
295.0103	C13H12O4S2	0.31	0.92	525.1802	C25H34O10S	0.40	1.36
295.0490	C10H16O8S	0.80	1.60	535.0188	C22H16O14S	0.64	0.73
295.0856	C11H20O7S	0.64	1.82	543.1845	C32H32O6S	0.19	1.00
295.1217	C12H24O6S	0.50	2.00	544.9666	C22H10O15S	0.68	0.45
295.1585	C13H28O5S	0.38	2.15	549.1021	C32H22O7S	0.22	0.69
297.0470	C10H18O6S2	0.60	1.80	553.2841	C29H46O8S	0.28	1.59
297.0590	C17H14O3S	0.18	0.82	574.9563	C26H8O14S	0.54	0.31
297.0646	C10H18O8S	0.80	1.80	585.2893	C33H46O7S	0.21	1.39
297.1166	C15H22O4S	0.27	1.47	587.3569	C38H52O3S	0.08	1.37
297.1528	C16H26O3S	0.19	1.63	594.9621	C29H8O13S	0.45	0.28
298.9694	C11H8O6S2	0.55	0.73	603.0356	C15H24O23S	1.53	1.60
298.9840	C15H8O3S2	0.20	0.53	609.3405	C40H50O3S	0.08	1.25
				616.9724	C21H14O20S	0.95	0.67

Table S6: Negative ESI mode UHRMS data for all detected CHONS compounds on SOA filter samples from the ATTO site. Compounds, which were detected only once, are excluded.

m/z [M-H] ⁻	Elemental composition	O/C	H/C	m/z [M-H] ⁻	Elemental composition	O/C	H/C
133.9918	C3H5NO3S	1.00	1.67	348.2210	C17H35NO4S	0.24	2.06
152.0023	C3H7NO4S	1.33	2.33	350.0124	C10H13N3O7S2	0.70	1.30
164.0023	C4H7NO4S	1.00	1.75	351.1341	C12H24N4O6S	0.50	2.00
164.0387	C5H11NO3S	0.60	2.20	352.0080	C21H7NO3S	0.14	0.33
165.9815	C3H5NO5S	1.67	1.67	353.0118	C10H14N2O8S2	0.80	1.40
166.0178	C4H9NO4S	1.00	2.25	353.0278	C14H14N2O5S2	0.36	1.00
168.0337	C4H11NO4S	1.00	2.75	353.1135	C11H22N4O7S	0.64	2.00
178.0183	C5H9NO4S	0.80	1.80	354.0031	C12H9N3O8S	0.67	0.75

178.0542	C6H13NO3S	0.50	2.17	356.0270	C14H15NO6S2	0.43	1.07
180.0335	C5H11NO4S	0.80	2.20	359.0671	C12H16N4O7S	0.58	1.33
181.9917	C7H5NO3S	0.43	0.71	360.0791	C11H23NO8S2	0.73	2.09
182.0129	C4H9NO5S	1.25	2.25	360.9709	C13H6N4O5S2	0.38	0.46
187.9811	C9H3NO2S	0.22	0.33	362.1218	C22H21NO2S	0.09	0.95
189.9968	C9H5NO2S	0.22	0.56	362.1279	C15H25NO7S	0.47	1.67
196.0107	C5H11NO3S2	0.60	2.20	362.9622	C6H8N2O14S	2.33	1.33
196.0282	C5H11NO5S	1.00	2.20	368.0330	C8H19NO11S2	1.38	2.38
200.0023	C7H7NO4S	0.57	1.00	369.0868	C14H18N4O6S	0.43	1.29
201.9968	C10H5NO2S	0.20	0.50	370.2428	C20H37NO3S	0.15	1.85
204.0126	C10H7NO2S	0.20	0.70	371.0769	C11H20N2O10S	0.91	1.82
206.0491	C7H13NO4S	0.57	1.86	372.0329	C21H11NO4S	0.19	0.52
211.0184	C8H8N2O3S	0.38	1.00	372.0799	C12H23NO8S2	0.67	1.92
211.9812	C11H3NO2S	0.18	0.27	372.1339	C13H27NO9S	0.69	2.08
211.9869	C4H7NO7S	1.75	1.75	373.1546	C15H26N4O5S	0.33	1.73
212.0057	C5H11NO4S2	0.80	2.20	374.0284	C24H9NO2S	0.08	0.38
213.9637	C7H5NO3S2	0.43	0.71	374.1218	C23H21NO2S	0.09	0.91
213.9969	C11H5NO2S	0.18	0.45	376.9831	C13H6N4O8S	0.62	0.46
214.0025	C4H9NO7S	1.75	2.25	379.0429	C16H16N2O5S2	0.31	1.00
216.0127	C11H7NO2S	0.18	0.64	380.1744	C16H31NO7S	0.44	1.94
217.9917	C10H5NO3S	0.30	0.50	381.0544	C19H14N2O5S	0.26	0.74
220.0071	C10H7NO3S	0.30	0.70	381.0590	C16H18N2O5S2	0.31	1.13
223.9481	C8H3NO3S2	0.38	0.38	381.9603	C16H5N3O5S2	0.31	0.31
224.0232	C6H11NO6S	1.00	1.83	383.1026	C15H20N4O6S	0.40	1.33
226.0027	C5H9NO7S	1.40	1.80	384.0585	C16H19NO6S2	0.38	1.19
226.9768	C7H4N2O5S	0.71	0.57	384.9778	C16H6N2O8S	0.50	0.38
228.0184	C5H11NO7S	1.40	2.20	388.2897	C21H43NO3S	0.14	2.05
228.0547	C6H15NO6S	1.00	2.50	391.0136	C18H8N4O5S	0.28	0.44
229.9917	C11H5NO3S	0.27	0.45	392.0918	C17H19N3O6S	0.35	1.12
230.0282	C12H9NO2S	0.17	0.75	393.1807	C15H30N4O6S	0.40	2.00
230.0489	C9H13NO4S	0.44	1.44	393.9675	C6H9N3O15S	2.50	1.50
232.0073	C11H7NO3S	0.27	0.64	394.2268	C18H37NO6S	0.33	2.06
234.0230	C11H9NO3S	0.27	0.82	394.9337	C6H8N2O14S2	2.33	1.33
236.0963	C9H19NO4S	0.44	2.11	396.9710	C16H6N4O5S2	0.31	0.38
237.9640	C9H5NO3S2	0.33	0.56	396.9922	C21H6N2O5S	0.24	0.29
238.0755	C8H17NO5S	0.63	2.13	397.1114	C14H26N2O7S2	0.50	1.86
239.9431	C8H3NO4S2	0.50	0.38	398.0738	C17H21NO6S2	0.35	1.24
240.0126	C13H7NO2S	0.15	0.54	398.2328	C16H37N3O6S	0.38	2.31
241.9977	C5H9NO8S	1.60	1.80	401.0876	C12H22N2O11S	0.92	1.83
242.0282	C13H9NO2S	0.15	0.69	402.1168	C24H21NO3S	0.13	0.88
242.0701	C7H17NO6S	0.86	2.43	403.0047	C8H12N4O13S	1.63	1.50
244.0132	C5H11NO8S	1.60	2.20	404.1742	C18H31NO7S	0.39	1.72
245.0448	C5H14N2O7S	1.40	2.80	408.2058	C18H35NO7S	0.39	1.94
245.9869	C11H5NO4S	0.36	0.45	408.9930	C22H6N2O5S	0.23	0.27
248.0023	C11H7NO4S	0.36	0.64	410.2153	C25H33NO2S	0.08	1.32
249.9637	C10H5NO3S2	0.30	0.50	412.0140	C19H11NO8S	0.42	0.58
249.9968	C14H5NO2S	0.14	0.36	412.2157	C21H35NO5S	0.24	1.67
250.0180	C11H9NO4S	0.36	0.82	413.1130	C16H22N4O7S	0.44	1.38
252.0126	C14H7NO2S	0.14	0.50	415.0199	C13H12N4O10S	0.77	0.92

252.0733	C9H19NO3S2	0.33	2.11	422.2216	C19H37NO7S	0.37	1.95
252.0912	C9H19NO5S	0.56	2.11	423.1338	C18H24N4O6S	0.33	1.33
254.9390	C4H4N2O7S2	1.75	1.00	424.1947	C25H31NO3S	0.12	1.24
254.9874	C12H4N2O3S	0.25	0.33	424.9658	C17H6N4O6S2	0.35	0.35
256.0437	C14H11NO2S	0.14	0.79	426.1124	C21H21N3O5S	0.24	1.00
256.0501	C7H15NO7S	1.00	2.14	428.0924	C20H19N3O6S	0.30	0.95
256.0649	C11H15NO4S	0.36	1.36	428.1742	C20H31NO7S	0.35	1.55
256.0857	C8H19NO6S	0.75	2.38	428.9933	C20H6N4O6S	0.30	0.30
258.0229	C13H9NO3S	0.23	0.69	430.1898	C20H33NO7S	0.35	1.65
260.0023	C12H7NO4S	0.33	0.58	431.1703	C15H32N2O10S	0.67	2.13
260.0083	C5H11NO9S	1.80	2.20	432.1739	C16H35NO8S2	0.50	2.19
260.0386	C13H11NO3S	0.23	0.85	432.2058	C20H35NO7S	0.35	1.75
260.0596	C10H15NO5S	0.50	1.50	437.0080	C20H10N2O8S	0.40	0.50
262.0065	C5H13NO7S2	1.40	2.60	440.1214	C20H27NO6S2	0.30	1.35
262.1120	C11H21NO4S	0.36	1.91	441.0142	C18H10N4O8S	0.44	0.56
264.0124	C15H7NO2S	0.13	0.47	441.0798	C18H22N2O7S2	0.39	1.22
266.9825	C8H4N4O5S	0.63	0.50	441.1698	C20H30N2O7S	0.35	1.50
268.0075	C14H7NO3S	0.21	0.50	442.0389	C24H13NO6S	0.25	0.54
270.0232	C14H9NO3S	0.21	0.64	442.1533	C20H29NO8S	0.40	1.45
271.0139	C8H8N4O5S	0.63	1.00	443.0244	C12H16N2O14S	1.17	1.33
272.0082	C6H11NO9S	1.50	1.83	443.0297	C18H12N4O8S	0.44	0.67
272.0387	C14H11NO3S	0.21	0.79	443.1963	C19H32N4O6S	0.32	1.68
272.9818	C8H6N2O7S	0.88	0.75	443.9642	C22H7NO6S2	0.27	0.32
273.0294	C8H10N4O5S	0.63	1.25	444.3162	C24H47NO4S	0.17	1.96
273.0338	C13H10N2O3S	0.23	0.77	444.9725	C16H6N4O10S	0.63	0.38
273.9599	C7H5N3O5S2	0.71	0.71	446.1810	C15H33N3O10S	0.67	2.20
275.0450	C8H12N4O5S	0.63	1.50	448.1956	C27H31NO3S	0.11	1.15
277.0170	C5H14N2O7S2	1.40	2.80	448.2003	C20H35NO8S	0.40	1.75
282.0230	C15H9NO3S	0.20	0.60	449.0454	C22H14N2O7S	0.32	0.64
282.0595	C16H13NO2S	0.13	0.81	449.1496	C20H26N4O6S	0.30	1.30
284.0444	C8H15NO8S	1.00	1.88	450.0813	C27H17NO4S	0.15	0.63
284.0812	C9H19NO7S	0.78	2.11	451.0190	C28H8N2O3S	0.11	0.29
284.9930	C8H6N4O6S	0.75	0.75	451.0198	C16H12N4O10S	0.63	0.75
285.0294	C9H10N4O5S	0.56	1.11	452.9343	C15H6N2O11S2	0.73	0.40
285.0551	C11H14N2O5S	0.45	1.27	453.0346	C28H10N2O3S	0.11	0.36
286.0967	C9H21NO7S	0.78	2.33	453.0354	C16H14N4O10S	0.63	0.88
286.9646	C5H8N2O8S2	1.60	1.60	453.2061	C22H34N2O6S	0.27	1.55
286.9763	C12H4N2O5S	0.42	0.33	454.0392	C25H13NO6S	0.24	0.52
287.0086	C8H8N4O6S	0.75	1.00	455.2063	C18H36N2O9S	0.50	2.00
288.0334	C14H11NO4S	0.29	0.79	457.1178	C21H22N4O6S	0.29	1.05
288.0400	C7H15NO9S	1.29	2.14	457.9888	C12H13NO16S	1.33	1.08
289.0607	C9H14N4O5S	0.56	1.56	459.1799	C20H32N2O8S	0.40	1.60
289.9729	C7H5N3O8S	1.14	0.71	459.2014	C17H36N2O10S	0.59	2.12
293.0116	C5H14N2O8S2	1.60	2.80	459.2165	C21H36N2O7S	0.33	1.71
294.0229	C16H9NO3S	0.19	0.56	460.9825	C20H6N4O8S	0.40	0.30
294.0653	C10H17NO7S	0.70	1.70	460.9884	C13H10N4O13S	1.00	0.77
294.1379	C12H25NO5S	0.42	2.08	463.9389	C17H7NO11S2	0.65	0.41
295.9539	C7H7NO8S2	1.14	1.00	464.0695	C17H23NO10S2	0.59	1.35
295.9909	C8H11NO7S2	0.88	1.38	465.1805	C21H30N4O6S	0.29	1.43

296.0444	C9H15NO8S	0.89	1.67	466.1704	C14H33N3O12S	0.86	2.36
297.0872	C8H18N4O6S	0.75	2.25	469.1858	C18H34N2O10S	0.56	1.89
297.9339	C6H5NO9S2	1.50	0.83	469.9559	C9H13NO17S2	1.89	1.44
297.9847	C11H9NO5S2	0.45	0.82	474.9626	C7H12N2O20S	2.86	1.71
299.0086	C9H8N4O6S	0.67	0.89	475.1971	C17H36N2O11S	0.65	2.12
299.0450	C10H12N4O5S	0.50	1.20	475.9608	C15H11NO13S2	0.87	0.73
300.0006	C11H11NO5S2	0.45	1.00	477.9443	C20H5N3O8S2	0.40	0.25
301.0243	C9H10N4O6S	0.67	1.11	478.2838	C23H45NO7S	0.30	1.96
301.0607	C10H14N4O5S	0.50	1.40	478.9679	C17H8N2O13S	0.76	0.47
302.0556	C8H17NO9S	1.13	2.13	484.1378	C32H23NO2S	0.06	0.72
304.0278	C6H15N3O7S2	1.17	2.50	484.9723	C23H6N2O9S	0.39	0.26
305.9677	C7H5N3O9S	1.29	0.71	486.1797	C22H33NO9S	0.41	1.50
306.0230	C17H9NO3S	0.18	0.53	489.2021	C20H34N4O8S	0.40	1.70
306.1015	C12H21NO6S	0.50	1.75	503.0504	C32H12N2O3S	0.09	0.38
307.0348	C8H12N4O7S	0.88	1.50	503.0506	C20H16N4O10S	0.50	0.80
308.1174	C12H23NO6S	0.50	1.92	503.1598	C23H28N4O7S	0.30	1.22
309.0545	C13H14N2O5S	0.38	1.08	515.1864	C26H32N2O7S	0.27	1.23
310.0605	C10H17NO8S	0.80	1.70	515.2426	C24H40N2O8S	0.33	1.67
311.1646	C12H28N2O5S	0.42	2.33	520.1374	C35H23NO2S	0.06	0.66
312.0006	C12H11NO5S2	0.42	0.92	525.1808	C26H30N4O6S	0.23	1.15
313.0243	C10H10N4O6S	0.60	1.00	529.2071	C20H38N2O12S	0.60	1.90
313.0606	C11H14N4O5S	0.45	1.27	530.2112	C30H33N3O4S	0.13	1.10
313.1183	C9H22N4O6S	0.67	2.44	531.0452	C33H12N2O4S	0.12	0.36
314.0699	C13H17NO6S	0.46	1.31	535.0195	C23H12N4O10S	0.43	0.52
315.0399	C10H12N4O6S	0.60	1.20	541.0358	C27H14N2O9S	0.33	0.52
315.0978	C8H20N4O7S	0.88	2.50	547.9685	C23H7N3O12S	0.52	0.30
316.0711	C9H19NO9S	1.00	2.11	549.1027	C20H26N2O14S	0.70	1.30
317.0191	C9H10N4O7S	0.78	1.11	549.2957	C24H46N4O8S	0.33	1.92
320.1898	C15H31NO4S	0.27	2.07	550.1061	C21H29NO12S2	0.57	1.38
320.9817	C12H6N2O7S	0.58	0.50	550.2999	C33H45NO4S	0.12	1.36
323.1066	C15H20N2O4S	0.27	1.33	559.1499	C25H28N4O9S	0.36	1.12
323.9975	C16H7NO5S	0.31	0.44	569.3256	C29H50N2O7S	0.24	1.72
324.1059	C19H19NO2S	0.11	1.00	583.0824	C30H20N2O9S	0.30	0.67
324.1122	C12H23NO7S	0.58	1.92	593.1299	C22H30N2O15S	0.68	1.36
324.9887	C10H6N4O7S	0.70	0.60	594.9625	C17H12N2O20S	1.18	0.71
326.0161	C13H13NO5S2	0.38	1.00	603.0354	C28H16N2O12S	0.43	0.57
326.0551	C10H17NO9S	0.90	1.70	603.0358	C16H20N4O19S	1.19	1.25
326.9598	C7H8N2O9S2	1.29	1.14	604.3168	C29H51NO10S	0.34	1.76
327.0762	C12H16N4O5S	0.42	1.33	605.0304	C31H14N2O10S	0.32	0.45
328.9718	C10H6N2O9S	0.90	0.60	605.0309	C19H18N4O17S	0.89	0.95
329.0290	C8H14N2O10S	1.25	1.75	612.2589	C40H39NO3S	0.08	0.98
329.0556	C11H14N4O6S	0.55	1.27	616.9732	C22H10N4O16S	0.73	0.45
330.0869	C10H21NO9S	0.90	2.10	620.0252	C27H15N3O13S	0.48	0.56
331.0350	C10H12N4O7S	0.70	1.20	621.0464	C16H22N4O20S	1.25	1.38
331.9390	C6H7NO11S2	1.83	1.17	622.2757	C37H41N3O4S	0.11	1.11
332.9930	C12H6N4O6S	0.50	0.50	622.9895	C26H12N2O15S	0.58	0.46
333.0222	C11H14N2O6S2	0.55	1.27	626.2741	C29H45N3O10S	0.34	1.55
334.9551	C11H4N4O5S2	0.45	0.36	631.3939	C39H56N2O3S	0.08	1.44
335.0185	C10H12N2O9S	0.90	1.20	640.2858	C37H43N3O5S	0.14	1.16

6 Appendix

336.0734	C16H19NO3S2	0.19	1.19	657.9628	C22H13NO21S	0.95	0.59
337.0904	C12H22N2O5S2	0.42	1.83	673.1144	C33H26N2O12S	0.36	0.79
337.9401	C7H5N3O9S2	1.29	0.71	691.0463	C26H20N4O17S	0.65	0.77
338.0492	C18H13NO4S	0.22	0.72	695.5078	C36H76N2O6S2	0.17	2.11
338.9720	C15H4N2O6S	0.40	0.27	699.3004	C29H52N2O15S	0.52	1.79
339.0035	C11H8N4O7S	0.64	0.73	705.3257	C36H54N2O8S2	0.22	1.50
339.0291	C13H12N2O7S	0.54	0.92	705.3262	C32H54N2O13S	0.41	1.69
342.0497	C10H17NO10S	1.00	1.70	713.4738	C33H70N4O10S	0.30	2.12
342.1014	C15H21NO6S	0.40	1.40	714.1234	C31H29N3O15S	0.48	0.94
342.1230	C12H25NO8S	0.67	2.08	714.4773	C34H73N3O8S2	0.24	2.15
342.9778	C13H4N4O6S	0.46	0.31	715.1290	C28H32N2O18S	0.64	1.14
343.9569	C7H7NO13S	1.86	1.00	716.4729	C33H71N3O11S	0.33	2.15
343.9711	C11H7NO10S	0.91	0.64	719.5447	C39H80N2O5S2	0.13	2.05
344.1025	C11H23NO9S	0.82	2.09	740.4930	C36H75N3O8S2	0.22	2.08
346.9552	C12H4N4O5S2	0.42	0.33	741.4954	C36H74N2O11S	0.31	2.06
347.9858	C11H11NO8S2	0.73	1.00	745.2293	C35H42N2O14S	0.40	1.20

6.4 List of Related Publications and Presentations

Peer-reviewed publications:

Zannoni, N., Leppla, D., Lembo Silveira de Assis, P. I., Hoffmann, T., Sá, M., Araújo, A., and Williams, J.: Surprising chiral composition changes over the Amazon rainforest with height, time and season, *Commun. Earth Environ.* (Communications Earth & Environment), 1, 9317, <https://doi.org/10.1038/s43247-020-0007-9>, 2020

Tong, H., Zhang, Y., Filippi, A., Wang, T., Li, C., Liu, F., Leppla, D., Kourtchev, I., Wang, K., Keskinen, H.-M., Levula, J. T., Arangio, A. M., Shen, F., Ditas, F., Martin, S. T., Artaxo, P., Godoi, R. H. M., Yamamoto, C. I., Souza, R. A. F. de, Huang, R.-J., Berkemeier, T., Wang, Y., Su, H., Cheng, Y., Pope, F. D., Fu, P., Yao, M., Pöhlker, C., Petäjä, T., Kulmala, M., Andreae, M. O., Shiraiwa, M., Pöschl, U., Hoffmann, T., and Kalberer, M.: Radical Formation by Fine Particulate Matter Associated with Highly Oxygenated Molecules, *Environmental science & technology*, 53, 12506–12518, <https://doi.org/10.1021/acs.est.9b05149>, 2019

Oral presentations:

03/2019

Leppla D., Praß M., Holanda B., Ditas F., Pöhlker C., Solci M.C., Hoffmann T.: “Chemical characterization of submicrometer aerosol particles from the Amazon rainforest” *ANAKON*, Münster, Germany

Poster presentations:

09/2018

Leppla D., Hoffmann T.: “Chemical characterization of submicrometer aerosol particles from the Amazon rainforest” *Umwelt 2018*, Münster, Germany

04/2019

Leppla D., Praß M., Ditas F., Pöhlker C., Hoffmann T.: “High resolution mass spectrometric study of secondary organic aerosol particles from the Amazon rainforest” *European Geoscience Union*, Vienna, Austria

09/2019

Leppla D., Praß M., Zannoni N., Ditas F., Pöhlker C., Williams J., Hoffmann T.: “High resolution mass spectrometric study of secondary organic aerosol particles from the Amazon rainforest” ATTO Workshop, Manaus, Brazil

10/2019

Leppla D., Praß M., Zannoni N., Ditas F., Pöhlker C., Williams J., Hoffmann T.: “High resolution mass spectrometric study of secondary organic aerosol particles from the Amazon rainforest” The Fourth Sino-European School on Atmospheric Chemistry (SESAC4), Shanghai, China

05/2020

Leppla D., Zannoni N., Kremper L., Praß M., Ditas F., Pöhlker C., Williams J., Vogel A., Hoffmann T.: “High resolution mass spectrometric study of secondary organic aerosol particles from the Amazon rainforest” *European Geoscience Union*, Online Conference

